PHD

The analysis of planar waveguide structures by the extended spectral domain approach

Fan, Zhibo

Award date:
1994

Awarding institution:
University of Bath

THE ANALYSIS OF PLANAR WAVEGUIDE STRUCTURES BY THE EXTENDED SPECTRAL DOMAIN APPROACH

Submitted by
Zhibo Fan
for the degree of
Doctor of Philosophy
of the University of Bath

Author's Signature Fan Zhibo Date July 12, 1994

ProQuest LLC
789 East Eisenhower Parkway
P.O. Box 1346
Ann Arbor, MI 48106-1346

To my wife Huang Huang

SUMMARY

This thesis is concerned with the analysis of several planar waveguide structures by using the extended spectral domain approach and the demonstration of their various circuit applications.

This extended method offers several additional advantages such as the applicability to non-uniform cross section geometries, use of only one set of basis functions and easy derivation of dyadic Green's function by a recursive algorithm. Fast convergence is achieved and the accuracy of the method is verified by comparison with measured results.

The method is applied to CPW loaded IDG, broadside coupled strip IDG, parallel coupled IDGs, asymmetrical multilayer ferrite–loaded finline and two–layer ferrite–loaded IDG. The effects of various structural and material parameters on the electrical characteristics such as S-parameters and nonreciprocal propagation constants are investigated. There exist the optimum values of these parameters for the best performance of the circuits.

Attractive advantages of CPW loaded IDG are identified for the use in MMICs. Feasibility of strong and weak directional couplers using broadside coupled strip IDG is demonstrated. Usefulness of parallel coupled IDGs for broadband flat coupling is also illustrated. In addition, high nonreciprocity of asymmetrical multilayer ferrite–loaded finline and two–layer ferrite–loaded IDG is shown for the realization of efficient nonreciprocal phase shifters.

ACKNOWLEDGEMENTS

The author would like to thank Dr. S.R. Pennock not only for his supervision and discussion during the course of this work, but also for his help and encouragement.

The author also thanks fellow postgraduate students in the Wolfson Laboratory and D. Hatten for their friendship and many useful contributions to the experimental aspect of the work.

This work was funded by a technical cooperation grant from the British Council and Chinese Government, and the author is grateful for their support.

PUBLICATIONS ARISING FROM THIS WORK

1. Z. Fan and S. R. Pennock, "Propagation characteristics of ferrite loaded inset dielectric guide," in *Proceedings of the 23rd European Microwave Conference*, Madrid, Spain, September 1993, pp.129–131.

2. Z. Fan and S. R. Pennock, "Analysis of Broadside coupled strip inset dielectric guide," in *IEEE MTT–S International Microwave Symposium Digests*, Atlanta, USA, June 1993, pp.839–842.

3. Z. Fan and S. R. Pennock, "Some recent work on inset dielectric guides with anisotropic substrate or magnetized ferrite," in *Proceedings of the Progress in Electromagnetics Research Symposium*, California, USA, July 1993, p.750.

4. Z. Fan and S. R. Pennock, "Asymmetrical fin lines containing anisotropic dielectric substrate or magnetized ferrite," in *Proceedings of URSI Radio Science Meeting*, Michigan, USA, June 1993, p.396.

5. Z. Fan and S. R. Pennock, "Analysis of coplanar waveguide loaded inset dielectric guide by the extended transverse resonance diffraction method," in *Proceedings of URSI Radio Science Meeting*, Michigan, USA, June 1993, p.300.

6. Z. Fan and S. R. Pennock, "Rigorous analysis of asymmetrical ferrite loaded unilateral finline," in *Proceedings of CSEEE Electrical and Electronic Engineering Meeting*, London, UK, Nov. 1993, pp.130–134.

7. Z. Fan, S. R. Pennock and J. Huang, "Coplanar waveguide loaded inset dielectric guide — a novel MIC transmission line," accepted for presentation in *the International Conference on Computational Electromagnetics and its Applications*, Beijing, P.R. China, November 1994.

8. Z. Fan and S. R. Pennock, "Broadside coupled–strip inset dielectric guide and its directional coupler application," submitted for publication in *IEEE Trans. Microwave Theory Tech.*

9. Z. Fan and S. R. Pennock, "Analysis of asymmetrical multilayer ferrite–loaded finlines," accepted for presentation in *the 24th European Microwave Conference*, Cannes, France, September 1994.

10. Z. Fan and S. R. Pennock, "Characteristics of coplanar waveguide loaded inset dielectric guide," accepted for presentation in *the 24th European Microwave Conference*, Cannes, France, September 1994.

Contents

Chapter 1

INTRODUCTION

1.1 Microwave and Millimeter Wave Technologies

Microwave techniques have been increasingly adopted in such diverse applications as radio astronomy, long–distance communications, space navigation, radar systems, and missile electronic systems. In recent years there have been evolutionary developments in microwave techniques, including novel system architectures with more operational capabilities and the creation of new commercial and medical applications. Such developments are attributed to advances in solid–state devices, insulating and semiconducting materials, manufacturing techniques, and the simultaneous evolution of computing techniques. As a result, monolithic microwave integrated circuits (MMICs) have been realized, intensively investigated and widely used in many system applications [1]. These planar circuits offer potential advantages in respect of their small size, low weight, low cost, high reliability and reproducibility when combined with photolithographic techniques.

Microstrip has been the most popular transmission line used in MMIC design, partly because of the vast amount of design information available and because a

large number of circuit elements can be made with it [2]. However, one disadvantage of using microstrip is that via holes are required to mount shunt devices. These via holes can introduce significant inductance and degrade performance. Another drawback is the sensitivity to substrate thickness, which further increases design problem at higher frequencies.

Because of these inherent limitations in microstrip, the search continues for alternative transmission media which would present potential advantages over the microstrip line or supplement it. For instance, coplanar waveguide has been suggested for use in MMICs [3]. It allows easy series and shunt device mounting and offers improved electrical characteristics such as lower conductor loss, less sensitivity to substrate thickness, and wider range of impedance. These advantages have aroused considerable recent interest in MMIC design. Finline has also emerged as an alternative to the microstrip line for microwave integrated circuits [4]. It can be integrated with other planar structures, compatible with standard waveguide and is superior to microstrip line in a number of aspects. Almost all the types of components, passive and active, reciprocal and nonreciprocal, have been realized using the finline integration technique. Besides there are several other planar transmission structures developed for use in MMICs, among them are slot lines, coplanar strips, and suspended (and inverted) striplines [5].

In the past decade, much research has been directed toward the use of millimeter and submillimeter–wave frequencies for the transmission of information. The application of the millimeter and submillimeter–wave technology offers a number of commonly known advantages. These include smaller and lighter devices, greater information–carrying capacity, and more antenna gain for a given physical antenna size.

However, at these higher frequencies, the above–mentioned planar transmission structures have several drawbacks. As to microstrip and coplanar waveguide, these drawbacks include frequency–dependent mechanisms such as parasitic coupling due to the propagation of surface waves and radiation occurring at discontinuities. These effects can seriously deteriorate electrical performance, and result in time–intensive and costly design cycles. To reduce or eliminate these deleterious effects, very sophisticated packages are often required, leading to higher cost, larger volume and higher circuit weight [6].

As the wavelength involved becomes shorter, it is more difficult to fabricate components using conventional finline technology and the cost of the circuits increases dramatically because of more stringent mechanical tolerances.

In order to overcome performance and manufacturing problems encountered with the conventional millimeter–wave technology, conventional planar waveguide structures need to be modified or new planar lines need to be invented. Consequently new millimeter–wave integrated circuits with superior electrical performance could be developed with easier fabrication and lower cost. This in effect was the stimulus for the work presented in this thesis. Also the development of accurate and efficient computer–aided design (CAD) technique is of considerable importance to achieve optimum performance at low cost because the designs of the millimeter–wave circuits cannot easily be tuned and adjusted after fabrication.

1.2 Modified Coplanar Waveguide

Coplanar waveguide (CPW) consists of a centre strip on the surface of a substrate with two ground planes located parallel to and in the plane of the strip, as shown in Figure 1.1.a. Since it was invented by Wen in 1969 as a planar transmission line [7], CPW has received increasing attention. When compared to microstrip which has been widely used in the MMICs, CPW possesses several distinct advantages [3]. Its uniplanar structure eliminates the need for via holes to connect the centre conductor to ground planes and thus simplifies the fabrication process. It also permits easy series and shunt connections of passive and active solid–state devices. CPW has been shown to exhibit lower conductor loss than microstrip for a wide range of line impedances. It is easy to make transitions from CPW to other transmission lines, which leads to greater flexibility in the design of circuits [8]. Due to these attractive features, the use of CPW is becoming more important in the design of the MMICs and interest is expected to increase dramatically within next several years [9]–[10]. To emphasize the importance of the use of CPW in the design of MMICs and to present the future trends in millimeter–wave components and subsystems, a special issue of IEEE Transaction on Microwave Theory and Technique was published in September 1993. In this special issue, a number of theoretical analyses for the characterization of the uniform CPW and discontinuities were presented and various novel high–performance circuits using CPW were described.

The main disadvantage of the CPW is that a coupled slotline mode can be excited by nonsymmetrical CPW discontinuities such as bends and T–junctions. This mode has opposite potentials on the two ground planes with zero potential at the centre strip. It may cause the CPW to radiating excessively and increase the cross–talk between lines, and must therefore be eliminated. Usually air bridges

are used to equate the potentials of the two ground planes and thus eliminate the parasitic mode [11]. However, use of the air bridges increases the complexity in the design of the MMICs, and also may cause parasitic effects such as radiation depending their electrical size and location. Furthermore, these air bridges are potentially costly to build, especially in large CPW circuits where a large number of these air bridges may be needed.

Practical realizations of CPWs usually have an additional ground conducting plane on the opposite side of the substrate (Figure 1.1.b). The most important purpose of this additional plane is to provide a mechanism to remove the heat from the active devices in the CPW circuits. It also improves mechanical strength, and reduces radiation effects and the dispersion. Unfortunately, parallel–plate modes exist between the circuit plane and the additional ground plane [12]. These modes can provide a means for undesirable coupling between circuit elements. Also the loss due to leakage in the form of the lowest–order parallel–plate mode without cutoff frequency is unavoidable. In addition, this additional plane increases the complexity and cost in the realization of potential equalization for all the three ground planes.

In order to overcome the above–mentioned problems, the CPW structure needs to be further modified. One aim of this thesis is to consider the combination of CPW with inset dielectric guide (Figure 1.1.c). and to present computed and measured results for propagation characteristics of this new structure. Inset dielectric guide (IDG) has been recently proven to be a low–cost and low–loss transmission line [13]. With good mechanical and electrical properties, it has shown considerable potential for microwave and millimeter–wave circuit and antenna applications. This guide possesses an air–dielectric interface. Planar transmission lines may be fabricated at this interface with little difficulty. Indeed, simple integration of a

microstrip line has been realized [14].

The modified CPW, proposed here, is obtained by placing the CPW on the air–dielectric interface of the IDG. This CPW loaded IDG combines the advantages of CPW and IDG without some of the problems associated the conventional CPW.

1. No air bridges are needed for ground plane equalization.
2. Due to good field confinement in the groove, low–permittivity dielectric substrate can be used. This results in a low effective dielectric constant, and as the physical size can then be larger for a given monomode bandwidth, mechanical tolerances are relaxed.
3. In coplanar waveguide propagating surface modes in the substrate allow stray coupling between circuits and radiation loss from discontinuities in the circuits. The side walls of the groove prevent propagation of such surface modes.
4. Heat–sinking capability is greatly improved due to the proximity of the IDG conductor block.
5. With 4 structural dimensions and the substrate permittivity as design degrees of freedom, a wide range of characteristic impedance and single–mode frequency range can be obtained, making the design process more flexible.

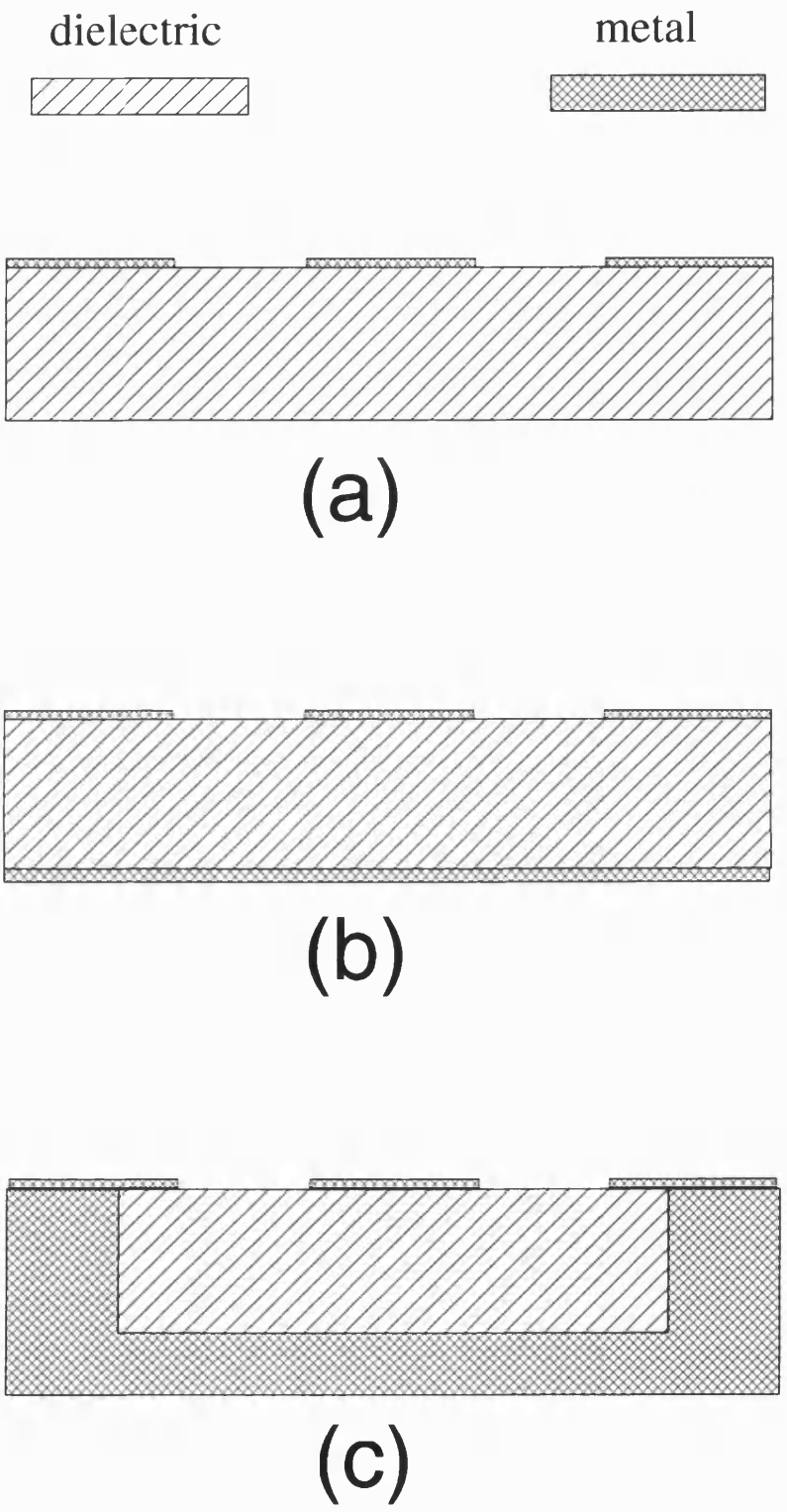

Figure 1.1: (a) Coplanar waveguide, (b) Conductor–backed coplanar waveguide and (c) Coplanar waveguide loaded inset dielectric guide

1.3 Asymmetrical Finline

Finline has been extensively used as a planar transmission medium for constructing millimeter–wave circuits [15]. Desirable features of finline include wide single–mode bandwidth, moderate attenuation, compatibility with beam–lead and chip devices, easy transition to the standard waveguide, possible combination with other types of planar transmission media. Due to these attractive advantages, almost every type of component has been realized using the finline integration technique. The typical finline is the slot line enclosed in a waveguide–like split–block housing, as shown in Figure 1.2.a. This traditional structure exhibits certain disadvantages, such as, requirement of fairly precise machining of the casing to ensuring that the dielectric is properly supported, poor intrinsic isolation between adjacent circuit elements resulting in unwanted feedback paths, and others which are listed in [16].

Asymmetrical finline (Figure 1.2.b) was proposed by Espes et al for space applications [16]. It consists of a slotline inserted into an asymmetrical housing. This new type of finline offers several advantages over the traditional (symmetrical) finline,

1. Better electromagnetic isolation of the line
2. Simplified machining of the enclosure
3. Ease of substrate and device mounting
4. Wider single–mode bandwidth
5. An additional degree of freedom to obtain the characteristic parameters

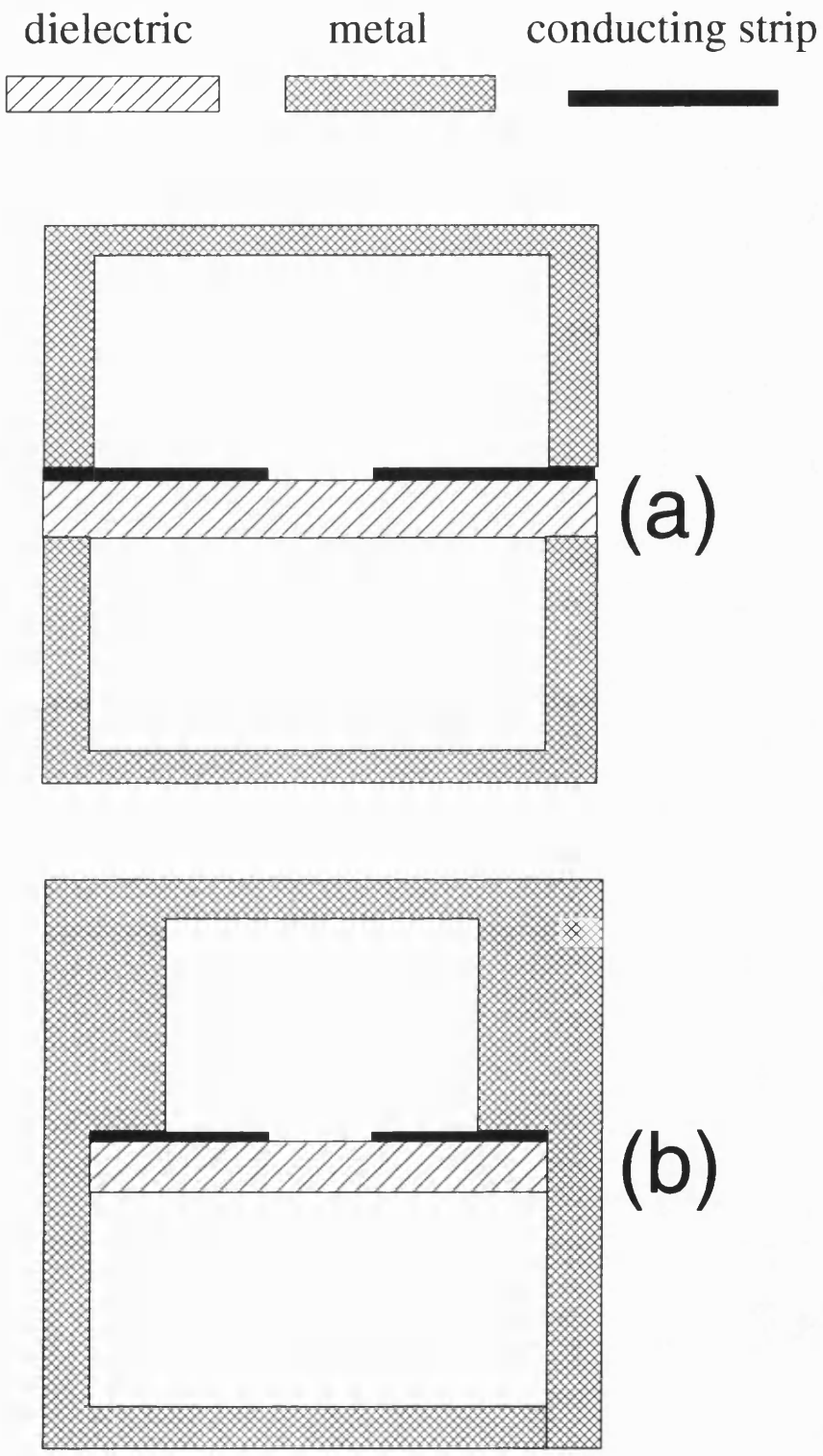

Figure 1.2: (a) Traditional finline and (b) Asymmetrical finline

Several devices such as filters and mixers were developed in the asymmetrical finline form and the spectral domain method was also applied to the analysis of the propagation characteristics of the asymmetrical finlines with a dielectric substrate [16]–[17]. For the realization of nonreciprocal components at millimeter wave frequencies, ferrite layers need to be inserted into multilayer media. However, so far no efforts have been devoted to the analysis of asymmetrical multilayer finlines with magnetized ferrites. On the other hand, several methods which include the field expansion, mode–matching, network analysis and the spectral domain approach [18]–[21] have been reported for the analysis of symmetrical single and two–layer ferrite–loaded finlines. However, only single–ferrite structures were considered and only the differential phase shift was discussed.

One of the the purposes of this thesis is to extend the spectral domain method for the accurate full wave analysis of asymmetrical ferrites containing one or more magnetized ferrites and to investigate effects of various multilayer configurations on nonreciprocity and bandwidth.

1.4 Inset Dielectric Guide

Inset dielectric guide (IDG) has become a useful planar transmission structure appropriate for applications in microwave and millimeter–wave frequency range [22]. This structure may be considered as a practical evolution from the image line, retaining many advantages of the image line without fabrication and loss problems. It is composed of a dielectric–filled groove in a metal ground plane, whose cross section is shown in Figure 1.3.a. As a transmission line it demonstrates some excellent advantages:

1. Good confinement of the electromagnetic field
2. Low radiation loss at bends and low transmission loss
3. Ease of fabrication by use of plastic moulding and spray metallization techniques
4. Very wide single–mode frequency range achieved by use of the multilayer dielectric
5. Easy inclusion of active devices

For the purpose of signal feeding and processing, it would be useful to employ microstrip–type circuitry. It is well known that the main problem of open microstrip circuits is the excitation of surface waves from discontinuities in circuits. The surface waves cause stray coupling between components, and may degrade the circuit performance. However, the propagation of the surface waves can be prevented if the microstrip circuit is housed in an IDG. Furthermore, the electrical characteristics can be controlled by the dimensions of the IDG and the location of the circuits. This results in the recent developments of several novel waveguide structures. They include microstrip loaded IDG [14], embedded strip IDG [23] and broadside coupled strip IDG [24]. These structures have been receiving considerable attention.

The IDG has found useful applications in antennas [25]–[26]. Leaky–wave dipole array antennas can be easily obtained by placing conducting strips on the air–dielectric surface, which form radiating dipoles. The polarization properties of IDG allow fabrication of both horizontally and vertically polarized antennas. One and two–dimensional antenna arrays have been developed, and desirable features such as good input match, low cross polarization, high efficiency and low mutual coupling have been demonstrated experimentally.

The IDG has also shown the potential for directional coupler applications [27]–[28]. These couplers can be designed by using parallel coupled IDGs and have shown very low reflection coefficient and high isolation. It has also been found that broadband flat coupling characteristic can be achieved by the use of holes in the separating wall between two deep IDGs [29].

There has been considerable interest in theoretical investigations of single–line IDG structures. The effective dielectric constant method was first used by Zhou and Itoh to analyze the IDG [30]. It gave useful approximate results for the fundamental mode. By taking into account the field singular boundary condition at the 90^0 metal edges, Rozzi and Hedges used transverse resonance diffraction (TRD) to obtain accurate results for the propagation characteristics of the first few modes of the IDG [13]. The TRD was then extended to analyze microstrip loaded IDG, embedded strip IDG and broadside coupled strip IDG [23] [24]. Published data for broadside coupled strip IDG (Figure 1.3.b) are limited to the propagation constants of two fundamental modes only. However, the propagation constants of higher order modes should be determined in order to determine the frequency range where only two fundamental modes propagate. Furthermore, a knowledge of the characteristic impedances of two fundamental modes is required if circuits, such as couplers, filters and antennas, are to be designed using broadside coupled strip IDG.

The TRD technique has also been applied to the analysis of the parallel coupled–line IDGs [27]–[28]. Since the analysis was based on the LSE and LSM field approximation, it was valid only for two special cases, that is, deep and shallow slots. The analysis was also inadequate for the frequencies near the cutoff. Although the parallel coupled IDGs (Figure 1.3.c) are useful for the design of directional couplers, the effects of various structural parameters on the coupling

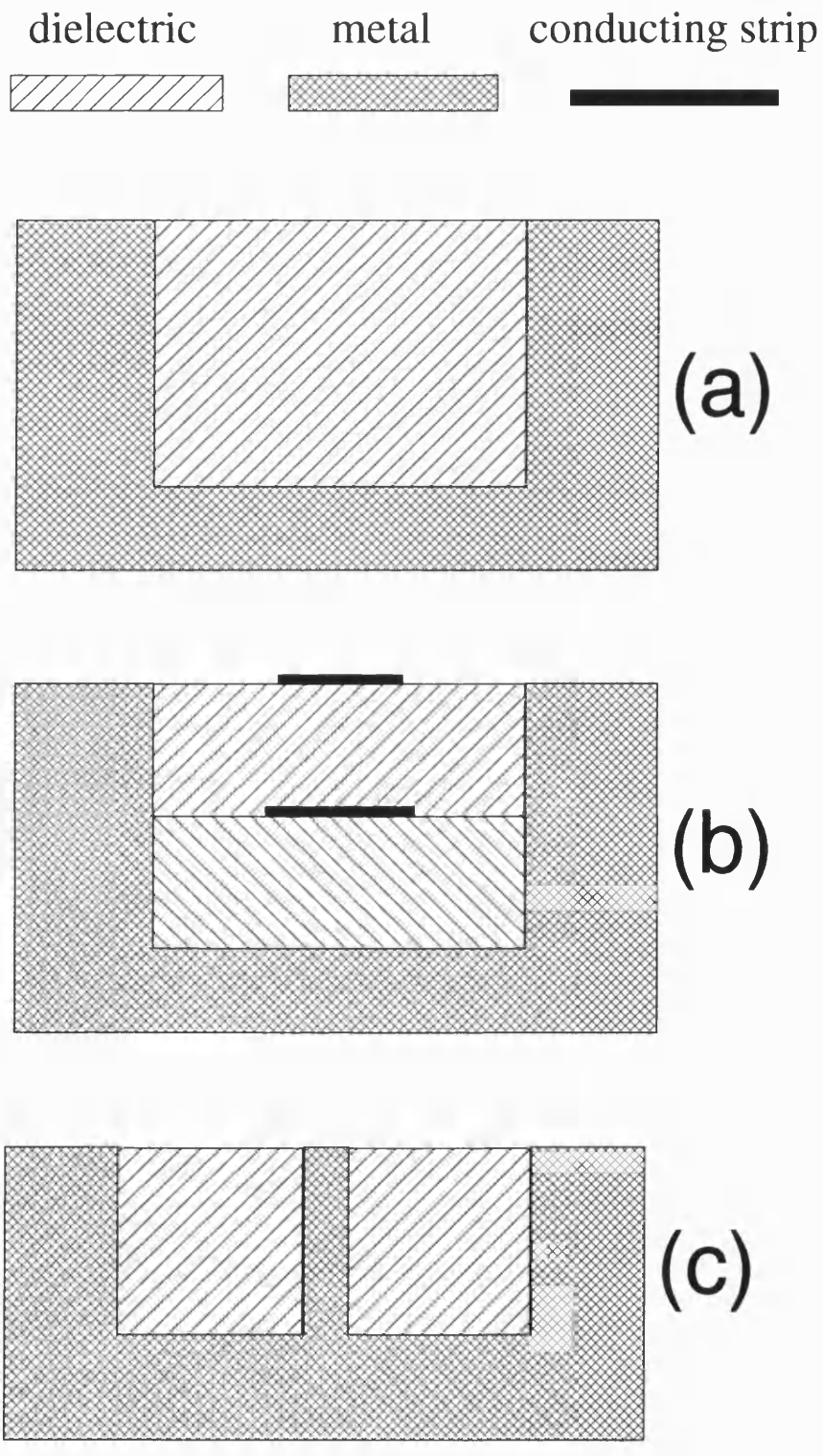

Figure 1.3: (a) Inset dielectric guide, (b) broadside coupled strip inset dielectric guide and (c) parallel coupled inset dielectric guide

characteristic and bandwidth have not been investigated. Therefore, a rigorous hybrid–mode analysis is needed to study these effects.

In all the above analyses of the IDG structures, isotropic dielectric substrates were assumed. However, the ferrite substrates are often used to realize the nonreciprocal devices such as nonreciprocal phase shifters and circulators. Therefore, for the design of the nonreciprocal devices using the IDG technique, the analysis of multilayer IDG with magnetized ferrites is required.

Some of the work presented in this thesis is devoted to the accurate analyses of the electrical characteristics of broadside coupled strip IDG, parallel coupled IDGs and multilayer ferrite–loaded IDG, and demonstration of their possible applications to directional couplers and nonreciprocal phase shifters. The effects of various structural and material parameters on these characteristics are illustrated and obtained results can be useful for the accurate design of these components.

1.5 Survey of Methods of Analysis

Microwave and millimeter–wave integrated circuits are very expensive to manufacture. Once fabricated, they are very difficult to tune for optimum performance. An accurate knowledge of the electrical properties of the circuit media are required so that device performance can be predicted confidently, thus avoiding time–consuming, and costly, design cycles. Various methods of analysis have been described in the literature to analyze planar transmission structures. In general, they can be divided into two groups, that is, quasi–static methods and dynamic full–wave methods.

In the quasi–static methods, the nature of the mode of propagation is considered to be pure or quasi TEM. Conformal mapping techniques [31] and numerical techniques [32] are often used to solve the Laplace's equation for the electric field potential with given boundary conditions. The capacitance is computed for the derived potential and the static parameters such as propagation constant and characteristic impedance can in turn be derived in terms of the capacitance. These quasi–static methods are very simple and computationally efficient, and adequate for designing circuits at lower frequencies. However, they are not valid at high frequencies and cannot be used for lines where the propagation of quasi–TEM mode is not present.

The dynamic full–wave methods are used to solve the actual electromagnetic field in waveguides and are of importance for rigorously determining characteristics in a wide frequency band, for the study of higher modes and for the accurate calculation of their cutoff frequencies. The methods include finite element method, finite difference technique, transmission line matrix method, mode matching, method of lines, transverse resonance diffraction and spectral domain approach. Many of these methods are discussed in great detail in [33]. Each of these methods has advantages and disadvantages. For instance, the finite element method is time consuming, it gives slow convergence to a solution and requires a large amount of computer memory, but it may be easily applied to structures with complex geometries. On the other hand, the spectral domain approach is numerically efficient, but its range of applicability is limited. In reality, a suitable method is chosen on basis of the trade-offs between accuracy, storage requirement, versatility, etc. and is often structure dependent. In the following two subsections, the brief review of the transverse resonance diffraction and spectral domain method will be given, and their advantages and disadvantages will be illustrated.

1.5.1 Transverse Resonance Diffraction

Transverse resonance diffraction is a space–domain method [13]. In this method, the field is constructed from the superposition of a suitable set of LSE and LSM modes, whose components consists of five field components. The admittance operators are then derived in the space domain, relating the magnetic field to the electric field in each of regions. By enforcing boundary conditions on the field components at the interface between various regions and applying Galerkin's method, the eigenvalue equation for the propagation constant can be obtained.

This method has several advantages. Only one set of basis functions is needed for the expansion of two tangential field or current components and as a result the numerical efficiency is increased. Accuracy of the solutions can be improved by increasing the number of basis functions and few terms are needed for adequate convergence. This method can be applicable to structures with non–uniform cross–sectional geometry. It has been used to efficiently analyze various waveguides including microstrip [34], image line [35], finline [36] and IDG [22], and accurate results have been demonstrated through comparison with measurements. However, the method has not been applied to analyze the structures with anisotropic media such as magnetized ferrites.

1.5.2 Spectral Domain Approach

Generally speaking, the spectral domain approach (SDA) refers to the application of integral transforms, such as the Fourier transforms, together with Galerkin's procedure to the solution of boundary-value problems [37]. By a means of integral transforms, the partial differential Maxwell's equations can be reduced to

ordinary ones, which in many cases are amenable to further analytical processing. The spectral domain approach has been applied to analyze a number of planar transmission lines structures, and proven to be powerful, accurate and numerically efficient [38]. The SDA has several features: 1. easy formulation of the problem by using integral transforms, 2. variational nature in determination of the propagation constant, 3. identification of the physical nature of the mode for each solution corresponding to the basis functions, 4. high numerical efficiency due to a significant analytical preprocessing and 5. permission of systematic improvement of the solution to a desired degree of accuracy. Because of its advantages, SDA has become the most preferred and prominently used numerical technique for the analysis of planar circuits in layered media.

The application of SDA first requires the computation of the spectral dyadic Green's function. A large number of works can be found in the literature dealing with the Green's function. The spectral domain immitance approach was proposed by Itoh for the analysis of the planar structures with isotropic dielectric media [39]. The method is based on the decomposition of fields into TE and TM modes. The transverse equivalent circuit concept in conjunction with a simple coordinate transformation rule is used to derive the dyadic Green's function in the transformed domain. This method can be easily extended to uniaxial anisotropic dielectric with its optical axis perpendicular to the interfaces, in which the fields can be also written as a superposition of TE and TM waves. The particular advantage of the method is the simplicity of the formulation process, which can be accomplished almost by inspection. However, this method cannot be applied to the structures with non-uniform cross-sectional geometry. To overcome this difficulty, a mixed spectral domain approach was suggested by Chan, et al., where different Fourier transforms are used for different regions [17]. The magnetic field Green's function for different regions is also derived by using the equivalent

transmission lines for the TE and TM modes. In more general anisotropic substrates such as magnetized ferrites, all fields are coupled and are neither TE or TM. Therefore these anisotropic substrates can not be analyzed by the spectral domain immitance approach or the mixed spectral domain approach. The matrix method, proposed by Krowne, can deal with these anisotropic media, which does not require splitting the fields into TE and TM [40]. In this method, the fields are described based on four–element vectors and the Green's function is derived by employing a 4 x 4 matrix in the spectral domain. This method can allow simultaneous permittivity, permeability, and optical activity anisotropy. Nevertheless, there is no simple way to build up a general algorithm to analyze general multilayered and multiconductor structures. To deal with any numbers of layers and conductors and any kind of substrate, the equivalent boundary method was developed by Mesa, et al. [41]. The method is partly based on the equivalence and uniqueness theorems of electromagnetic fields, and makes possible the reduction of the multilayer problem to a chain of much simpler problems of just one or two layers. However, one of the limitations of the matrix method and equivalent boundary method is that no discontinuity in the substrate in the lateral direction is allowed.

Next step in applying the SDA is to enforce the boundary conditions on the conductors or slots by employing Galerkin's method. This results in a matrix equation for the electric field or current expansion coefficients. Two sets of basis functions are often used to expand two tangential electric field or current components, which satisfy different singular conditions. In order to main high accuracy and fast convergence solutions, basis functions are usually chosen such that they satisfy the edge conditions and they are Fourier transformable.

In this thesis the spectral domain approach is further extended to analyze several

planar structures with non–uniform cross–sectional geometry and /or with magnetized ferrites. This extended spectral domain method offers several additional advantages including

1. Applicability to the structures with non–uniform cross–sectional geometry
2. Easy derivation of dyadic Green's function for anisotropic multilayer media by a recursive algorithm
3. Use of only one set of basis functions for the calculation of Fourier transforms of two expanded tangential electric field or current components at one interface

1.6 Outline of the Thesis

This section briefly outlines the content of this thesis. The remainder of the work is divided into 5 chapters.

In chapter 2 CPW loaded IDG is described, in comparison with conventional coplanar waveguide, and analyzed using the extended spectral domain method. The resonant section technique and time-domain step response facility on an HP8510B Network Analyzer are used to measure propagation constants and characteristic impedances, respectively. Comparison between computed and measured data shows good agreement. Numerical results are presented to illustrate effects of various structural and material parameters on propagation characteristics.

Chapter 3 presents the analysis of broadside coupled strip inset dielectric guide.

In addition to propagation constants for two fundamental and higher order modes, the characteristic impedances for two fundamental modes are calculated using the total propagating power and longitudinal strip currents. A 4–port equivalent circuit is described. The effects of various structural parameters on S parameters are investigated. The brief outline of the coupler design procedure is given, with two examples of -3 dB and -16 dB directional couplers with good input match and high directivity. Measurements of the S parameters are described and these results are in good agreement with the analysis. The usefulness of the proposed coupler with transitions to coaxial cables is confirmed experimentally.

Chapter 4 is devoted to an efficient hybrid–mode analysis of parallel coupled IDGs. The simple expression for scattering coefficients is given, based on the difference of propagation constants of the dominant even and odd modes. Good convergence of the solution is shown. By comparison to experimental data this model is seen to give accurate calculations of propagation and coupling characteristics. The accuracy of the method is also checked by examining the results for the limiting cases. Numerical results are shown as a function of frequency, guide separation and slot height. An example of -3 dB coupler is given and shows quite broadband flat coupling characteristic.

In chapter 5 the analysis of asymmetrical multilayer finlines containing magnetized ferrites is described. The field in magnetized ferrites with the permeability tensor is derived. A recursive algorithm is introduced to obtain the Fourier transformed dyadic Green's function for different regions. Numerical results are first compared with the available calculated and measured data for particular cases and then given for various structural and material parameters. The advantages of asymmetrical version of finlines are demonstrated and the effects of various multilayer configurations on nonreciprocity and bandwidth are investigated. High

nonreciprocity and wide bandwidth of the four–layer dual–ferrite structure are demonstrated.

With a view to applying the IDG structures to nonreciprocal devices such as nonreciprocal phase shifters, the analysis of multilayer ferrite-loaded IDG is also presented. Numerical results for nonreciprocal propagation characteristics are shown for different values of the permittivity of the dielectric layer. A wide range of differential phase shift of the two–layer ferrite–dielectric structure is illustrated.

Finally, in chapter 6 the main conclusions are drawn from the work described herein and further research is suggested.

References

[1] I. Kneppo and J. Fabian, "Microwave Integrated Circuits," *Chapman & Hall*, 1994

[2] D. A. Williams, "Millimeter–wave components and subsystems built using microstrip technology," *IEEE Trans. Microwave Theory Tech.*, vol.MTT-39, pp.768–774, May 1991.

[3] R. W. Jackson,"Considerations in the use of coplanar waveguide for millimeter–wave integrated circuits," *IEEE Trans. Microwave Theory Tech.*, vol.MTT-34, pp.1450–1456, Dec. 1986.

[4] P.J. Meier, "Integrated fin–line millimeter components," *IEEE Trans. Microwave Theory Tech.*, vol.MTT-22, pp.1209–1216, Dec. 1974.

[5] T. Itoh, "Overview of quasi–planar transmission lines," *IEEE Trans. Microwave Theory Tech.*, vol.MTT-37, pp.275–280, Feb. 1989.

[6] R.S. Pengelly and P. Schumacher, "High performance 20 GHz Package for GaAs MMICs," *Microwave Systems News & Microwave Techniques*, pp.10–19, Jan. 1988

[7] C.P. Wen, "Coplanar waveguide: a surface strip transmission line suitable for nonreciprocal gyromagnetic device applications," *IEEE Trans. Microwave Theory Tech.*, vol.MTT–17, pp.1087–1090, Dec. 1969.

[8] T. Hirota, Y. Tarusawa and H. Ogawa, "Uniplanar MMIC hybrids — a proposed new MMIC structure," *IEEE Trans. Microwave Theory Tech.*, vol.MTT-35, pp.576–581, June 1987.

[9] J.K.A. Everard and K.K.M. Cheng, "High performance direct coupled bandpass filters on coplanar waveguide," *IEEE Trans. Microwave Theory Tech.*, vol.MTT–41, pp.1568–1573, Sept. 1993.

[10] V. Radisic, V. Jevremovic and Z.B. Popovic, "CPW oscillator configuration for an electric–optic modulator," *IEEE Trans. Microwave Theory Tech.*, vol.MTT-41, pp.1645–1647, Sept. 1993.

[11] N. H. Koster, et al., "Investigation of air bridges used for MMIC's in CPW technique," in *Proc. of 19th European Microwave conference*, pp.666–671, Sept. 1989.

[12] W. E. McKinzie and N.G. Alexopoulos, "Leakage losses for the dominant mode of conductor–backed coplanar waveguide," *IEEE Microwave and Guided Wave Letters*, vol.2, pp.65–66, Feb. 1992.

[13] T. Rozzi and S. J. Hedges, "Rigorous analysis and network modeling of the inset dielectric guide", *IEEE Trans. Microwave Theory Tech.*, Vol.MTT-35, pp.823-833, Sept. 1987.

[14] T. Rozzi, A. Morini and G. Gerini, "Analysis and applications of microstrip loaded inset dielectric waveguide", *IEEE Trans. Microwave Theory Tech.*, Vol.MTT-40, pp.272-278, Feb. 1992.

[15] H.H. Meinel, "Millimeter–wave technology advances since 1985 and future trends," *IEEE Trans. Microwave Theory Tech.*, vol.MTT–39, pp.759–767, May 1991.

[16] P. Espes et al., "Asymmetrical finline for space applications using Millimeter waves," *IEEE Trans. Microwave Theory Tech.*, vol.MTT-37, pp.289–297, Feb. 1989.

[17] C. H. Chan, et al., "A mixed spectral–domain approach for dispersion analysis of suspended planar transmission lines with pedestals," *IEEE Trans. Microwave Theory Tech.*, vol.MTT-37, pp.1716–1723, Nov. 1989.

[18] A. Beyer and K. Solbach, "A new fin–line ferrite isolator for integrated millimeter–wave circuits," *IEEE Trans. Microwave Theory Tech.*, vol.MTT–29, pp.1344-1348, Dec. 1981.

[19] G. Bock, "New multilayered slot line structures with high nonreciprocity," *Elec. Lett.*, vol.19, pp.966-968, Nov. 1983.

[20] Y. Hayashi and R. Mittra, "An analytical investigation of finlines with magnetized ferrite substrate," *IEEE Trans. Microwave Theory Tech.*, vol.MTT-31, pp.495–498, June 1983.

[21] T. Kitazawa, "Analysis of shielded striplines and finlines with finite metallization thickness containing magnetized ferrites" *IEEE Trans. Microwave Theory Tech.*, vol.MTT-39, pp.70–74, Jan. 1991.

[22] S. R. Pennock, N. Izzat and T. Rozzi, "Very wideband operation of twin-layer inset dielectric guide", *IEEE Trans. Microwave Theory Tech.*, Vol.MTT-40, pp.1910-1917, Oct. 1992.

[23] T. Rozzi, G. Gerini, A. Morini and M. Santis, "Multilayer buried microstrip inset guide", in *Proc. 21th European Microwave Conf.*, Stultgart pp.673-678, 1991

[24] N. Izzat. "Space domain analysis of inhomogeneous waveguides of the microstrip and inset guide families", *Ph.D Thesis*, Bath University, Bath, 1991.

[25] T. Rozzi, L. Ma, R. Deleo and A. Morini, "Equivalent network of transverse dipoles on inset dielectric guide: application to linear arrays", *IEEE Trans. Antennas Propagat.*, Vol.AP-38, pp.380-385, 1990.

[26] L. Ma, T. Rozzi and S. R. Pennock, "Design of multiple array flat millimetric antennas in IDG", *Proc. 21th European Microwave Conf.*, pp.641-646, 1991.

[27] S. R. Pennock, D. M. Boskovic and T. Rozzi, "Analysis of coupled inset dielectric guides under LSE and LSM polarization," *IEEE Trans. Microwave Theory Tech.*, vol.MTT-40, pp.916-924, May 1992.

[28] T. Rozzi, S. R. Pennock and D. Boskovic, "Dispersion characteristic of coupled inset dielectric guide," in *Proc. 20th European Microwave Conf.*, Budapest, pp.1175-1180, Sept. 1990

[29] S. R. Pennock, D. Boskovic and T. Rozzi, "Broadband inset dielectric guide coupler," in *Proc. 21th European Microwave Conf.*, Stultgart, pp.1142-1147, 1991

[30] W. Zhou and T. Itoh, "Analysis of trapped image guides using effective dielectric constant and surface impedances", *IEEE Trans. Microwave Theory Tech.*, Vol.MTT-30, pp.2163-2166, Dec. 1982.

[31] H.A. Wheeler, "Transmission line properties of parallel wide strips by conformal mapping approximation," *IEEE Trans. Microwave Theory Tech.*, vol.MTT–12, pp.280–289, 1964.

[32] E. Drake, F. Medina and M. Horno, "Improved quasi–TEM spectral domain analysis of boxed coplanar multiconductor microstrip lines," *IEEE Trans. Microwave Theory Tech.*, vol.MTT–41, pp.260–268, Feb. 1993.

[33] T. Itoh, "Numerical techniques for microwave and millimeter wave passive structure," 1989

[34] C.J. Railton and T. Rozzi, "Complex modes on boxed microstrip," *IEEE Trans. Microwave Theory Tech.*, vol.MTT–36, pp.865—874, May 1988.

[35] J. Kot and T. Rozzi, "Rigorous modelling of single and coupled rectangular dielectric waveguides by transverse resonance diffraction," in *Proc. of 14th European Microwave conference*, pp.424–429, Liege, 1984.

[36] C.A. Olley and T.E. Rozzi, "Systematic characterization of the spectrum of unilateral finline," *IEEE Trans. Microwave Theory Tech.*, vol.MTT–34, pp.1147-1155, Nov. 1986.

[37] T. Itoh and R. Mittra, "Spectral–domain approach for calculating the dispersion characteristics of microstrip lines," *IEEE Trans. Microwave Theory Tech.*, vol.MTT–21, pp.496–499, 1973.

[38] R.H. Jansen, "The spectral–domain approach for microwave integrated circuits," *IEEE Trans. Microwave Theory Tech.*, vol.MTT–33, pp.1043–1054, Oct. 1985.

[39] T. Itoh, "Spectral domain immitance approach for dispersion characteristics of generalized printed transmission lines," *IEEE Trans. Microwave Theory Tech.*, vol.MTT–28, pp.733–736, July 1980.

[40] C.M. Krowne, "Determination of the Green's function in the spectral domain using a matrix method: application to radiators or resonators immersed in a complex anisotropic layered medium," *IEEE Trans. Antennas Propagat.*, vol.AP–34, pp.247–253, Feb. 1986.

[41] F.L.Mesa, R.Marques and M. Horno, "A general algorithm for computing bidimensional spectral Green's dyad in multilayered complex bianisotropic media: the equivalent boundary method," *IEEE Trans. Microwave Theory Tech.*, vol.MTT-39, pp.1640–1649, Sept. 1991.

Chapter 2

ANALYSIS OF COPLANAR WAVEGUIDE LOADED INSET DIELECTRIC GUIDE

2.1 Introduction

The purpose of this chapter is to extend the spectral domain approach for the analysis of coplanar waveguide loaded inset dielectric guide, which has several interesting features useful for microwave and millimeter wave applications. The detailed formulation is given for the field solution of discrete modes. The propagation constant is derived from the determinantal equation and the characteristic impedance is obtained from the power–current definition. Rapid convergence of the solutions for propagation characteristics is also demonstrated.

Numerical results are presented to illustrate the effects of various structural and material parameters on propagation characteristics. By suitable choice of these parameters, wide single–mode bandwidth and a wide range of characteristic impedance can be achieved.

Experimental work on propagation constant and characteristic impedance is discussed. Measured results for several coplanar waveguide geometries are presented and are found to be in excellent agreement with computed values, demonstrating the accuracy of the method of analysis.

2.2 Field Component Representation in the Groove Region

Figure 2.1 illustrates the cross–sectional view of the coplanar waveguide loaded inset dielectric guide and the coordinate system used in the analysis.

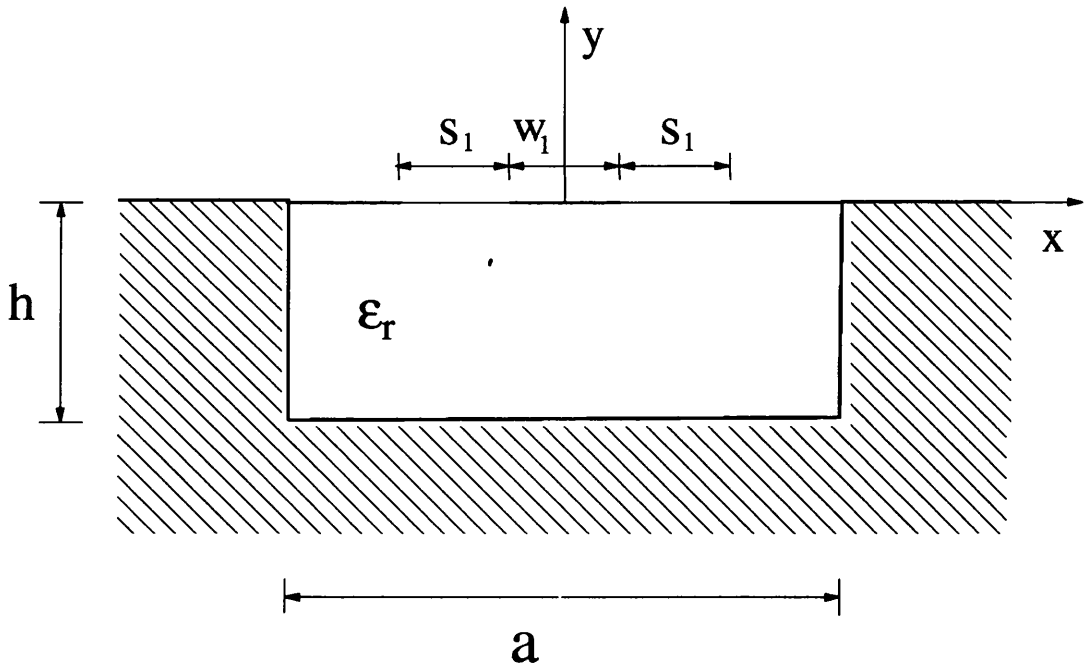

Figure 2.1: Cross–sectional view of a coplanar waveguide loaded inset dielectric guide and the coordinate system used in the analysis

It is assumed that the dependence of fields on the time t and the longitudinal coordinate z is given by $\exp j(\omega t - \beta z)$, where β is the propagation constant and ω is the operating angular frequency. In the following analysis, time and z

dependence will be omitted for the sake of brevity.

Due to the symmetry of the structure with respect to the $x = 0$ plane, the structure is capable of supporting both odd and even modes. By definition, the mode is called odd when E_z is an odd function of x and the mode is called even when E_z is an even function of x. Electromagnetic field components can be represented through their Fourier transforms [1]

$$E_y(x,y) = \frac{1}{a}\sum_{n=-\infty}^{\infty} \tilde{E}_y(\alpha_n, y)e^{-j\alpha_n x} \tag{2.1}$$

$$H_y(x,y) = \frac{1}{a}\sum_{n=-\infty}^{\infty} \tilde{H}_y(\alpha_n, y)e^{-j\alpha_n x} \tag{2.2}$$

and similarly for other field components. In the above equations $\tilde{E}_y$ and $\tilde{H}_y$ are Fourier transforms of E_y and H_y in the x direction, respectively. The discrete transform variables α_n are determined satisfying the electric field boundary conditions at the sidewalls of the groove ($E_y = E_z = 0$, for $x = \pm\frac{a}{2}, -h < y < 0$).

For the E_z odd modes

$$\alpha_n = \frac{2n\pi}{a} \qquad n = 0, \pm 1, \pm 2, \cdots \tag{2.3}$$

For the E_z even modes including the fundamental mode

$$\alpha_n = \frac{(2n+1)\pi}{a} \qquad n = 0, \pm 1, \pm 2, \cdots \tag{2.4}$$

To find the solution for the electromagnetic field in the groove region, Maxwell's curl equations are used

$$\nabla \times \vec{E} = -j\omega\mu_0\vec{H} \tag{2.5}$$

$$\nabla \times \vec{H} = j\omega\varepsilon_0\varepsilon_r \cdot \vec{E} \tag{2.6}$$

Equations (2.5) and (2.6) can be simplified by allowing $\frac{\partial}{\partial t} \rightarrow j\omega$ and $\frac{\partial}{\partial z} \rightarrow -j\beta$. Further simplification is obtained when electromagnetic field components are written in the form of (2.1) and (2.2). This results in six first-order linear differential equations [2], which can be put in the matrix form

$$\begin{bmatrix} 0 & j\beta & \frac{\partial}{\partial y} \\ -j\beta & 0 & j\alpha_n \\ -\frac{\partial}{\partial y} & -j\alpha_n & 0 \end{bmatrix} \begin{bmatrix} \tilde{E}_x \\ \tilde{E}_y \\ \tilde{E}_z \end{bmatrix} = -j\omega\mu_0 \begin{bmatrix} \tilde{H}_x \\ \tilde{H}_y \\ \tilde{H}_z \end{bmatrix} \tag{2.7}$$

$$\begin{bmatrix} 0 & j\beta & \frac{\partial}{\partial y} \\ -j\beta & 0 & j\alpha_n \\ -\frac{\partial}{\partial y} & -j\alpha_n & 0 \end{bmatrix} \begin{bmatrix} \tilde{H}_x \\ \tilde{H}_y \\ \tilde{H}_z \end{bmatrix} = j\omega\varepsilon_0\varepsilon_r \begin{bmatrix} \tilde{E}_x \\ \tilde{E}_y \\ \tilde{E}_z \end{bmatrix} \tag{2.8}$$

From (2.7) - (2.8), x and z field components in the Fourier transform domain can be obtained in terms of y field components in the Fourier transform domain

$$(\alpha_n^2 + \beta^2)\tilde{H}_x = -j\alpha_n \frac{\partial \tilde{H}_y}{\partial y} - \omega\varepsilon_0\varepsilon_r\beta\tilde{E}_y \tag{2.9}$$

$$(\alpha_n^2 + \beta^2)\tilde{H}_z = -j\beta \frac{\partial \tilde{H}_y}{\partial y} + \omega\varepsilon_0\varepsilon_r\alpha_n\tilde{E}_y \tag{2.10}$$

$$(\alpha_n^2 + \beta^2)\tilde{E}_x = -j\alpha_n \frac{\partial \tilde{E}_y}{\partial y} + \omega\mu_0\beta\tilde{H}_y \tag{2.11}$$

$$(\alpha_n^2 + \beta^2)\tilde{E}_z = -j\beta \frac{\partial \tilde{E}_y}{\partial y} - \omega\mu_0\alpha_n\tilde{H}_y \tag{2.12}$$

$\tilde{E}_y$ and $\tilde{H}_y$ satisfy the following wave equations

$$\frac{\partial^2 \tilde{E}_y}{\partial y^2} - \gamma_g^2 \tilde{E}_y = 0 \tag{2.13}$$

$$\frac{\partial^2 \tilde{H}_y}{\partial y^2} - \gamma_g^2 \tilde{H}_y = 0 \tag{2.14}$$

where

$$\gamma_g^2 = \alpha_n^2 + \beta^2 - \kappa_0^2 \varepsilon_r, \qquad \kappa_0^2 = \omega^2 \mu_0 \varepsilon_0 \tag{2.15}$$

Due to the boundary condition that electric field components transverse to y vanish on the base of the groove, appropriate solutions to equations (2.13) and (2.14) are

$$\tilde{E}_y = C^e \cosh \gamma_g (y + h) \tag{2.16}$$

$$\tilde{H}_y = C^h \sinh \gamma_g (y + h) \tag{2.17}$$

where C^e and C^h are unknown amplitude coefficients.

In order to determine the modal amplitude coefficients, the electric field components transverse to y at $y = 0$ are introduced

$$E_x(x, 0^-) = E_x^b(x) \tag{2.18}$$

$$E_z(x, 0^-) = E_z^b(x) \tag{2.19}$$

where E_x^b and E_z^b are x, z components of the electric field on the $y = 0$ interface, which are non-zero only for $(\frac{w_1}{2} < |x| < \frac{w_1}{2} + s_1, y = 0)$.

By transforming (2.18) and (2.19) into the Fourier transform domain, substituting Fourier–transformed field components into (2.18) and (2.19), and solving the resulting equations, C^e and C^h can be expressed in terms of unknowns $\tilde{E}_x^b(\alpha_n)$, $\tilde{E}_z^b(\alpha_n)$.

$$C^e = \frac{j(\alpha_n \tilde{E}_x^b + \beta \tilde{E}_z^b)}{\gamma_g \sinh \gamma_g h} \tag{2.20}$$

$$C^h = \frac{(\beta \tilde{E}_x^b - \alpha_n \tilde{E}_z^b)}{\omega \mu_0 \sinh \gamma_g h} \tag{2.21}$$

2.3 Field Component Representation in the Air Region

Since the air region is unbounded in x, field components are expressed in terms of continuous Fourier spectra [3]

$$E_y(x,y) = \frac{1}{2\pi}\int_{-\infty}^{\infty} \tilde{E}_y(\alpha,y)e^{-j\alpha x}\,d\alpha \tag{2.22}$$

$$H_y(x,y) = \frac{1}{2\pi}\int_{-\infty}^{\infty} \tilde{H}_y(\alpha,y)e^{-j\alpha x}\,d\alpha \tag{2.23}$$

and similarly for other field components.

Following the similar procedure for the derivation of the field in the groove region, wave equations for $\tilde{E}_y$ and $\tilde{H}_y$ in the air region are derived as

$$\frac{\partial^2 \tilde{E}_y}{\partial y^2} - \gamma_0^2 \tilde{E}_y = 0 \tag{2.24}$$

$$\frac{\partial^2 \tilde{H}_y}{\partial y^2} - \gamma_0^2 \tilde{H}_y = 0 \tag{2.25}$$

where

$$\gamma_0^2 = \alpha^2 + \beta^2 - \kappa_0^2 \tag{2.26}$$

The solutions of (2.24) and (2.25) which satisfy outgoing wave conditions at $y \to \infty$ are

$$\tilde{E}_y = D^e e^{-\gamma_0 y} \tag{2.27}$$

$$\tilde{H}_y = D^h e^{-\gamma_0 y} \tag{2.28}$$

The remaining field components can be obtained from (2.9)—(2.12) by replacing α_n and ε_r by α and 1, respectively.

The modal coefficients D^e and D^h are deduced by introducing the electric field components transverse to y at the $y = 0$ interface

$$E_x(x, 0^+) = E_x^b(x) \tag{2.29}$$

$$E_z(x, 0^+) = E_z^b(x) \tag{2.30}$$

When (2.29) and (2.30) are Fourier transformed with respect to x and substituted into the tangential electric components, we obtain

$$D^e = \frac{1}{j\gamma_0}[\alpha \tilde{E}_x^b(\alpha) + \beta \tilde{E}_z^b(\alpha)] \tag{2.31}$$

$$D^h = \frac{1}{j\omega\mu_0}[\beta \tilde{E}_x^b(\alpha) - \alpha \tilde{E}_z^b(\alpha)] \tag{2.32}$$

2.4 Formulation of Integral Equations

In order to derive the integral equations which are satisfied by unknown tangential electric field components at the $y = 0$ interface, we have to first obtain expressions for the tangential magnetic field components at either side of the $y = 0$ interface.

Substituting C^e and C^h in (2.20) (2.21) into (2.16) (2.17), and using (2.9) (2.10), we can obtain the following matrix equation, which relates tangential magnetic field components to tangential electric field components at the $y = 0$ interface for the groove region

$$\begin{bmatrix} \tilde{H}_z(\alpha_n, 0^-) \\ -\tilde{H}_x(\alpha_n, 0^-) \end{bmatrix} = [Y^g] \begin{bmatrix} \tilde{E}_x^b(\alpha_n) \\ \tilde{E}_z^b(\alpha_n) \end{bmatrix} \tag{2.33}$$

where elements of $[Y^g]$ are given by

$$Y_{11}^g = j \coth \gamma_g h(-\frac{\gamma_g}{\omega\mu_0}\beta^2 + \frac{\omega\varepsilon_0\varepsilon_r}{\gamma_g}\alpha_n^2)/(\alpha_n^2 + \beta^2) \tag{2.34}$$

$$Y_{22}^g = j \coth \gamma_g h(-\frac{\gamma_g}{\omega\mu_0}\alpha_n^2 + \frac{\omega\varepsilon_0\varepsilon_r}{\gamma_g}\beta^2)/(\alpha_n^2 + \beta^2) \tag{2.35}$$

$$Y_{12}^g = Y_{21}^g = j\alpha_n\beta \coth \gamma_g h(\frac{\gamma_g}{\omega\mu_0} + \frac{\omega\varepsilon_0\varepsilon_r}{\gamma_g})/(\alpha_n^2 + \beta^2) \tag{2.36}$$

According to the form of (2.1), the equation (2.33) can be rewritten in the space domain.

$$\begin{bmatrix} H_z(x,0^-) \\ -H_x(x,0^-) \end{bmatrix} = \frac{1}{a}\sum_{n=-\infty}^{\infty}[Y^g]\begin{bmatrix} \tilde{E}_x^b(\alpha_n) \\ \tilde{E}_z^b(\alpha_n) \end{bmatrix} e^{-j\alpha_n x} \tag{2.37}$$

In the similar way, we obtain the following matrix equation for the air region

$$\begin{bmatrix} -\tilde{H}_z(\alpha,0^+) \\ \tilde{H}_x(\alpha,0^+) \end{bmatrix} = [Y^a]\begin{bmatrix} \tilde{E}_x^b(\alpha) \\ \tilde{E}_z^b(\alpha) \end{bmatrix} \tag{2.38}$$

where elements of $[Y^a]$ are given by

$$Y_{11}^a = j(-\frac{\gamma_0}{\omega\mu_0}\beta^2 + \frac{\omega\varepsilon_0}{\gamma_0}\alpha^2)/(\alpha^2 + \beta^2) \tag{2.39}$$

$$Y_{22}^a = j(-\frac{\gamma_0}{\omega\mu_0}\alpha^2 + \frac{\omega\varepsilon_0}{\gamma_0}\beta^2)/(\alpha^2 + \beta^2) \tag{2.40}$$

$$Y_{12}^a = Y_{21}^a = j\alpha\beta(\frac{\gamma_0}{\omega\mu_0} + \frac{\omega\varepsilon_0}{\gamma_0})/(\alpha^2 + \beta^2) \tag{2.41}$$

According to the form of (2.22), the equation (2.38) gives the following equivalent expression for z and x magnetic field components in the space domain.

$$\begin{bmatrix} -H_z(x,0^+) \\ H_x(x,0^+) \end{bmatrix} = \frac{1}{2\pi}\int_{-\infty}^{\infty}[Y^a]\begin{bmatrix} \tilde{E}_x^b(\alpha) \\ \tilde{E}_z^b(\alpha) \end{bmatrix} e^{-j\alpha x}\, d\alpha \tag{2.42}$$

The boundary conditions to be satisfied on the $y = 0$ interface are expressed as follows

$$-H_z(x,0^+) + H_z(x,0^-) = -J_x(x) \tag{2.43}$$

$$H_x(x,0^+) - H_x(x,0^-) = -J_z(x) \tag{2.44}$$

$$E_x(x,0^+) = E_x(x,0^-) = E_x^b(x) \tag{2.45}$$

$$E_z(x,0^+) = E_z(x,0^-) = E_z^b(x) \tag{2.46}$$

where J_x and J_z are x and z components of the current on the conducting strips at $y = 0$, respectively. It should be noted that equations (2.45) and (2.46) have been used in (2.18), (2.19), (2.29) and (2.30).

Substituting (2.42) and (2.37) into (2.43) and (2.44) and using for the boundary condition $J_x(x) = J_z(x) = 0$ for $\frac{w_1}{2} < |x| < \frac{w_1}{2} + s_1$, we obtain the integral equations for tangential electric field components at the $y = 0$ interface as follows

$$\frac{1}{2\pi}\int_{-\infty}^{\infty}[Y^a]\begin{bmatrix}\tilde{E}_x^b(\alpha)\\ \tilde{E}_z^b(\alpha)\end{bmatrix}e^{-j\alpha x}d\alpha + \frac{1}{a}\sum_{n=-\infty}^{\infty}[Y^g]\begin{bmatrix}\tilde{E}_x^b(\alpha_n)\\ \tilde{E}_z^b(\alpha_n)\end{bmatrix}e^{-j\alpha_n x} = 0 \quad \text{for} \quad \frac{w_1}{2} < |x| < \frac{w_1}{2} + s_1 \tag{2.47}$$

with

$$\tilde{E}_x^b(\alpha_n) = \left(\int_{-\frac{w_1}{2}-s_1}^{-\frac{w_1}{2}} + \int_{\frac{w_1}{2}}^{\frac{w_1}{2}+s_1}\right)E_x^b(x)e^{j\alpha_n x}dx \tag{2.48}$$

$$\tilde{E}_x^b(\alpha_n) = \left(\int_{-\frac{w_1}{2}-s_1}^{-\frac{w_1}{2}} + \int_{\frac{w_1}{2}}^{\frac{w_1}{2}+s_1}\right)E_x^b(x)e^{j\alpha_n x}dx \tag{2.49}$$

$$\tilde{E}_z^b(\alpha_n) = \left(\int_{-\frac{w_1}{2}-s_1}^{-\frac{w_1}{2}} + \int_{\frac{w_1}{2}}^{\frac{w_1}{2}+s_1}\right)E_z^b(x)e^{j\alpha_n x}dx$$

(2.48) and (2.49) by replacing α_n by α, respectively.

2.5 Application of Galerkin's Method

In order to obtain the determinantal equation for the propagation constant, Galerkin's method [4] is applied to the integral equations (2.47). As a first step, the unknown electric field components E_x^b and E_z^b are expanded in terms of known basis functions as follows

$$E_x^b(x) = \sum_{m=0}^{N_x} C_{xm} E_{xm}^b(x) \tag{2.50}$$

$$E_z^b(x) = \sum_{m=1}^{N_z} C_{zm} E_{zm}^b(x) \tag{2.51}$$

where C_{xm} and C_{zm} are unknown expansion coefficients. $E_{xm}^b(x)$ and $E_{zm}^b(x)$ are chosen to be zero except for $\frac{w_1}{2} < |x| < \frac{w_1}{2} + s_1$.

Now we substitute (2.50) and (2.51) into the integral equations (2.47), and take the inner product of the resulting equations with E_{xi}^b, E_{zi}^b for different values of i, respectively. This step yields a homogeneous matrix equation for the unknown expansion coefficients C_{xm} and C_{zm} as

$$\begin{bmatrix} K_{im}(x,x) & K_{im}(x,z) \\ K_{im}(z,x) & K_{im}(z,z) \end{bmatrix} \begin{bmatrix} C_{xm} \\ C_{zm} \end{bmatrix} = 0 \tag{2.52}$$

The elements of matrix [K] are given by

$$K_{im}(x,x) = \frac{1}{2\pi} \int_{-\infty}^{\infty} \tilde{E}_{xi}^b(-\alpha) Y_{11}^a \tilde{E}_{xm}^b(\alpha) d\alpha + \frac{1}{a} \sum_{n=-\infty}^{\infty} \tilde{E}_{xi}^b(-\alpha_n) Y_{11}^g \tilde{E}_{xm}^b(\alpha_n) \tag{2.53}$$

$$K_{im}(x,z) = \frac{1}{2\pi} \int_{-\infty}^{\infty} \tilde{E}_{xi}^b(-\alpha) Y_{12}^a \tilde{E}_{zm}^b(\alpha) d\alpha + \frac{1}{a} \sum_{n=-\infty}^{\infty} \tilde{E}_{xi}^b(-\alpha_n) Y_{12}^g \tilde{E}_{zm}^b(\alpha_n) \tag{2.54}$$

$$K_{im}(z,x) = \frac{1}{2\pi} \int_{-\infty}^{\infty} \tilde{E}_{zi}^b(-\alpha) Y_{21}^a \tilde{E}_{xm}^b(\alpha) d\alpha + \frac{1}{a} \sum_{n=-\infty}^{\infty} \tilde{E}_{zi}^b(-\alpha_n) Y_{21}^g \tilde{E}_{xm}^b(\alpha_n) \tag{2.55}$$

$$K_{im}(z,z) = \frac{1}{2\pi}\int_{-\infty}^{\infty} \tilde{E}^b_{zi}(-\alpha)Y^a_{22}\tilde{E}^b_{zm}(\alpha)d\alpha + \frac{1}{a}\sum_{n=-\infty}^{\infty} \tilde{E}^b_{zi}(-\alpha_n)Y^g_{22}\tilde{E}^b_{zm}(\alpha_n) \quad (2.56)$$

with

$$\tilde{E}^b_{xm}(\alpha_n) = (\int_{-\frac{w_1}{2}-s_1}^{-\frac{w_1}{2}} + \int_{\frac{w_1}{2}}^{\frac{w_1}{2}+s_1})E^b_{xm}(x)e^{j\alpha_n x}dx \quad (2.57)$$

$$\tilde{E}^b_{zm}(\alpha_n) = (\int_{-\frac{w_1}{2}-s_1}^{-\frac{w_1}{2}} + \int_{\frac{w_1}{2}}^{\frac{w_1}{2}+s_1})E^b_{zm}(x)e^{j\alpha_n x}dx \quad (2.58)$$

For nontrivial solutions for C_{xm} and C_{zm}, the determinant of the coefficient matrix in (2.52) must be zero. This condition results in the determinantal equation for the propagation constant.

$$Det\ [K] = 0 \quad (2.59)$$

2.6 Choice of Basis Functions

In order to evaluate elements of the matrix [K] in (2.59) numerically, the Fourier transforms of basis functions in (2.57) and (2.58) need to be obtained first. For the easier numerical evaluation, the basis functions should be chosen to be analytically Fourier transformable. Furthermore, the basis functions should contain the singular behaviour [5] of the electric field components at the edges of conducting strips in order to achieve the highly efficient numerical and accurate solutions of the determinantal equation with a small size of the matrix [K]. Because two tangential electric field components at the edges of the strips satisfy different edge conditions, different sets of basis functions are used for the field expansion in the conventional spectral domain approach [1] [6]. Here we will show that only one

set of basis functions need be used for the calculation of both Fourier transforms in (2.57) and (2.58). As a result, the computational time will be reduced.

Integrating (2.58) by parts and taking into account the boundary condition that requires that z electric field component must be zero at conducting edges on the $y = 0$ surface, the following expression for $\tilde{E}^b_{zm}(\alpha_n)$ is obtained

$$\tilde{E}^b_{zm}(\alpha_n) = \frac{j}{\alpha_n}\left(\int_{-\frac{w_1}{2}-s_1}^{-\frac{w_1}{2}} + \int_{\frac{w_1}{2}}^{\frac{w_1}{2}+s_1}\right)\frac{\partial E^b_{zm}(x)}{\partial x}e^{j\alpha_n x}dx \tag{2.60}$$

Because $\frac{\partial E^b_z(x)}{\partial x}$ satisfies the same boundary and singular edge conditions as $E^b_x(x)$, basis functions for $\frac{\partial E^b_{zm}(x)}{\partial x}$ can be chosen to be the same as those for $E^b_{xm}(x)$. Also the appearance of the factor $\frac{j}{\alpha_n}$ in (2.60) improves the convergence of the solutions of the determinantal equation.

The presence of strip edges (at $|x| = \frac{w_1}{2}$ and $\frac{w_1}{2} + s_1$) introduces singularity in the field distribution. The singularity in $E^b_x(x)$ and $\frac{\partial E^b_z(x)}{\partial x}$ can be shown to be of the order $r^{-\frac{1}{2}}$ [5]. In order to model this singular behaviour, the following weight function is introduced

$$W(x) = \left(1 - x'^2\right)^{-\frac{1}{2}} \tag{2.61}$$

where

$$x' = 2(|x| - x_0)/s_1, \qquad x_0 = (w_1 + s_1)/2 \tag{2.62}$$

A set of functions that are orthogonal with respect to this weight function are Chebychev polynomials $T_m(x')$ [7]. Thus the basis functions are chosen as

For the E_z odd mode:

$$E^b_{xm}(x) = \frac{\partial E^b_{zm}(x)}{\partial x} = W(x)\begin{cases} T_m(x') & \text{for } \frac{w_1}{2} < x < \frac{w_1}{2} + s_1 \\ T_m(x') & \text{for } -\frac{w_1}{2} - s_1 < x < -\frac{w_1}{2} \end{cases} \tag{2.63}$$

For the E_z even mode:

$$E^b_{xm}(x) = \frac{\partial E^b_{zm}(x)}{\partial x} = W(x) \begin{cases} T_m(x') & \text{for } \frac{w_1}{2} < x < \frac{w_1}{2} + s_1 \\ -T_m(x') & \text{for } -\frac{w_1}{2} - s_1 < x < -\frac{w_1}{2} \end{cases} \tag{2.64}$$

where m is chosen to start at 0 for $E^b_{xm}(x)$, but at 1 for $\frac{\partial E^b_{zm}(x)}{\partial x}$. The reasons for this are:

(a) E^b_z is zero at the strip edges ($x = \frac{w_1}{2}$ and $\frac{w_1}{2} + s_1$) so that $\frac{\partial E^b_z}{\partial x}$ must have zero average in the range and

(b) $\int_{\frac{w_1}{2}}^{\frac{w_1}{2}+s_1} \frac{\partial E^b_{z0}}{\partial x}\, dx \neq 0$.

2.7 Characteristic Impedance

In addition to the propagation constants of the dominant and higher–order modes, a knowledge of the characteristic impedance of the dominant mode is also important for the design of the microwave and millimeter–wave integrated circuits using the structure. Due to the hybrid mode nature in the electromagnetic field, a unique definition does not exist [8]. However, by considering the fact that the total longitudinal current is a physical quantity which is conserved when the centre strip is connected to a load or a driver and that the same power should be used in the equivalent TEM transmission line, the adoption of the power–current definition is most suitable for the circuit description of the structure considered here [9] [10]. Therefore, the characteristic impedance is obtained here based on this definition

$$Z_0 = \frac{2P}{I_0^2} \tag{2.65}$$

where P is the total average power flow along the guide and I_0 is the total longitudinal current on the centre strip of the coplanar waveguide.

Once the propagation constant of the dominant mode is found, the expansion coefficients for the tangential electric field components can be obtained from the equation (2.52) and in turn the Fourier transforms of the field components in the air and groove regions can be derived.

Total power flow along the guide can be evaluated by integrating the Poynting vector over the transverse guide cross section, which is given by

$$\begin{aligned} P &= \frac{1}{2}\int_s \vec{E}\times\vec{H}^*\cdot\vec{z}\,ds \\ &= \frac{1}{2}\int_0^\infty\int_{-\infty}^\infty (E_xH_y^* - E_yH_x^*)\,dx\,dy \\ &+ \frac{1}{2}\int_{-h}^0\int_{-\frac{a}{2}}^{\frac{a}{2}} (E_xH_y^* - E_yH_x^*)\,dx\,dy \end{aligned} \tag{2.66}$$

Parseval's theorem [11] [12] is applied to the above integrals to obtain

$$\begin{aligned} P_0 &= \frac{1}{4\pi}\int_{-\infty}^\infty\int_0^\infty (\tilde{E}_x\tilde{H}_y^* - \tilde{E}_y\tilde{H}_x^*)\,dy\,d\alpha \\ &+\frac{1}{2a}\sum_{n=-\infty}^{\infty}\int_{-h}^0 (\tilde{E}_x\tilde{H}_y^* - \tilde{E}_y\tilde{H}_x^*)\,dy \end{aligned} \tag{2.67}$$

As the y dependence of the expressions for field components in each region is simple, integration with respect to y can be accomplished analytically. This results in the equation of the following form

$$P_0 = \frac{1}{4\pi}\int_{-\infty}^\infty S^a\,d\alpha + \frac{1}{2a}\sum_{n=-\infty}^{\infty} S_n \tag{2.68}$$

The above integral and summation are evaluated numerically.

Since the total longitudinal current in the centre strip is only treated as a dependent variable here, a closed form expression for it does not exist. However, it can be evaluated from the boundary condition in (2.44) for the x component of the magnetic field at the $y = 0$ interface as follows

$$\begin{aligned} I_0 &= \int_{-w_1/2}^{w_1/2} J_z(x)\, dx \\ &= -\frac{1}{2\pi}\int_{-\infty}^{\infty} [Y_{21}^a \tilde{E}_x^b(\alpha) + Y_{22}^a \tilde{E}_z^b(\alpha)] \frac{2\sin(0.5\alpha w_1)}{\alpha}\, d\alpha \\ &\quad -\frac{1}{a}\sum_{n=-\infty}^{\infty} [Y_{21}^g \tilde{E}_x^b(\alpha_n) + Y_{22}^g \tilde{E}_z^b(\alpha_n)] \frac{2\sin(0.5\alpha_n w_1)}{\alpha_n} \end{aligned} \tag{2.69}$$

2.8 Convergence of Solutions

Computational time critically depends on the number of basis functions used in the actual calculations. Table 2.1 shows the convergence of solutions for normalized propagation constant β/κ_0 and characteristic impedance Z_0 of the dominant mode at the frequency of 10 GHz for two different values of the aperture width s_1 by using different values of the upper summation limit $N = N_x = N_z$ in (2.50) and (2.51). The solutions for β/k_0 are found to converge with a small number of N. The table shows that accurate solutions for β/k_0 to four significant digits can be achieved by using $N = 1$. The rapid convergence is a consequence of stationarity of the expression for β and appropriate choice of the basis functions. It can be also seen from the table that the convergence of solutions for Z_0 is lower than that for β/κ_0. The reason for this is that higher order of expansion is required to obtain accurate electromagnetic field as the field is not a variational quantity. In fact, $N = 4$ is needed to obtain to accurate solutions for Z_0 to three significant digits.

$N_x = N_z$	β/k_0		Z_0	
	$s_1 = 0.5w_1$	$s_1 = 2.0w_1$	$s_1 = 0.5w_1$	$s_1 = 2.0w_1$
1	1.24032	1.25756	103.2	148.3
2	1.24035	1.25756	101.6	141.7
3	1.24035	1.25756	101.4	140.3
4	1.24038	1.25756	100.5	139.7
5	1.24038	1.25756	100.4	139.4
6	1.24038	1.25756	100.2	139.1

Table 2.1: Convergence of solutions for β/κ_0 and Z_0 of the dominant mode at the frequency of 10 GHz for two different values of s_1 (ε_r=2.04, a =6.0e–3 m, h=3.0e–3 m, and w_1=1.0e–3 m)

2.9 Comparison with Measured Results

In order to verify the validity of the method of analysis presented in the previous sections, measurements of propagation constants and characteristic impedances have been performed.

2.9.1 Propagation Constant

The resonant section technique [13] is first used to measure propagation constants of the E_z even and odd modes. In this experimental work, metal plates are fixed at both ends of a section of coplanar waveguide loaded inset dielectric guide, forming short circuits. Energy is then coupled into the structure by inserting magnetic probes over the air–dielectric surface through the short circuits. By suitable choice of the distance between the probes and the surface, very weak coupling transmission peak (< 25 dB) can be achieved. Thus, the section is virtually short–circuited at both ends. As a results, this structure supports only standing waves that have zero electric field components (tangential to the short

circuits) at each end. This is only satisfied for specific waveguide wavelengths

$$\frac{k\lambda_g}{2} = L \tag{2.70}$$

where k is an integer

λ_g is the guided wavelength

L is the length of section

Thus, only at discrete resonant frequencies, corresponding to guided wavelengths that satisfy (2.70), is energy significantly coupled to the section. As a result, the transmission response over a range of frequencies shows resonant peaks, which correspond to these resonant frequencies (see Figure 2.2).

In addition, propagation constants of the E_z even and odd modes can be measured independently by changing the orientation of the magnetic probes which are placed symmetrically (at $x = 0$). For the E_z even modes, H_x is finite and H_y is zero. But, for the E_z odd modes, H_x is zero and H_y is finite. Therefore, x–directed (horizontally oriented) probes will preferentially excite the even modes and y–directed (vertically oriented) probes will preferentially excite the odd modes.

The measurement procedure is described as follows. First, swept frequency transmission response is obtained by using an HP8510B Network Analyzer. The source is then tuned to a specific resonant frequency. The integer k is determined using a field probe to monitor the standing wave pattern and the guided wavelength λ_g is obtained from (2.70). Finally the normalized propagation constant β/κ_0 can be computed as λ_0/λ_g.

Successive resonant frequencies must correspond to successive values of k. Thus, after having determined k for one resonant frequency, k for other resonant frequencies can be determined. It should be noted that the minimum value of k for the fundamental mode which has no cut-off frequency is 1 and corresponds to the first resonant frequency.

Figure 2.3 shows the comparison of the computed and measured propagation constants of the dominant and first higher–order modes. Clearly, the agreement between computed and measured data is good for the propagation constants of the dominant and first higher–order modes. In fact, the agreement is within 0.8 percent.

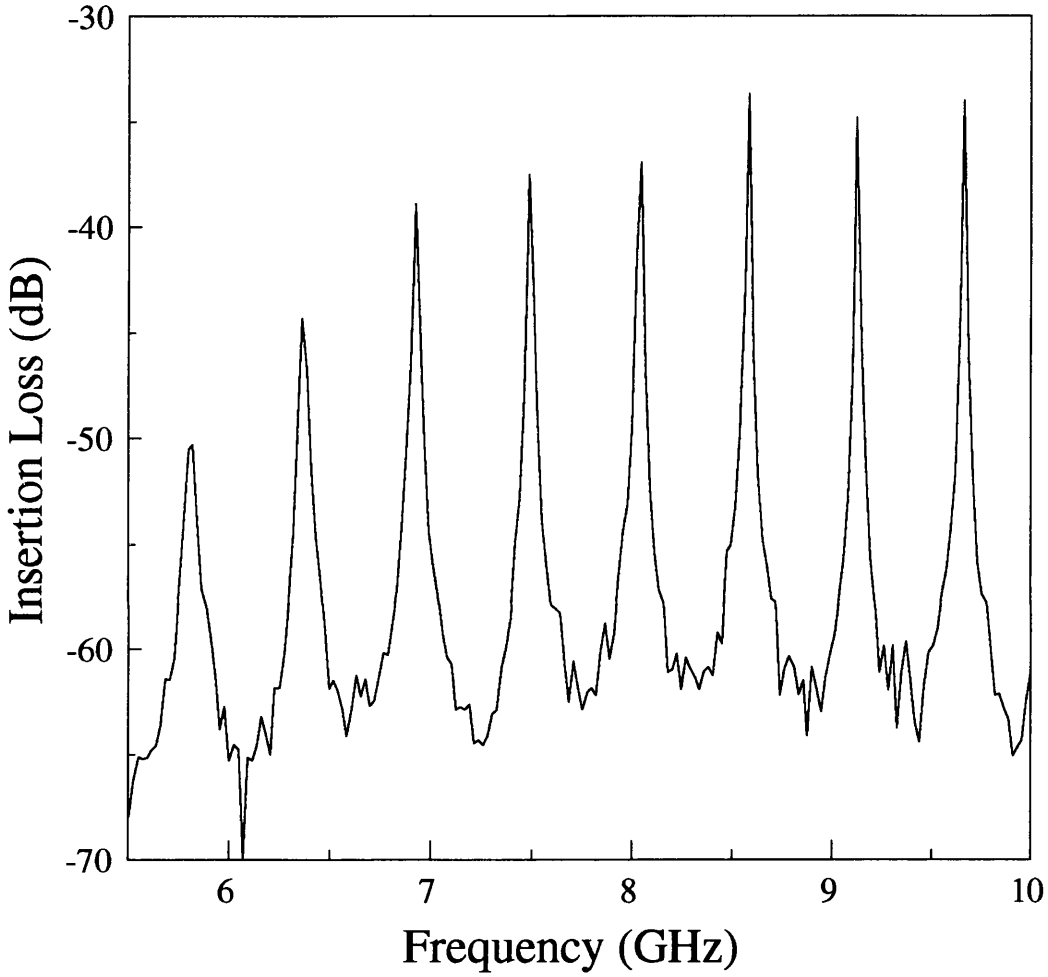

Figure 2.2: Measured insertion loss of the first E_z odd mode of a resonant section of CPW loaded IDG used to determine the propagation constant (ε_r=2.04, a=2.286e–2 m, h=1.016e–2 m, w_1=7.0e–3 m, s_1=3.0e–3 m and L=2.032e–1 m)

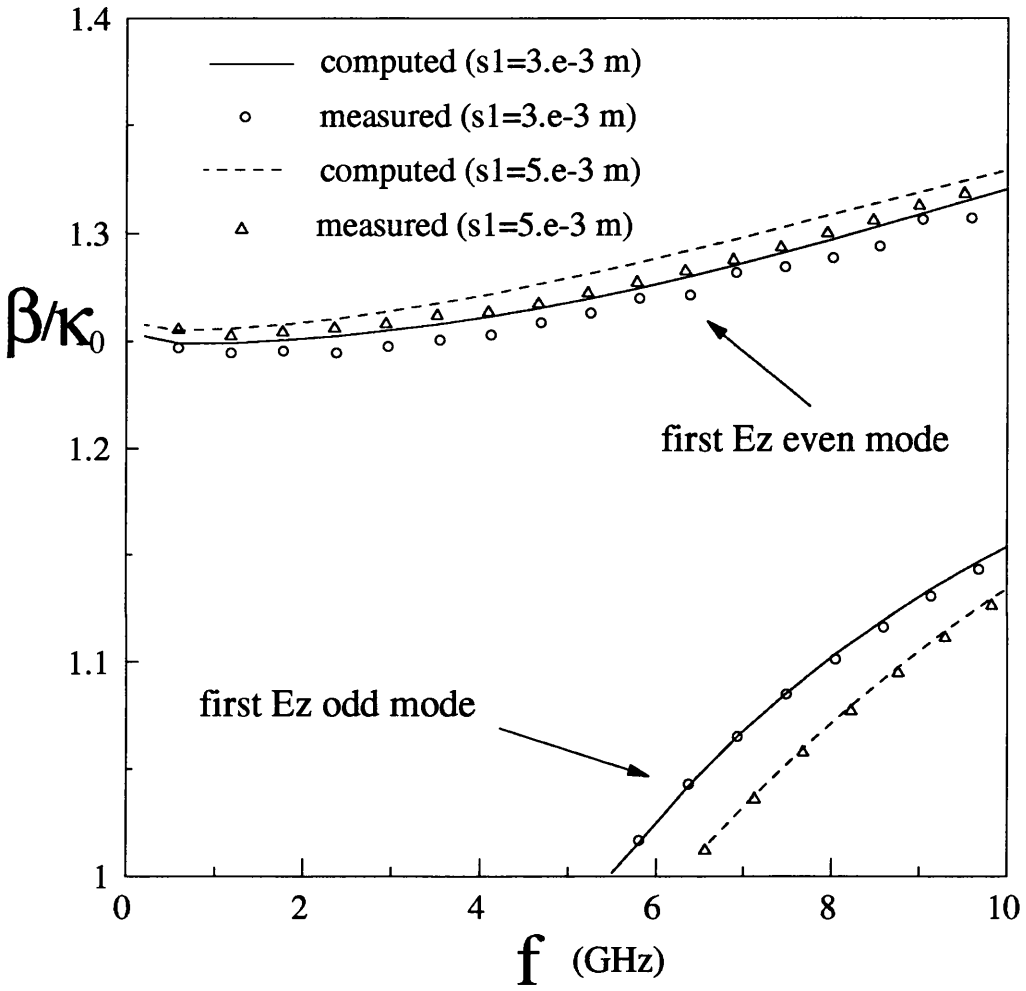

Figure 2.3: Computed and measured propagation constants of the dominant and first higher–order modes as a function of frequency for different values of s_1 (ε_r=2.04, a=2.286e–2 m, h=1.016e–2 m and w_1=7.0e–3 m)

2.9.2 Characteristic Impedance

The time–domain step response facility on the HP8510B Network Analyzer is used to measure the characteristic impedance of the CPW loaded IDG [14]. A conducting plate with a hole is fixed at each end of a section of the line. A 50–ohm microwave coaxial cable is then inserted through each hole, and its inner conductor is extended beyond the conducting plane and soldered to the centre strip of the CPW. The purpose of the conducting plane at each end is to realize the potential equalization of IDG ground and the outer conductor of each cable and to fix the cable firmly. After being calibrated to 50–ohm coaxial cable, the two ports of the HP8510B Network Analyzer are connected to the coaxial cables at both ends of the measured structure. The reflection coefficient from the input port is easily determined from the measured time–domain step response (see Figure 2.4). Finally, the characteristic impedance is calculated in terms of the measured reflection coefficient.

Figure 2.5 shows the comparison of computed and measured characteristic impedances of the dominant mode for various values of the centre strip width and aperture width of the coplanar waveguide. The agreement between theory and experiment is found to be good. In fact, calculated and measured results differ by less than 1.25 percent.

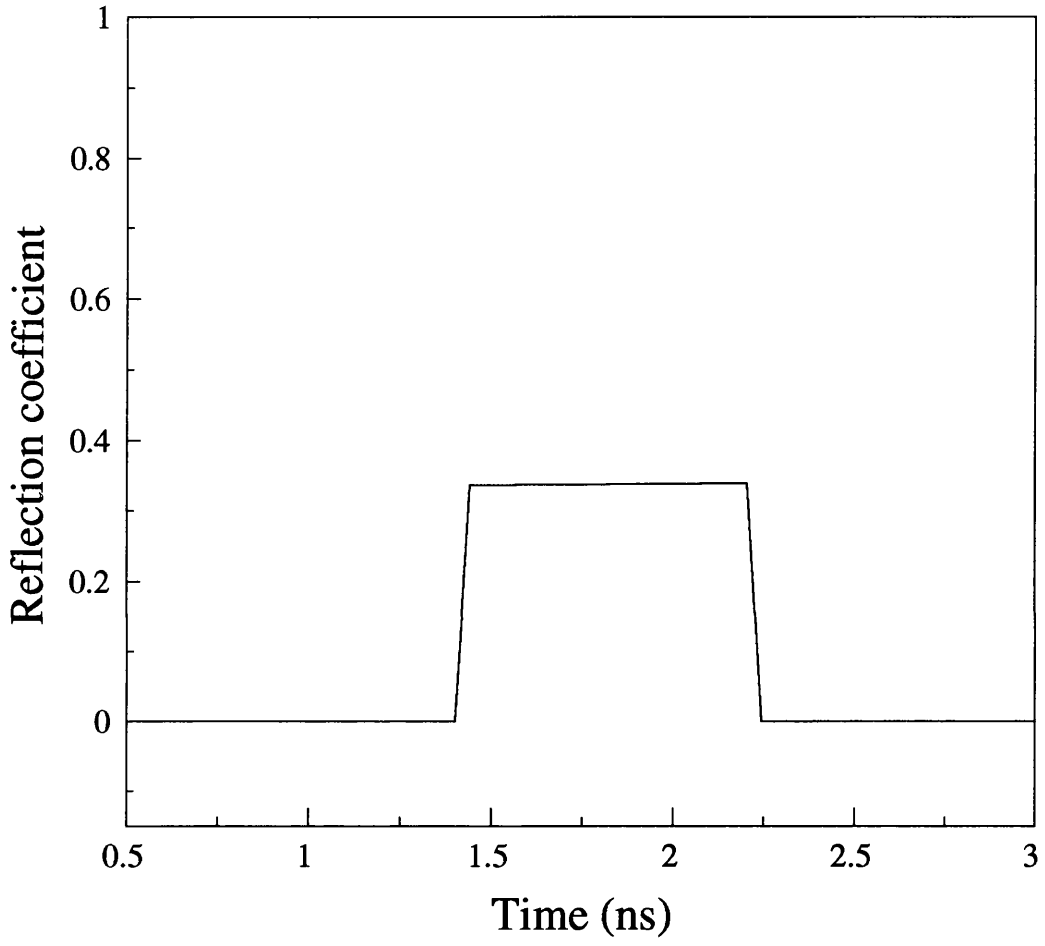

Figure 2.4: Measured time–domain step response of the dominant mode of a section of CPW loaded IDG used to determine the characteristic impedance (ε_r=2.04, a=2.286e–2 m, h=1.016e–2 m, w_1=7.0e–3 m, s_1=5.0e–3 m and L=2.032e–1 m)

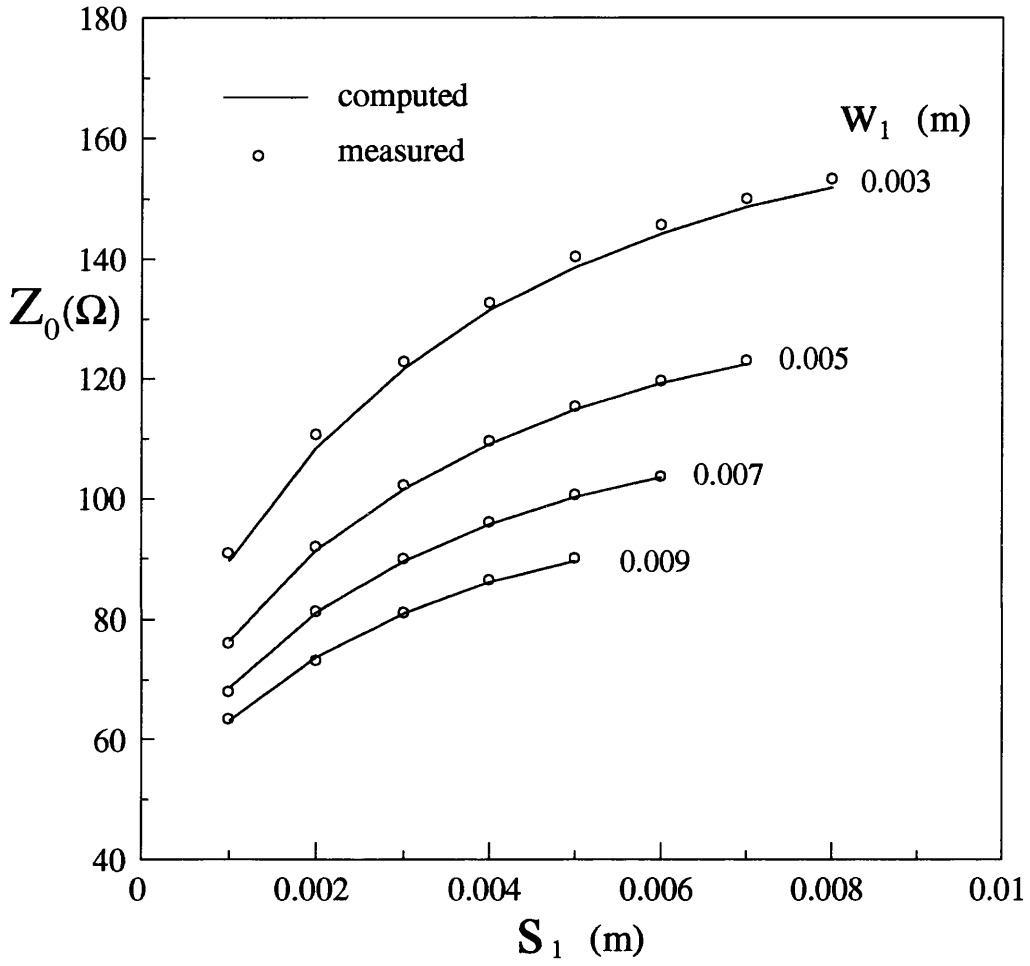

Figure 2.5: Computed and measured characteristic impedances of the dominant mode as a function of s_1 for different values of w_1 (ε_r=2.04, a=2.286e–2 m, h=1.016e–2 m and f=1.0 GHz)

2.10 Numerical Results

Figure 2.6 shows the propagation constant of the first few modes as a function of frequency up to 40 GHz. It is seen that the first E_z even mode is the fundamental mode with no cutoff frequency. In this case, the first higher–order mode is the first E_z odd mode, whose finite cutoff frequency determines the single–mode bandwidth. The cutoff frequency of the first higher–order mode can be controlled by changing the dimensions of the IDG. The propagation constant of the dominant and first higher–order modes is shown in Figure 2.7 and 2.8 as a function of frequency for different values of h and a, respectively. It is apparent that decreasing the height and width of the groove can increase the cut-off frequency of the first higher–order mode, resulting in the wider single–mode bandwidth.

Figure 2.9 shows the propagation constant of the dominant mode as a function of a for different values of h. It is clearly seen that the propagation constant of the dominant mode increases as h and a decrease. Therefore, as the IDG dimensions are reduced, the field becomes more concentrated within the groove. This higher concentration of the field within the groove may result in reduced coupling between parallel tracks, and may also give lower radiation loss at discontinuities.

Figure 2.10 shows the propagation constant of the fundamental and first higher–order modes as a function of frequency for different values of the aperture width s_1. The corresponding characteristic impedance of the fundamental mode is shown in Figure 2.11. It is apparent that as the frequency increases from zero, the propagation constant and characteristic impedance of the dominant mode initially decrease slightly and then increase. This phenomenon is more evident for small values of s_1. It is more interesting to note that in the single–mode frequency range, the propagation constant and characteristic impedance of the

fundamental mode change very little with increasing frequency although they change rapidly beyond this range. This behaviour is more pronounced for small values of s_1.

Figure 2.12 shows characteristic impedance as a function of s_1 for different values of w_1. It is clearly observed that a wide range of characteristic impedance can be obtained by changing s_1 and w_1. The characteristic impedance is decreased with decreasing s_1 and increasing w_1. The characteristic impedance can also be decreased by increasing the relative permittivity of the dielectric in the groove. This is clearly seen in Figure 2.13 where the characteristic impedance is shown as a function of ε_r. Figure 2.14 shows characteristic impedance of the dominant mode as a function of a for different values of h. The decrease in a and h is found to decrease the characteristic impedance. The effect is more pronounced for the small values of a and h. However, the effect is much smaller than that obtained by changing s_1 and w_1. As there are many parameters that can be chosen, a very wide range of impedance can be realized.

Conventional coplanar waveguide uses air bridges to eliminate the coupled slot–mode that has no cut-off frequency. In addition high–permittivity dielectric substrate has to be used to obtain good confinement of the electromagnetic fields [15] – [17]. From the above discussion, it is apparent that the coplanar waveguide loaded inset dielectric guide offers the following advantages over conventional coplanar waveguide:

(1) By suitable choice of IDG dimensions no higher–order mode can propagate in any specific frequency range of interest, so no air bridge is needed.

(2) Because the field is concentrated in the groove, low–permittivity dielectric substrate can be used, resulting the larger circuit dimensions which improves mechanical tolerance.

(3) The dispersion in propagation constant and characteristic impedance is very small in the single–mode frequency range.

(4) A wide range of characteristic impedance can be achieved, leading to great flexibility in circuit design.

(5) The side walls of the groove prevent the propagation of the surface modes of the dielectric slab, which often degrades the performance of the conventional coplanar waveguide.

(6) The mechanical stability and heat removal from the active devices are significantly improved because of the IDG shielding.

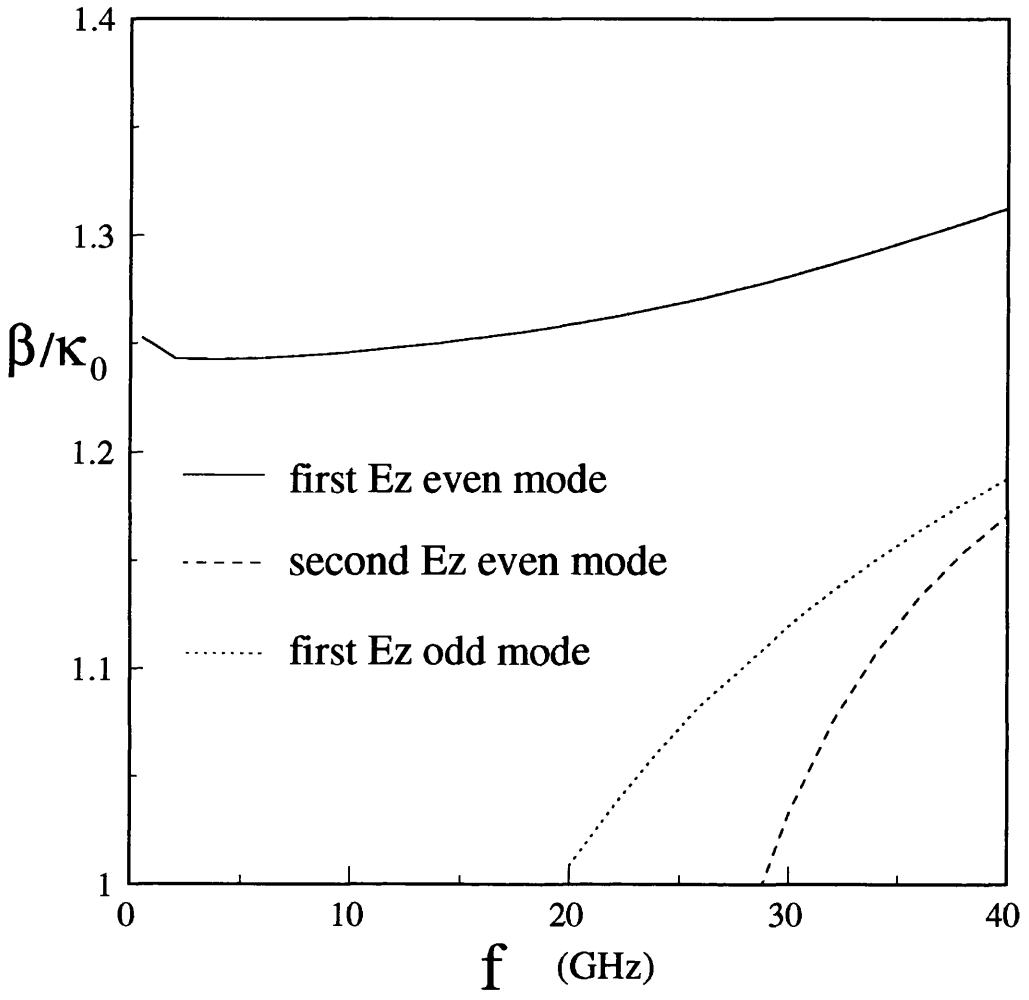

Figure 2.6: Propagation constant of the first few E_z even and odd modes as a function of frequency up to 40 GHz (ε_r=2.04, a=6.0e–3 m, h=3.0e–3 m, s_1=1.0e–3 m, w_1=1.0e–3 m)

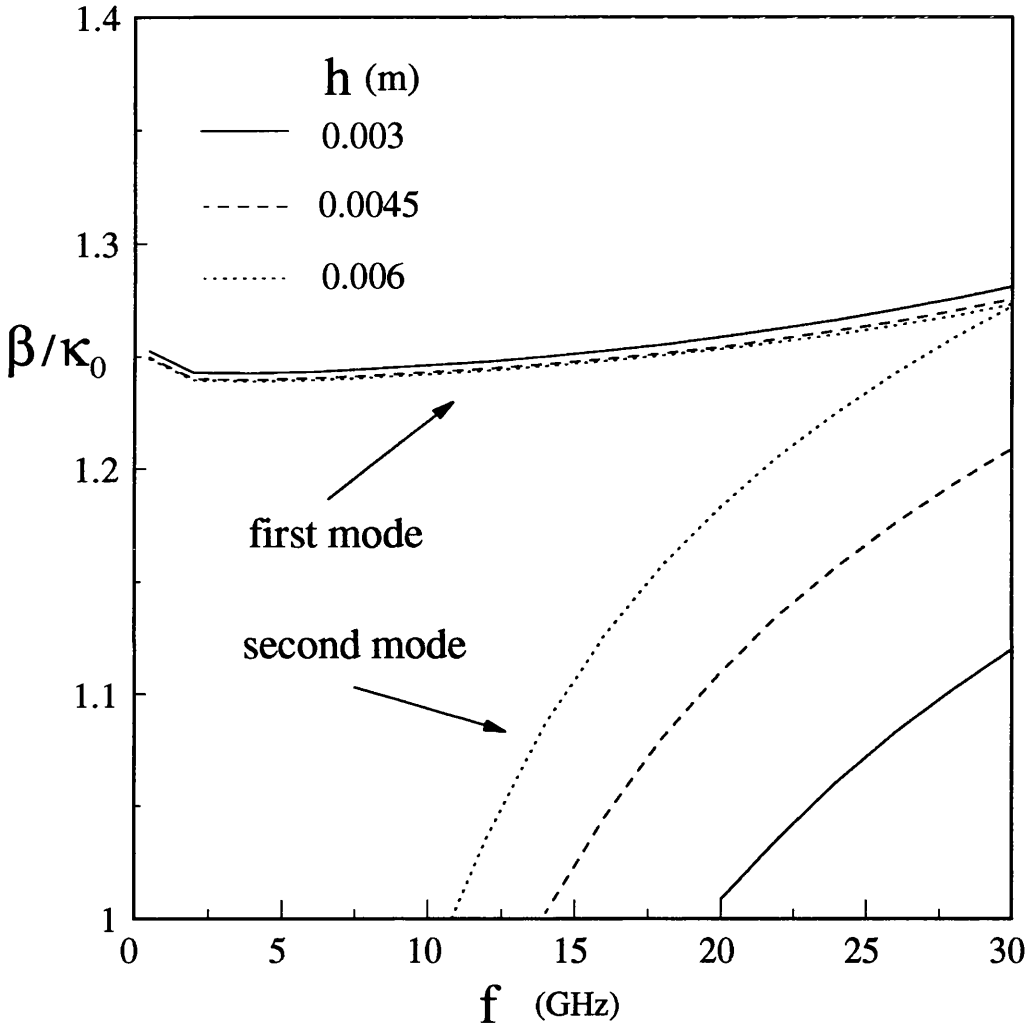

Figure 2.7: Propagation constant of the dominant and first higher–order modes as a function of frequency for different values of h (ε_r=2.04, a=6.0e–3m, s_1=1.0e–3 m, w_1=1.0e–3 m)

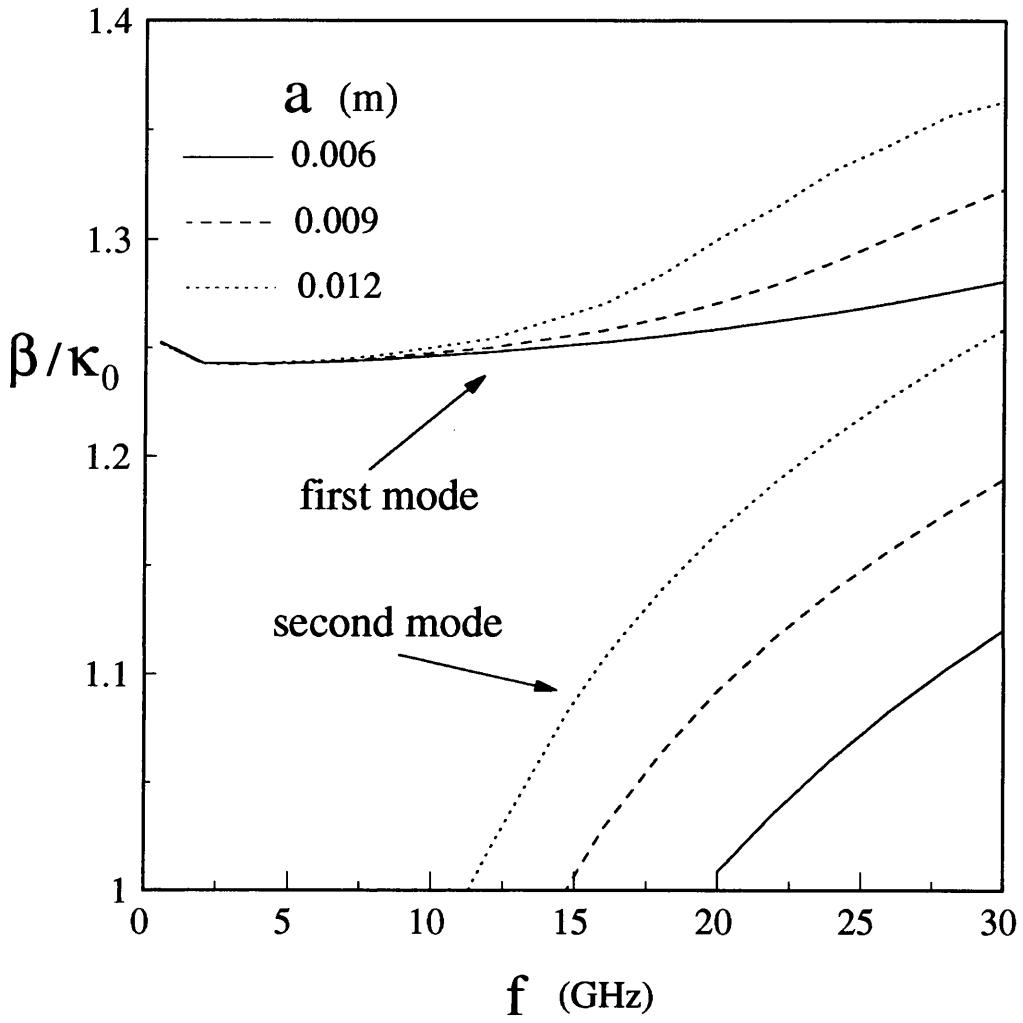

Figure 2.8: Propagation constant of the dominant and first higher-order modes as a function of frequency for different values of a (ε_r=2.04, h=3.0e-3 m, s_1=1.0e-3 m, w_1=1.0e-3 m)

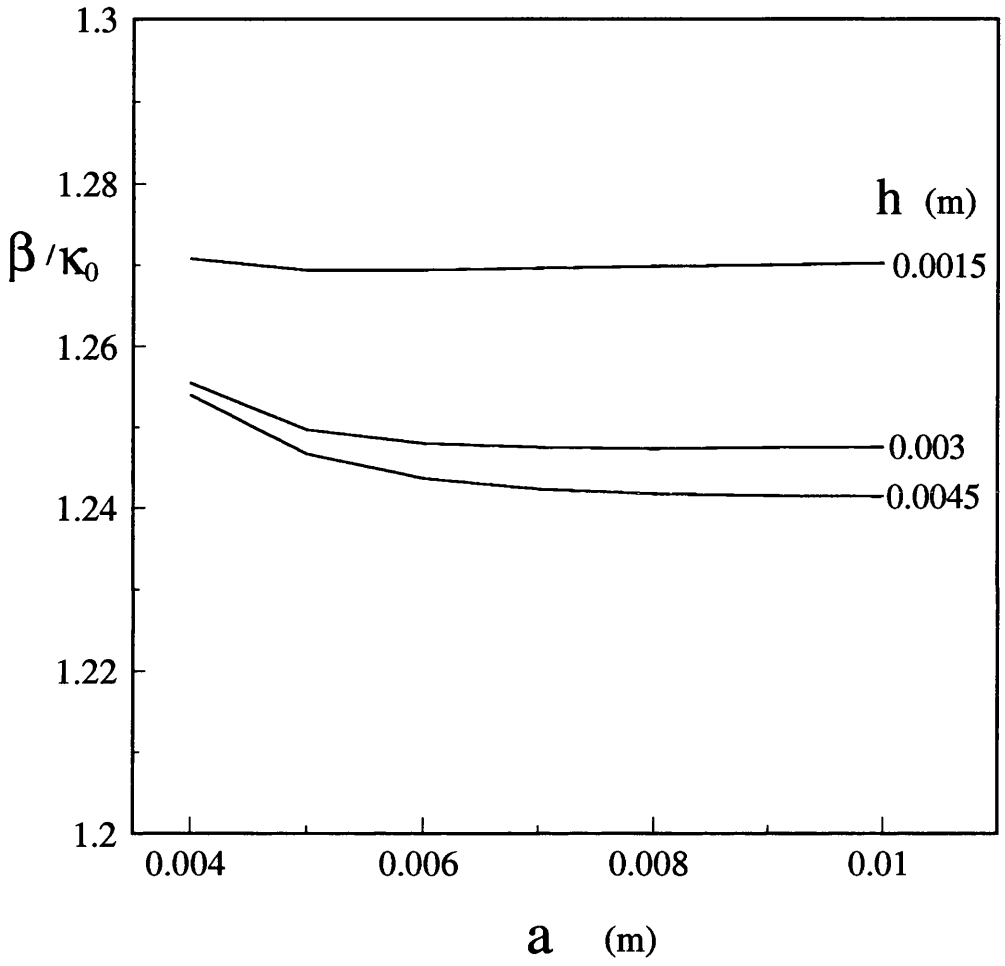

Figure 2.9: Propagation constant of the dominant mode as a function of a for different values of h (ε_r=2.04, s_1=0.75e–3 m, w_1=2.0e–3 m, f=5.0 GHz)

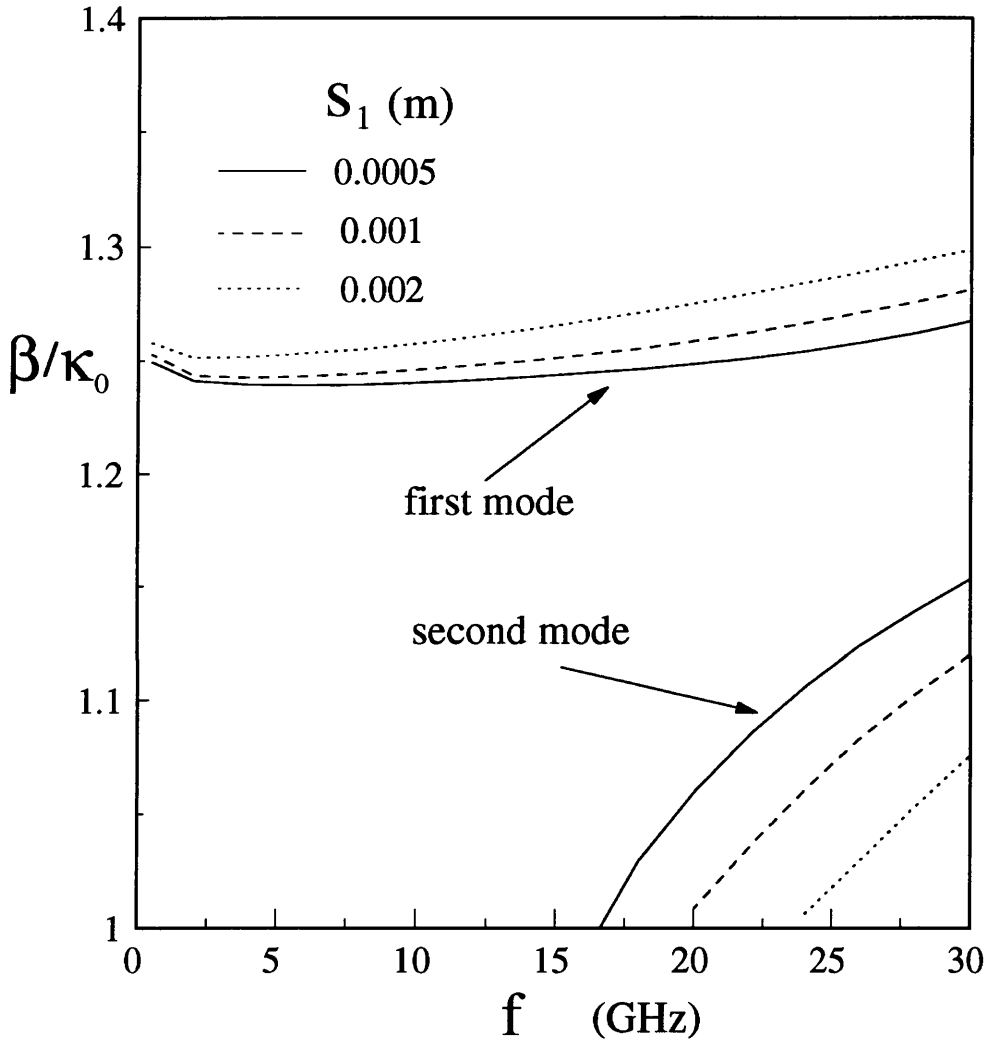

Figure 2.10: Propagation constant of the dominant and first higher–order modes as a function of frequency for different values of s_1 (ε_r=2.04, a=6.0e–3 m, h=3.0e–3 m, w_1=1.0e–3 m)

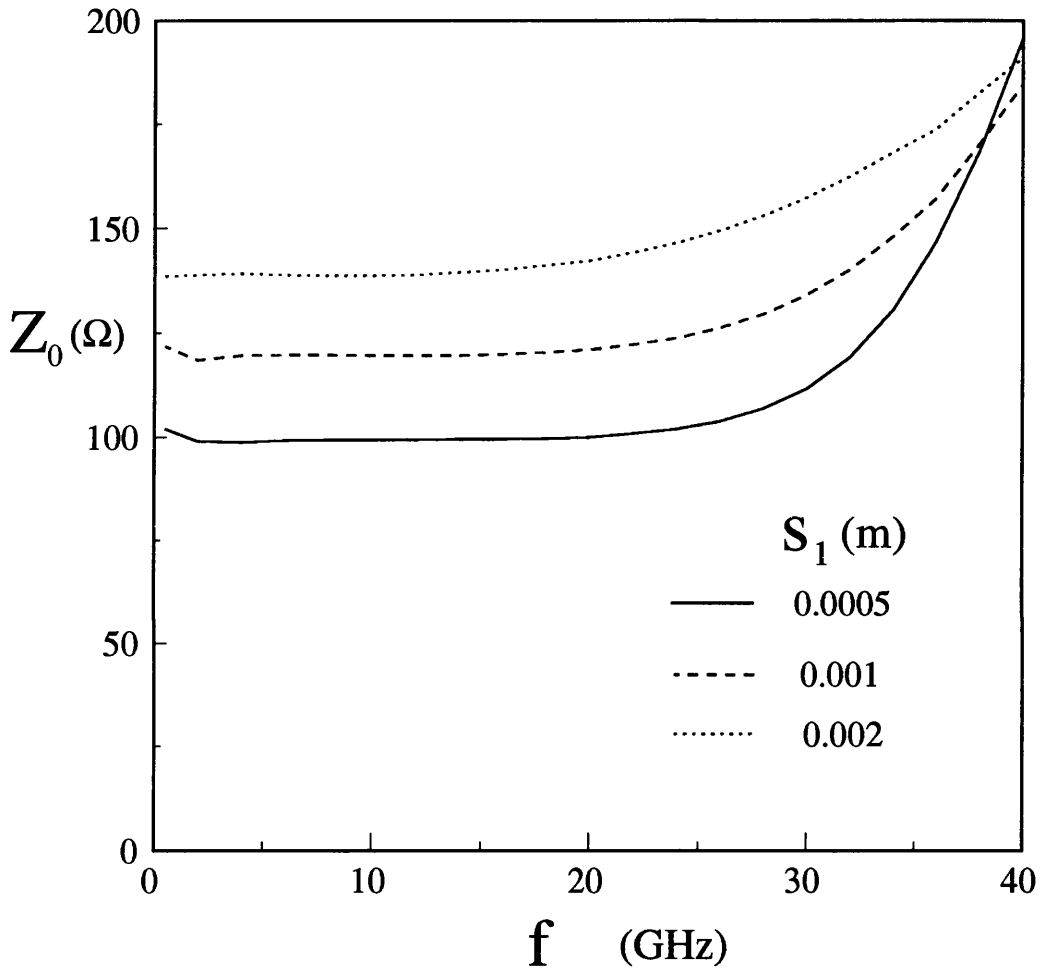

Figure 2.11: Characteristic impedance of the dominant mode as a function of frequency up to 40 GHz for different values of s_1 (ε_r=2.04, a=6.0e–3 m, h=3.0e–3 m, w_1=1.0e–3 m)

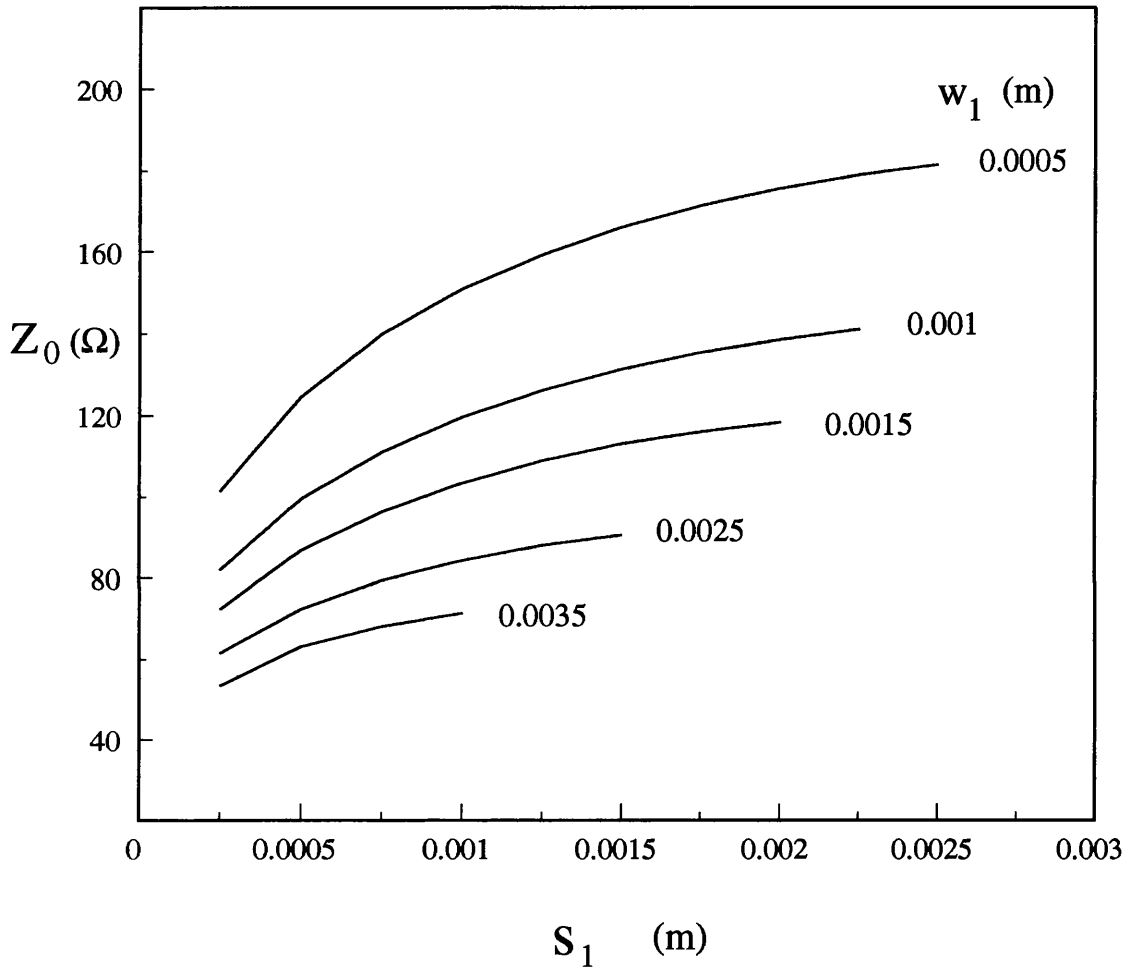

Figure 2.12: Characteristic impedance of the dominant mode as a function of s_1 for different values of w_1 (ε_r=2.04, a=6.0e–3 m, h=3.0e–3 m, f=10.0 GHz)

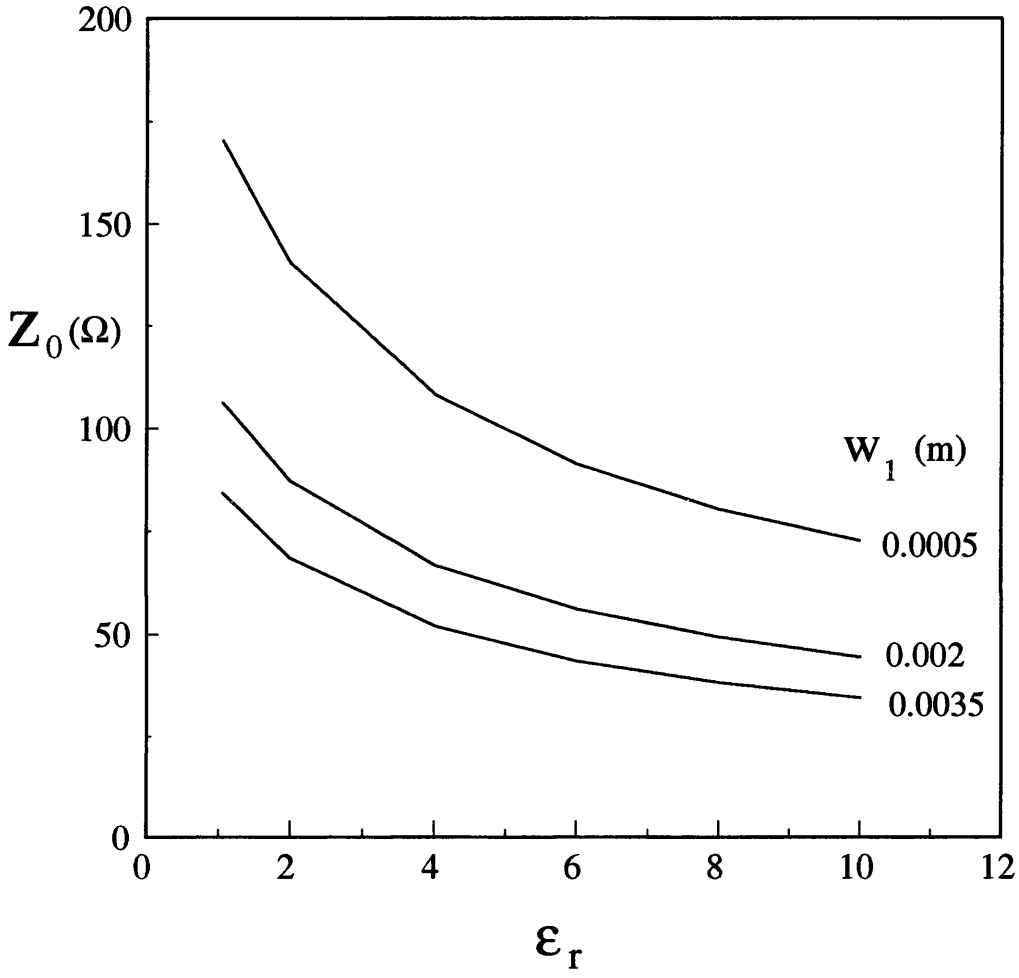

Figure 2.13: Characteristic impedance of the dominant mode as a function of ε_r for different values of w_1 (s_1=0.75e–3 m, a=6.0e–3 m, h=3.0e–3 m, f=4.0 GHz)

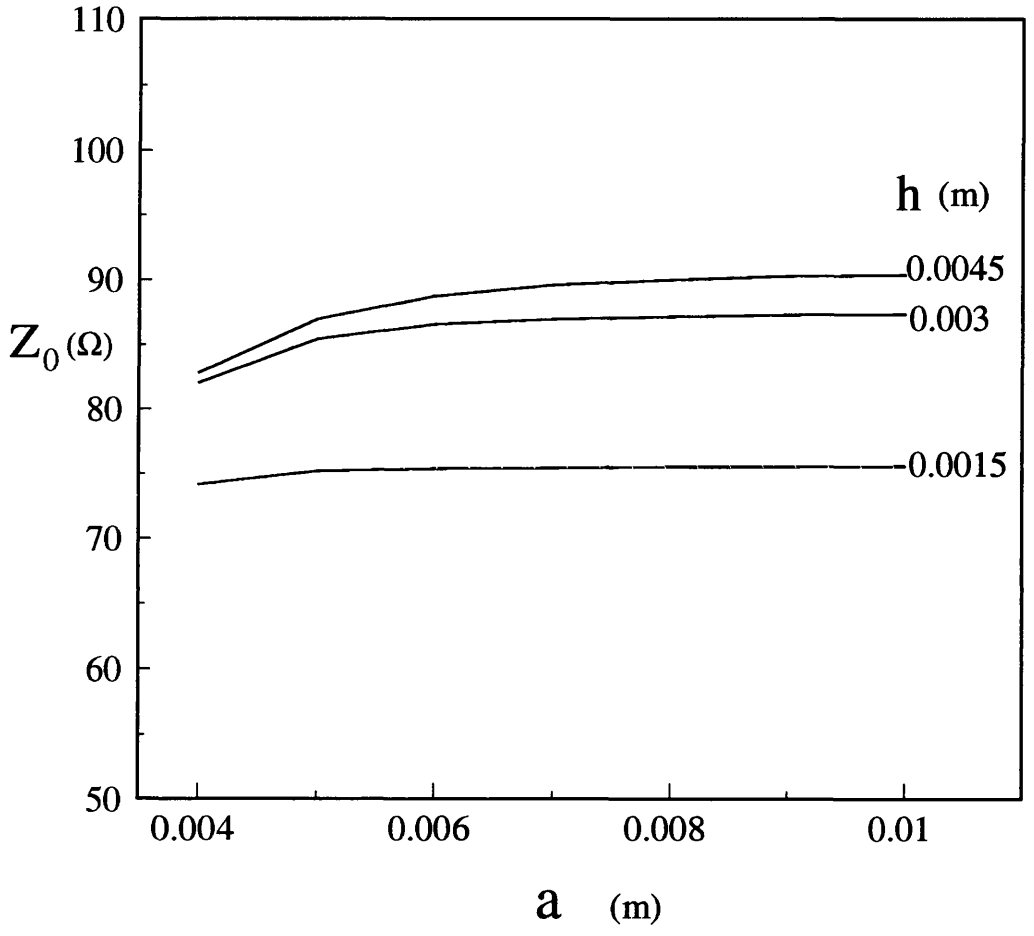

Figure 2.14: Characteristic impedance of the dominant mode as a function of a for different values of h (ε_r=2.04, s_1=0.75e–3 m, w_1=2.0e–3 m, f=5.0 GHz)

2.11 Conclusion

This chapter has presented an analysis for the propagation constant and characteristic impedance of the coplanar waveguide loaded inset dielectric guide. Good convergence of the solutions has been demonstrated and the accuracy of the analysis has been verified by comparison with experimental results. The numerical results are also shown for different values of structural and material parameters.

The dispersion in propagation constant and characteristic impedance is very small in the single–mode frequency range. Also, by decreasing the IDG dimensions the single–mode bandwidth can be widened. By suitable choice of the 5 available parameters (4 dimensions of the structure and the permittivity of the dielectric), a wide range of impedance can be achieved, leading to great flexibility in circuit design.

This structure shows promise for microwave and millimeter wave applications due to several attractive advantages. They include no use of air bridges for ground equalization, improvement of mechanical tolerance and heat sinking, ease of fabrication, good confinement of electromagnetic fields, suppression of propagation of surface modes, reduction of electromagnetic interference, a wide range of characteristic impedance and low dispersion.

References

[1] L.P. Schmidt and T. Itoh, "Spectral domain analysis of dominant and higher order modes in fin–lines," *IEEE Trans. Microwave Theory Tech.*, vol.MTT–28, pp.981–985, Sept. 1980.

[2] Y. Chen and B. Beker, "Analysis of single and coupled microstrip lines on anisotropic substrates using differential matrix operators and the spectral domain method," *IEEE Trans. Microwave Theory Tech.*, vol.MTT–41, pp.123–128, January 1993.

[3] T. Itoh and R. Mittra, "Spectral domain approach for calculating the dispersion characteristics of microstrip lines," *IEEE Trans. Microwave Theory Tech.*, vol.MTT–21, pp.496–499, July 1973.

[4] R.F. Harrington, "Field computation by moment methods," Malabar, Fla.: Krieger, 1982

[5] R. E. Collin, "Field theory of guided waves", McGraw-Hill Book Company Inc., 1960.

[6] T. Kitazawa, "Variational method for multiconductor coupled striplines with stratified anisotropic media," *IEEE Trans. Microwave Theory Tech.*, vol.MTT–37, pp.484–490, March 1989.

[7] I. S. Gradshteyn and I. M. Ryshik, "Tables of integrals, series and products", Academic Press, 1965.

[8] J. R. Brews, "Characteristic impedance of microstrip lines", *IEEE Trans. Microwave Theory Tech.*, Vol.MTT-35, pp.30-33, Jan. 1987.

[9] W.J. Getsinger, "Measurement and modeling of the apparent characteristic impedance of microstrip," *IEEE Trans. Microwave Theory Tech.*, vol.MTT–31, pp.624–632, August 1983.

[10] N. Fache and D. Dezutter, "Circuit parameters for single and coupled microstrip lines by a rigorous full–wave space–domain analysis," *IEEE Trans. Microwave Theory Tech.*, vol.MTT–37, pp.421–425, Feb 1989.

[11] J.B. Knorr and A. Tufekcioglu, "Spectral domain calculation of microstrip characteristic impedance," *IEEE Trans. Microwave Theory Tech.*, vol.MTT–23, pp.725–728, Sept. 1975.

[12] L.P. Schmidt, T. Itoh and H. Hofmann, "Characteristics of unilateral fin–line structures with arbitrarily located slots," *IEEE Trans. Microwave Theory Tech.*, vol.MTT–29, pp.352–355, April 1981.

[13] S.J. Hedges, "The analysis of inset dielectric guide by transverse resonance diffraction," *Ph.D Thesis*, Bath University, Bath, 1987.

[14] N. Izzat. "Space domain analysis of inhomogeneous waveguides of the microstrip and inset guide families," *Ph.D Thesis*, Bath University, Bath, 1991.

[15] R. W. Jackson,"Considerations in the use of coplanar waveguide for millimeter–wave integrated circuits," *IEEE Trans. Microwave Theory Tech.*, vol.MTT-34, pp.1450–1456, Dec. 1986.

[16] N.I. Dib, P.B. Katehi and G.E. Ponchak, "Analysis of shielded CPW discontinuities with air–bridges," in *1991 IEEE MTT–S international Microwave Symposium Digest*, pp.469–472.

[17] W. E. McKinzie and N.G. Alexopoulos, "Leakage losses for the dominant mode of conductor–backed coplanar waveguide," *IEEE Microwave and Guided Wave Letters*, vol.2, pp.65–66, Feb. 1992.

Chapter 3

ANALYSIS OF BROADSIDE COUPLED STRIP INSET DIELECTRIC GUIDE

3.1 Introduction

In this chapter the extended spectral domain approach is applied to the analysis of broadside-coupled strip inset dielectric guide. The solution for propagation constants for two fundamental and higher order modes is described briefly. Based on the total propagating power and the longitudinal strip currents, the characteristic impedances for the two fundamental modes are also calculated. The propagation characteristics of the two fundamental modes are then used to compute the 4-port circuit parameters of the coupled lines. These data are essential for accurate analysis and design of coupled line circuits.

The effects of various structural parameters on the S parameters are investigated. It is found that with suitable choice of widths of strips minimum value of reflection and maximum value of isolation can be obtained. Also, by changing the distance between the strips, both tight and loose coupling values can be achieved. There-

fore, this broadside coupled strip IDG structure is useful for the realization of both high and low coupling value directional couplers.

The simple procedure for the design of these couplers is described. Examples of strong and weak directional couplers with low return loss and high isolation are given.

Furthermore, the usefulness of the proposed couplers with transitions to coaxial cables is confirmed experimentally. The propagation constants and S parameters of coaxially excited coupled strips are measured. These results are in good agreement with the computed data and the validity of the method is confirmed.

3.2 Formulation of Integral Equations

Figure 3.1 shows the cross section of broadside-coupled strip inset dielectric guide and the coordinate system used in the analysis. The extended spectral domain approach for the analysis of CPW loaded IDG has been described in detail in the preceding chapter and has shown very good accuracy and efficiency. The method is used here to analyze broadside coupled strip IDG and only the key steps are given.

Solutions to the wave equations in the Fourier transformed domain are obtained for the different regions of the structure (air, upper and lower dielectric layers in the groove). The solutions contain coefficients, which are determined by applying the boundary conditions at infinity, on the base of the groove and across the lower interface ($y = -h_1$), and introducing the electric field components transverse to y at the upper interface ($y = 0$). Enforcing the conditions that the current density

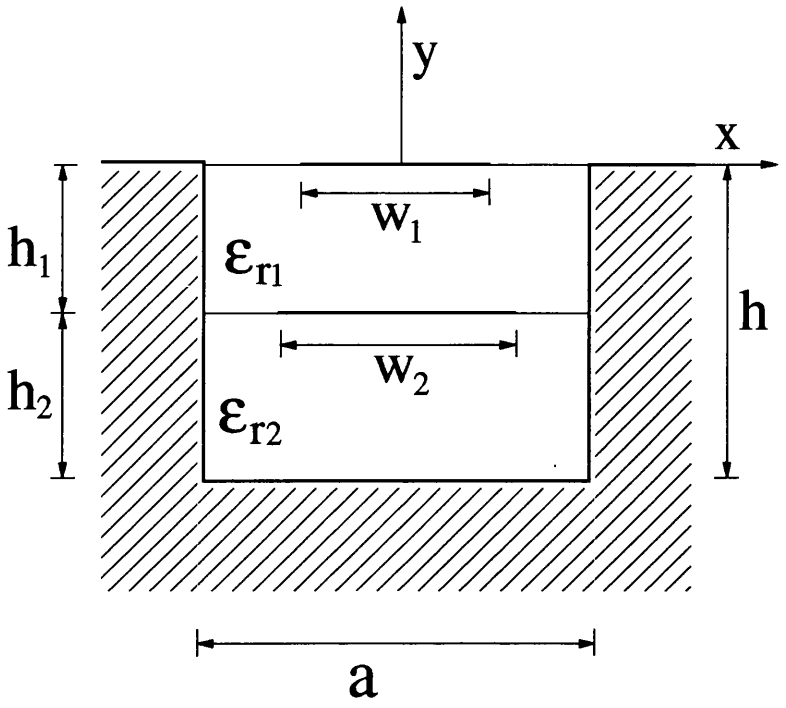

Figure 3.1: Cross section of a broadside coupled strip inset dielectric guide and the coordinate system used in the analysis

components at $y = 0$ vanish for $\frac{w_1}{2} < |x| < \frac{a}{2}$ and that the tangential electric field components at $y = -h_1$ vanish for $|x| < \frac{w_2}{2}$ leads to four integral equations for tangential electric field components at $y = 0$ and current components at $y = -h_1$.

$$\frac{1}{2\pi}\int_{-\infty}^{\infty}[Y_{i1}^{a}\tilde{E}_x^u(\alpha)+Y_{i2}^{a}\tilde{E}_z^u(\alpha)]e^{-j\alpha x}d\alpha$$
$$+\frac{1}{a}\sum_{n=-\infty}^{\infty}[Y_{i1}^{s}\tilde{E}_x^u(\alpha_n)+Y_{i2}^{s}\tilde{E}_z^u(\alpha_n)+Y_{i3}^{s}\tilde{J}_x^l(\alpha_n)+Y_{i4}^{s}\tilde{J}_z^l(\alpha_n)]e^{-j\alpha_n x}$$
$$= 0 \quad \text{for} \quad \frac{w_1}{2} < |x| < \frac{a}{2} \quad i = 1,2 \tag{3.1}$$

$$\frac{1}{a}\sum_{n=-\infty}^{\infty}[Y_{i1}^{s}\tilde{E}_x^u(\alpha_n)+Y_{i2}^{s}\tilde{E}_z^u(\alpha_n)+Y_{i3}^{s}\tilde{J}_x^l(\alpha_n)+Y_{i4}^{s}\tilde{J}_z^l(\alpha_n)]e^{-j\alpha_n x}$$
$$= 0 \quad \text{for} \quad |x| < \frac{w_2}{2} \quad i = 3,4 \tag{3.2}$$

where $\tilde{E}_x^u$ and $\tilde{E}_z^u$ are the Fourier transforms of the x and z electric field components on the upper interface. $\tilde{J}_x^l$ and $\tilde{J}_z^l$ are Fourier transforms of x and z current

components on the lower conducting strip.

$$\tilde{E}_x^u(\alpha_n) = (\int_{-\frac{a}{2}}^{-\frac{w_1}{2}} + \int_{\frac{w_1}{2}}^{\frac{a}{2}}) E_x^u(x) e^{j\alpha_n x} dx \tag{3.3}$$

$$\tilde{E}_z^u(\alpha_n) = (\int_{-\frac{a}{2}}^{-\frac{w_1}{2}} + \int_{\frac{w_1}{2}}^{\frac{a}{2}}) E_z^u(x) e^{j\alpha_n x} dx \tag{3.4}$$

$$\tilde{J}_x^l(\alpha_n) = \int_{-\frac{w_2}{2}}^{\frac{w_2}{2}} J_x^l(x) e^{j\alpha_n x} dx \tag{3.5}$$

$$\tilde{J}_z^l(\alpha_n) = \int_{-\frac{w_2}{2}}^{\frac{w_2}{2}} J_z^l(x) e^{j\alpha_n x} dx \tag{3.6}$$

The elements of Fourier–transformed Green's function for the air region $[Y^a]$ in (3.1) have been given in (2.39) – (2.41) in chapter 2. The elements of $[Y^s]$ in (3.1) and (3.2) are written as

$$Y_{11}^s = j(G_1\alpha_n^2 - G_4\beta^2)D^s, \quad Y_{12}^s = Y_{21}^s = j\alpha_n\beta(G_1 + G_4)D^s$$

$$Y_{22}^s = j(G_1\beta^2 - G_4\alpha_n^2)D^s, \quad Y_{13}^s = Y_{31}^s = (G_2\alpha_n^2 + G_5\beta^2)D^s$$

$$Y_{14}^s = Y_{41}^s = Y_{23}^s = Y_{32}^s = \alpha_n\beta(G_2 - G_5)D^s$$

$$Y_{24}^s = Y_{42}^s = (G_2\beta^2 + G_5\alpha_n^2)D^s, \quad Y_{33}^s = j(G_3\alpha_n^2 - G_6\beta^2)D^s$$

$$Y_{34}^s = Y_{43}^s = j\alpha_n\beta(G_3 + G_6)D^s, \quad Y_{44}^s = j(G_3\beta^2 - G_6\alpha_n^2)D^s$$

with

$$G_1 = \frac{1}{Q_e}\omega\varepsilon_0\varepsilon_{t1}(\gamma_{e2}\varepsilon_{t1}\tanh\gamma_{e2}h_2\tanh\gamma_{e1}h_1 + \gamma_{e1}\varepsilon_{t2})$$

$$G_2 = \frac{1}{Q_e}\frac{\gamma_{e1}\gamma_{e2}\varepsilon_{t1}}{\cosh\gamma_{e1}h_1}\tanh\gamma_{e2}h_2$$

$$G_3 = \frac{1}{Q_e}\frac{\gamma_{e1}^2\gamma_{e2}}{\omega\varepsilon_0}\tanh\gamma_{e1}h_1\tanh\gamma_{e2}h_2$$

$$G_4 = \frac{1}{Q_h}\gamma_{h1}(\gamma_{h2} + \gamma_{h1}\tanh\gamma_{h1}h_1\tanh\gamma_{h2}h_2)$$

$G_5 = \frac{1}{Q_h}\frac{\omega\mu_0\gamma_{h1}}{\cosh\gamma_{h1}h_1}\tanh\gamma_{h2}h_2$

$G_6 = \frac{1}{Q_h}(\omega\mu_0)^2\tanh\gamma_{h2}h_2\tanh\gamma_{h1}h_1$

$Q_e = \gamma_{e1}(\gamma_{e2}\varepsilon_{t1}\tanh\gamma_{e2}h_2 + \gamma_{e1}\varepsilon_{t2}\tanh\gamma_{e1}h_1)$

$Q_h = \omega\mu_0(\gamma_{h2}\tanh\gamma_{h1}h_1 + \gamma_{h1}\tanh\gamma_{h2}h_2)$

$D^s = 1/(\alpha_n^2+\beta^2), \quad \gamma_i^2 = \alpha_n^2+\beta^2-\kappa_0^2\varepsilon_{ri}$ for $i = 1,2$

3.3 Application of Galerkin's Method

In order to solve the integral equations (3.1) and (3.2), Galerkin's method is applied. Expanding the electric field components at $y = 0$ and the current components at $y = -h_1$ in terms of known basis functions, and taking the inner product of the integral equations with basis functions, yields a homogeneous matrix equation for the unknown expansion coefficients.

$$\begin{bmatrix} K_{im}^{a11}+K_{im}^{s11} & K_{im}^{a12}+K_{im}^{s12} & K_{im}^{s13} & K_{im}^{s14} \\ K_{im}^{a21}+K_{im}^{s21} & K_{im}^{a22}+K_{im}^{s22} & K_{im}^{s23} & K_{im}^{s24} \\ K_{im}^{s31} & K_{im}^{s32} & K_{im}^{s33} & K_{im}^{s34} \\ K_{im}^{s41} & K_{im}^{s42} & K_{im}^{s43} & K_{im}^{s44} \end{bmatrix} \begin{bmatrix} C_{xm}^E \\ C_{zm}^E \\ C_{xm}^J \\ C_{zm}^J \end{bmatrix} = [0] \tag{3.7}$$

where elements of the matrix [K] are given by

$$K_{im}^{spr} = \frac{1}{a}\sum_{n=-\infty}^{\infty} K_i^{sp}(-\alpha_n)\ Y_{pr}^s\ K_m^{sr}(\alpha_n) \quad p,r = 1,2,3,4 \tag{3.8}$$

$$K_{im}^{apr} = \frac{1}{2\pi}\int_{-\infty}^{\infty} K_i^{ap}(-\alpha)\ Y_{pr}^a\ K_m^{ar}(\alpha)\,d\alpha \quad p,r = 1,2 \tag{3.9}$$

$K_m^{sp}(\alpha_n)$ and $K_m^{ap}(\alpha)$ are defined as

$$K_m^{s1}(\alpha_n) = \tilde{E}_{xm}^u(\alpha_n), \quad K_m^{s2}(\alpha_n) = \tilde{E}_{zm}^u(\alpha_n) \tag{3.10}$$

$$K_m^{s3}(\alpha_n) = \tilde{J}_{xm}^l(\alpha_n), \quad K_m^{s4}(\alpha_n) = \tilde{J}_{zm}^l(\alpha_n) \tag{3.11}$$

$$K_m^{a1}(\alpha) = \tilde{E}_{xm}^u(\alpha), \quad K_m^{a2}(\alpha) = \tilde{E}_{zm}^u(\alpha) \tag{3.12}$$

with

$$\tilde{E}_{xm}^u(\alpha_n) = (\int_{-\frac{a}{2}}^{-\frac{w_1}{2}} + \int_{\frac{w_1}{2}}^{\frac{a}{2}}) E_{xm}^u(x) e^{j\alpha_n x} dx \tag{3.13}$$

$$\tilde{E}_{zm}^u(\alpha_n) = (\int_{-\frac{a}{2}}^{-\frac{w_1}{2}} + \int_{\frac{w_1}{2}}^{\frac{a}{2}}) E_{zm}^u(x) e^{j\alpha_n x} dx \tag{3.14}$$

$$\tilde{J}_{xm}^l(\alpha_n) = \int_{-\frac{w_2}{2}}^{\frac{w_2}{2}} J_{xm}^l(x) e^{j\alpha_n x} dx \tag{3.15}$$

$$\tilde{J}_{zm}^l(\alpha_n) = \int_{-\frac{w_2}{2}}^{\frac{w_2}{2}} J_{zm}^l(x) e^{j\alpha_n x} dx \tag{3.16}$$

Nontrivial solutions for the unknown expansion coefficients may be obtained by requiring the determinant of the coefficient matrix in (3.7) to be zero. This condition results in the determinantal equation for the propagation constant.

3.4 Choice of Basis Functions

The calculations of the Fourier transforms of the basis functions in (3.13) – (3.16) are required in order to numerically evaluate the matrix elements in (3.7). The boundary conditions require the z component of the electric field to be zero at

the conducting edges on the upper surface and the x component of the current on the lower strip to be zero at the edges of the lower strip. Integrating (3.14) and (3.15) by parts and using the boundary conditions, the following expressions for $\tilde{E}^u_{zm}(\alpha_n)$ and $\tilde{J}^l_{xm}(\alpha_n)$ are obtained

$$\tilde{E}^u_{zm}(\alpha_n) = \frac{j}{\alpha_n}\left(\int_{-\frac{a}{2}}^{-\frac{w_1}{2}} + \int_{\frac{w_1}{2}}^{\frac{a}{2}}\right)\frac{\partial E^u_{zm}(x)}{\partial x}e^{j\alpha_n x}dx \tag{3.17}$$

$$\tilde{J}^l_{xm}(\alpha_n) = \frac{j}{\alpha_n}\int_{-\frac{w_2}{2}}^{\frac{w_2}{2}}\frac{\partial J^l_{xm}(x)}{\partial x}e^{j\alpha_n x}dx \tag{3.18}$$

As $\frac{\partial E^u_z(x)}{\partial x}$ and $\frac{\partial J^l_z(x)}{\partial x}$ satisfy the same boundary and singular edge conditions as $E^u_x(x)$ and $J^l_z(x)$ respectively [1], the basis functions for $\frac{\partial E^u_{zm}(x)}{\partial x}$ and $\frac{\partial J^l_{xm}(x)}{\partial x}$ can be chosen to be the same as $E^u_{xm}(x)$ and $J^l_{zm}(x)$, respectively. As a consequence, the computational time is reduced. Furthermore, the convergence in computing the matrix elements (3.8) and (3.9) is improved because the factor $\frac{j}{\alpha_n}$ appears in (3.17) and (3.18).

In order to achieve fast convergence to the solutions of the determinantal equation, the edge conditions satisfied by tangential electric field components on the upper interface and current components on the lower strip should be accounted for in choosing the basis functions. Here, basis functions are chosen to be a complete set of orthogonal functions weighted by an appropriate singular function which describes the edge conditions.

Due to the presence of the metallic corners at $x = \pm\frac{a}{2}$ and the edges of the upper conducting strip at $x = \pm\frac{w_1}{2}$, the electric field is singular at the corners and the edges. It can be shown that E^u_x and $\frac{\partial E^u_z}{\partial x}$ have the same singular behaviour of type $r^{-\frac{1}{3}}$ at metallic corners and of type $r^{-\frac{1}{2}}$ at the edges of the strip [2]. In order to include this singular behaviour in the basis function, the following basis

functions E^u_{xm} and $\frac{\partial E^u_{zm}}{\partial x}$ are chosen

$$E^u_{xm}(x) = \frac{\partial E^u_{zm}(x)}{\partial x} = (1-x')^{-\frac{1}{3}}(1+x')^{-\frac{1}{2}} \begin{cases} P_m^{(-\frac{1}{3},-\frac{1}{2})}(x') & \text{for } \frac{w_1}{2} < x < \frac{a}{2} \\ \pm P_m^{(-\frac{1}{3},-\frac{1}{2})}(x') & \text{for } -\frac{a}{2} < x < -\frac{w_1}{2} \end{cases} \tag{3.19}$$

where $x' = 2(|x| - x_0)/w_s$, $x_0 = (a + w_1)/4$ and $w_s = (a - w_1)/2$. $P_m^{(-\frac{1}{3},-\frac{1}{2})}$ are Jacobi polynomials [3]. The plus and minus signs in $\pm$ are chosen for the E_z odd and even modes, respectively. It should be noted that for E^u_{xm} the series starts at 0, but for $\frac{\partial E^u_{zm}}{\partial x}$ the series starts at 1. The reason for this is that

(a) E^u_z is zero at the strip edge ($x = \frac{w_1}{2}$) and the metallic corner ($x = \frac{a}{2}$) so that $\frac{\partial E^u_z}{\partial x}$ must have zero average in the range and

(b) $\int_{\frac{w_1}{2}}^{\frac{a}{2}} \frac{\partial E^u_{z0}(x)}{\partial x}\, dx \neq 0$.

Similarly, the presence of the edges of the lower conducting strip at $x = \pm\frac{w_2}{2}$ introduces singularities in the current distribution. The singularity is of type $r^{-\frac{1}{2}}$ at the strip edges [4]. Taking the edge singularity into account, the basis functions $\frac{\partial J^l_{xm}}{\partial x}$ and J^l_{zm} are chosen as follows

$$\frac{\partial J^l_{xm}(x)}{\partial x} = J^l_{zm}(x) = \left[1 - (\frac{2x}{w_2})^2\right]^{-\frac{1}{2}} T_n(\frac{2x}{w_2}) \quad \text{for } |x| < \frac{w_2}{2} \tag{3.20}$$

where T_n are Chebyshev polynomials [3]. $n = 2m + 1$ and $n = 2m$ are chosen for the E_z odd and even modes, respectively. Note that $m = 0, 1, 2\ldots$ except that $m = 1, 2, \ldots$ for $\frac{\partial J^l_{xm}}{\partial x}$ for the E_z even mode since the zeroth term of $J^l_x(x)$ for the E_z even mode is not zero at the edges of the lower strip as boundary conditions require.

3.5 Characteristic Impedances of Two Fundamental Modes

The existence of two conducting strips in the IDG structure implies that two fundamental modes without cut-off frequencies can be supported by the structure. At low enough frequencies the longitudinal components of electric and magnetic field are negligible compared to the corresponding transverse field components, and so these two modes can be referred to as quasi-TEM modes [5] [6]. The following discussion and analysis are restricted to the quasi-TEM type fundamental modes (rather than higher-order modes which are assumed to be evanescent).

In order to obtain an equivalent coupled line circuit for the structure considered here, which is useful in analysis and design of coupled-strip structure such as directional couplers and filters, the characteristic impedances of these two modes must be first determined. However, for the quasi-TEM structure, unique definition does not exist due to the existence of longitudinal field components (specially at higher frequencies). The different results for the characteristic impedances are found from different definitions. These differences stem from different choices of the primary or independent quantities, and the derived quantities [8] [9]. From a practical point of view, the primary quantity (either current or voltage) is chosen to be the most accessible one. In the microstrip-like or other quasi-TEM structure, currents are primary and voltages are derived. This is due to the fact that the total longitudinal current is a physical quantity which is conserved when the strip is connected to a load or a driver. Also, the power flowing through the cross section of the structure is an important quantity for the definition of characteristic impedances used in the circuit description because both waveguide and its equivalent TEM coupled line should propagate the same power. Due to the above reasons, we use the definition based on the total transported power

and currents on both strips [10].

It is known from the previous sections that after the propagation constants of two fundamental modes, β_1 and β_2 are found, the expansion coefficients can be obtained from the matrix equation (3.7) and the Fourier-transformed field components can be in turn determined. Based on the derived field components and expansion coefficients, the total power flow along the guide for each mode and the total longitudinal current on each conducting strip for each mode can be evaluated. The power flow associated with mode j propagating in the positive z direction is denoted by P_j. The total longitudinal current flowing in the positive z direction on conducting strip i (line i) due to mode j is defined as I_{ij} where i=1 for the lower strip, 2 for the upper strip; and j=1 for mode 1, 2 for mode 2. The circuit voltage V_{ij} at strip i due to mode j can be found by using the following definition of modal power P_j and the reciprocity theorem.

The definition of modal power [10] is given by

$$P_j = \frac{1}{2}\int_s \vec{E}_j \times \vec{H}_j^{\,*} \cdot d\vec{s} = \frac{1}{2}\sum_{k=1}^{2} V_{kj} I_{kj}^* \quad (j = 1,2) \tag{3.21}$$

The reciprocity theorem [1] can be used to obtain the following equations

$$\frac{1}{2}\int_s \vec{E}_i \times \vec{H}_j \cdot ds = \frac{1}{2}\sum_{k=1}^{2} V_{ki} I_{kj} = 0 \quad (i,j = 1,2;\ \ i \neq j) \tag{3.22}$$

As we restrict the analysis to the lossless structure, I_{ij} can be chosen to be purely real. The above equations can be written in the following matrix form

$$\begin{bmatrix} 2P_1 & 0 \\ 0 & 2P_2 \end{bmatrix} = \begin{bmatrix} V_{11} & V_{21} \\ V_{12} & V_{22} \end{bmatrix} \begin{bmatrix} I_{11} & I_{12} \\ I_{21} & I_{22} \end{bmatrix} \tag{3.23}$$

A characteristic impedance Z_{ij} of strip i for mode j propagating in the positive z direction is defined as

$$Z_{ij} = \frac{V_{ij}}{I_{ij}} \tag{3.24}$$

From the definition and (3.23), we obtain the following expressions for the characteristic impedances

$$Z_{11} = \frac{2P_1}{I_{11}^2} \frac{1}{1 - R_1^i/R_2^i} \tag{3.25}$$

$$Z_{22} = \frac{2P_2}{I_{22}^2} \frac{1}{1 - R_1^i/R_2^i} \tag{3.26}$$

$$Z_{12} = -\frac{2P_2}{I_{12}^2} \frac{1}{R_2^i/R_1^i - 1} \tag{3.27}$$

$$Z_{21} = -\frac{2P_1}{I_{21}^2} \frac{1}{R_2^i/R_1^i - 1} \tag{3.28}$$

In the above expressions, R_j^i is current ratio for mode j, given by

$$R_j^i = \frac{I_{2j}}{I_{1j}} \tag{3.29}$$

From (3.23), voltage ratio for one mode can be obtained in terms of current ratio for the other mode.

$$R_1^v = \frac{V_{21}}{V_{11}} = -\frac{1}{R_2^i} \tag{3.30}$$

$$R_2^v = \frac{V_{22}}{V_{12}} = -\frac{1}{R_1^i} \tag{3.31}$$

Also, the following relations for characteristic impedances can be found.

$$\frac{Z_{11}}{Z_{21}} = \frac{Z_{12}}{Z_{22}} = -R_1^i R_2^i \tag{3.32}$$

It is clearly shown in the above equation that the ratio of the characteristic impedance of strip 1 to the characteristic impedance of strip 2 is the same for each mode and that this ratio can be expressed in terms of the current ratios of two fundamental modes. The relations (3.30) – (3.32) are the same as those given in [11], which were derived based on the reciprocity which must be satisfied by the transmission line equations.

3.6 The Equivalent Circuit

3.6.1 Voltage and Current Representation

Figure 3.2 shows the equivalent coupled-line circuit for the broadside coupled strip IDG. The total voltages on both lines are a linear combination of the incident and reflected waves of two fundamental modes [12]

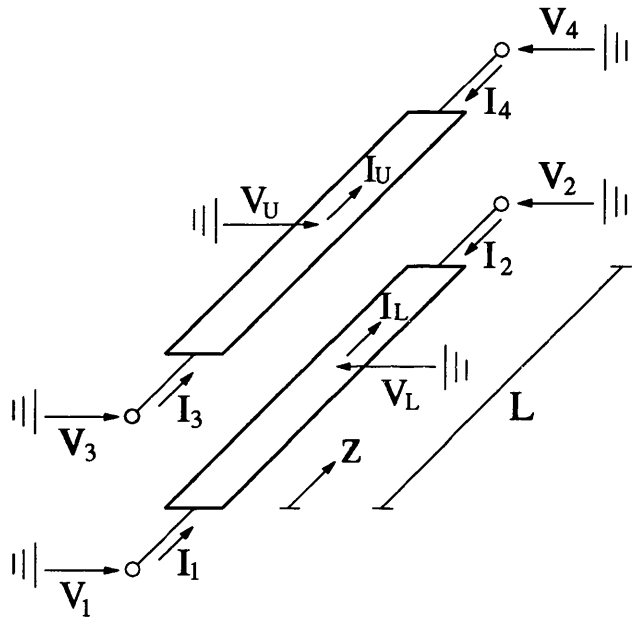

Figure 3.2: Equivalent circuit for the broadside couple strip IDG

$$V_L = C_1 e^{-j\beta_1 z} + C_2 e^{j\beta_1 z} + C_3 e^{-j\beta_2 z} + C_4 e^{j\beta_2 z} \tag{3.33}$$

$$V_U = R_1^v C_1 e^{-j\beta_1 z} + R_1^v C_2 e^{j\beta_1 z} + R_2^v C_3 e^{-j\beta_2 z} + R_2^v C_4 e^{j\beta_2 z} \tag{3.34}$$

where C_1, C_2, C_3 and C_4 are unknown coefficients. The corresponding currents on the lines are given by

$$I_L = \frac{C_1}{Z_{11}} e^{-j\beta_1 z} - \frac{C_2}{Z_{11}} e^{j\beta_1 z} + \frac{C_3}{Z_{12}} e^{-j\beta_2 z} - \frac{C_4}{Z_{12}} e^{j\beta_2 z} \tag{3.35}$$

$$I_U = \frac{R_1^v C_1}{Z_{21}} e^{-j\beta_1 z} - \frac{R_1^v C_2}{Z_{21}} e^{j\beta_1 z} + \frac{R_2^v C_3}{Z_{22}} e^{-j\beta_2 z} - \frac{R_2^v C_4}{Z_{22}} e^{j\beta_2 z} \tag{3.36}$$

3.6.2 Four–Port Parameters

The impedance matrix for four ports can now be derived by solving port voltages in terms of port currents. The port voltages can be expressed in terms of coefficients as follows

$$\begin{bmatrix} V_1 \\ V_2 \\ V_3 \\ V_4 \end{bmatrix} = \begin{bmatrix} 1 & 1 & 1 & 1 \\ e^{-j\beta_1 L} & e^{j\beta_1 L} & e^{-j\beta_2 L} & e^{j\beta_2 L} \\ R_1^v & R_1^v & R_2^v & R_2^v \\ R_1^v e^{-j\beta_1 L} & R_1^v e^{j\beta_1 L} & R_2^v e^{-j\beta_2 L} & R_2^v e^{j\beta_2 L} \end{bmatrix} \begin{bmatrix} C_1 \\ C_2 \\ C_3 \\ C_4 \end{bmatrix} \tag{3.37}$$

or in the simplified form

$$[V] = [U][C] \tag{3.38}$$

Similarly, the port currents are given by

$$\begin{bmatrix} I_1 \\ I_2 \\ I_3 \\ I_4 \end{bmatrix} = \begin{bmatrix} \frac{1}{z_{11}} & -\frac{1}{z_{11}} & \frac{1}{z_{12}} & -\frac{1}{z_{12}} \\ -\frac{1}{z_{11}} e^{-j\beta_1 L} & \frac{1}{z_{11}} e^{j\beta_1 L} & -\frac{1}{z_{12}} e^{-j\beta_2 L} & \frac{1}{z_{12}} e^{j\beta_2 L} \\ \frac{R_1^v}{Z_{21}} & -\frac{R_1^v}{Z_{21}} & \frac{R_2^v}{Z_{22}} & -\frac{R_2^v}{Z_{22}} \\ -\frac{R_1^v}{Z_{21}} e^{-j\beta_1 L} & \frac{R_1^v}{Z_{21}} e^{j\beta_1 L} & -\frac{R_2^v}{Z_{22}} e^{-j\beta_2 L} & \frac{R_2^v}{Z_{22}} e^{j\beta_2 L} \end{bmatrix} \begin{bmatrix} C_1 \\ C_2 \\ C_3 \\ C_4 \end{bmatrix} \tag{3.39}$$

or in the following form

$$[I] = [W][C] \tag{3.40}$$

Inverting (3.40) and substituting the resulting expressions for coefficients into (3.38), we obtain the following matrix equation which relates port voltages to

port currents

$$\begin{bmatrix} V_1 \\ V_2 \\ V_3 \\ V_4 \end{bmatrix} = [Z] \begin{bmatrix} I_1 \\ I_2 \\ I_3 \\ I_4 \end{bmatrix} \tag{3.41}$$

Where $[Z] = [U][W]^{-1}$ is the impedance matrix, $[W]^{-1}$ is the inverse matrix of [W].

Scattering matrix can be obtained [13] from impedance matrix using the following relation

$$[S] = ([Z] - Z_0[I])([Z] + Z_0[I])^{-1} \tag{3.42}$$

where $[I]$ is the unit matrix and Z_0 represents the normalizing impedance at each port.

3.7 Numerical Results

3.7.1 Propagation Characteristics

It has been found from numerical results that two or three basis functions for each expansion quantity are sufficient to obtain accurate solutions for propagation constants to four significant digits, but more basis functions are required for accurate solutions for the characteristic impedances. In fact, the solutions for the characteristic impedances are stable to less than 0.5 percent by using six basis functions for each expansion quantity. Figure 3.3 shows the dispersion characteristics of the first few even and odd modes up to 10 GHz. It can be seen from the figure that the two fundamental modes which have no cut-off frequencies are the first two E_z even modes.

Figures 3.4 and 3.5 show the frequency dependence of strip current ratios and characteristic impedances of two fundamental modes for $\varepsilon_{r1} = 2.04$, respectively. It can be seen that Z_{11} and Z_{22} change very little as frequency increases. Values of Z_{21} and Z_{12} are negative and change as frequency increases. As can be seen from the relation for the characteristic impedances in (3.32) in the section 3.5, the reason for this is that the values of R_1^i and R_2^i are negative.

It has been found that at very low frequency the results for characteristic impedances, obtained here by using the total power and strip currents, are the same as those obtained by using the strip currents and voltages on two strips. These voltages are determined by integrating the electric field from the strips to the IDG conducting surfaces.

It has been also found from numerical results that R_1^i is always negative and it absolute value increases as ε_{r1} increases. In addition R_2^i is negative for small value of ε_{r1}, but positive for large value of ε_{r1} and $1/R_2^i$ increases as ε_{r1} increases. As a result, for higher values of ε_{r1}, R_1^i is negative and R_2^i is positive, and thus, the values of Z_{21} and Z_{12} become positive. This can be observed from Figure 3.6 and 3.7 which show frequency dependence of strip current ratios and characteristic impedances of two fundamental modes for $\varepsilon_{r1} = 4.7$, respectively.

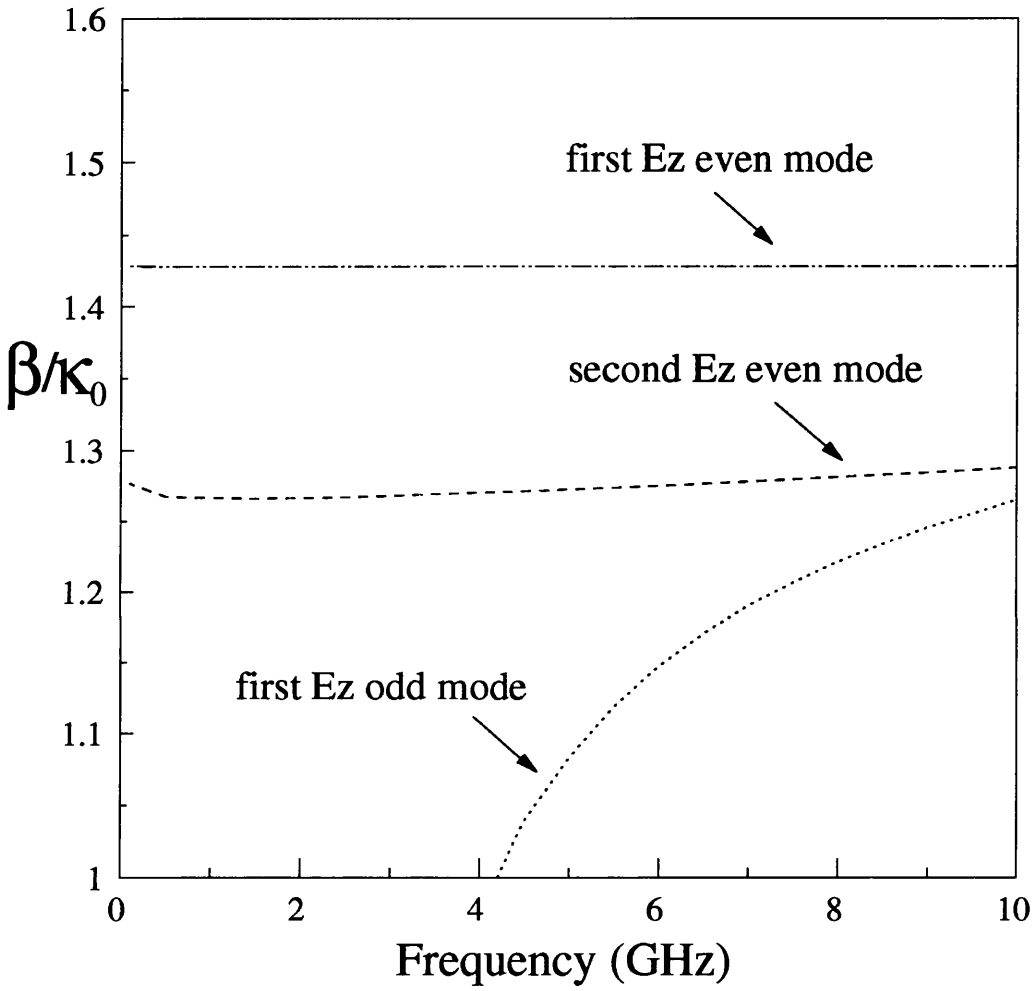

Figure 3.3: Dispersion characteristics of the first few even and odd modes (a =1.016e–2 m, h_1 =2.54e–3 m, h_2 =1.27e–2 m, $\varepsilon_{r1} = \varepsilon_{r2} = 2.04$, w_1 =7.0e–3 m and w_2 =5.0e–3 m)

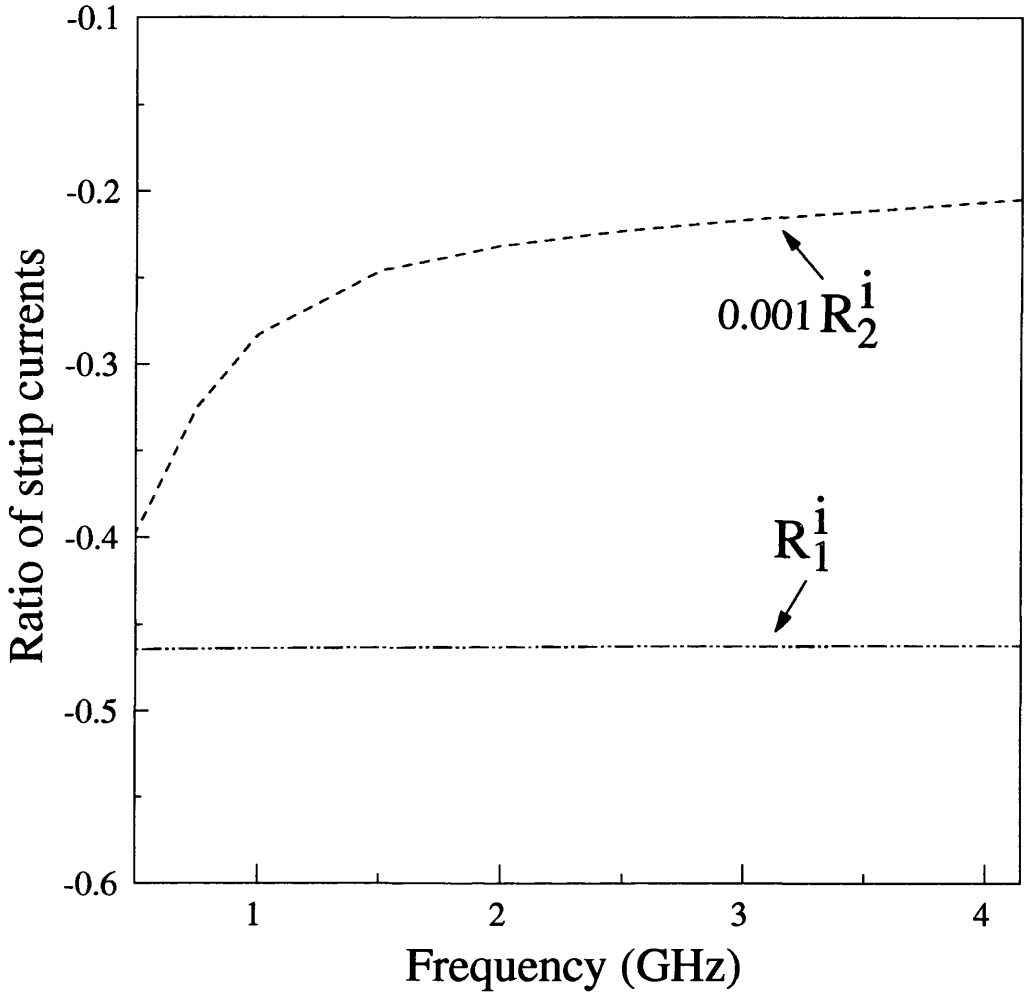

Figure 3.4: Frequency dispersion of strip current ratios of two fundamental modes for $\varepsilon_{r1} = 2.04$ (a =1.016e–2 m, h_1 =2.54e–3 m, h_2 =1.27e–2 m, $\varepsilon_{r2} = 2.04$, w_1 =7.0e–3 m and w_2 =5.0e–3 m)

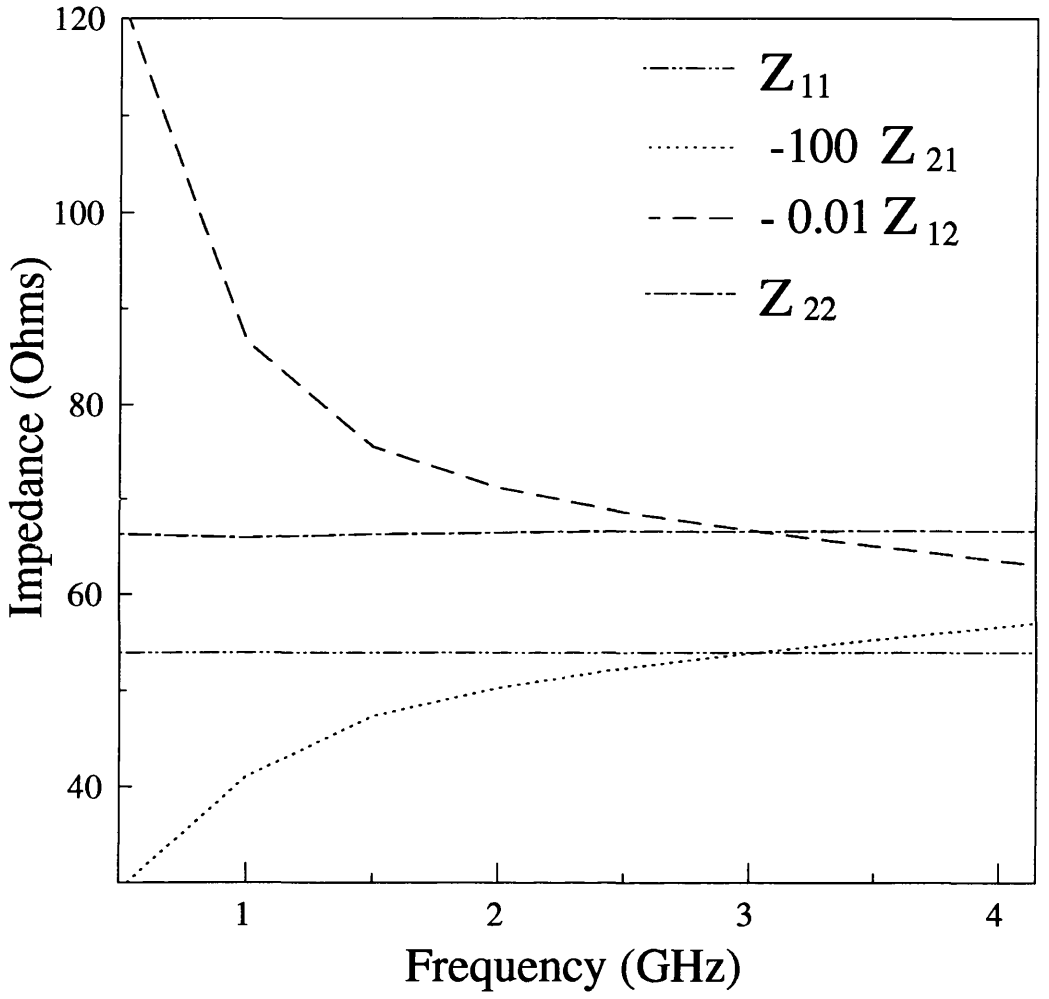

Figure 3.5: Frequency dispersion of characteristic impedances of two fundamental modes for $\varepsilon_{r1} = 2.04$ (a =1.016e–2 m, h_1 =2.54e–3 m, h_2 =1.27e–2 m, $\varepsilon_{r2} = 2.04$, w_1 =7.0e–3 m and w_2 =5.0e–3 m)

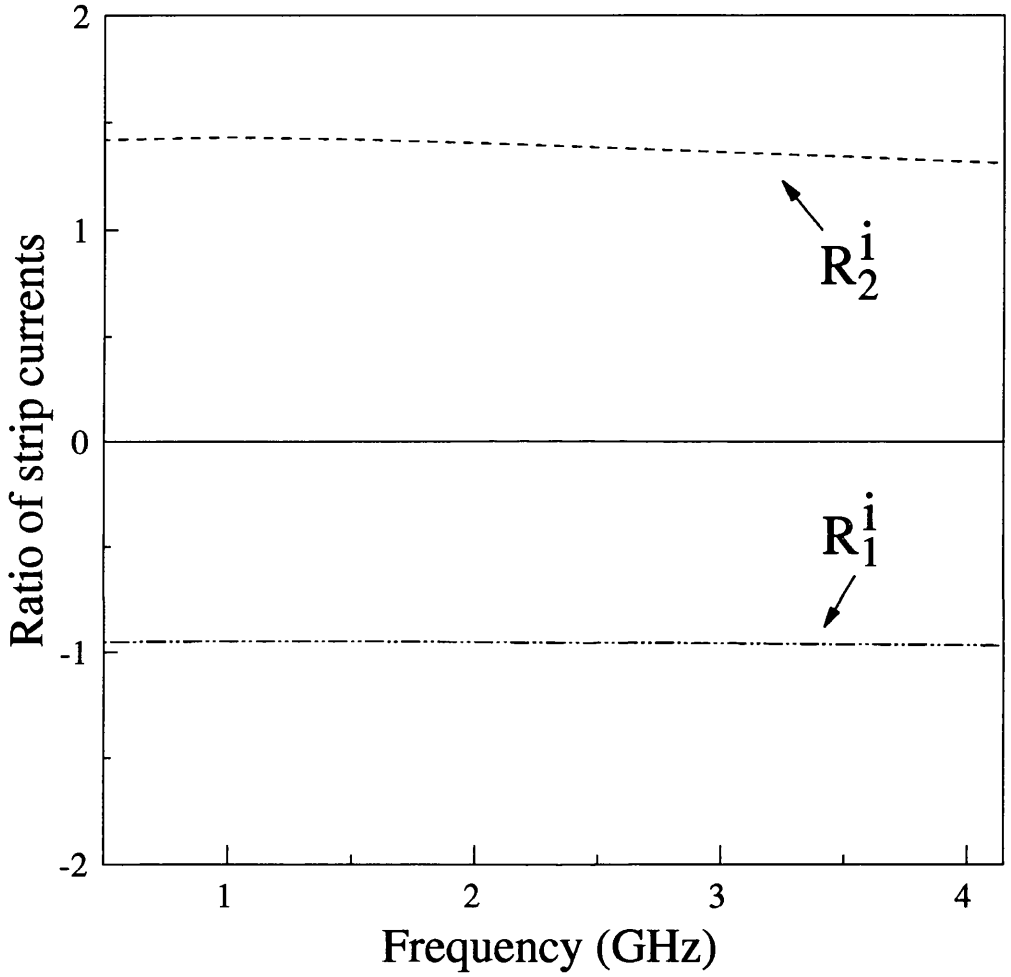

Figure 3.6: Frequency dispersion of strip current ratios of two fundamental modes for $\varepsilon_{r1} = 4.7$ (a =1.016e–2 m, h_1 =2.54e–3 m, h_2 =1.27e–2 m, $\varepsilon_{r2} = 2.04$, w_1 =7.0e–3 m and w_2 =5.0e–3 m)

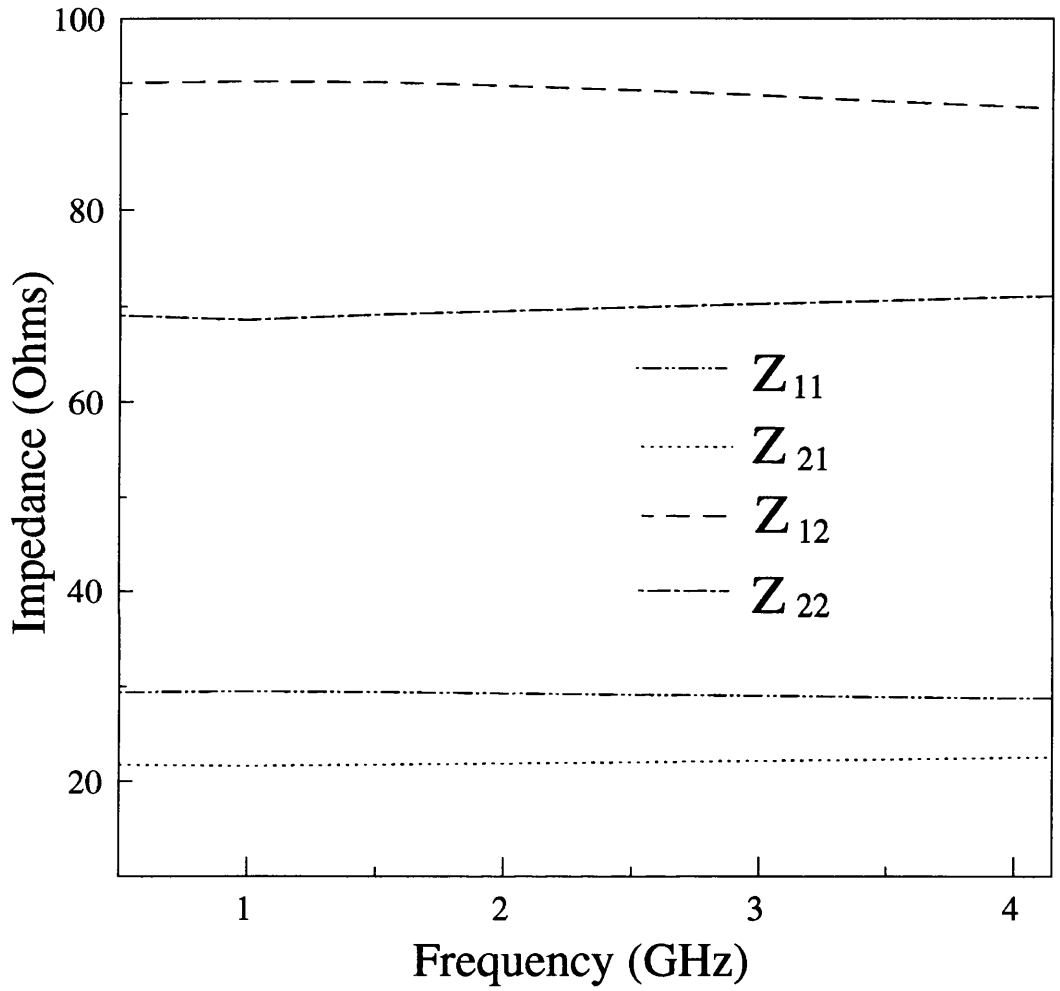

Figure 3.7: Frequency dispersion of characteristic impedances of two fundamental modes for $\varepsilon_{r1} = 4.7$ (a =1.016e–2 m, h_1 =2.54e–3 m, h_2 =1.27e–2 m, $\varepsilon_{r2} = 2.04$, w_1 =7.0e–3 m and w_2 =5.0e–3 m)

3.7.2 Effects of Structural Parameters on S Parameters

The S-parameters S_{11}, S_{21}, S_{31} and S_{41} are shown in Figure 3.8 as a function of frequency. Clearly port 4 is the isolated port, and the reflection coefficient S_{11} is small. As is expected, the coupler is a backward coupler, with coupling to port 3. It is also observed that the maximum coupling (S_{31}) from port 1 to port 3 is obtained when $(\beta_1 + \beta_2)l = \pi$, at 2 GHz in this example.

Figure 3.9 shows the S-parameters as a function of the width of the upper strip. It can be observed that S_{41} is most greatly affected by the change of w_1. There also exists a minimum value of S_{41} (maximum isolation) at a certain value of w_1.

Figure 3.10 presents S-parameters as a function of the width of the lower strip. As w_2 increases, S_{21} and S_{31} change very little, but S_{11} and S_{41} change rapidly. There is an optimum value for minimum reflection coefficient, but there is also a different optimum value of w_2 for maximum isolation.

Figure 3.11 shows the S-parameters as a function of the thickness of the upper substrate. It can be found that coupling S_{31} increases as h_1 decreases and S_{41} is always smaller than S_{31}.

Hence, the change of h_1 enables both tight and loose coupling values to be achieved. With the appropriate choices of values of w_1 and w_2 minimum reflection coefficient and maximum isolation can be obtained. Therefore, the broadside coupled strip IDG structure can realize both high and low coupling value directional couplers with good input match and high directivity.

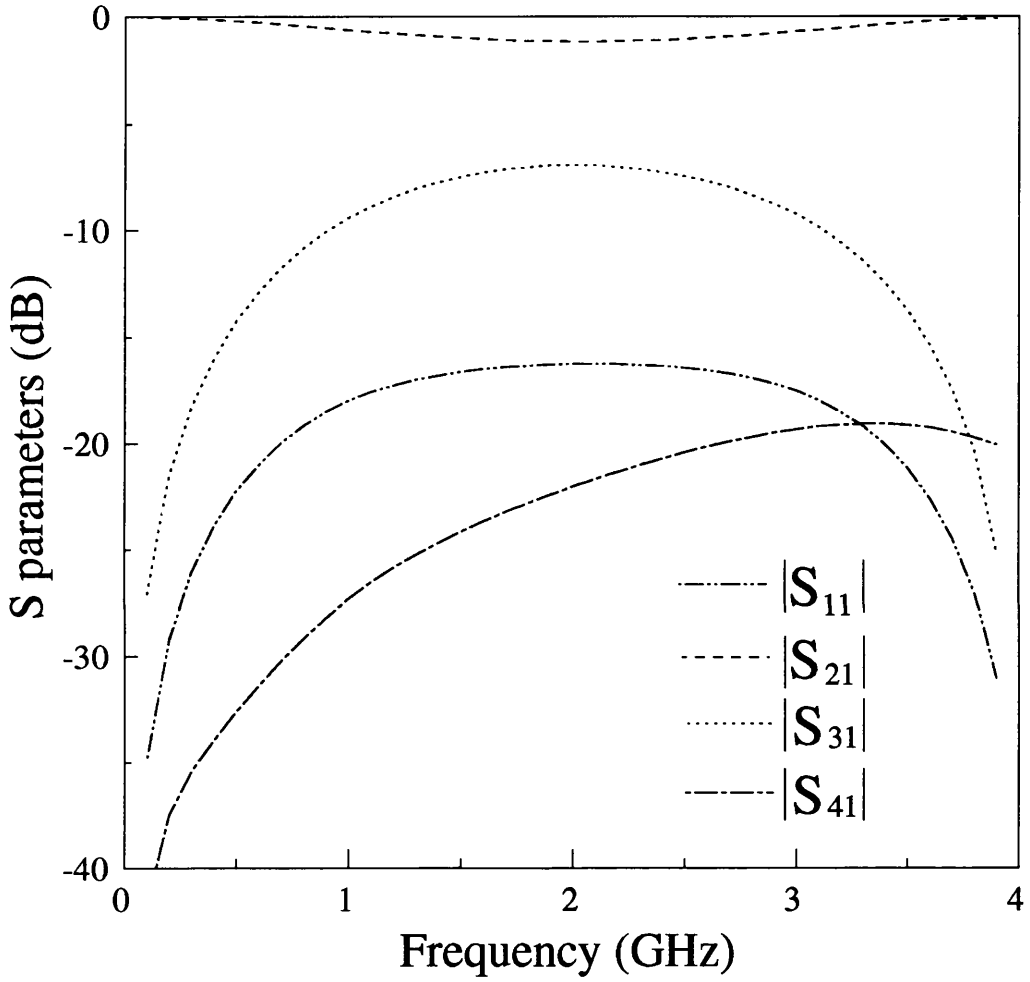

Figure 3.8: S parameters as a function of frequency (a =1.016e–2 m, h_1 =2.54e–3 m, h_2 =1.27e–2 m, $\varepsilon_{r1} = \varepsilon_{r2} = 2.04$, w_1 =7.0e–3 m, w_2 =5.0e–3 m, $Z_0 = 50\ \Omega$ and L =2.784e–2 m)

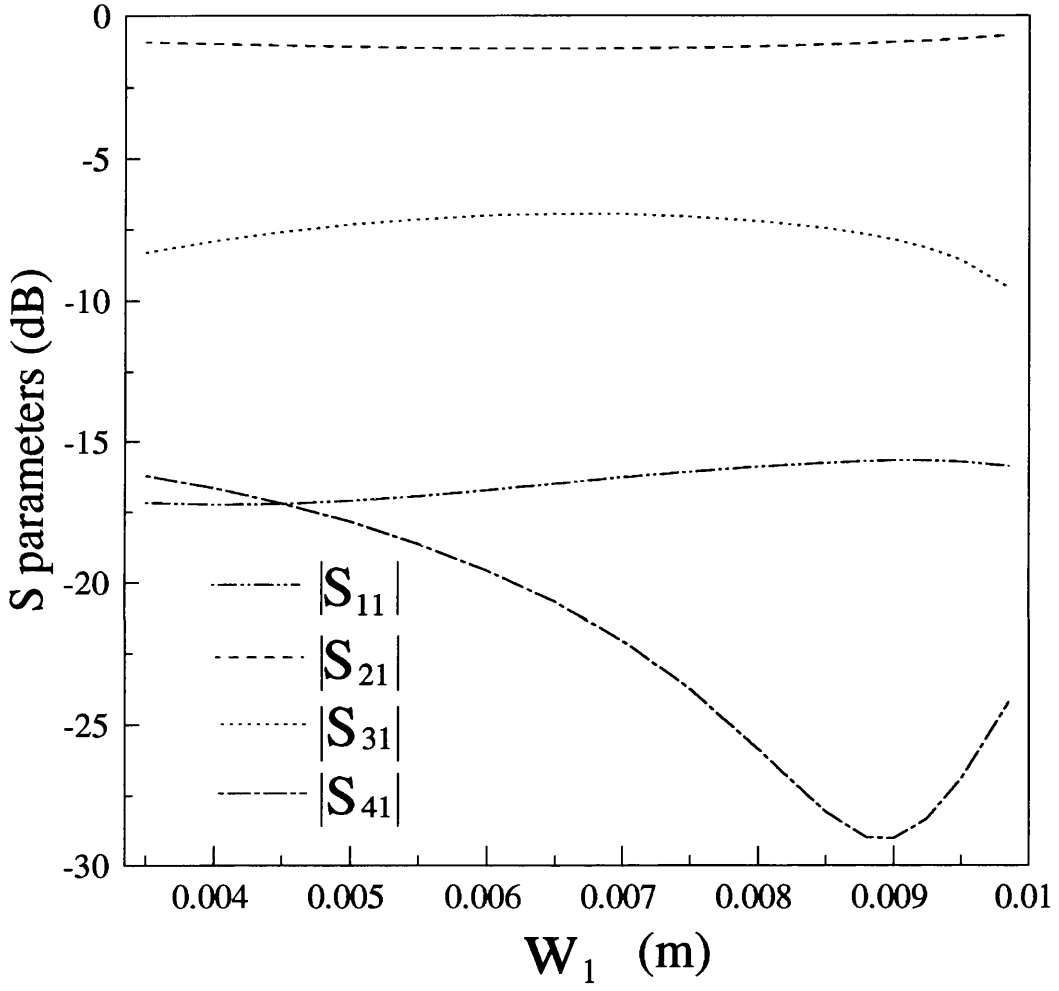

Figure 3.9: S parameters as a function of w_1 (a =1.016e–2 m, h_1 =2.54e–3 m, h_2 =1.27e–2 m, $\varepsilon_{r1} = \varepsilon_{r2} = 2.04$, w_2 =5.0e–3 m, f =2 GHz, $Z_0 = 50\ \Omega$ and $L = \pi/(\beta_1 + \beta_2)$)

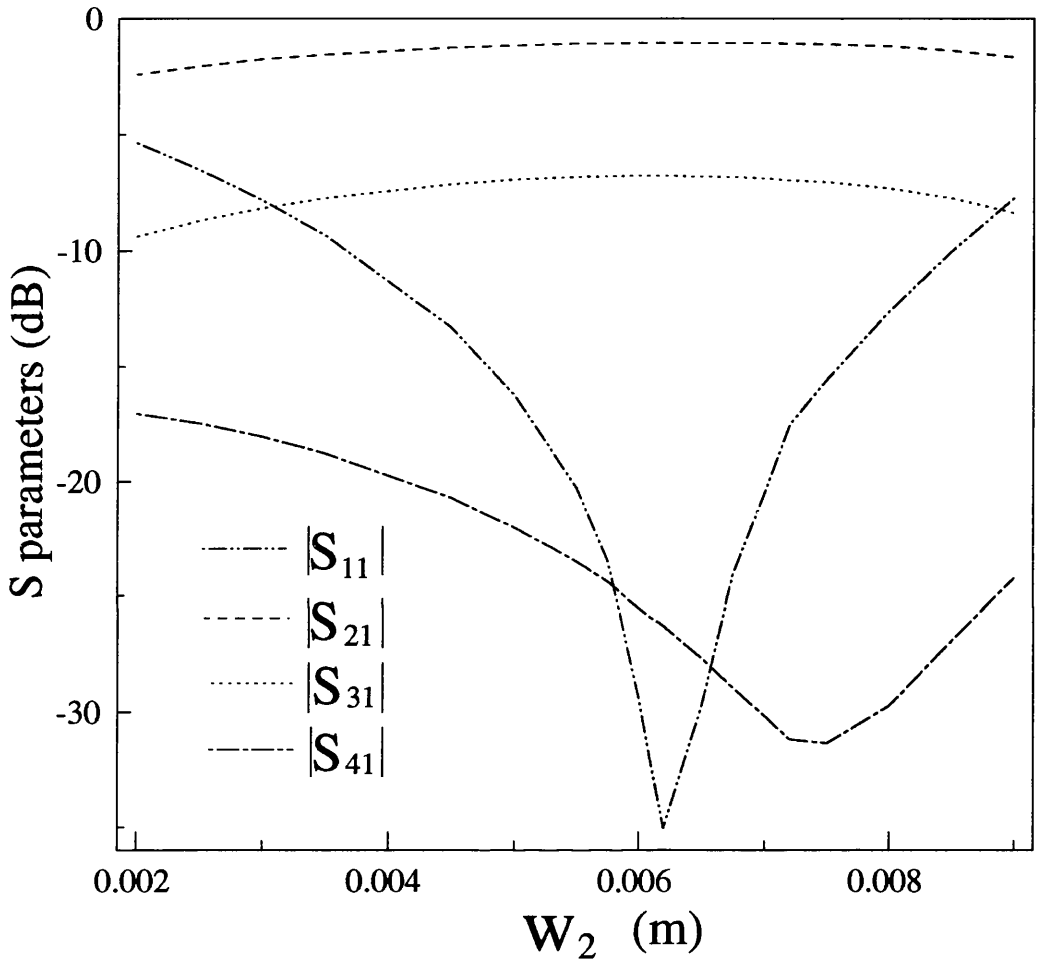

Figure 3.10: S parameters as a function of w_2 (a =1.016e–2 m, h_1 =2.54e–3 m, h_2 =1.27e–2 m, $\varepsilon_{r1} = \varepsilon_{r2} = 2.04$, w_1 =7.0e–3 m, f =2 GHz, $Z_0 = 50\ \Omega$ and $L = \pi/(\beta_1 + \beta_2)$)

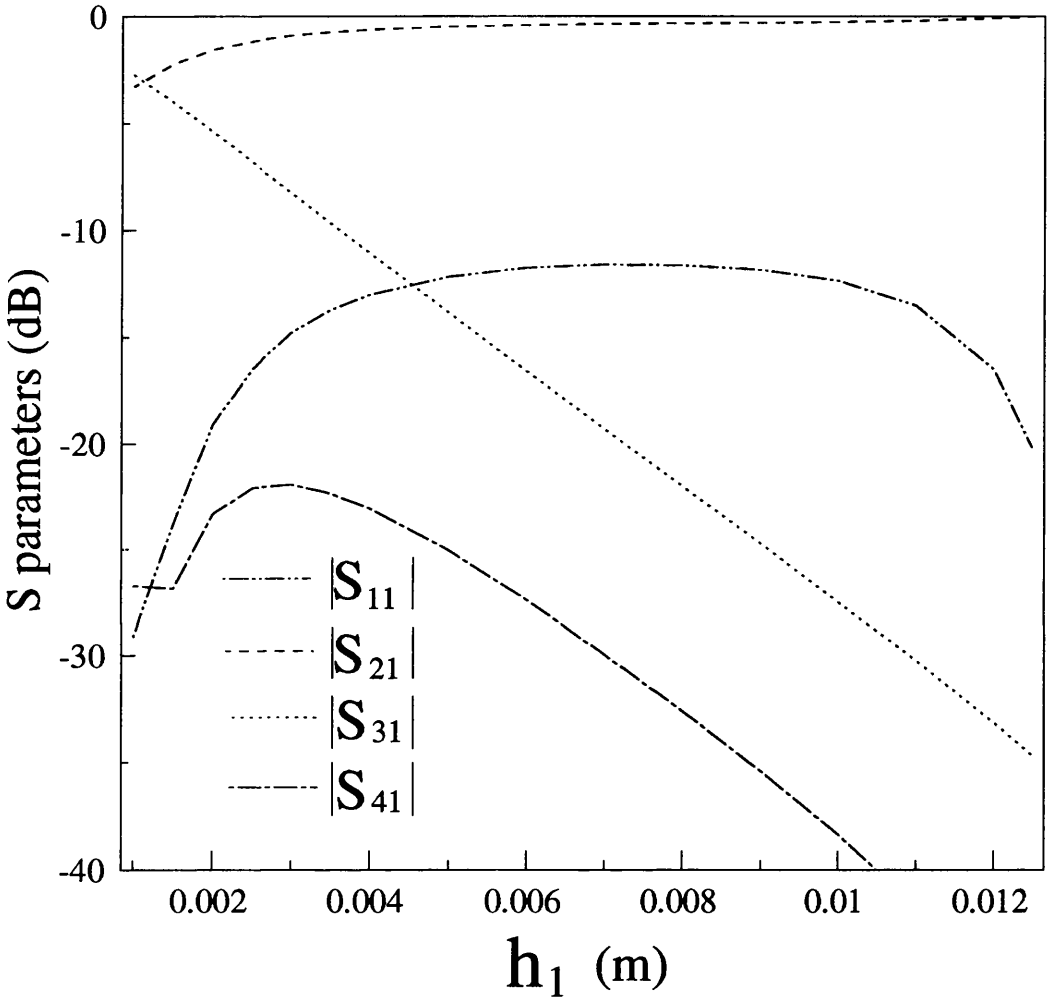

Figure 3.11: S parameters as a function of h_1 (a =1.016e–2 m, h =1.524e–2 m, $\varepsilon_{r1} = \varepsilon_{r2} = 2.04$, w_1 =7.e–3 m, w_2 =5.0e–3 m, f =2 GHz, $Z_0 = 50\ \Omega$ and $L = \pi/(\beta_1 + \beta_2)$)

3.7.3 Procedure for the Design of Couplers

To successfully design the directional couplers using the broadside coupled strip IDG, the following procedure is followed:

Firstly, the IDG structural dimensions and material parameters, that is, a, h, ε_{r1} and ε_{r2}, are determined from the available IDG structures and dielectric materials.

Secondly, numerical results for S parameters as function of h_1 for certain values of w_1 and w_2 are obtained based on the method presented in the above sections and h_1 is chosen to be such value that the specified value of the coupling is achieved.

Thirdly, w_1 and w_2 are optimized so that both S_{11} and S_{41} have very low values.

Fourthly, the value of h_1 in the second step is slightly adjusted so that the coupling for the optimum values of w_1 and w_2 is the specified one.

Finally, the length of the coupler is determined by using the following expression $L = \pi/(\beta_1 + \beta_2)$ at the centre frequency.

Following the above steps, the -3 dB and -16 dB directional couplers have been designed. Figures 3.12 and 3.13 show the magnitude of the S parameters for both couplers near the centre frequency of 2 GHz, respectively. It is seen from these two figures that both couplers have very low reflection coefficient and very little output at the isolated port. It is also found that both couplers have a about 90^0 phase relationship between two output ports. In these couplers, the coupling occurs in the backward direction.

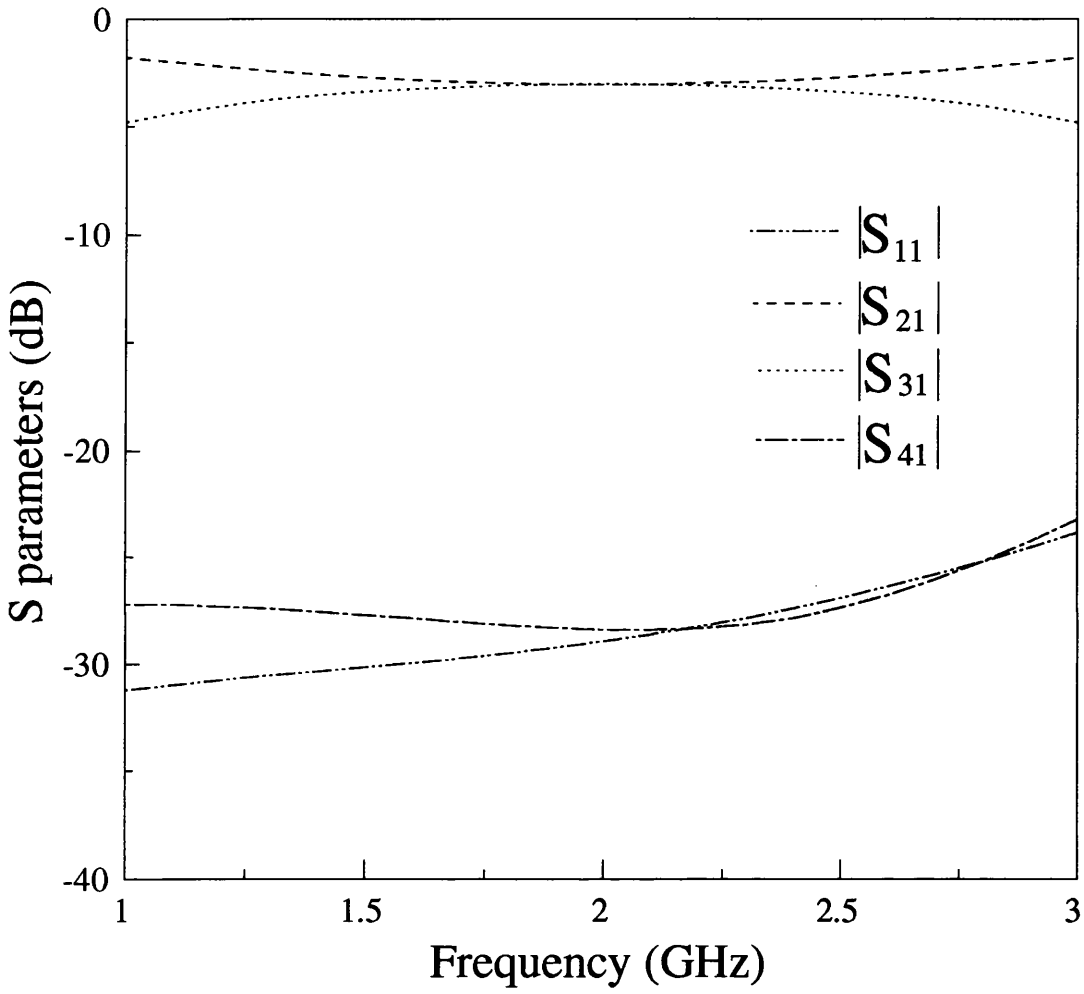

Figure 3.12: S parameters near the frequency of 2 GHz for the -3 dB coupler (a =1.016e–2 m, h_1 =1.1e–3 m, h_2 =1.414e–2 m, $\varepsilon_{r1} = \varepsilon_{r2} = 2.04$, w_1 =7.0e–3 m, w_2 =5.0e–3 m, $Z_0 = 50\ \Omega$ and L =2.784e–2 m)

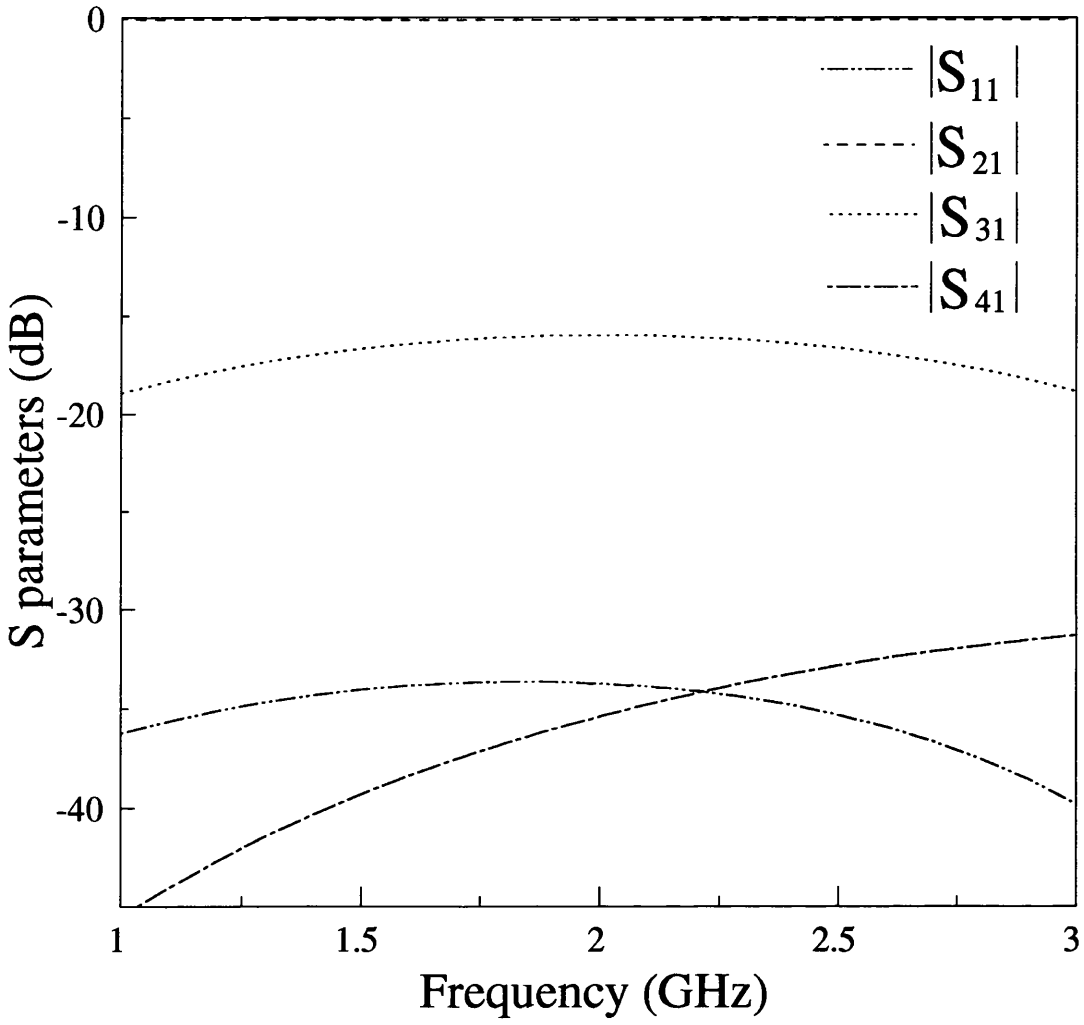

Figure 3.13: S parameters near the frequency of 2 GHz for the -16 dB coupler (a =1.016e–2 m, h_1 =5.78e–3 m, h_2 =9.46e–3 m, $\varepsilon_{r1} = \varepsilon_{r2} = 2.04$, w_1 =7.7e–3 m, w_2 =7.0e–3 m, $Z_0 = 50\ \Omega$ and L =2.781e–2 m)

3.8 Experimental Verification

3.8.1 Propagation Constants

In order to assess the accuracy of the analysis presented in the previous sections, measured results have been obtained for comparison with computed results. Propagation constants were measured using the resonant section method which has been described in chapter 2. This method has been shown to be capable of measuring the propagation constants of the E_z even and odd modes independently by changing the orientation of the magnetic probes. These probes are inserted at the line centre over the upper surface, through short circuit plates at both ends of the IDG section.

Comparison between measured and computed results for the propagation constants is shown in Figure 3.14. The agreement between experiment and theory for the second E_z even mode and the first E_z odd mode is good - within 1%. No comparison for the first E_z even mode is presented as the positioning of the magnetic probes over the structure produces little excitation of this mode. The fields of the first E_z mode of this structure is concentrated in the region between the two strips.

Comparison of the present results with calculated and measured results available in [14] is shown in Figure 3.15 for the propagation constants of the first and second E_z even modes. Clearly the agreement between these data for two fundamental modes is good.

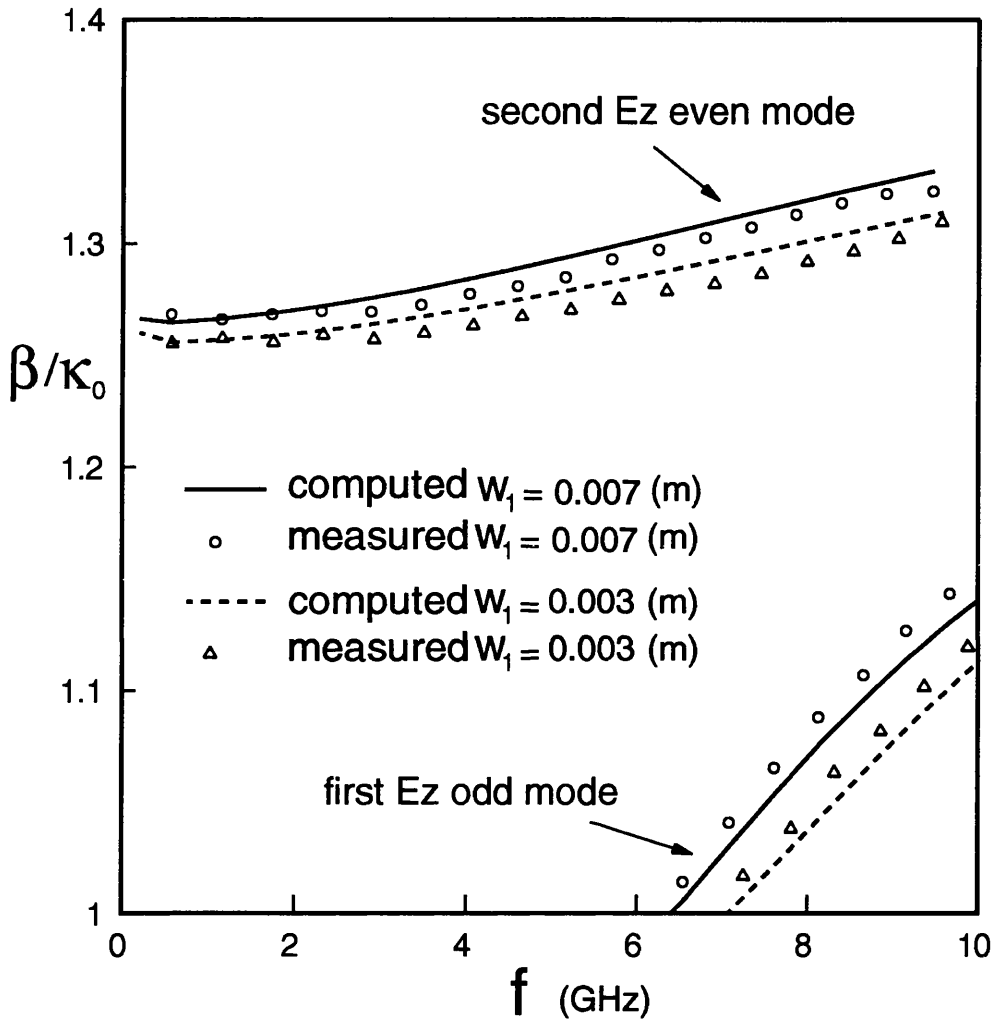

Figure 3.14: Comparison of computed and measured propagation constants for the second E_z even mode and first E_z odd mode (a =2.286e–2 m, h_1 =2.16e–3 m, h_2 =8.0–3 m, $\varepsilon_{r1} = \varepsilon_{r2} = 2.04$ and $w_2 = w_1$)

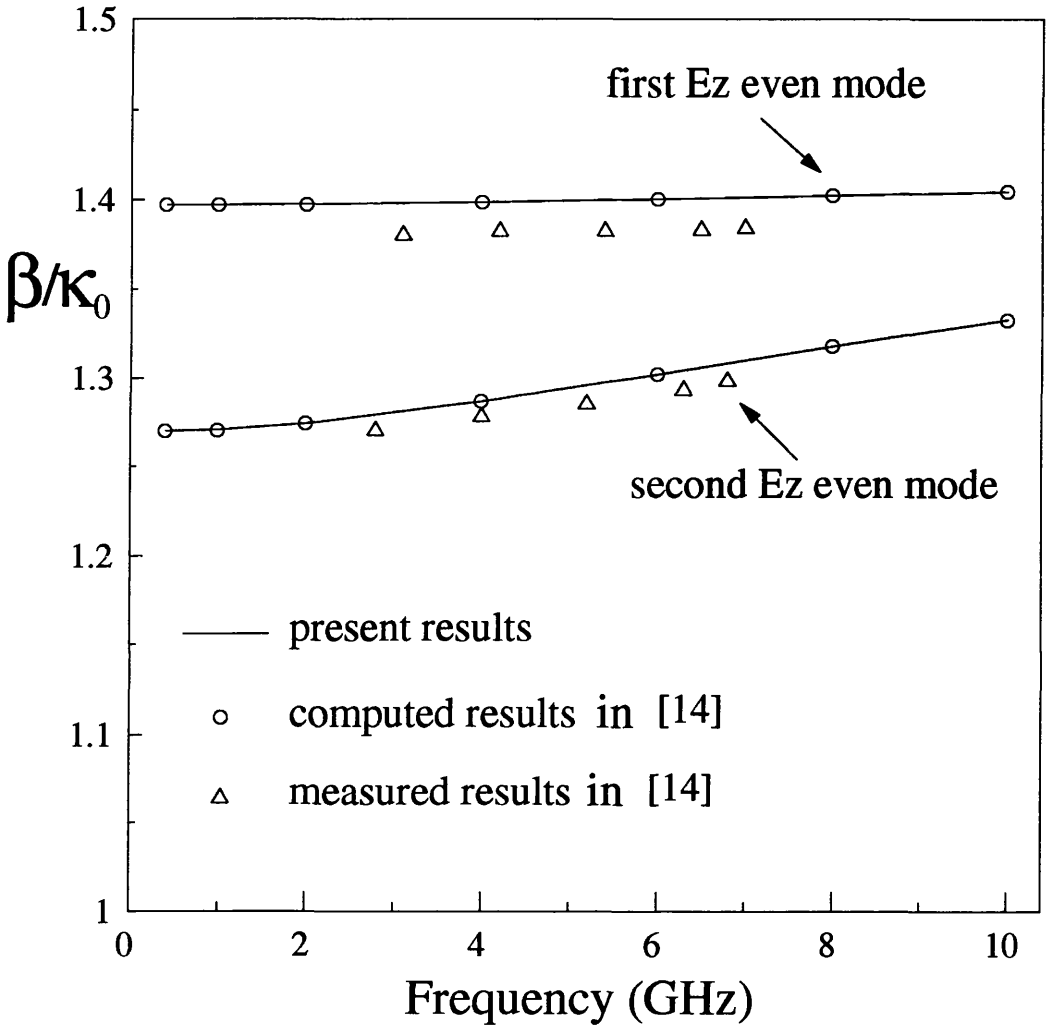

Figure 3.15: Comparison of present computed propagation constants with computed and measured data obtained by Izzat in [14] for two fundamental modes (a =2.286e–2 m, h_1 =2.16e–3 m, h_2 =8.0e–3 m, $\varepsilon_{r1} = \varepsilon_{r2} = 2.04$, w_1 =5.0e–3 m and w_2 =1.0e–2 m)

3.8.2 *S* Parameters

To demonstrate the experimental feasibility of a directional coupler using the broadside coupled strip IDG and to assess the accuracy of the predicted S parameters, the configuration, whose top and end views are shown in Figure 3.16 and 3.17, was used, and S parameters were measured. In experiment, 4 50–ohm microwave coaxial cables were used to individualize input and output ports of the coupler. The transitions between the coaxial cables and a section of broadside coupled strip IDG were fabricated as follows. Firstly two conducting plates with two holes were placed at both ends of the IDG section which was filled with two layers of dielectric (PTFE). Then four coaxial cables were inserted into these holes, the outer conductors of which contacted the surfaces of the holes. Finally inner conductors were extended beyond the conducting planes and soldered to the conducting strips in the IDG section. It should be pointed out that the use of two conducting planes is of importance in order to fix the coaxial cables firmly and to realize the potential equalization for the IDG ground plane and outer conductors of cables. The spacing between the coupled strips was quite small in some cases, and so the excitation points needed to be offset from the centre of the groove, as shown in Figure 3.16 and 3.17. To minimise discontinuity series inductance at the excitation points, short tapered ends of the conducting strips were used.

S parameters of the IDG coupler with above–mentioned transitions to the coaxial cables were measured using an HP8510B Network Analyzer. The Analyser was calibrated on $3.5mm$ coaxial cable ports, and connected to the coupler ports i and j. The remaining coupler ports were terminated by coaxial matched loads. The input reflection and forward transmission coefficients for this arrangement can be measured, and as a result, measured S parameters S_{ii}, S_{jj}, S_{ij} and S_{ji} of

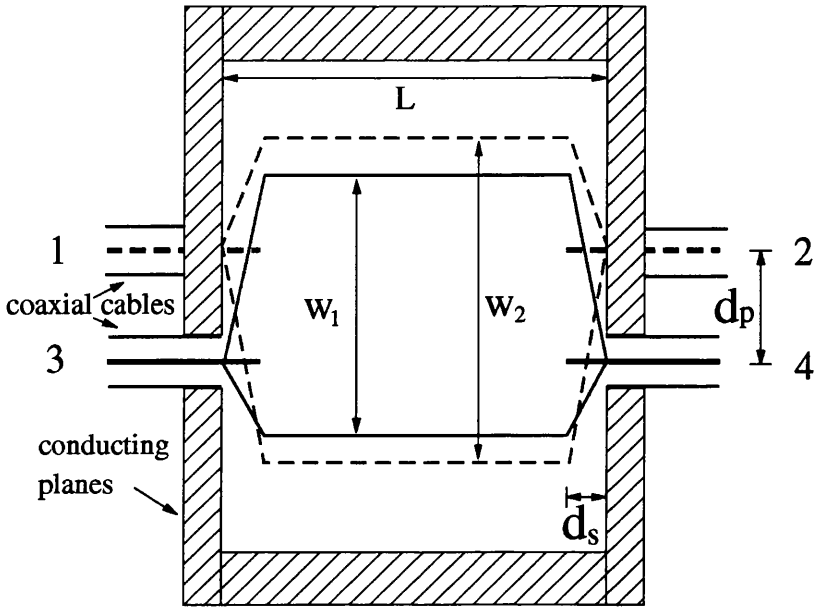

Figure 3.16: Top view of the experimental structure for measurements of S–parameters

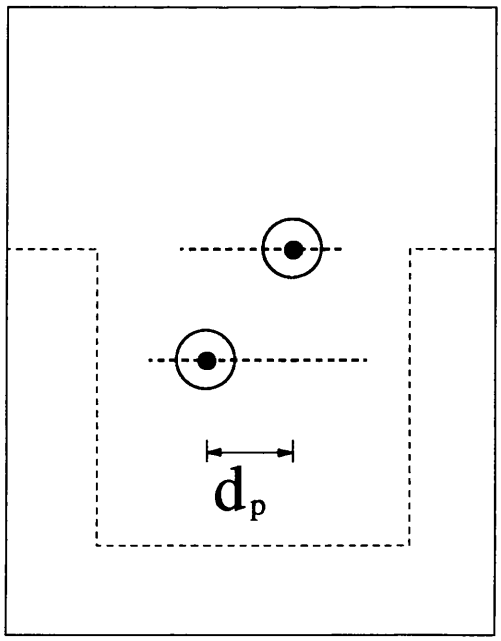

Figure 3.17: End view of the experimental structure for measurements of S–parameters

the coupler are obtained.

Two experimental samples are used, showing the possibility of adjustable strong and weak coupling of the IDG coupler. For Sample 1 with about - 3 dB coupling, h_1 =2.16 mm, h_2 =8.0 mm, and $w_1 = w_2$ =10.0 mm are chosen. For Sample 2 with about - 15 dB coupling, h_1 =8.0 mm, h_2 =2.16 mm, and $w_1 = w_2$ =7.0 mm are chosen. Other structural and material parameters are the same and will be given in the following figures.

Due to the symmetry of the structure there are only six independent S-parameters: S_{11}, S_{21}, S_{31}, S_{41}, S_{33} and S_{43}. The relations $S_{22} = S_{11}$, $S_{32} = S_{41}$, $S_{42} = S_{31}$ and $S_{44} = S_{33}$ have been verified by computed and measured results. Therefore, computed and measured results for only these six S parameters are compared in the following figures.

Figures 3.18 and 3.19 show the comparison of the computed and measured S parameters for Sample 1. It is clearly seen that there is an excellent agreement between theory and experiment for the coupling S_{31}. There is little difference between the computed and measured S_{21} and S_{43}. There is also reasonable agreement between theory and experiment for the reflection coefficients S_{11} and S_{33} and isolation S_{41}. In fact the computed and measured curves for S_{11}, S_{33} and S_{41} reach peaks at almost the same values of frequency and differences at most of these peaks are less than 2 dB. These small discrepancies arise as the discontinuities between the IDG section and cables are not taken into account in the theoretical model. There may also be a small air gap between two layers of dielectric in the practical structure, and there is a tolerance of 1%–2% in the permittivity of dielectric.

Figures 3.20 and 3.21 show the comparison of the computed and measured S parameters for Sample 2. Again good agreement between theory and experiment is obtained for all the S parameters. It is noted that reflection coefficients from port 1 and port 3, S_{11} and S_{33}, are very different. This implies that there are different optimum values of strip widths for the lowest reflection coefficients from port 1 and port 3, respectively.

The computed and measured results for the coupling and isolation are presented for frequencies up to 4 GHz in Figures 3.22 and 3.23. It is found that the maximum coupling for both samples occurs at frequencies where $(\beta_1 + \beta_2)L = \pi, 3.2\pi, 5.4\pi, 7.6\pi, \ldots$ and in general decreases slightly at higher value. The curves for S_{41} also reach peaks at different values of frequency. However with increasing frequency peak value for S_{41} increases very quickly and consequently the isolation becomes much worse. Therefore, it is demonstrated theoretically and experimentally that for the high directivity coupler, the length of the IDG section should be chosen to be $\pi/(\beta_1 + \beta_2)$ at the centre frequency.

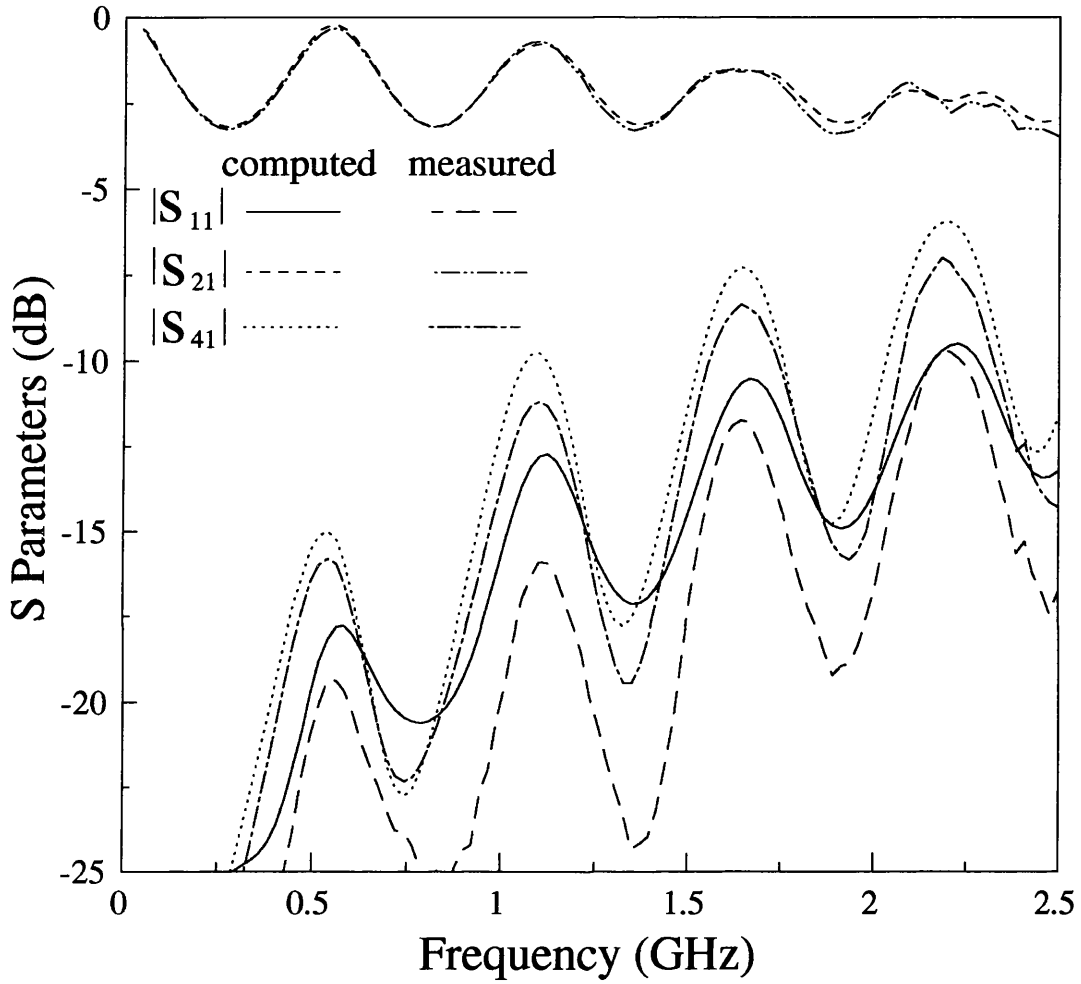

Figure 3.18: Comparison of computed and measured S–parameters S_{11}, S_{21} and S_{41} of Sample 1 ($\varepsilon_{r1} = 2.04$, $\varepsilon_{r2} = 2.04$, a =2.286e–2 m, h_1 =2.16e–3 m, h_2 =8.0–3 m, $w_1 = w_2$ =1.0e–2 m and L =2.032e–1 m)

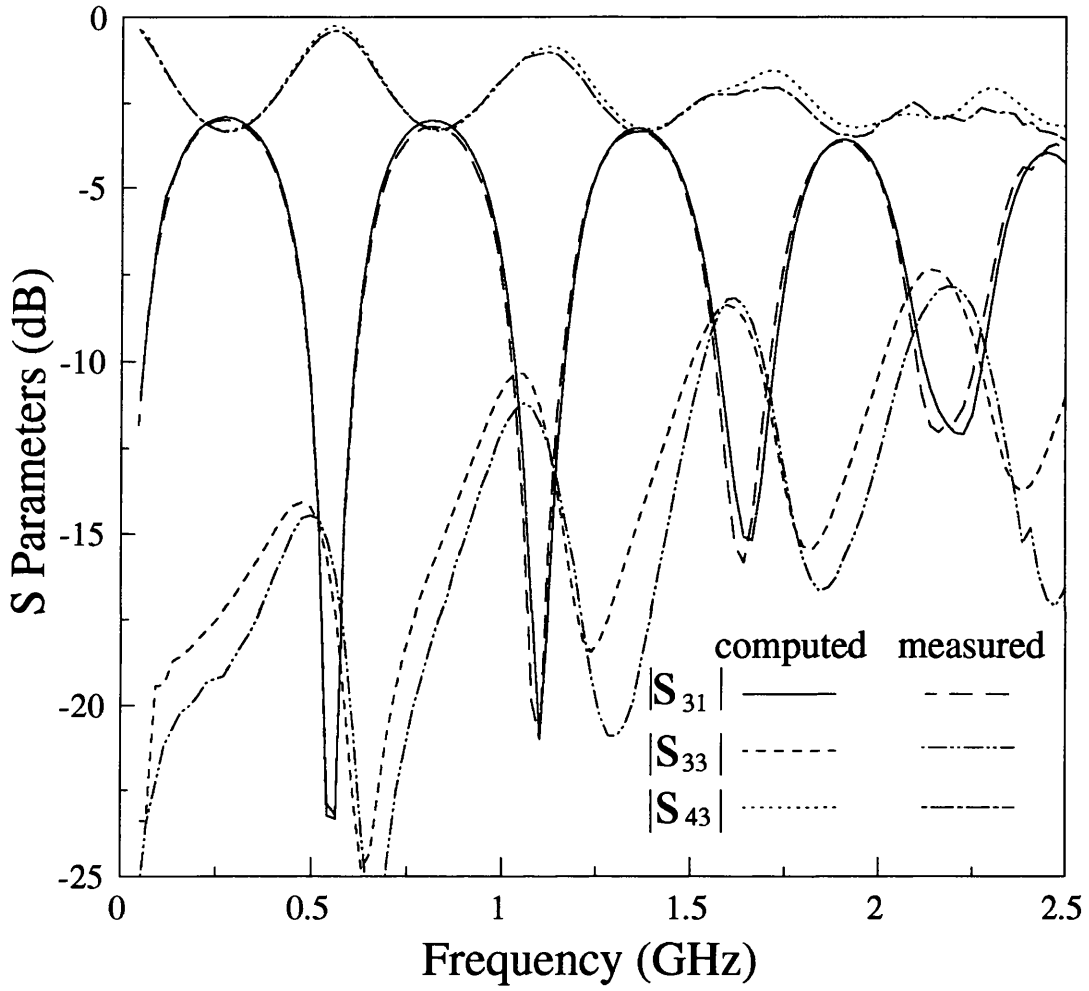

Figure 3.19: Comparison of computed and measured S–parameters S_{31}, S_{33} and S_{43} of Sample 1 ($\varepsilon_{r1} = 2.04$, $\varepsilon_{r2} = 2.04$, a =2.286e–2 m, h_1 =2.16e–3 m, h_2 =8.0–3 m, $w_1 = w_2$ =1.0e–2 m and L =2.032e–1 m)

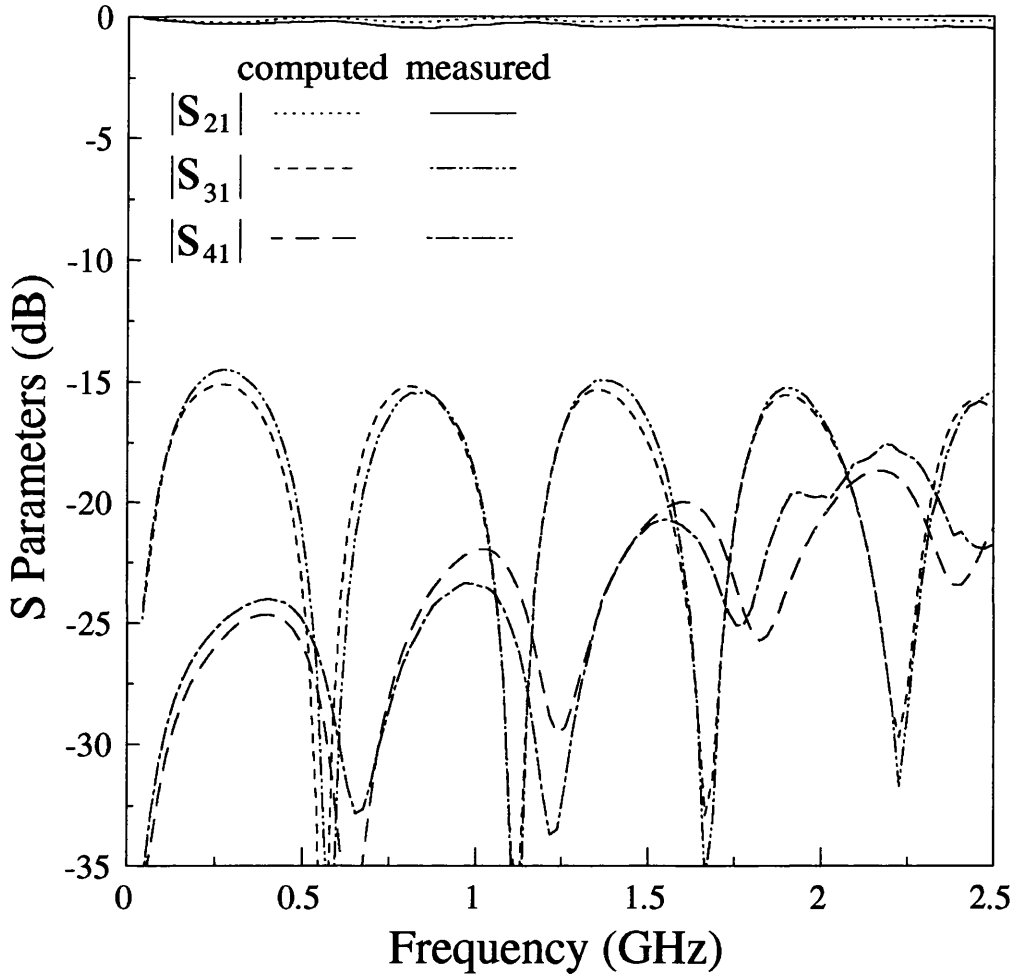

Figure 3.20: Comparison of computed and measured S–parameters S_{21}, S_{31} and S_{41} of Sample 2 ($\varepsilon_{r1} = 2.04$, $\varepsilon_{r2} = 2.04$, a =2.286e–2 m, h_1 =8.0e–3 m, h_2 =2.16–3 m, $w_1 = w_2$ =7.0e–3 m and L =2.032e–1 m)

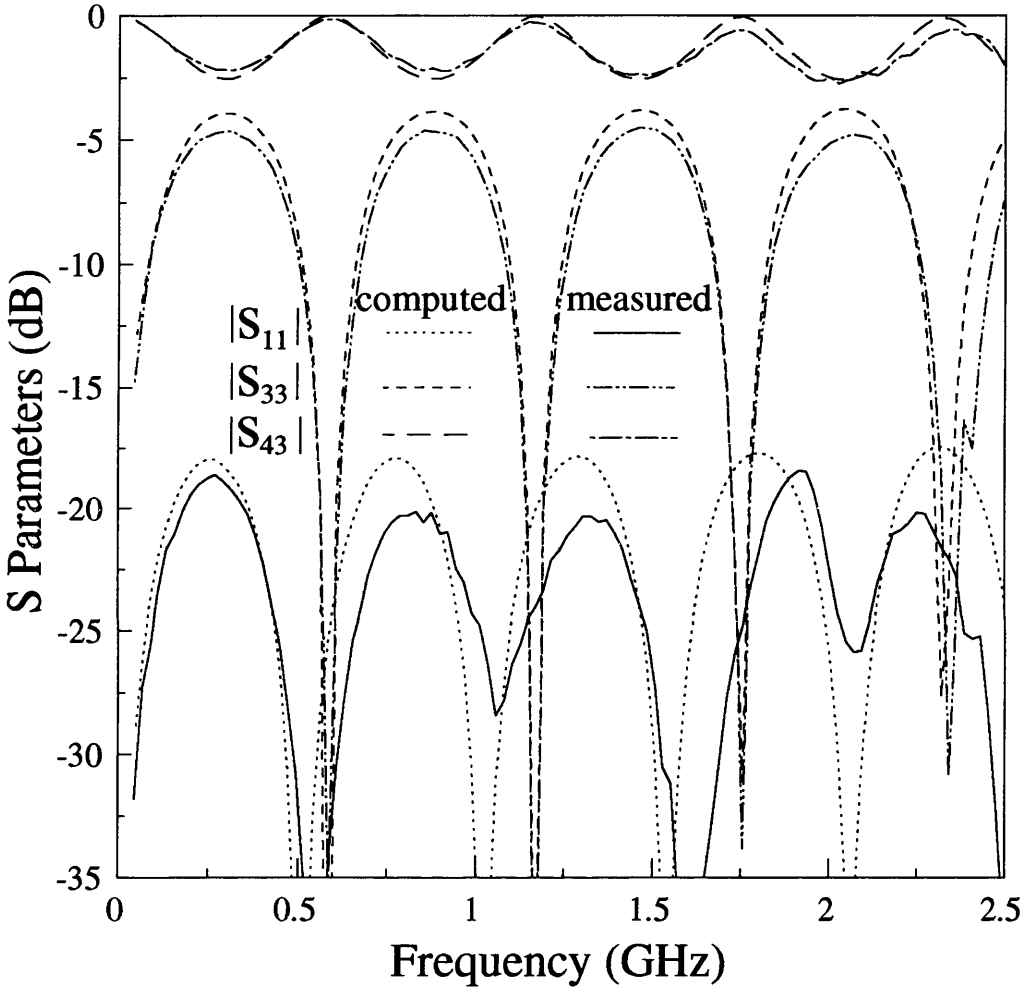

Figure 3.21: Comparison of computed and measured S–parameters S_{11}, S_{33} and S_{43} of Sample 2 ($\varepsilon_{r1} = 2.04$, $\varepsilon_{r2} = 2.04$, a =2.286e–2 m, h_1 =8.0e–3 m, h_2 =2.16–3 m, $w_1 = w_2$ =7.0e–3 m and L =2.032e–1 m)

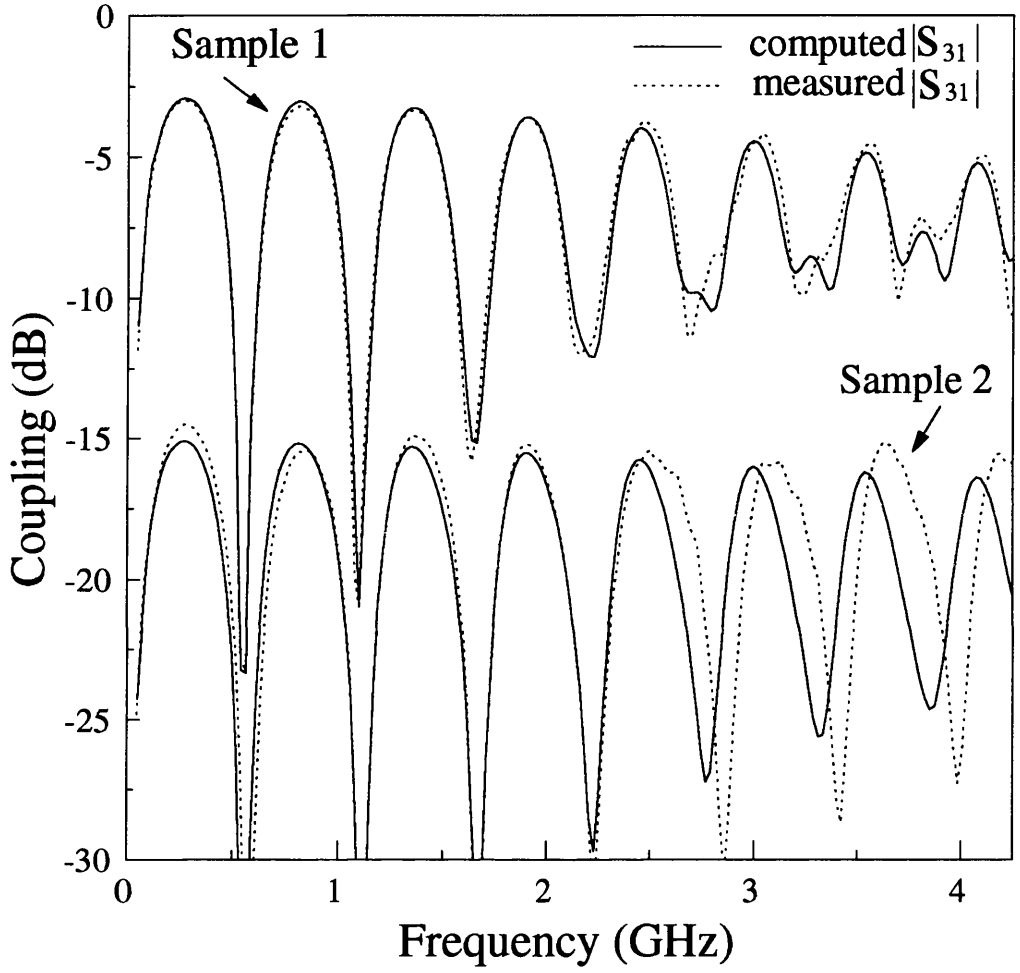

Figure 3.22: Comparison of computed and measured coupling S_{31} of Sample 1 and Sample 2 ($\varepsilon_{r1} = 2.04$, $\varepsilon_{r2} = 2.04$, a =2.286e–2 m, L =2.032e–1 m; Sample 1: h_1 =2.16e–3 m, h_2 =8.0–3 m and $w_1 = w_2$ =1.0e–2 m; Sample 2: h_1 =8.0e–3 m, h_2 =2.16–3 m and $w_1 = w_2$ =7.0e–3 m)

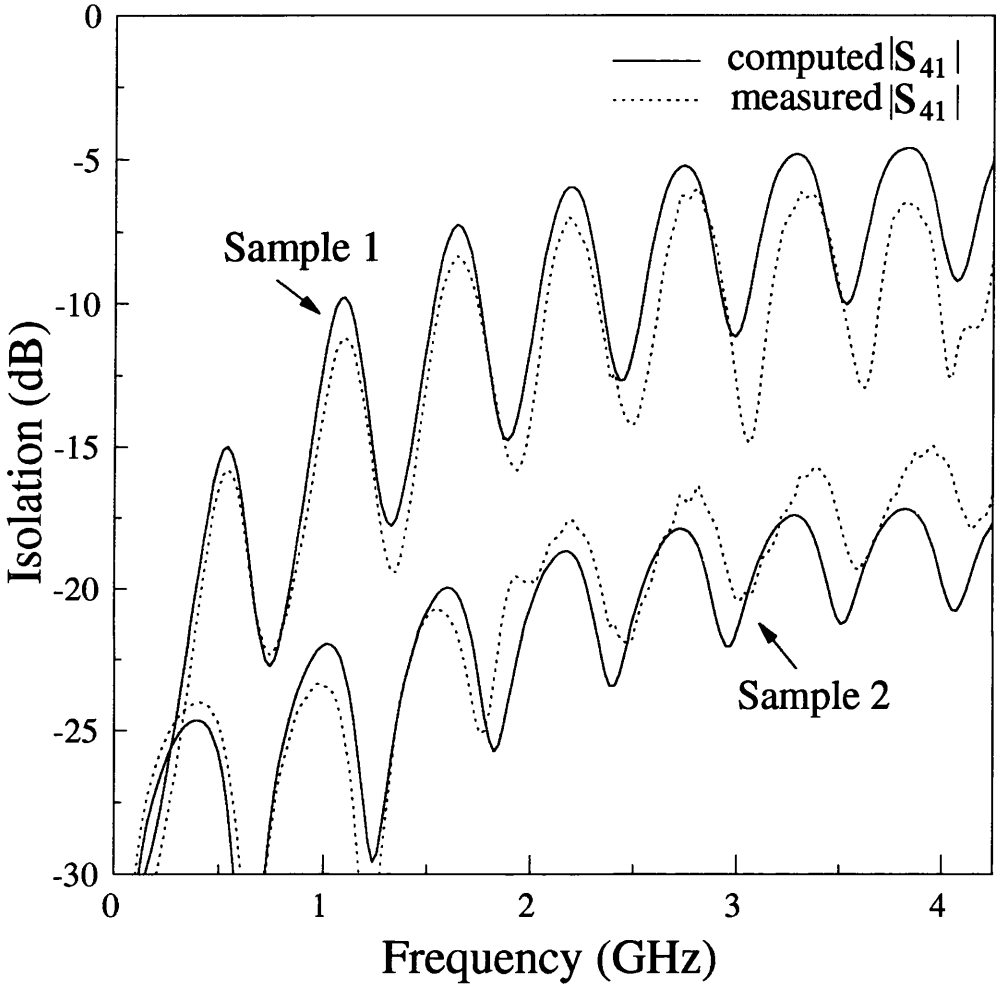

Figure 3.23: Comparison of computed and measured isolation S_{41} of Sample 1 and Sample 2 ($\varepsilon_{r1} = 2.04$, $\varepsilon_{r2} = 2.04$, a =2.286e–2 m, L =2.032e–1 m; Sample 1: h_1 =2.16e–3 m, h_2 =8.0–3 m and $w_1 = w_2$ =1.0e–2 m; Sample 2: h_1 =8.0e–3 m, h_2 =2.16–3 m and $w_1 = w_2$ =7.0e–3 m)

3.9 Conclusion

This chapter has presented the analysis of propagation constants and characteristic impedances of broadside coupled strip IDG by means of the extended spectral domain approach. Numerical results for propagation constants and characteristic impedances have been presented and good agreement between calculated and measured results for propagation constants has been obtained.

The 4–port equivalent circuit has been described, whose parameters such as scattering matrix are derived from propagation characteristics of two fundamental modes.

Numerical results for scattering parameters have been presented for various values of structural parameters. It has been clearly shown that both strong and weak directional couplers can be realized by using a section of this structure with appropriate choices of the distance between the strips and the widths of the strips. A simple procedure for the design of these couplers has been outlined. Based on this procedure, - 3 dB and - 16 dB directional couplers with good input match and high directivity have been designed.

Broadside coupled strip directional couplers have been realized, excited via coaxial cables, for both high and low peak coupling value couplers. Measured S-parameters obtained using a Network Analyzer have been in good agreement with theoretical predictions.

References

[1] R. E. Collin, "Field theory of guided waves", McGraw-Hill Book Company Inc., 1960.

[2] T. Rozzi, A. Morini and G. Gerini, "Analysis and applications of microstrip loaded inset dielectric waveguide", *IEEE Trans. Microwave Theory Tech.*, Vol.MTT-40, pp.272-278, Feb. 1992.

[3] I. S. Gradshteyn and I. M. Ryshik, "Tables of integrals, series and products", Academic Press, 1965.

[4] T. Rozzi, G. Gerini, A. Morini and M. Santis, "Multilayer buried microstrip inset guide", in *Proc. 21th European Microwave Conf.*, Stultgart pp.673-678, 1991

[5] J. R. Brews, "Characteristic impedance of microstrip lines", *IEEE Trans. Microwave Theory Tech.*, Vol.MTT-35, pp.30-33, Jan. 1987.

[6] N. Fache and D. Dezutter, "Circuit parameters for single and coupled microstrip lines by a rigorous full–wave space–domain analysis," *IEEE Trans. Microwave Theory Tech.*, vol.MTT–37, pp.421–425, Feb 1989.

[7] N. Fache and D. Dezutter, "New high–frequency circuit model for coupled lossless and lossy waveguide structures," *IEEE Trans. Microwave Theory Tech.*, vol.MTT–38, pp.252–259, March 1990.

[8] V. Tripathi and H. Lee, "Spectral domain computation of characteristic impedances and multiport parameters of multiple coupled microstrip lines," *IEEE Trans. Microwave Theory Tech.*, vol.MTT–37, pp.215–220, January 1989.

[9] T. Kitazawa and Y. Hayashi, "Asymmetrical three–line coupled striplines with anisotropic substrate," *IEEE Trans. Microwave Theory Tech.*, vol.MTT–34, pp.767–771, July 1986.

[10] F. L. Mesa, G. Cano, F. Medina, R. Marques and M. Horno, "On the quasi TEM and full wave approaches applied to coplanar multistrip on lossy dielectric layered media", *IEEE Trans. Microwave Theory Tech.*, Vol.MTT-40, pp.524-532, March 1992.

[11] V.K. Tripathi, "Asymmetric coupled transmission lines in an inhomogeneous medium," *IEEE Trans. Microwave Theory Tech.*, vol.MTT–23, pp.734–739, Sept.1975.

[12] L. Carin and K. Webb, "An equivalent circuit model for terminated hybrid–mode multiconductor transmission lines," *IEEE Trans. Microwave Theory Tech.*, vol.MTT–37, pp.1784–1793, Nov. 1989.

[13] K.C. Gupta, R. Garg and R. Chadha, "Computer aided design of microwave circuits," Dedham, Mass.: Artech, 1981.

[14] N. Izzat. "Space domain analysis of inhomogeneous waveguides of the microstrip and inset guide families", *Ph.D Thesis*, Bath University, Bath, 1991.

Chapter 4

ANALYSIS OF PARALLEL COUPLED INSET DIELECTRIC GUIDES

4.1 Introduction

This chapter presents a rigorous hybrid–mode analysis of parallel coupled inset dielectric guides. The extended spectral domain approach is used to accurately determine propagation constants of even and odd modes. The convergence of solutions is investigated in order to show the numerical efficiency of the method. The computed results for propagation constants are compared with the measured data in the literature, demonstrating excellent agreement. Also, the numerical results for the limiting cases as the guide separation approaches infinity and becomes very small are examined in comparison with the data for the single–line inset dielectric guide to further examine the accuracy of the method.

The scattering coefficients are obtained based on the difference between the propagation constants of the dominant even and odd modes. Comparison with measured coupling coefficients also shows good agreement. The computed results

improved in comparison with previous investigation.

Numerical results for propagation and coupling characteristics are presented as a function of frequency and guide separation, and for different values of groove height. It is found that high and flat coupling coefficients can be obtained by using very small guide separation and with the appropriate choice of the groove height. Therefore, this structure appears to be very useful for broadband coupler applications.

4.2 Integral Equation Formulation

The cross section of the parallel coupled inset dielectric guides and coordinate systems used in the analysis are shown in Figure 4.1. Since the structure under consideration is composed of two identical IDGs which are placed in parallel, there exist E_z even and odd modes with respect to the $x = 0$ plane, propagating along the z direction. The E_z even and odd modes can be obtained by placing magnetic and electric walls at the $x = 0$ plane, respectively. As a result, only the right–hand half cross section needs to be considered. Due to the coupling of two grooves, the electromagnetic field in the right–hand groove is not antisymmetrical or symmetrical with respect to the center of the groove. However, the total field can be expressed in terms of combinations of antisymmetrical and symmetrical fields, which can be represented through their discrete Fourier transforms, for instance:

$$\begin{aligned} E_{x'}(x', y') &= E^o_{x'}(x', y') + E^e_{x'}(x', y') \\ &= \frac{1}{a} \sum_{n=-\infty}^{\infty} \tilde{E}^o_{x'}(\alpha^o_n, y') e^{-j\alpha^o_n x'} + \frac{1}{a} \sum_{n=-\infty}^{\infty} \tilde{E}^e_{x'}(\alpha^e_n, y') e^{-j\alpha^e_n x'} \end{aligned} \tag{4.1}$$

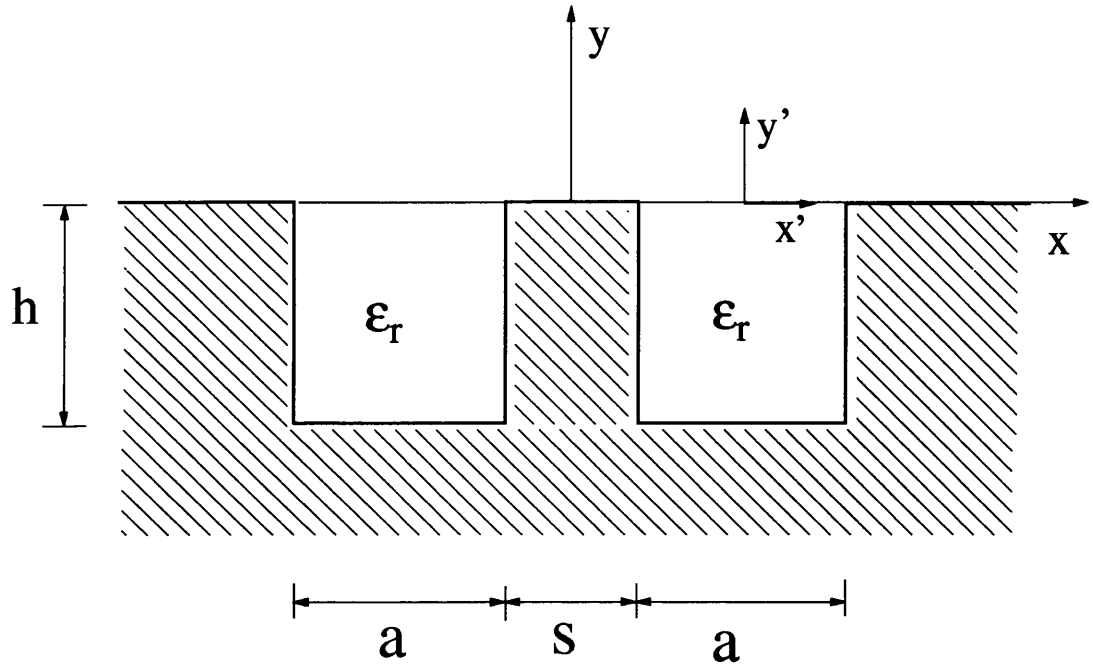

Figure 4.1: Cross section of parallel coupled inset dielectric guides and coordinate systems used in the analysis

where o and e are associated with the antisymmetrical and symmetrical fields whose corresponding z electric field components E_z^o and E_z^e are odd and even functions of x', respectively. The Fourier variables are constrained to be equal to $\alpha_n^o = \frac{2n\pi}{a}$ and $\alpha_n^e = \frac{(2n+1)\pi}{a}$ with $n = 0, \pm 1, \pm 2, \cdots$, in order to satisfy the electric field boundary conditions at the side walls of the groove. It should be noted that when the grooves are uncoupled (when the guide separation is infinite), these antisymmetrical and symmetrical fields can exist independently, and they have been defined as the E_z odd and even modes for the single IDG in chapters 2 and 3, respectively. Note that the (x', y') coordinate system is used to represent the field in the right-hand groove, where $x' = x - \frac{a+s}{2}$ and $y' = y$.

Continuous Fourier transforms have to be used to express the field components

in the air region, for instance:

$$E_x(x,y) = \frac{1}{2\pi}\int_{-\infty}^{\infty} \tilde{E}_x(\alpha,y)e^{-j\alpha x}\,d\alpha \tag{4.2}$$

The solutions for the Fourier–transformed field components are obtained for the air and right–hand groove regions by applying the boundary conditions at infinity and on the base of the groove, and introducing the tangential electric field components on the air–dielectric interface $E_{x'}(x') = E^o_{x'}(x') + E^e_{x'}(x')$ and $E_z(x') = E^o_z(x') + E^e_z(x')$. By applying the continuity conditions for the tangential magnetic field components at the air–dielectric interface, the following integral equations for the tangential electric field components at this interface can be obtained for the E_z even modes of the coupled IDGs.

$$\begin{aligned}
&\frac{1}{2\pi}\int_{-\infty}^{\infty} 2j\sin(q)e^{-jq}[Y^a(\alpha)]\begin{bmatrix}\tilde{E}^o_{x'}(\alpha)\\ \tilde{E}^o_z(\alpha)\end{bmatrix}e^{-j\alpha x'}d\alpha \\
&\qquad +\frac{1}{a}\sum_{n=-\infty}^{\infty}[Y^g(\alpha^o_n)]\begin{bmatrix}\tilde{E}^o_{x'}(\alpha^o_n)\\ \tilde{E}^o_z(\alpha^o_n)\end{bmatrix}e^{-j\alpha^o_n x'} \\
&+\frac{1}{2\pi}\int_{-\infty}^{\infty} 2\cos(q)e^{-jq}[Y^a(\alpha)]\begin{bmatrix}\tilde{E}^e_{x'}(\alpha)\\ \tilde{E}^e_z(\alpha)\end{bmatrix}e^{-j\alpha x'}d\alpha \\
&\qquad +\frac{1}{a}\sum_{n=-\infty}^{\infty}[Y^g(\alpha^e_n)]\begin{bmatrix}\tilde{E}^e_{x'}(\alpha^e_n)\\ \tilde{E}^e_z(\alpha^e_n)\end{bmatrix}e^{-j\alpha^e_n x'} \\
&\qquad\qquad = 0 \quad \text{for } |x'| < \frac{a}{2}
\end{aligned} \tag{4.3}$$

with

$$\tilde{E}^o_{x'}(\alpha^o_n) = \int_{-\frac{a}{2}}^{\frac{a}{2}} E^o_{x'}(x')e^{j\alpha^o_n x'}dx' \tag{4.4}$$

$$\tilde{E}^o_z(\alpha^o_n) = \frac{j}{\alpha^o_n}\int_{-\frac{a}{2}}^{-\frac{a}{2}} \frac{\partial E^o_z(x')}{\partial x'}e^{j\alpha^o_n x'}dx' \tag{4.5}$$

$$\tilde{E}^e_{x'}(\alpha^e_n) = \int_{-\frac{a}{2}}^{\frac{a}{2}} E^e_{x'}(x')e^{j\alpha^e_n x'}dx' \tag{4.6}$$

$$\tilde{E}_z^e(\alpha_n^e) = \frac{j}{\alpha_n^e} \int_{-\frac{a}{2}}^{-\frac{a}{2}} \frac{\partial E_z^e(x')}{\partial x'} e^{j\alpha_n^e x'} dx' \tag{4.7}$$

where $q = 0.5\alpha(s+a)$ and $[Y^a]$ and $[Y^g]$ are the magnetic field Green's functions in the Fourier transform domain for the air and groove regions, respectively. These Green functions have been given in (2.34) - (2.36) and (2.39) - (2.41) in chapter 2. For the E_z odd modes, sin and cos in (4.3) are exchanged. Note that $\frac{\partial E_z^o(x')}{\partial x'}$ and $\frac{\partial E_z^e(x')}{\partial x'}$ are used instead of $E_z^o(x')$ and $E_z^e(x')$ because they satisfy the same boundary and singular edge conditions as $E_{x'}^o(x')$ and $E_{x'}^e(x')$, respectively. As a result, in the Galerkin's procedure the basis functions for $\frac{\partial E_z^o(x')}{\partial x'}$ and $\frac{\partial E_z^e(x')}{\partial x'}$ can be chosen to be the same as those for $E_{x'}^o(x')$ and $E_{x'}^e(x')$, respectively.

4.3 Galerkin's Procedure

The integral equations (4.3) can be solved by Galerkin's method. The first step is to expand tangential electric field components at $y = 0$ in terms of basis functions:

$$E_{x'}^o(x') = \sum_{m=0}^{N_o} C_{x'm}^o F_m^o(x') \tag{4.8}$$

$$\frac{\partial E_z^o(x')}{\partial x'} = \sum_{m=1}^{N_o} C_{zm}^o F_m^o(x') \tag{4.9}$$

$$E_{x'}^e(x') = \sum_{m=0}^{N_e} C_{x'm}^e F_m^e(x') \tag{4.10}$$

$$\frac{\partial E_z^e(x')}{\partial x'} = \sum_{m=0}^{N_e} C_{zm}^e F_m^e(x') \tag{4.11}$$

where $C_{x'm}^o$, C_{zm}^o, $C_{x'm}^e$ and C_{zm}^e are unknown coefficients. The first basis function is given with $m = 0$ for $E_{x'}^o(x')$, $E_{x'}^e(x')$ and $\frac{\partial E_z^e}{\partial x'}(x')$, and with $m = 1$ for $\frac{\partial E_z^o}{\partial x'}(x')$.

The basis functions must be chosen to approximate the true but unknown electric field components in order to achieve fast convergence of the solutions. Therefore, the edge conditions satisfied by the tangential electric field components at the 90^0 metal corners should be taken into account. Thus, the appropriate complete set of basis functions is provided by the Gegenbauer polynomials [1], whose weight function fits the required singularity at the metal corners, which is of order $r^{-1/3}$ [2]

$$F_m^o(x') = \left[1 - (\frac{2x'}{a})^2\right]^{-\frac{1}{3}} C_{2m}^{1/6}(\frac{2x'}{a}) \tag{4.12}$$

$$F_m^e(x') = \left[1 - (\frac{2x'}{a})^2\right]^{-\frac{1}{3}} C_{2m+1}^{1/6}(\frac{2x'}{a}) \tag{4.13}$$

The Fourier transforms of the above basis functions can be expressed in terms of Bessel functions. Note that $m \neq 0$ for the expansion of $\frac{\partial E_z^o}{\partial x'}(x')$ since the $m = 0$ term is not zero at the metal corners as the boundary conditions require.

Substituting (4.8) - (4.11) into (4.3), multiplying the resulting equations by $E_{x'i}^o(x')$, $E_{zi}^o(x')$, $E_{x'i}^e(x')$, and $E_{zi}^e(x')$, and integrating with respect to x' from $x' = -\frac{a}{2}$ to $\frac{a}{2}$, we obtain the following matrix equation for the expansion coefficients for the E_z even modes:

$$\begin{bmatrix} A_{im}^{x'x'} & A_{im}^{x'z} & B_{im}^{x'x'} & B_{im}^{x'z} \\ A_{im}^{zx'} & A_{im}^{zz} & B_{im}^{zx'} & B_{im}^{zz} \\ C_{im}^{x'x'} & C_{im}^{x'z} & D_{im}^{x'x'} & D_{im}^{x'z} \\ C_{im}^{zx'} & C_{im}^{zz} & D_{im}^{zx'} & D_{im}^{zz} \end{bmatrix} \begin{bmatrix} C_{x'm}^o \\ C_{zm}^o \\ C_{x'm}^e \\ C_{zm}^e \end{bmatrix} = 0 \tag{4.14}$$

where the elements of the coefficient submatrices $[A]$, $[B]$, $[C]$ and $[D]$ are given by

$$A_{im}^{pr} = \frac{1}{2\pi}\int_{-\infty}^{\infty} 2j\sin(q)e^{-jq}\tilde{E}_{pi}^{o}(-\alpha)Y_{pr}^{a}(\alpha)\tilde{E}_{rm}^{o}(\alpha)\,d\alpha + \frac{1}{a}\sum_{n=-\infty}^{\infty}\tilde{E}_{pi}^{o}(-\alpha_n^o)Y_{pr}^{g}(\alpha_n^o)\tilde{E}_{rm}^{o}(\alpha_n^o) \tag{4.15}$$

$$B_{im}^{pr} = \frac{1}{2\pi}\int_{-\infty}^{\infty} 2\cos(q)e^{-jq}\tilde{E}_{pi}^{o}(-\alpha)Y_{pr}^{a}(\alpha)\tilde{E}_{rm}^{e}(\alpha)\,d\alpha \tag{4.16}$$

$$C_{im}^{pr} = \frac{1}{2\pi}\int_{-\infty}^{\infty} 2j\sin(q)e^{-jq}\tilde{E}_{pi}^{e}(-\alpha)Y_{pr}^{a}(\alpha)\tilde{E}_{rm}^{o}(\alpha)\,d\alpha \tag{4.17}$$

$$D_{im}^{pr} = \frac{1}{2\pi}\int_{-\infty}^{\infty} 2\cos(q)e^{-jq}\tilde{E}_{pi}^{e}(-\alpha)Y_{pr}^{a}(\alpha)\tilde{E}_{rm}^{e}(\alpha)\,d\alpha + \frac{1}{a}\sum_{n=-\infty}^{\infty}\tilde{E}_{pi}^{e}(-\alpha_n^e)Y_{pr}^{g}(\alpha_n^e)\tilde{E}_{rm}^{e}(\alpha_n^e) \tag{4.18}$$

where p and r denote x' or z for the subscripts in the Fourier transforms of basis functions, and 1 or 2 for the subscripts in the Fourier–transformed Green's functions. For the E_z odd modes, sin and cos in (4.15) – (4.18) are replaced by cos and sin, respectively. The propagation constants can be obtained by setting the determinant of the coefficient matrix to zero and applying a root–seeking process.

4.4 Coupling Characteristics

The dominant E_z even and odd modes of the parallel coupled IDGs propagate above a certain frequency, their cutoff frequency. For certain frequency range,

only these dominant modes propagate. In this range, we can use the characteristics of these two modes to realize a directional coupler, where the coupling occurs in the forward direction [3] – [5]. It has been experimentally demonstrated that this kind of the IDG coupler has very low return loss and high isolation (better than -20 dB), using dielectric taper loaded metal waveguides to connect to the ports of the coupled IDGs [6]. As a result, perfect isolation and port matching can be assumed as a simplification for the theoretical investigation of this coupler. The scattering coefficients for the IDG coupler can be derived from the following simple expressions in terms of the difference between the propagation constants of the dominant even and odd modes.

$$|S_{31}| = \left|\sin\left(\frac{\beta_e - \beta_o}{2}L\right)\right| \tag{4.19}$$

$$|S_{21}| = \left|\cos\left(\frac{\beta_e - \beta_o}{2}L\right)\right| \tag{4.20}$$

where L is the length of the coupling section. β_e and β_o denote the propagation constants of the E_z even and odd modes, respectively. Ports of the coupler are defined in Figure 4.2. It is seen that Port 1, the input port, and port 3, the coupled port, are located diagonally. S_{31} is usually called the coupling coefficient.

From (4.19) and (4.20) it is apparent that the coupling length for a 3–dB directional coupler is determined by

$$L_{3dB} = \frac{\pi}{2(\beta_e - \beta_o)} \tag{4.21}$$

In order to transfer the total power of the incident wave from port 1 to port 3, the length must be twice the length for the 3–dB coupler. It is seen in the above equations that the difference of the propagation constants of the even and odd modes represents the effect of coupling. The degree of coupling [5] can be defined as

$$K = (\beta_e - \beta_o)/(\beta_e + \beta_o) \tag{4.22}$$

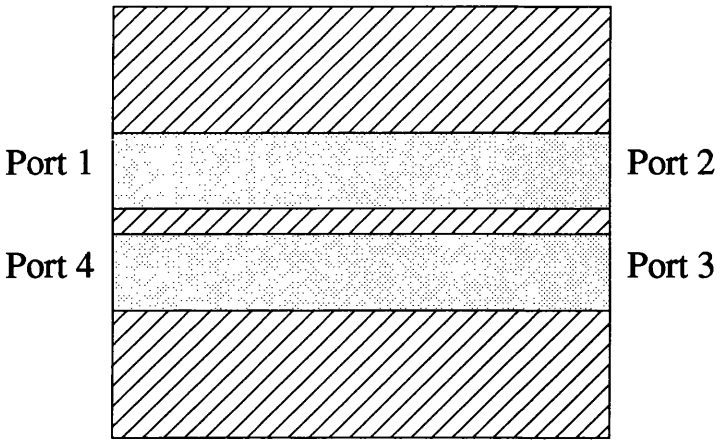

Figure 4.2: Top view of parallel coupled inset dielectric guides

4.5 Convergence Tests

It is well known that with an increasing number of basis functions used in the actual calculations, the solutions obtained by using the variational method become more accurate, but the computational time drastically increases. This is especially the case for the coupled–line structure. To show the efficiency and accuracy of the present method, the convergence of solutions is investigated. Table 4.1 shows the convergence of solutions for propagation constants of the dominant E_z even and odd modes of the coupled IDGs at the frequency of 9 GHz by using different values of N_o and N_e in (4.8) – (4.11). The solutions are found to converge with small values of N_o and N_e. This is typical of the convergence behaviour seen

at other frequencies and for other cross sections. It can be seen from this table that N_o =2 and N_e=1 can be used to achieve accurate solutions for propagation constants of both E_z even and odd modes to five significant digits and for their difference to four significant digits. Since the coupling characteristics of this kind of the coupled guides depend on the difference, accurate determination of this difference is necessary and important for the analysis and design of the coupled guide. From the above check of the convergence, the present method provides good convergence and numerical efficiency. All the data reported in the rest of the chapter were generated by the use of N_o=2 and N_e=1.

N_o	N_e	β_e/κ_0	β_o/κ_0	$(\beta_e - \beta_o)/\kappa_0$
1	1	1.242706	1.217498	.025208
2	1	1.242619	1.217407	.025212
2	2	1.242621	1.217408	.025213
3	2	1.242607	1.217395	.025212
3	3	1.242607	1.217395	.025212
4	3	1.242603	1.217391	.025212
4	4	1.242603	1.217391	.025212
5	5	1.242602	1.217390	.025212

Table 4.1: Convergence of solutions for propagation constants of the dominant E_z even and odd modes of the coupled IDGs at the frequency of 9 GHz on the number of the basis functions (ε_r=2.04, a=1.016e–2 m, h=1.524e–2 m and s=1.7e–3 m)

4.6 Comparison with Measured Results

The accuracy of the present method is now assessed by comparison with available measured results. Figure 4.3 shows the comparison of the present results for the propagation constants of the dominant E_z even and odd modes with the measured results given in [6]. The excellent agreement is clearly seen. In fact, the agreement is within 0.3 percent.

Figure 4.4 shows the comparison of the present results for the coupling characteristics of a coupled IDG section with measured and computed data reported in [7] and [6]. Compared with the computed results in [6], the present results agree much better with the measured coupling characteristics. The reason for this is that the present analysis is based on the hybrid–mode field description rather than the LSE and LSM approximation.

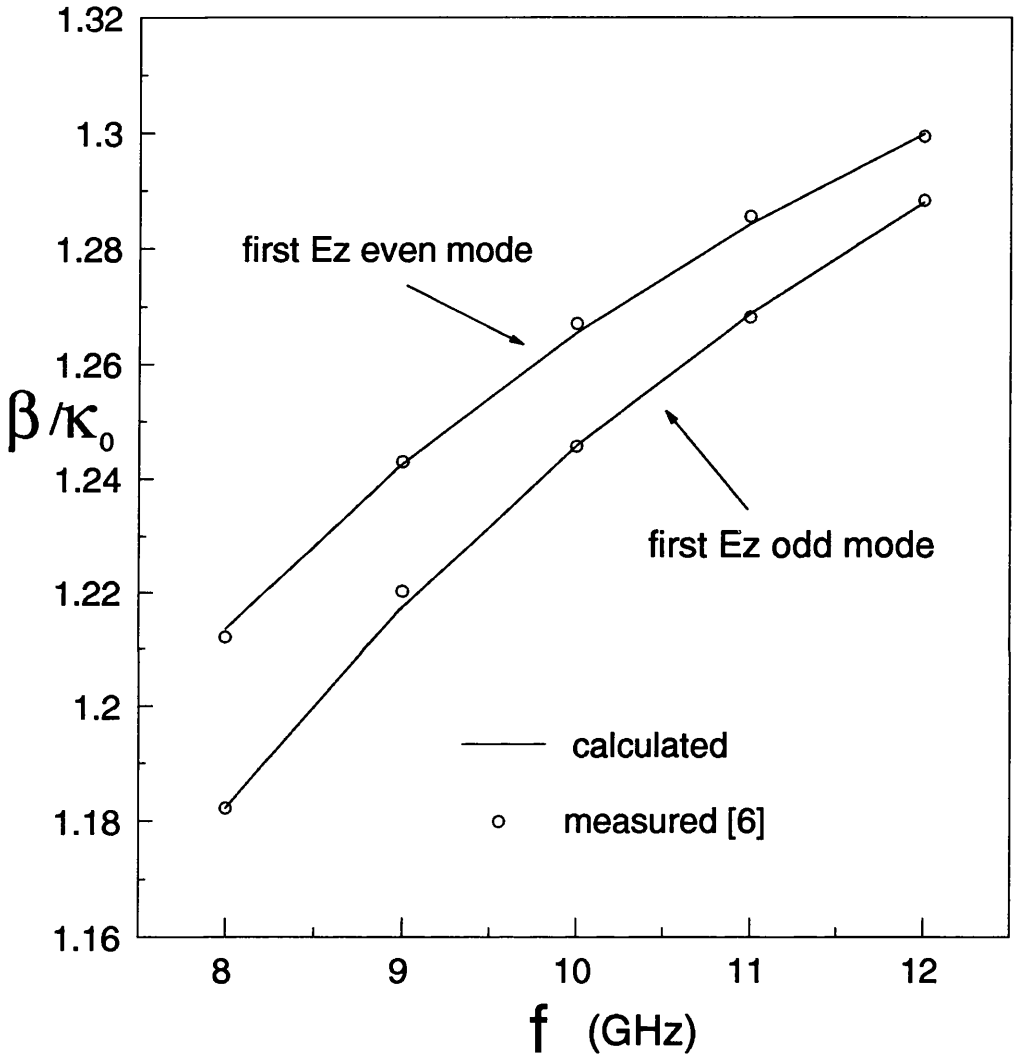

Figure 4.3: Comparison of computed propagation constants of the dominant E_z even and odd modes of the coupled IDGs with measured data reported in [6] (ε_r=2.04, a=1.016e–2 m, h=1.524e–2 m and s=1.7e–3 m)

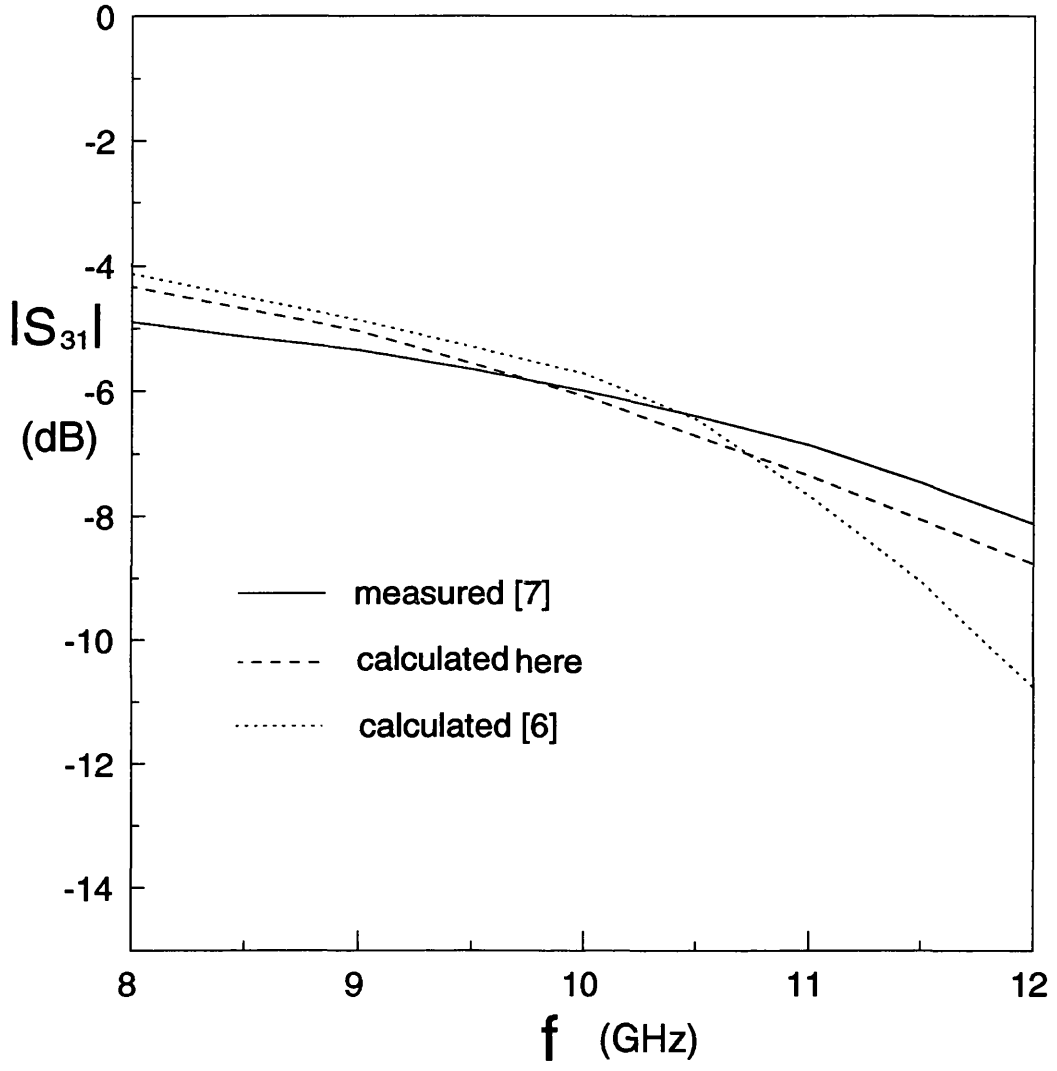

Figure 4.4: Comparison of computed Coupling characteristics of the dominant E_z even and odd modes of the 0.25 m – long coupled IDG section with measured and computed data reported in [7] and [6], respectively (ε_r=2.04, a=1.016e–2 m, h=1.524e–2 m and s=1.7e–3 m)

4.7 Numerical Results

A qualitative check on our analysis can be made by investigating the propagation constants of the coupled IDGs in the limiting cases as the guide separation s approaches infinity and becomes very small [8]. Figure 4.5 shows our prediction of propagation constants of the dominant E_z even and odd modes of the coupled IDGs as a function of s, for two different values of h. To make the comparison the propagation constants for the dominant E_z odd mode of the single IDG are included in the figure, where the single IDG groove width is equal to either the coupled IDG groove width, or twice the coupled IDG groove width.

As s increases, the propagation constants of both even and odd mode approach that of corresponding single IDG. It has been determined numerically for the above particular case that when s is greater than 6 cm, the two IDGs are essentially decoupled and the propagation constants of both even and odd modes are equal to that of the corresponding single IDG with groove width equaling the coupled IDG groove width.

On the other hand, when s decreases, the propagation constant of the E_z odd mode of the coupled IDGs decreases and approaches that of the E_z odd mode of the single IDG with groove width equaling twice the coupled IDG groove width. Clearly, when s is small enough, the separating metal wall at the center of the coupled guide has no or very little effect on the electric characteristics of the E_z odd mode because the electric field components tangential to the $x = 0$ plane is zero for this odd mode. Therefore, the electric characteristics of the E_z odd mode of the coupled IDGs with a very small separation should be the same as that of the single IDG with groove width which is equal to twice the coupled IDG groove width.

It can be also seen from this figure that:

1) The propagation constants of the even and odd modes of the coupled IDGs are larger and smaller than that of the corresponding single IDG, respectively.

2) The propagation constants of both even and odd modes are not symmetrically shifted from that of the corresponding single IDG.

3) When s decreases, the propagation constants of the even and odd modes increase and decrease respectively, leading to bigger difference between the even and odd mode propagation constants and consequently to higher coupling.

The degree of coupling, K, of the dominant E_z even and odd modes of the coupled IDG is shown in Figure 4.6 as a function of s for different values of h. It is observed that the degree of coupling increases as h decreases because the field becomes less concentrated in the groove, resulting in more interaction between grooves. It is also shown that the degree of coupling decreases as s increases due to the decay of the field from each groove. As a result, the length required for 3–dB coupling increases. This can clearly be seen in Figure 4.7 where L_{3dB} is shown as a function of s. Therefore, s should be chosen to be quite small for the design of the 3–dB coupler in order to achieve a short coupling length.

Figure 4.8 shows the propagation constants of the first two E_z even and odd modes of the coupled IDGs as a function of frequency. Clearly there is a frequency range where only the dominant E_z even and odd modes propagate. The cut-off frequencies of these dominant modes are nearly the same. The excitation of higher–order modes at high frequency limits the bandwidth over which the simple description of the coupling used above is valid. The presence of these modes can degrade the coupler performance. Therefore, it is important that the coupler should be operated in the frequency range where only the dominant modes propagate.

In contrast to the cut-off behaviour of the dominant modes, the cut-off frequency of the first higher–order even mode is much lower than that of the first higher–order odd mode. It is also seen that

(1) the propagation constant of the first higher–order even mode increases very slowly with increasing frequency near its cut-off;

(2) as frequency increases the difference between the propagation constants of even and odd modes becomes smaller because the field is more concentrated in the grooves, resulting in less interaction between two grooves. In this case, the propagation constants of even and odd modes approach that of the single IDG with no coupling.

Figure 4.9 shows the degree of coupling as a function of frequency for different values of h. Clearly there is a frequency where maximum degree of coupling occurs, and this frequency increases as h decreases.

Figure 4.10 shows the coupling characteristics of a coupled IDG section as a function of frequency for different values of h. In these cases the center band coupling is 3 dB. It is clearly seen that for the deep groove (h=0.01524 m) the coupling decreases with increasing frequency in the frequency range shown here. As h decreases, coupling decreases at the low end of the frequency range, but increases at the high end. As a result, the coupling becomes flatter. However, as h decreases further, coupling at the low end becomes much lower, and therefore the coupling becomes less flat. Hence, there is a optimum value of h for flat coupling over a broad frequency band.

The scattering characteristics of the 3–dB IDG coupler with the optimum value of h at the center frequency of 9.5 GHz is shown in Figure 4.11. It is seen that the coupling is quite flat for the frequency range considered here. In fact,

from 8.3 to 10.5 GHz, the variation in the coupling is in the ± 0.15 dB range. Therefore, the coupler has a 23% bandwidth for a tolerance of ± 0.15 dB deviation in coupling from 3 dB. This shows that quite wide bandwidth can be achieved by the appropriate choice of the height of the groove without resorting to the use of the holes in the separating walls [9].

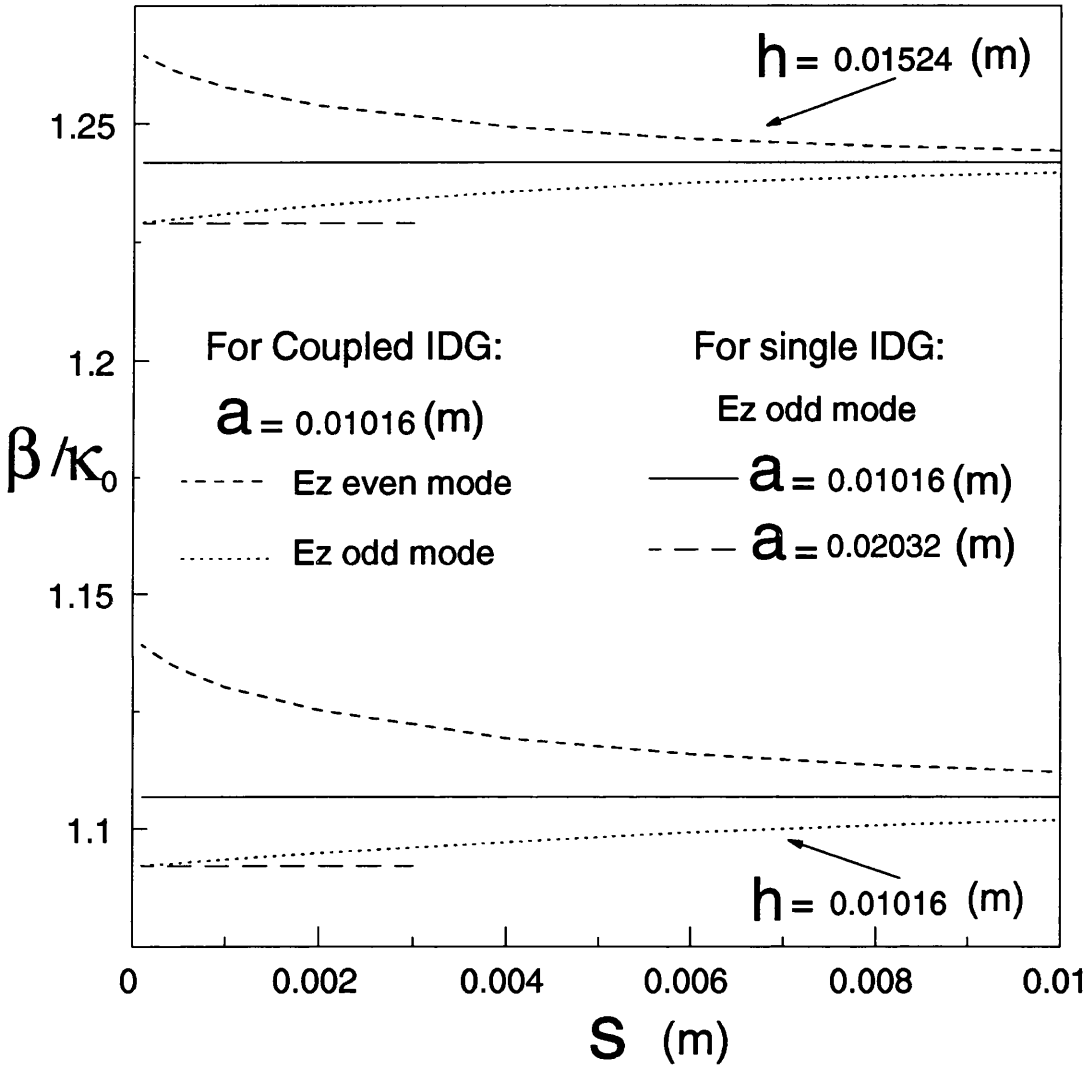

Figure 4.5: Propagation constants of the dominant E_z even and odd modes of the coupled IDGs and the dominant E_z odd mode of the single IDG as a function of s for different values of h (ε_r=2.04 and f= 9.5 GHz)

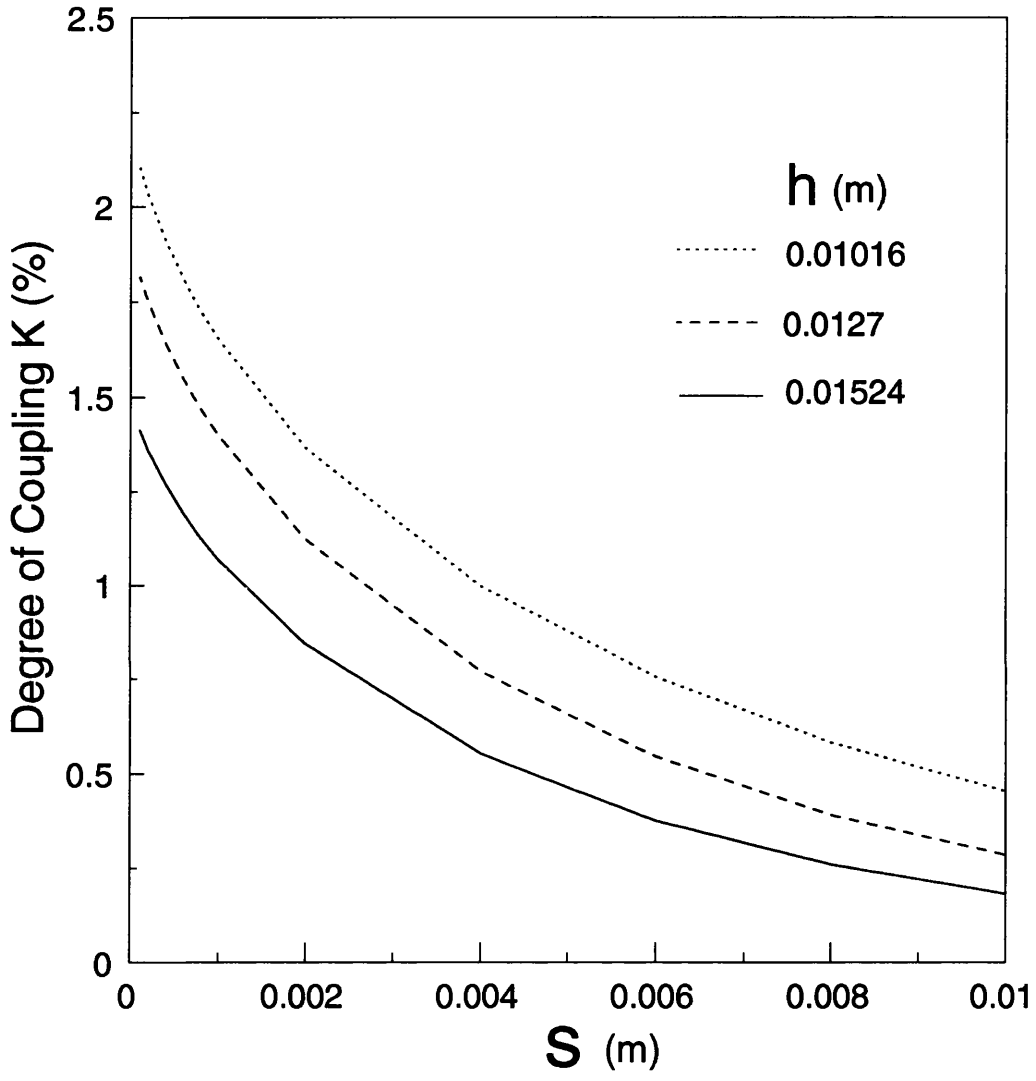

Figure 4.6: Degree of coupling of the dominant E_z even and odd modes of the coupled IDGs as a function of s for different values of h (ε_r=2.04, a=1.016e–2 m and f= 9.5 GHz)

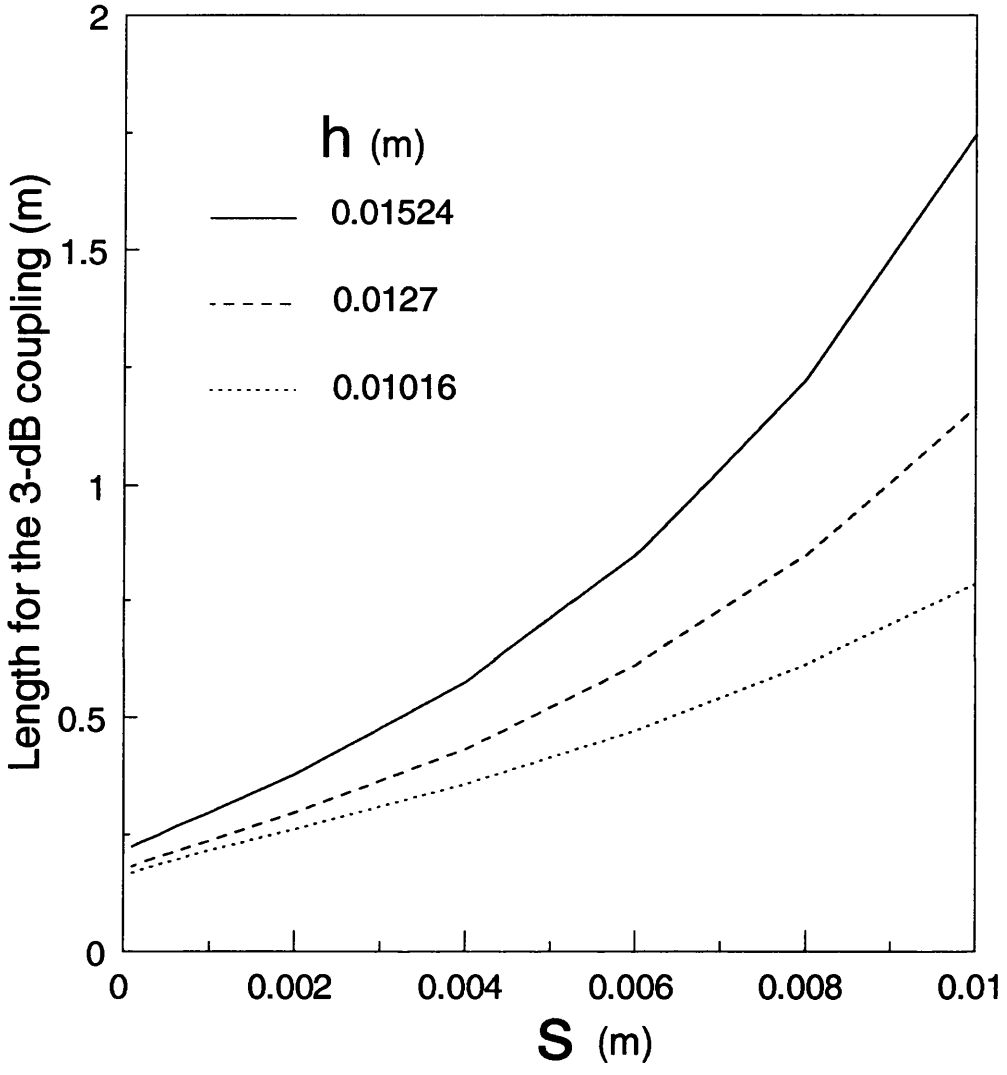

Figure 4.7: Length for the 3–dB coupling of the dominant E_z even and odd modes of the coupled IDGs as a function of s for different values of h (ε_r=2.04, a=1.016e–2 m and f= 9.5 GHz)

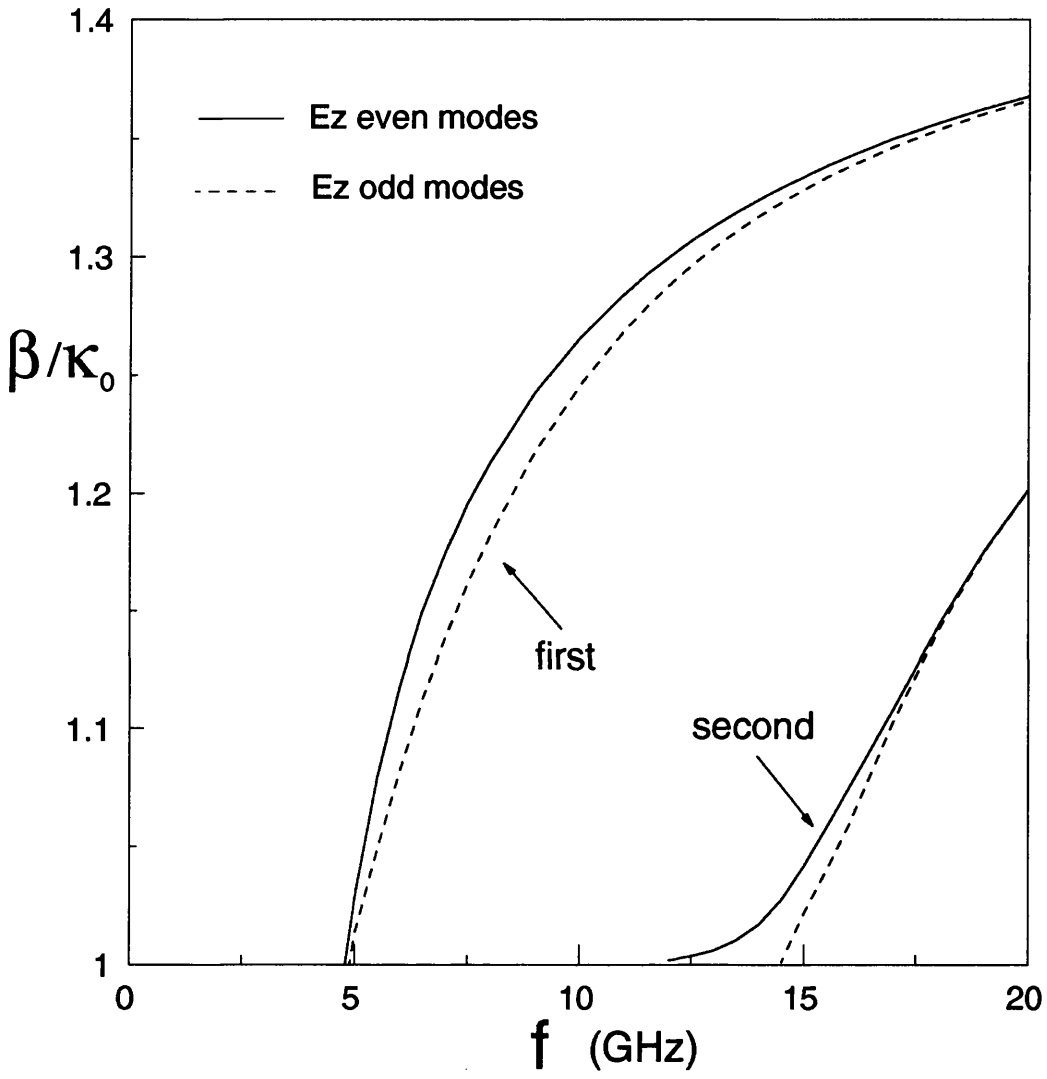

Figure 4.8: Propagation constants of the first two E_z even and odd modes of the coupled IDGs as a function of frequency (ε_r=2.04, a=1.016e–2 m, h=1.524e–2 m and s=1.7e–3 m)

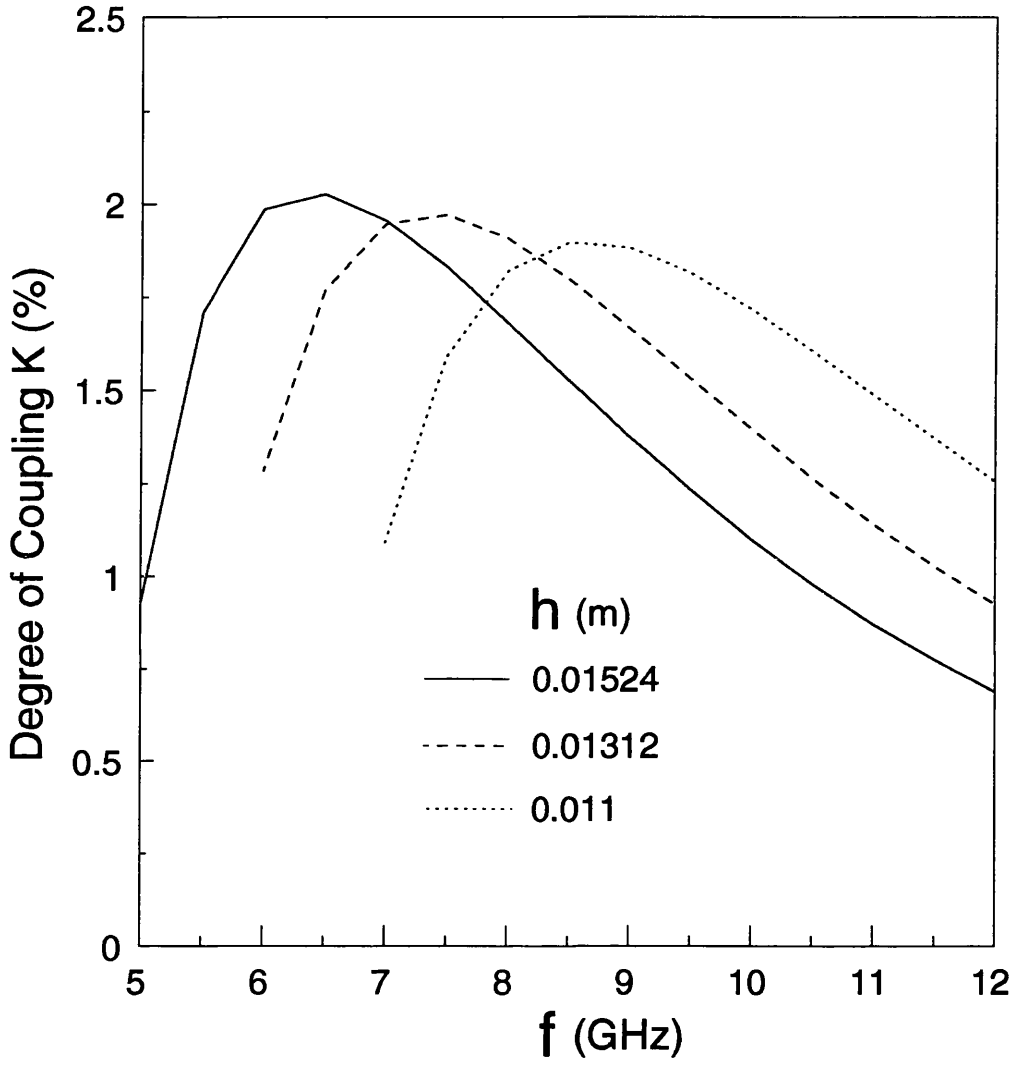

Figure 4.9: Degree of coupling of the dominant E_z even and odd modes of the coupled IDGs as a function of frequency for different values of h (ε_r=2.04, a=1.016e–2 m and s=5.0e–4 m)

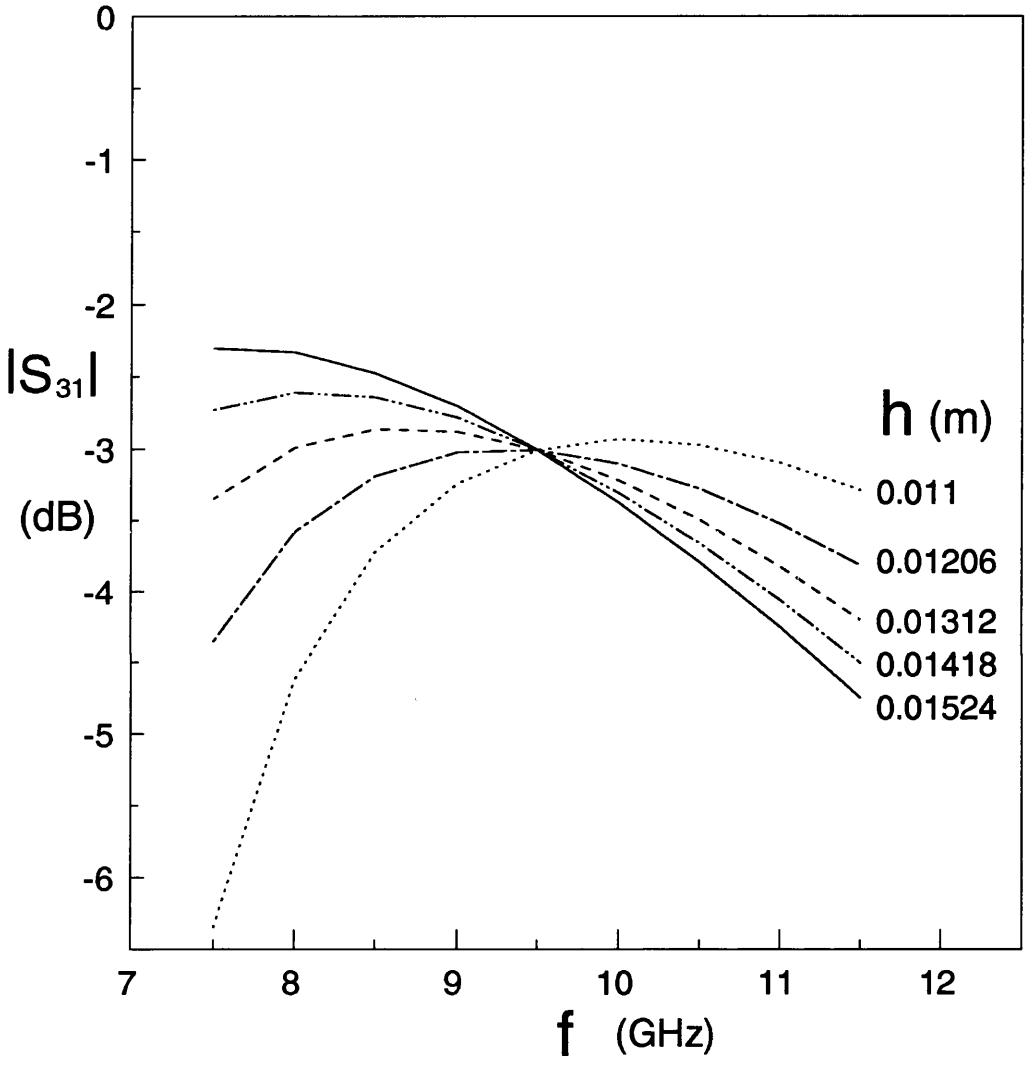

Figure 4.10: Coupling characteristics of the dominant E_z even and odd modes of the coupled IDG section as a function of frequency for different values of h (ε_r=2.04, a=1.016e–2 m, s=5.0e–4 m and $L = L_{3dB}$ at 9.5 GHz)

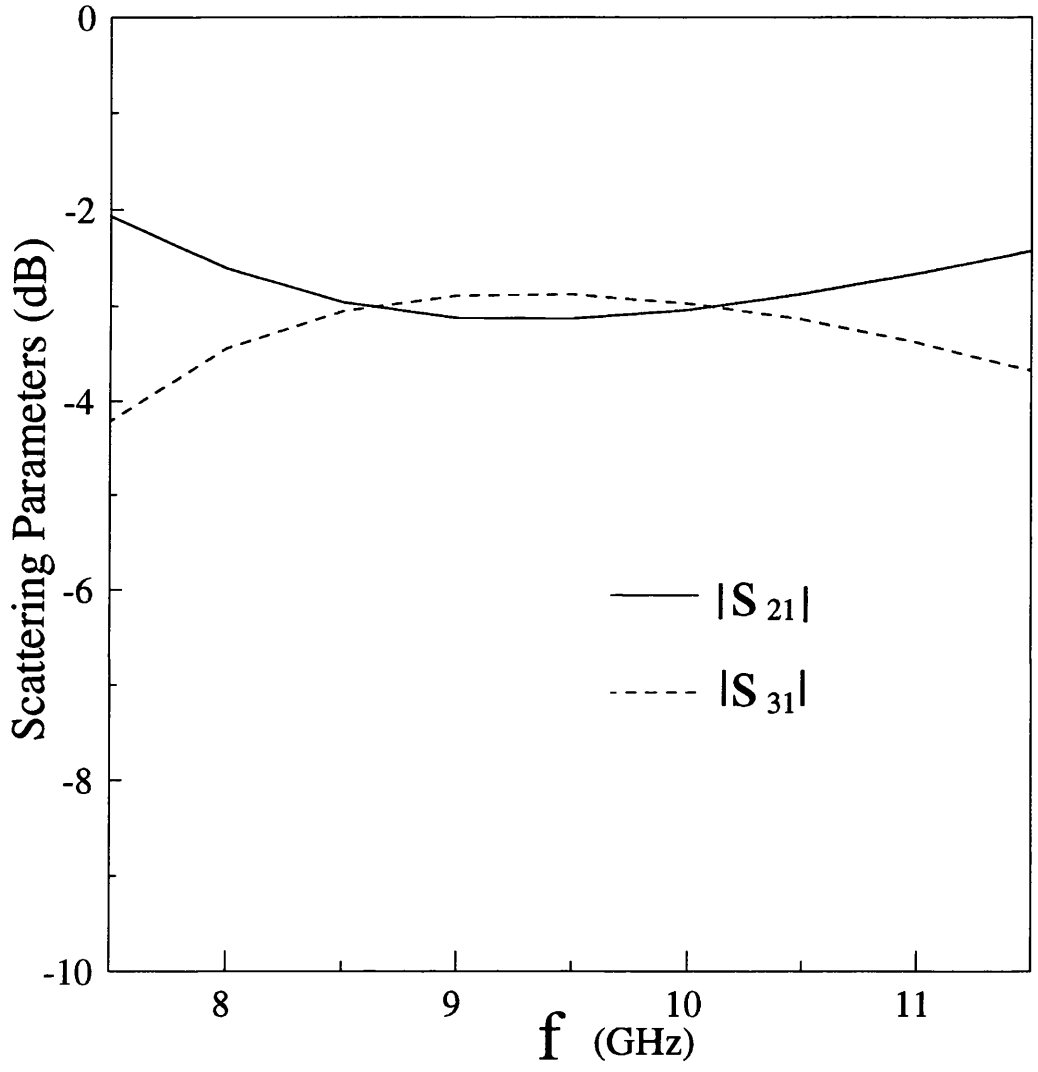

Figure 4.11: Scattering characteristics of the dominant E_z even and odd modes of the coupled IDG section as a function of frequency (ε_r=2.04, a=1.016e–2 m, h =1.206e–2 m, s=5.0e–4 m and L =0.203 m)

4.8 Conclusion

A rigorous full–wave analysis of propagation constants of parallel coupled inset dielectric guides has been described and simple expression for scattering coefficients has been given. The convergence and the numerical efficiency of the analysis have been demonstrated to be good. The accuracy of computed results has been verified by comparing present results with measured and approximate theoretical data available in the literature, and examining the results in the limiting cases.

Numerical results were presented for several structural parameters. It has been found that the propagation constants of the dominant even and odd modes of the coupled IDGs split, but do not shift symmetrically from the corresponding value of the single IDG and their difference is increased with increasing guide separation, leading to a higher coupling coefficient. It has also been shown that there is an optimum frequency for maximum degree of coupling. The optimum frequency is dependent on the slot depth.

It has also been found that there is an optimum value of the groove height in order to obtain flat coupling characteristics. With the choice of this value, the IDG coupler shows broadband flat coupling characteristics. In fact, the bandwidth has been found to be as high as 23 percent under the tolerance limit of ± 0.15 dB of deviation in coupling from 3 dB.

References

[1] I. S. Gradshteyn and I. M. Ryshik, "Tables of integrals, series and products", Academic Press, 1965.

[2] T. Rozzi and S. J. Hedges, "Rigorous analysis and network modeling of the inset dielectric guide," *IEEE Trans. Microwave Theory Tech.*, vol.MTT-35, pp.823-833, Sept. 1987.

[3] D.I. Kim, D. Kawabe, K. Araki and Y. Naito, "Directly connected image guide 3–dB couplers with very flat couplings," *IEEE Trans. Microwave Theory Tech.*, vol.MTT–32, pp.621–627, June 1984.

[4] T. Rozzi, M.N. Husain and L. Zappelli, "Rigorous analysis of multiple coupled rib waveguide," *IEEE Trans. Microwave Theory Tech.*, vol.MTT–40, pp.706–716, April 1992.

[5] J. Miao and T. Itoh, "Hollow image guide and overlayed image guide coupler," *IEEE Trans. Microwave Theory Tech.*, vol.MTT-30, pp.1826–1831, Nov. 1982.

[6] S. R. Pennock, D. M. Boskovic and T. Rozzi, "Analysis of coupled inset dielectric guides under LSE and LSM polarization," *IEEE Trans. Microwave Theory Tech.*, vol.MTT-40, pp.916-924, May 1992.

[7] T. Rozzi, S. R. Pennock and D. Boskovic, "Dispersion characteristic of coupled inset dielectric guide," in *Proc. 20th European Microwave Conf.*, Budapest, pp.1175-1180, Sept. 1990

[8] J.B. Knorr and K.D. Kucher, "Analysis of coupled slots and coplanar strips on dielectric substrate," *IEEE Trans. Microwave Theory Tech.*, vol.MTT-23, pp.541–548, July 1975.

[9] S. R. Pennock, D. Boskovic and T. Rozzi, "Broadband inset dielectric guide coupler," in *Proc. 21th European Microwave Conf.*, Stultgart, pp.1142-1147, 1991

Chapter 5

ANALYSIS OF ASYMMETRICAL MULTILAYER FINLINES CONTAINING MAGNETIZED FERRITES

5.1 Introduction

In this chapter the spectral domain approach is further extended for the analysis of asymmetrical multilayer finlines containing magnetized ferrites. The solution of the Fourier–transformed electromagnetic field is first described for magnetized ferrites, which are characterized by a permeability tensor. All of the field components are found to be coupled. A 4 x 4 matrix is next obtained for expressing the relationship between tangential magnetic and electric fields at two surfaces of a layer. Based on this matrix, a recursive algorithm is introduced to derive the Fourier transformed multilayer dyadic Green's function for different regions. Galerkin's procedure is then applied to obtain the determinantal equation for the propagation constants.

In order to show the efficiency and confirm the accuracy of the present method, the convergence of solutions is investigated and comparison of the present results is made with calculated and measured data available in the literature for some particular cases.

The advantages of the asymmetrical version of finlines are demonstrated. Numerical results are presented for various structural and material parameters and effects of various multilayer configurations on the differential phase shift and bandwidth are illustrated. It is found that a four–layer dual–ferrite structure is very suitable for the development of high–nonreciprocity structures and wide–bandwidth nonreciprocal phase shifters.

The analysis method is also applied to ferrite–loaded inset dielectric guide. Numerical results are presented for nonreciprocal propagation constants. It is shown that for wide bandwidth a thin ferrite layer should be used. It is also found that by using a large relative permittivity of a dielectric layer, a two–layer ferrite–dielectric IDG structure offers very high nonreciprocity in propagation constants for the realization of efficient nonreciprocal phase shifters.

5.2 Field Components in Magnetized Ferrites

Figure 5.1 illustrates the cross section of an asymmetrical multilayer finline and the coordinate system to be used in the analysis. This structure consists of asymmetrically shielded metal fins which are sandwiched between two multilayer substrates, where any layer can be a magnetized ferrite or a dielectric.

Discrete Fourier transforms are used to represent the field components in this

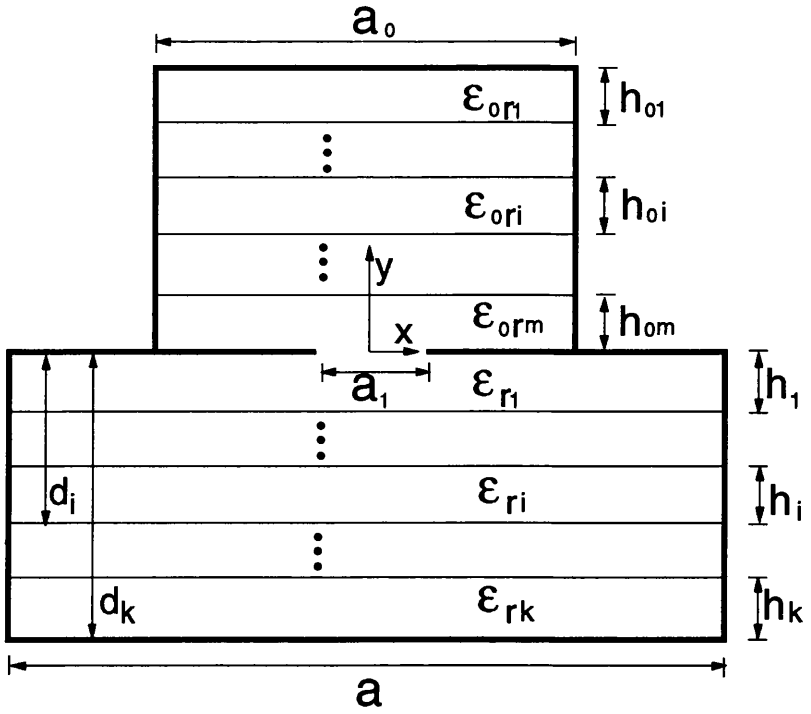

Figure 5.1: Cross section of an asymmetrical multilayer finline where any layer can be dielectric or ferrite; and coordinate system used in the analysis

structure. In order for the electric field boundary conditions at the sidewalls of the lower ($y < 0$) and upper ($y > 0$) regions to be satisfied, different transform variables α_n and α_{0n} have to be chosen for these regions. In the lower region ($y < 0$), the values of α_n are constrained to be equal to $\frac{2n\pi}{a}$ for the E_z odd modes and to $\frac{(2n+1)\pi}{a}$ for the E_z even modes with $n = 0, \pm 1, \pm 2, \cdots$. In the upper region ($y > 0$), the transform variable α_{0n} is chosen to be $\frac{2n\pi}{a_0}$ and $\frac{(2n+1)\pi}{a_0}$ for the E_z odd and even modes, respectively.

If the i^{th} layer in the lower region is a lossless ferrite which is magnetized to saturation in the x direction, it is characterized by a scalar relative permittivity ε_{ri} and a permeability tensor [1]

$$\hat{\mu} = \mu_0 \begin{bmatrix} 1 & 0 & 0 \\ 0 & \mu_r & -j\kappa \\ 0 & j\kappa & \mu_r \end{bmatrix} \tag{5.1}$$

with

$$\mu_r = 1 - \frac{\gamma^2 H_0 M_0}{\omega^2 - (\gamma H_0)^2} \tag{5.2}$$

$$\kappa = \frac{\gamma M_0 \omega}{\omega^2 - (\gamma H_0)^2} \tag{5.3}$$

where μ_0 and γ are the free-space permeability and the gyromagnetic ratio, respectively. H_0 is the applied dc magnetic field. $M_0(4\pi M_s)$ is the saturation magnetization of the ferrite.

To determine the solution for the electromagnetic field which exists within the ferrite, Maxwell's two curl equations are used. After they are Fourier transformed, a set of first-order linear differential equations for the Fourier transforms of electromagnetic field components are obtained, which are written in the following matrix form [2]

$$\begin{bmatrix} 0 & j\beta & \frac{\partial}{\partial y} \\ -j\beta & 0 & j\alpha_n \\ -\frac{\partial}{\partial y} & -j\alpha_n & 0 \end{bmatrix} \begin{bmatrix} \tilde{E}_x \\ \tilde{E}_y \\ \tilde{E}_z \end{bmatrix} = -j\omega\mu_0 \begin{bmatrix} 1 & 0 & 0 \\ 0 & \mu_r & -j\kappa \\ 0 & j\kappa & \mu_r \end{bmatrix} \begin{bmatrix} \tilde{H}_x \\ \tilde{H}_y \\ \tilde{H}_z \end{bmatrix} \tag{5.4}$$

$$\begin{bmatrix} 0 & j\beta & \frac{\partial}{\partial y} \\ -j\beta & 0 & j\alpha_n \\ -\frac{\partial}{\partial y} & -j\alpha_n & 0 \end{bmatrix} \begin{bmatrix} \tilde{H}_x \\ \tilde{H}_y \\ \tilde{H}_z \end{bmatrix} = j\omega\varepsilon_0\varepsilon_{ri} \begin{bmatrix} \tilde{E}_x \\ \tilde{E}_y \\ \tilde{E}_z \end{bmatrix} \tag{5.5}$$

Using (5.4) and (5.5) and carrying through some algebraic and differential manipulation (see Appendix A), we can express z directed field components $\tilde{H}_z$ and $\tilde{E}_z$ in terms of $\tilde{H}_x$, $\tilde{E}_x$ and their derivatives

$$\begin{aligned} [(\alpha_n^2 - \kappa_i^2\mu_r)^2 - (\kappa_i^2\kappa)^2]\tilde{H}_z &= \alpha_n\beta(\alpha_n^2 - \kappa_i^2\mu_r)\tilde{H}_x - \kappa_i^2\kappa\alpha_n\frac{\partial \tilde{H}_x}{\partial y} \\ &- j\omega\varepsilon_0\varepsilon_{ri}\kappa\beta\kappa_i^2\tilde{E}_x + j\omega\varepsilon_0\varepsilon_{ri}(\alpha_n^2 - \kappa_i^2\mu_r)\frac{\partial \tilde{E}_x}{\partial y} \end{aligned} \tag{5.6}$$

$$[(\alpha_n^2 - \kappa_i^2\mu_r)^2 - (\kappa_i^2\kappa)^2]\tilde{E}_z = j\omega\mu_0\kappa\alpha_n^2\beta\tilde{H}_x - j\omega\mu_0[\mu_r(\alpha_n^2 - \kappa_i^2\mu_r) + \kappa_i^2\kappa^2]\frac{\partial\tilde{H}_x}{\partial y} + \alpha_n\beta(\alpha_n^2 - \kappa_i^2\mu_r)\tilde{E}_x - \kappa_i^2\kappa\alpha_n\frac{\partial\tilde{E}_x}{\partial y} \quad (5.7)$$

and derive the following wave equations for the x-directed field components $\tilde{H}_x$ and $\tilde{E}_x$

$$\frac{\partial^2\tilde{H}_x}{\partial y^2} - \gamma_h^2\tilde{H}_x = \eta_h\tilde{E}_x \quad (5.8)$$

$$\frac{\partial^2\tilde{E}_x}{\partial y^2} - \gamma_e^2\tilde{E}_x = \eta_e\tilde{H}_x \quad (5.9)$$

where

$$\gamma_h^2 = \frac{\alpha_n^2}{\mu_r} + \beta^2 - \kappa_i^2, \quad \gamma_e^2 = \alpha_n^2 + \beta^2 - \kappa_i^2\mu_e \quad (5.10)$$

$$\eta_h = j\omega\varepsilon_0\varepsilon_{ri}\kappa\alpha_n/\mu_r, \quad \eta_e = -j\omega\mu_0\kappa\alpha_n/\mu_r \quad (5.11)$$

$$\mu_e = \mu_r - \kappa^2/\mu_r, \quad \kappa_i^2 = \omega^2\mu_0\varepsilon_0\varepsilon_{ri} \quad (5.12)$$

We can see that $\tilde{H}_x$ and $\tilde{E}_x$ are coupled. This is due to the permeability tensor in (5.1). In this case, TE and TM modes do not exist.

Multiplying equation (5.8) by η_e, operating $\frac{\partial^2}{\partial y^2} - \gamma_h^2$ on equation (5.9) and adding, results in the following fourth-order differential equation for $\tilde{E}_x$

$$\frac{\partial^4\tilde{E}_x}{\partial y^4} - (\gamma_h^2 + \gamma_e^2)\frac{\partial^2\tilde{E}_x}{\partial y^2} + (\gamma_h^2\gamma_e^2 - \eta_h\eta_e)\tilde{E}_x = 0 \quad (5.13)$$

This equation is factorized to give the expression

$$\left(\frac{\partial^2}{\partial y^2} - \gamma_+^2\right)\left(\frac{\partial^2}{\partial y^2} - \gamma_-^2\right)\tilde{E}_x = 0 \quad (5.14)$$

where

$$\gamma_{\pm}^2 = 0.5\left(\gamma_h^2 + \gamma_e^2 \pm \sqrt{(\gamma_h^2 - \gamma_e^2)^2 + 4\eta_h\eta_e}\right) \tag{5.15}$$

The solution of the biquadratic differential equation (5.14) is the sum of the two following differential equations

$$\left(\frac{\partial^2}{\partial y^2} - \gamma_+^2\right)\tilde{E}_x = 0 \tag{5.16}$$

$$\left(\frac{\partial^2}{\partial y^2} - \gamma_-^2\right)\tilde{E}_x = 0 \tag{5.17}$$

Thus the general solution of (5.14) can be written as

$$\begin{aligned}\tilde{E}_x &= A\sinh\gamma_+(y+d_i) + B\cosh\gamma_+(y+d_i) \\ &+ Z[C\sinh\gamma_-(y+d_i) + D\cosh\gamma_-(y+d_i)]\end{aligned} \tag{5.18}$$

where A, B, C and D are unknown modal amplitudes

From the solution for $\tilde{E}_x$ given by (5.18), $\tilde{H}_x$ can be found using (5.8) or (5.9)

$$\begin{aligned}\tilde{H}_x &= Y[A\sinh\gamma_+(y+d_i) + B\cosh\gamma_+(y+d_i)] \\ &+ C\sinh\gamma_-(y+d_i) + D\cosh\gamma_-(y+d_i)\end{aligned} \tag{5.19}$$

Z and Y in (5.18) and (5.19) are

$$Z = \eta_e/(\gamma_-^2 - \gamma_e^2), \quad Y = \eta_h/(\gamma_+^2 - \gamma_h^2) \tag{5.20}$$

It is clearly seen from (5.18) and (5.19) that the solution for the electromagnetic field contains the four unknown modal amplitudes. The coefficients can be determined by introducing the tangential electric field components on the upper

and lower surfaces of the layer. Then the relationship between the tangential magnetic and electric field components on the upper and low surfaces of the layer can be obtained in the following matrix form:

$$\begin{bmatrix} \tilde{H}_z(\alpha_n, d_{i-1}) \\ -\tilde{H}_x(\alpha_n, d_{i-1}) \\ \tilde{H}_z(\alpha_n, d_i) \\ -\tilde{H}_x(\alpha_n, d_i) \end{bmatrix} = \begin{bmatrix} P_i & S_i \\ R_i & T_i \end{bmatrix} \begin{bmatrix} \tilde{E}_x(\alpha_n, d_{i-1}) \\ \tilde{E}_z(\alpha_n, d_{i-1}) \\ \tilde{E}_x(\alpha_n, d_i) \\ \tilde{E}_z(\alpha_n, d_i) \end{bmatrix} \tag{5.21}$$

where 2 x 2 submatrices $[P_i]$, $[R_i]$, $[S_i]$ and $[T_i]$ depend only on the electromagnetic properties and the thickness of the i^{th} layer. These are given for the magnetised ferrite layer in Appendix B and will be used to derive the recursive algorithm in the following section.

If the i^{th} layer of the lower region is a dielectric ($\mu_r = 1$ and $\kappa = 0$), the wave equations for $\tilde{H}_x$ and $\tilde{E}_x$ will be uncoupled. In this case, there exist TE and TM modes and the solution for field components has been described in chapter 2. The elements of the submatrices in (5.21) can be easily obtained and are also given in Appendix B.

The matrix for expressing the relationship between the tangential magnetic and electric field components on the upper and lower surfaces of the i^{th} layer of the upper region can also be obtained in the similar way to (5.21).

5.3 Derivation of Green's Function by the Recursive Algorithm

In order to derive the integral equations for the tangential electric field components on the aperture plane ($y = 0$), the Green's function has to be obtained

first. Many techniques for deriving the multilayer Green's function, such as the spectral domain immitance approach [3], mixed spectral domain approach [4], matrix method [5], and equivalent boundary method [6], have been reported in the literature. Most of them assume isotropic media. Others can treat anisotropic media, but cannot be applied to structures with non–uniform cross sections. In this section a new recursive algorithm is presented to derive the Green's function for the multilayer anisotropic structure with a non–uniform cross section as shown in Figure 5.1. First we consider the lower region ($y < 0$). The relationship between the tangential magnetic and electric field components at the y=0 surface and the lower surface of the i-1th layer can be expressed in the following matrix:

$$\begin{bmatrix} \tilde{H}_z(\alpha_n, 0^-) \\ -\tilde{H}_x(\alpha_n, 0^-) \\ \tilde{H}_z(\alpha_n, d_{i-1}) \\ -\tilde{H}_x(\alpha_n, d_{i-1}) \end{bmatrix} = \begin{bmatrix} P^{(0,i-1)} & S^{(0,i-1)} \\ R^{(0,i-1)} & T^{(0,i-1)} \end{bmatrix} \begin{bmatrix} \tilde{E}_x(\alpha_n, 0^-) \\ \tilde{E}_z(\alpha_n, 0^-) \\ \tilde{E}_x(\alpha_n, d_{i-1}) \\ \tilde{E}_z(\alpha_n, d_{i-1}) \end{bmatrix} \tag{5.22}$$

It should be noted that in (5.21) and (5.22) the following continuous conditions for the tangential magnetic and electric field components at the interface between the i-1th and ith layers have been taken into consideration

$$\begin{bmatrix} \tilde{H}_z(\alpha_n, d_{i-1}^-) \\ \tilde{H}_x(\alpha_n, d_{i-1}^-) \\ \tilde{E}_x(\alpha_n, d_{i-1}^-) \\ \tilde{E}_z(\alpha_n, d_{i-1}^-) \end{bmatrix} = \begin{bmatrix} \tilde{H}_z(\alpha_n, d_{i-1}^+) \\ \tilde{H}_x(\alpha_n, d_{i-1}^+) \\ \tilde{E}_x(\alpha_n, d_{i-1}^+) \\ \tilde{E}_z(\alpha_n, d_{i-1}^+) \end{bmatrix} = \begin{bmatrix} \tilde{H}_z(\alpha_n, d_{i-1}) \\ \tilde{H}_x(\alpha_n, d_{i-1}) \\ \tilde{E}_x(\alpha_n, d_{i-1}) \\ \tilde{E}_z(\alpha_n, d_{i-1}) \end{bmatrix} \tag{5.23}$$

Similarly, we can establish the following relationship between the tangential magnetic and electric field components at the y=0 surface and the lower surface of the ith layer.

$$\begin{bmatrix} \tilde{H}_z(\alpha_n, 0^-) \\ -\tilde{H}_x(\alpha_n, 0^-) \\ \tilde{H}_z(\alpha_n, d_i) \\ -\tilde{H}_x(\alpha_n, d_i) \end{bmatrix} = \begin{bmatrix} P^{(0,i)} & S^{(0,i)} \\ R^{(0,i)} & T^{(0,i)} \end{bmatrix} \begin{bmatrix} \tilde{E}_x(\alpha_n, 0^-) \\ \tilde{E}_z(\alpha_n, 0^-) \\ \tilde{E}_x(\alpha_n, d_i) \\ \tilde{E}_z(\alpha_n, d_i) \end{bmatrix} \tag{5.24}$$

Combining (5.21) with (5.22), the submatrices in (5.24) can be derived in terms of the submatrices in (5.21) and (5.22). This results in the following recursive equations:

$$[P^{(0,i)}] = [P^{(0,i-1)}] + [S^{(0,i-1)}][V][R^{(0,i-1)}] \tag{5.25}$$

$$[R^{(0,i)}] = [R_i][V][R^{(0,i-1)}] \tag{5.26}$$

$$[S^{(0,i)}] = -[S^{(0,i-1)}][V][S_i] \tag{5.27}$$

$$[T^{(0,i)}] = -[R_i][V][S_i] + [T_i] \tag{5.28}$$

where i=2,3, ..., k (k is the number of layers in the lower region) and

$$[V] = [U]^{-1}, \quad [U] = [P_i] - [T^{(0,i-1)}] \tag{5.29}$$

For i=1, we have

$$\begin{bmatrix} P^{(0,1)} & S^{(0,1)} \\ R^{(0,1)} & T^{(0,1)} \end{bmatrix} = \begin{bmatrix} P_1 & S_1 \\ R_1 & T_1 \end{bmatrix} \tag{5.30}$$

Taking into account the boundary condition which requires that the tangential electric field components must be zero at the bottom conducting plane of the lower region, and using (5.24) with i=k, the magnetic field Green's function for the lower region can be obtained as follows:

$$\begin{bmatrix} \tilde{H}_z(\alpha_n, 0^-) \\ -\tilde{H}_x(\alpha_n, 0^-) \end{bmatrix} = [Y(\alpha_n)] \begin{bmatrix} \tilde{E}_x(\alpha_n, 0^-) \\ \tilde{E}_z(\alpha_n, 0^-) \end{bmatrix} \tag{5.31}$$

where $[Y] = [P^{(0,k)}]$.

Similarly the magnetic field Green's function for the upper region can be also obtained by using the recursive equations for the upper region similar to (5.25) - (5.28) and applying the boundary condition at the top conducting plane of the upper region:

$$\begin{bmatrix} -\tilde{H}_z(\alpha_{0n}, 0^+) \\ \tilde{H}_x(\alpha_{0n}, 0^+) \end{bmatrix} = [Y^0(\alpha_{0n})] \begin{bmatrix} \tilde{E}_x(\alpha_{0n}, 0^+) \\ \tilde{E}_z(\alpha_{0n}, 0^+) \end{bmatrix} \tag{5.32}$$

5.4 Formulation of Integral Equations

Transforming (5.31) and (5.32) into the space domain, and employing the boundary conditions for the tangential electric and magnetic field components at the aperture plane

$$\begin{bmatrix} -H_z(x, 0^+) \\ H_x(x, 0^+) \end{bmatrix} + \begin{bmatrix} H_z(x, 0^-) \\ -H_x(x, 0^-) \end{bmatrix} = 0 \tag{5.33}$$

$$\begin{bmatrix} E_x(x, 0^+) \\ E_z(x, 0^+) \end{bmatrix} = \begin{bmatrix} E_x(x, 0^-) \\ E_z(x, 0^-) \end{bmatrix} = \begin{bmatrix} E_x^b(x) \\ E_z^b(x) \end{bmatrix} \tag{5.34}$$

we obtain the following integral equations for the tangential electric field components at the aperture:

$$\begin{aligned} &\frac{1}{a_0} \sum_{n=-\infty}^{\infty} [Y^0(\alpha_{0n})] \begin{bmatrix} \tilde{E}_x^b(\alpha_{0n}) \\ \tilde{E}_z^b(\alpha_{0n}) \end{bmatrix} e^{-j\alpha_{0n}x} \quad + \\ &\quad \frac{1}{a} \sum_{n=-\infty}^{\infty} [Y(\alpha_n)] \begin{bmatrix} \tilde{E}_x^b(\alpha_n) \\ \tilde{E}_z^b(\alpha_n) \end{bmatrix} e^{-j\alpha_n x} \quad = 0 \qquad \text{for } |x| < \frac{a_1}{2} \end{aligned} \tag{5.35}$$

where $\tilde{E}_x^b$ and $\tilde{E}_z^b$ are the Fourier transforms of the x and z electric field components at the aperture ($y = 0$)

$$\tilde{E}_x^b(\alpha_n) = \int_{-\frac{a_1}{2}}^{\frac{a_1}{2}} E_x^b(x) e^{j\alpha_n x} dx \tag{5.36}$$

$$\tilde{E}_z^b(\alpha_n) = \int_{-\frac{a_1}{2}}^{\frac{a_1}{2}} E_z^b(x) e^{j\alpha_n x} dx \tag{5.37}$$

5.5 Determinantal Equation for Propagation Constants

Expanding the tangential electric field components at the aperture in terms of basis functions and taking the inner product of integral equations (5.35) with the basis functions, results in a homogeneous matrix equation for the unknown expansion coefficients

$$\begin{bmatrix} K_{im}(x,x) & K_{im}(x,z) \\ K_{im}(z,x) & K_{im}(z,z) \end{bmatrix} \begin{bmatrix} C_{xm} \\ C_{zm} \end{bmatrix} = 0 \tag{5.38}$$

The elements of matrix [K] are given by

$$\begin{aligned} K_{im}(p,r) &= \frac{1}{a_0} \sum_{n=-\infty}^{\infty} \tilde{E}^b_{pi}(-\alpha_{0n}) Y^0_{pr}(\alpha_{0n}) \tilde{E}^b_{rm}(\alpha_{0n}) \\ &+ \frac{1}{a} \sum_{n=-\infty}^{\infty} \tilde{E}^b_{pi}(-\alpha_n) Y_{pr}(\alpha_n) \tilde{E}^b_{rm}(\alpha_n) \end{aligned} \tag{5.39}$$

where p and r denote x or z and

$$\tilde{E}^b_{xm}(\alpha_n) = \int_{-\frac{a_1}{2}}^{\frac{a_1}{2}} E^b_{xm}(x) e^{j\alpha_n x} dx \tag{5.40}$$

$$\tilde{E}^b_{zm}(\alpha_n) = \frac{j}{\alpha_n} \int_{-\frac{a_1}{2}}^{-\frac{a_1}{2}} \frac{\partial E^b_{zm}(x)}{\partial x} e^{j\alpha_n x} dx \tag{5.41}$$

$\tilde{E}^b_{xm}(\alpha_{0n})$ and $\tilde{E}^b_{zm}(\alpha_{0n})$ can be obtained from $\tilde{E}^b_{xm}(\alpha_n)$ and $\tilde{E}^b_{zm}(\alpha_n)$ by simply replacing α_n by α_{0n}.

For (5.38) to yield a nontrivial solution, the determinant of [K] must to zero. This results in a determinantal equation for the propagation constants in the z positive and negative directions.

Since the presence of the fin edges introduces the same singularities in $\frac{\partial E_z^b(x)}{\partial x}$ and, $E_x^b(x)$, which is of the order $r^{-0.5}$ [7], $\frac{\partial E_{zm}^b(x)}{\partial x}$ can be chosen to be the same as $E_{xm}^b(x)$. The basis functions here are chosen as a set of Chebyshev polynomials [8] which are orthogonal with respect to the singular function that describes the edge conditions of the electric field

For the E_z even modes

$$E_{xm}^b(x) = \frac{\partial E_{zm}^b(x)}{\partial x} = \left[1 - (\frac{2x}{a_1})^2\right]^{-\frac{1}{2}} T_{2m+1}(\frac{2x}{a_1}) \quad m = 0, 1, \cdots, N \tag{5.42}$$

For the E_z odd modes, 2m+1 in the above equation is replaced by 2m. It should be noted that the series for $\tilde{E}_{zm}^b$ for the E_z odd modes starts from m=1 instead of 0 since the zeroth terms of $E_z^b(x)$ is not zero at the fin edges as the boundary condition requires.

5.6 Results and Discussions

Based on the analysis described in the previous sections, a Fortran computer program has been developed to compute the nonreciprocal propagation characteristics of the finline with arbitrary number of layers which can be either magnetized ferrite or dielectric. For the nonreciprocal structure, there exist two different solutions for the positive and negative z directions. β_+ and β_- are used to denote the propagation constants for the forward and backward waves, respectively. The differential phase shift is defined as $\triangle\beta = \beta_+ - \beta_-$.

In this section several configurations will be investigated. Figure 5.5 shows the cross section of an asymmetrical finline loaded with (a) sandwich ferrite–dielectric

(SWFD), (b) double layer ferrite–dielectric (DLFD) or (c) double layer dielectric–ferrite (DLDF). Figure 5.11 shows the cross section of an asymmetrical dual–ferrite (DF) loaded finline. Figure 5.14 shows the cross section of a modified asymmetrical dual–ferrite loaded finline.

5.6.1 Convergence Tests

In order to demonstrate the good efficiency of the analysis, the convergence of solutions is investigated. Tables 5.1 and 5.2 show the convergence of solutions for β_+/κ_0, β_-/κ_0 and $(\beta_+ - \beta_-)/\kappa_0$ with number of basis functions for the x and z electric field component expansion at 30 GHz, for the dominant mode of two finline configurations shown in Figure 5.5 (a) and Figure 5.14. It is clearly seen that good convergence can be achieved by using small values of N in (5.42). In fact, N=1 can be used to obtain the solutions of β_+/κ_0 and β_-/κ_0 to four significant digits and N=2 is found to be sufficient to achieve convergence of $(\beta_+ - \beta_+)/\kappa_0$ to four significant digits. This fast convergence is attributed not only to the variational nature of the determination of propagation constants using Galerkin's method, but also to the adequate choice of only one set of basis functions.

N	β_+/k_0	β_-/k_0	$(\beta_+ - \beta_-)/k_0$
1	2.36690	2.18964	.17726
2	2.36691	2.18960	.17731
3	2.36690	2.18958	.17732
4	2.36690	2.18956	.17734
5	2.36690	2.18957	.17733
6	2.36688	2.18954	.17734

Table 5.1: Convergence of solutions for β_+/κ_0, β_-/κ_0 and $(\beta_+ - \beta_-)/\kappa_0$ of the dominant mode of an asymmetrical sandwich ferrite–dielectric loaded finline at the frequency of 30 GHz on the number of the basis functions ($\varepsilon_{rf} = \varepsilon_{rd}$=12.5, $h_f = h_d$=2.5e–4 m, $h_0 = h_1$=3.306e–3 m, a_0=2.1336e–3 m, a=3.556e–3 m, a_1=1.2e–3 m, H_0=500 Oe and M_0=5000 Ga)

N	β_+/k_0	β_-/k_0	$(\beta_+ - \beta_-)/k_0$
1	2.57613	2.24992	.32621
2	2.57613	2.24991	.32622
3	2.57613	2.24989	.32624
4	2.57613	2.24991	.32622
5	2.57612	2.24988	.32624
6	2.57610	2.24988	.32622

Table 5.2: Convergence of solutions for β_+/κ_0, β_-/κ_0 and $(\beta_+ - \beta_-)/\kappa_0$ of the dominant mode of a modified asymmetrical dual–ferrite finline at the frequency of 30 GHz on the number of the basis functions (ε_{rf} = ε_{rd}=12.5, h_f=2.5e–4 m, h_d=4.0e–5 m, h_0 = h_1=3.266e–3 m, a_0=2.1336e–3 m, a=3.556e–3 m, a_1=1.2e–3 m, H_0=500 Oe and M_0=5000 Ga)

5.6.2 Comparisons for Particular Cases

To test the accuracy of our solutions, comparisons with calculated and measured data available in the literature for several particular cases are made in this subsection.

The first comparison is with computed data obtained by Kitazawa in [9], and by Geshiro and Itoh in [10] for the symmetrical double–layer finlines with a magnetic ferrite. The comparison is shown in Figure 5.2 and excellent agreement is apparent.

In Figure 5.3 the computed propagation constants are also compared with measured data reported by Espes et al. in [11] for the special asymmetrical case with a dielectric substrate. Note that in this case the propagation constants are reciprocal . Clearly, the agreement between theory and experiment is good. In fact, the difference is less than 1.5 percent.

The special symmetrical case with a dielectric substrate is also considered. Present

results are compared with both the computed results obtained by the TRD method and the measured results as reported by Olley in [12]. This comparison is shown in Figure 5.4. Again good agreement is obtained.

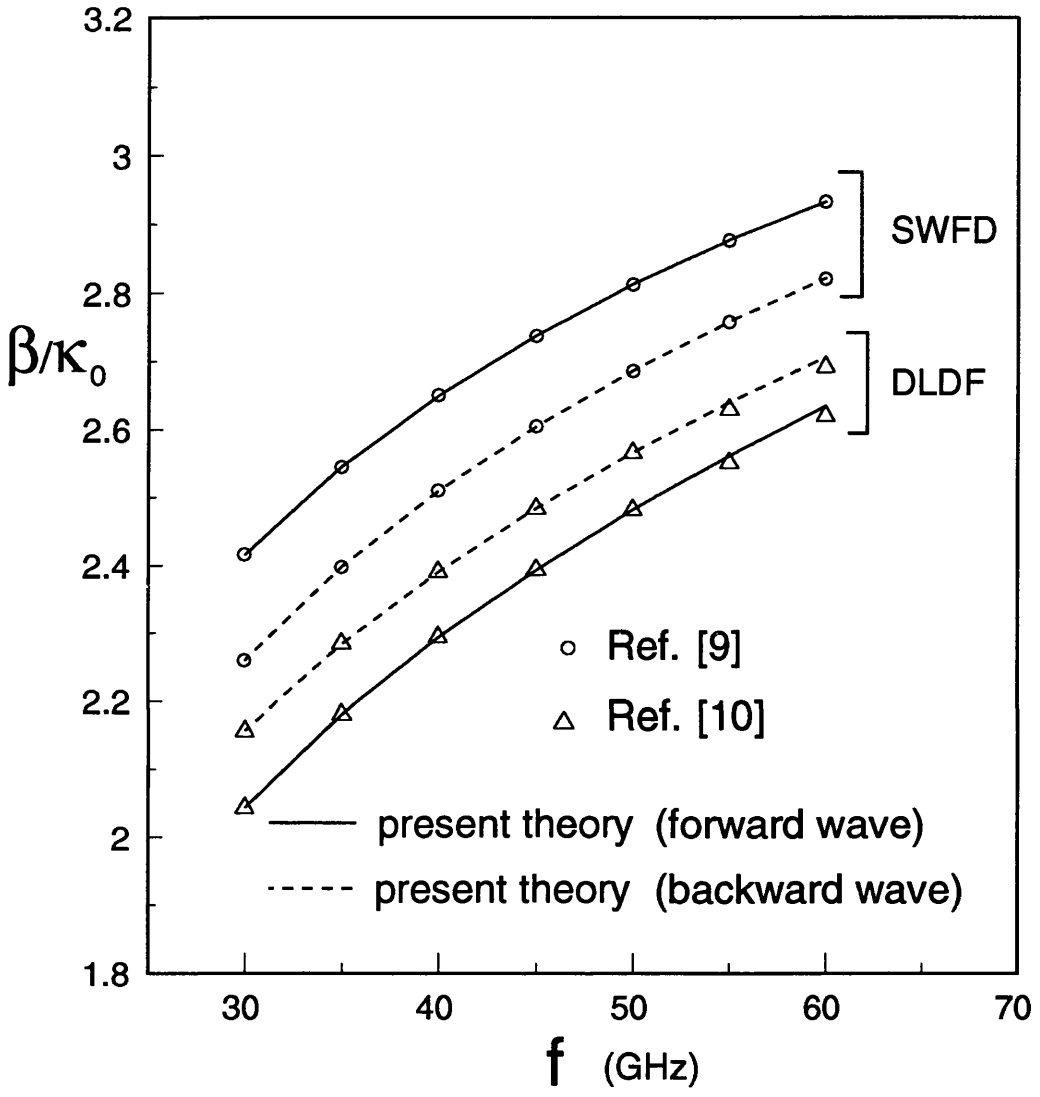

Figure 5.2: Comparison of the normalized propagation constants for the dominant mode of symmetrical SWFD and DLDF loaded fin lines with those reported by Kitazawa in [9]; and by Geshiro and Itoh in [10] ($\varepsilon_{rf} = \varepsilon_{rd}$=12.5, $h_f = h_d$=2.5e–4 m, $h_0 = h_1$=2.1e–3 m, $a_0 = a$=2.35e–3 m, a_1=1.0e–3 m, H_0=500 Oe and M_0=5000 Ga)

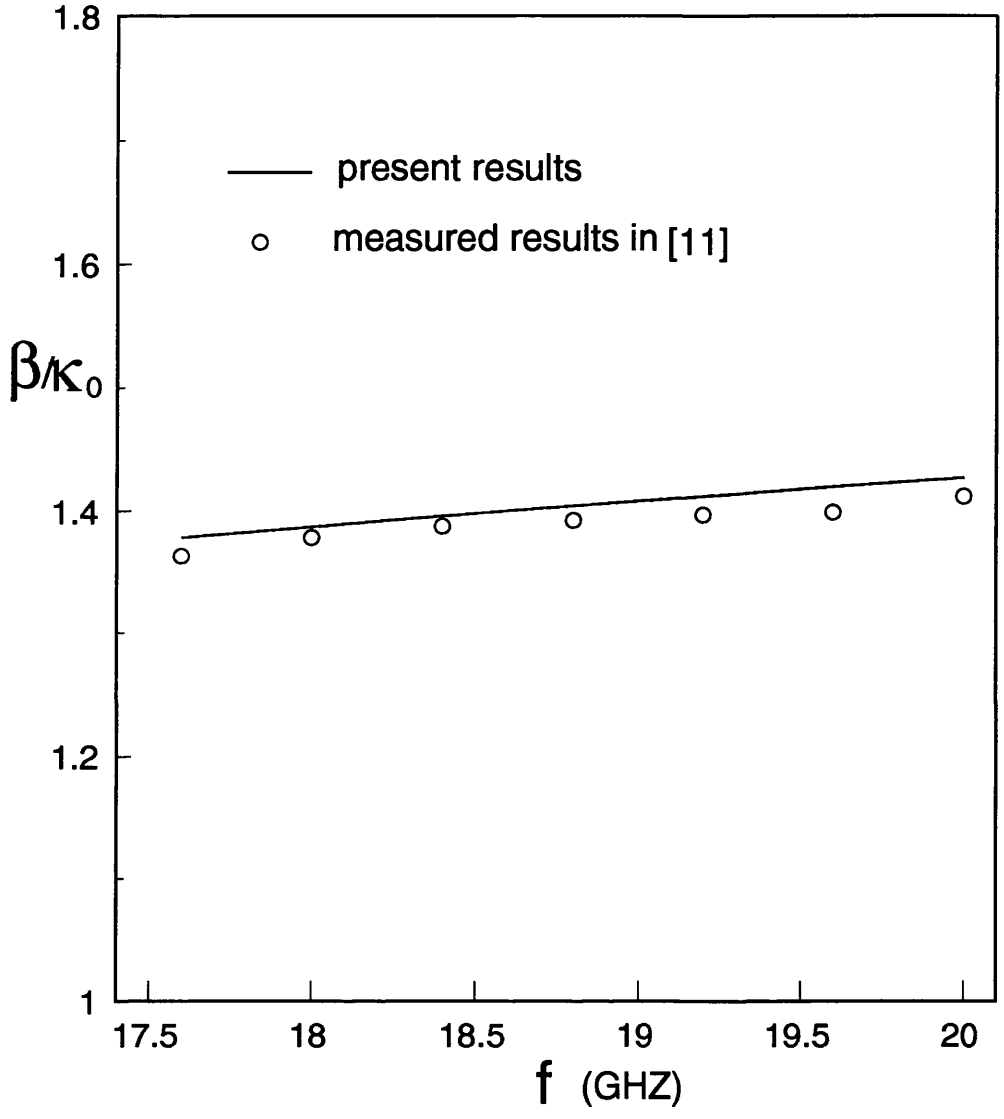

Figure 5.3: Comparison of the normalized propagation constants for the dominant mode of an asymmetrical single–layer dielectric loaded fin line with measured data reported by Espes et al. [11] (h_f = 0, ε_{rd} =9.9, h_d=2.54e–4 m, h_1=5.16e–3 m, a=6.42e–3 m, h_0=5.41e–3 m, a_0=4.42e–3 m and a_1 =1.25e-3 m)

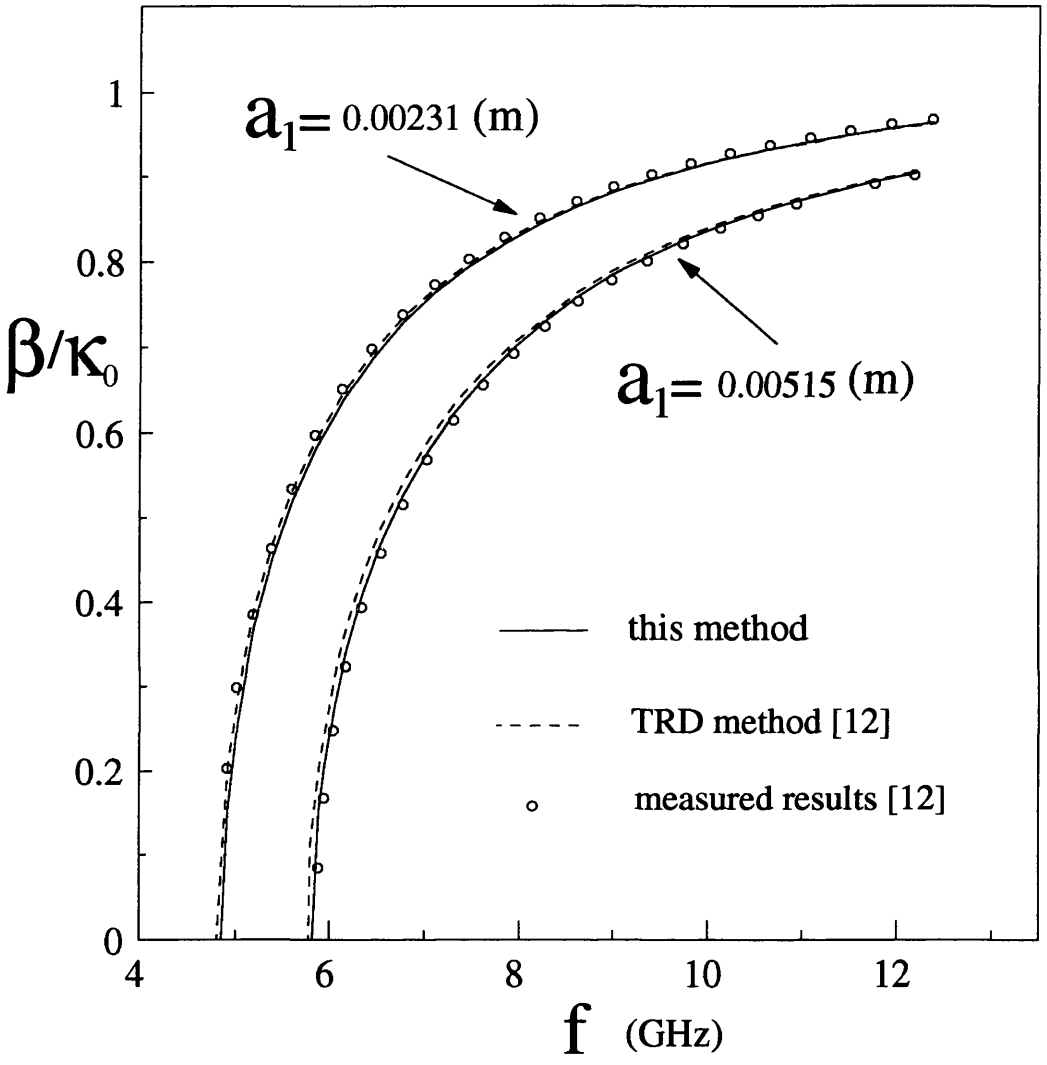

Figure 5.4: Comparison of the normalized propagation constants for the dominant mode of symmetrical single–layer dielectric loaded fin lines with computed and measured data reported by Olley in [12] (h_f = 0, ε_{rd} =2.2, h_d=2.54e–4 m, h_1=1.1176e–2 m, a=1.016e–2 m, h_0=1.143e–2 m and a_0=1.016e–2 m)

5.6.3 Single Ferrite Case

It is well known that the single–layer ferrite–loaded planar waveguide structures including symmetrical finlines do not exhibit high nonreciprocity [13]. An additional high–permittivity dielectric layer is often introduced to improve nonreciprocal characteristics [14]. Therefore, the results are presented here only for asymmetrical multilayer finline structures. First, we consider three configurations of the asymmetrical double–layered finline containing a magnetized ferrite, that is, sandwich ferrite–dielectric (SWFD), double layer ferrite–dielectric (DLFD) and double layer dielectric–ferrite (DLDF), as shown in Figure 5.5. The effects of these three configurations on the differential phase shift and the bandwidth are investigated in this subsection.

It is known that for a phase shifter, the bandwidth is always limited at low end by the magnetic loss of the ferrite [15] [16] and the lowest frequency of the bandwidth is determined by $f_l = \gamma M_0/0.7$. In this and next subsections M_0 is chosen to be 5000 Ga and therefore $f_l = 20$ GHz for this case. On the other hand, the excitation of the higher–order modes limits the bandwidth at the high end because signal propagation in the higher–order modes can degrade the performance of the phase shifter [17]. Therefore, in the phase shifter with a fixed value of magnetization saturation, a higher cut-off frequency of the first higher–order mode is desirable.

Figure 5.6 shows the normalized differential phase shifts of the dominant mode of the three structures as a function of a_0/a. It can be seen that as a_0/a decreases (asymmetry becomes higher), the normalized differential phase shift increases for the SWFD and DLFD configurations, but decreases for the DLDF one.

Figure 5.7 shows the normalized propagation constants of the backward wave of the dominant and first higher–order modes of the SWFD configuration as a function of a_0/a. It is observed from this figure that as the asymmetry increases, the cut-off frequency of the first higher–order mode increases, resulting in a increase in the bandwidth. This behaviour is also observed for the DLFD and DLDF configurations.

From the above results it is evident that the asymmetrical finline version offers an additional freedom to obtain the characteristic parameters and higher bandwidth, and exhibits higher nonreciprocity with the appropriate choice of the configuration.

Figure 5.8 shows normalized propagation constants of the backward waves of the dominant and first higher–order modes of three double–layer structures as a function of frequency. The cut-off frequencies of the first higher–order mode are almost the same for the DLFD and DLDF structures, but lower by about 5 GHz than that for the SWFD structure. Therefore, the bandwidth of the SWFD structure is much wider than that of other two structures.

The differential phase shifts of the dominant mode of the three configurations are presented in Figure 5.9 as a function of frequency. It is observed that
(a) the differential phase shift of the DLDF one is negative and its absolute value increases with increasing frequency and
(b) the differential phase shift is positive for both the SWFD and the DLFD but increases more slowly for the SWFD than for the DLFD, giving the SWFD a flatter phase shift characteristic.

Figure 5.10 presents the comparison of the normalized differential phase shifts

of the dominant mode for the three structures as a function of the relative permittivity ε_{rd} of the dielectric layer and for different values of the thickness h_d of the dielectric layer. For the SWFD and DLFD structures the differential phase shift is always positive and increases with the increase in ε_{rd} and h_d. The reason for this is that propagation constant for the forward wave increases more quickly with increasing ε_{rd} and h_d than that for the backward wave. This is due to the difference in the field distributions in the dielectric layer of these two counter-propagating waves. On the other hand, for the DLDF the differential phase shift is positive for small values of ε_{rd}, and can be equal to zero at a specific value of ε_{rd}. Beyond this value of ε_{rd} the shift becomes negative and it absolute value increases as ε_{rd} increases. It is also evident that the SWFD structure offers the highest nonreciprocity in propagation constants.

According to the above results, the sandwich ferrite–dielectric one is the best choice among the double–layer single–ferrite loaded structures for the realization of good performance phase shifters in terms of nonreciprocity and bandwidth.

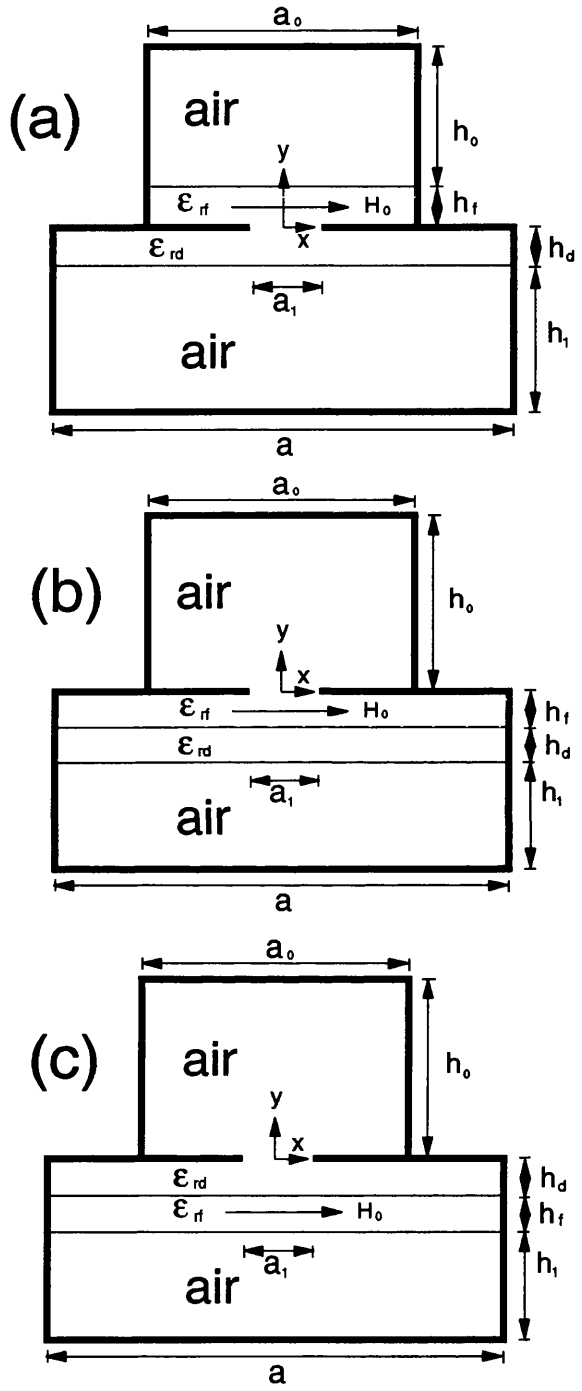

Figure 5.5: Cross section of an asymmetrical finline loaded with (a) sandwich ferrite–dielectric (SWFD), (b) double layer ferrite–dielectric (DLFD) or (c) double layer dielectric–ferrite (DLDF).

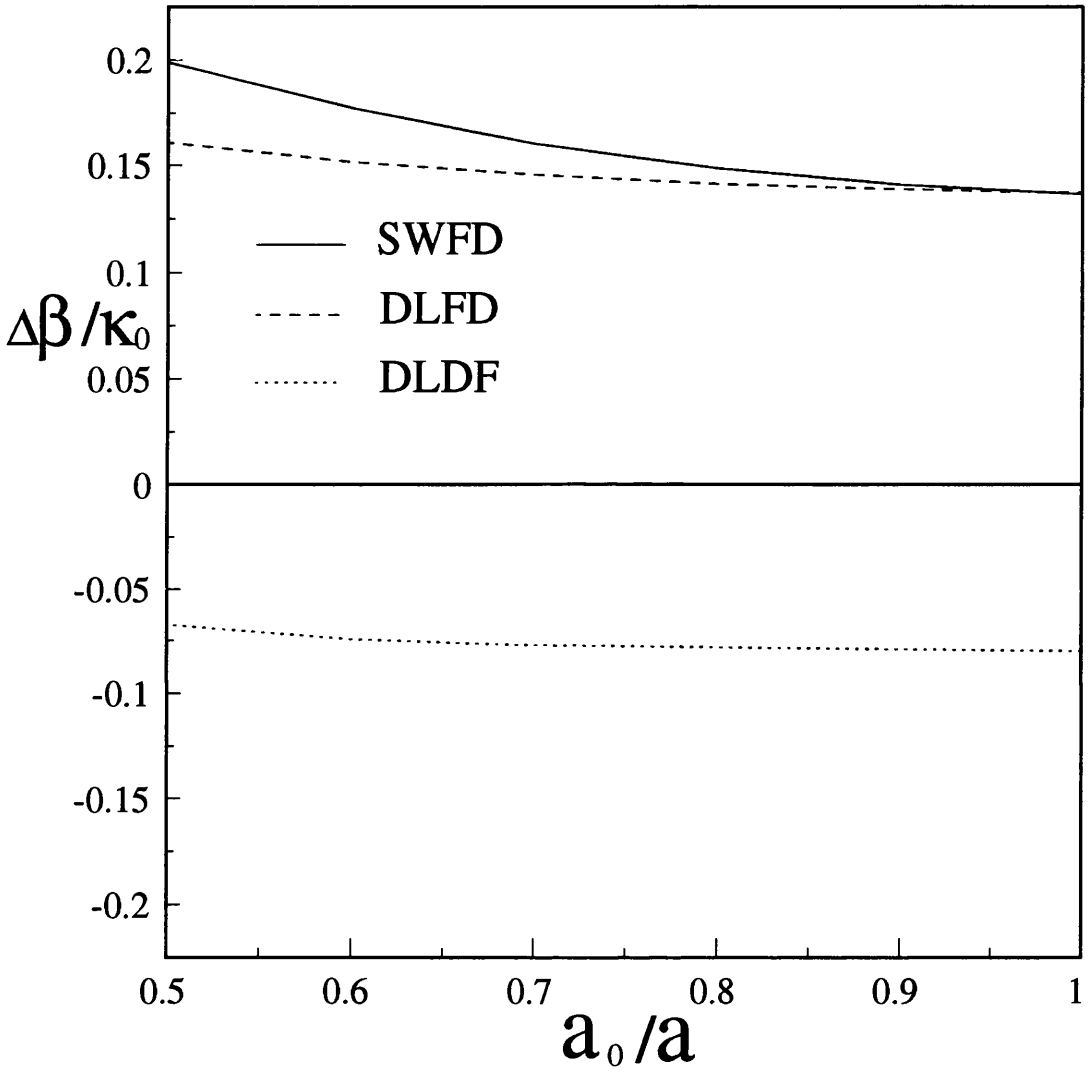

Figure 5.6: Normalized differential phase shifts of the dominant mode of the asymmetrical SWFD, DLFD and DLDF loaded finlines as a function of a_0/a (ε_{rf} = ε_{rd}=12.5, h_f = h_d=2.5e–4 m, h_0 = h_1=3.306e–3 m, a=3.556e–3 m, a_1=1.2e–3 m, H_0=500 Oe, M_0=5000 Ga and f=30.0 GHz)

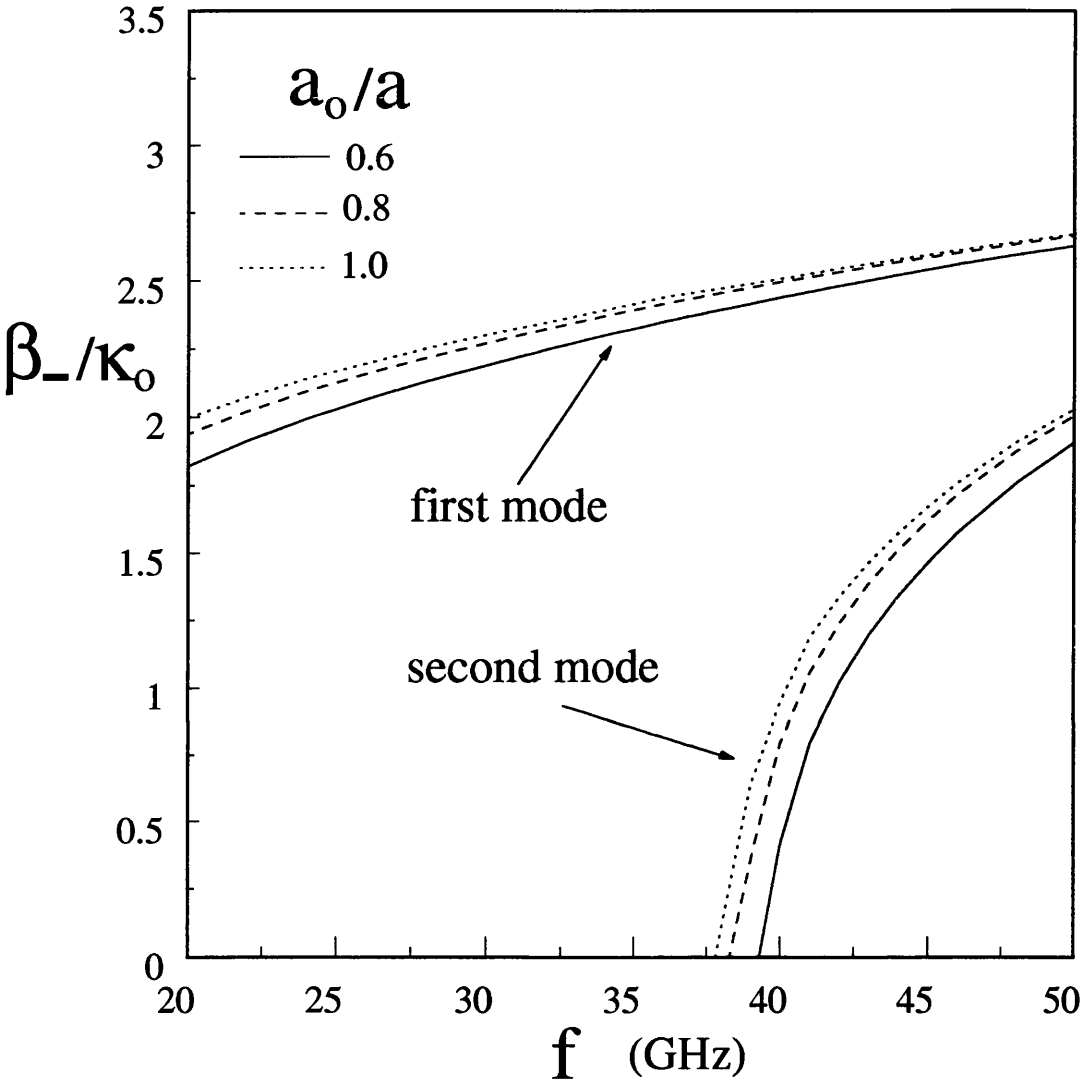

Figure 5.7: Normalized propagation constants of the backward waves of the dominant and first higher–order modes of the asymmetrical SWFD loaded finline as a function of frequency for various values of a_0/a ($\varepsilon_{rf} = \varepsilon_{rd}$=12.5, $h_f = h_d$=2.5e–4 m, $h_0 = h_1$=3.306e–3 m, a=3.556e–3 m, a_1=1.2e–3 m, H_0=500 Oe and M_0=5000 Ga)

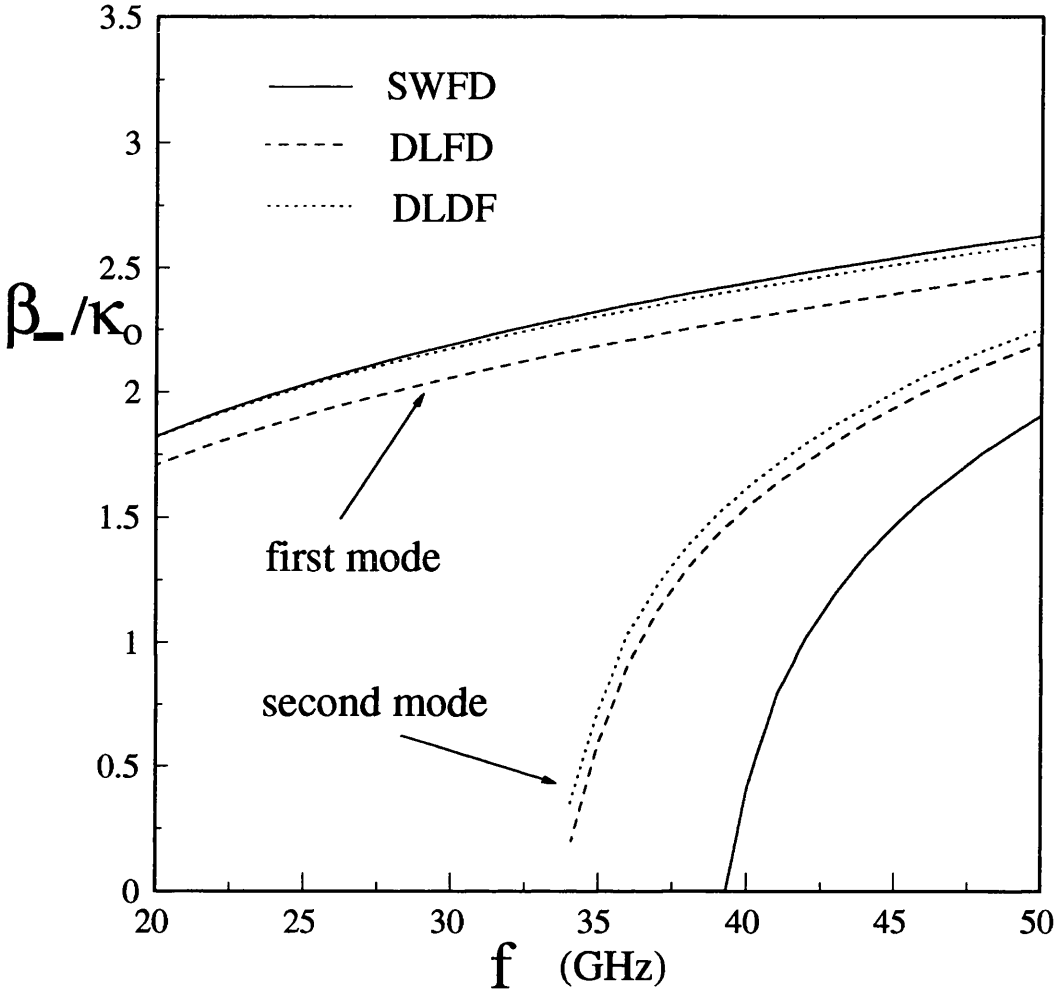

Figure 5.8: Normalized propagation constants of the backward waves of the dominant and first higher–order modes of asymmetrical SWFD, DLFD and DLDF loaded finlines as a function of frequency ($\varepsilon_{rf} = \varepsilon_{rd}$=12.5, $h_f = h_d$=2.5e–4 m, $h_0 = h_1$=3.306e–3 m, a_0=2.1336e–3 m, a=3.556e–3 m, a_1=1.2e–3 m, H_0=500 Oe and M_0=5000 Ga)

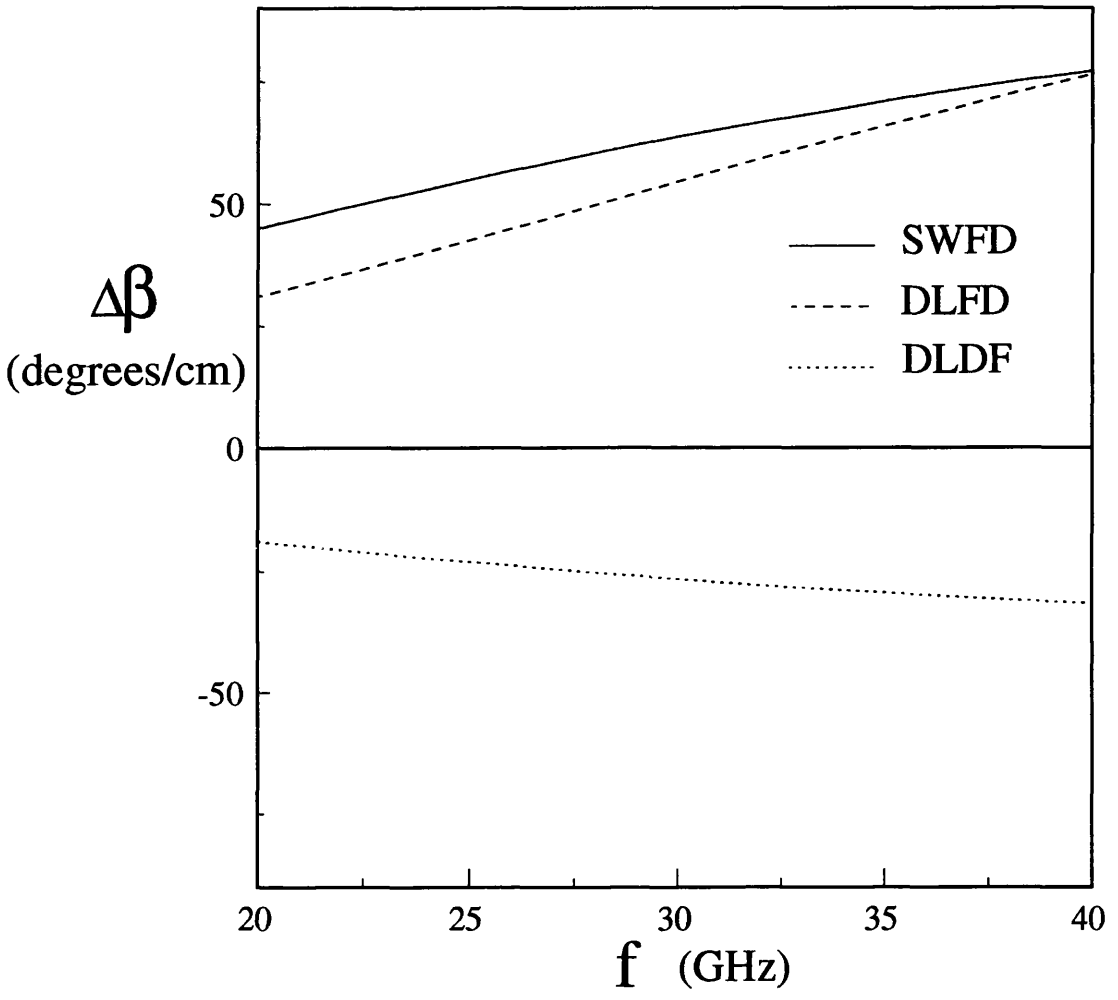

Figure 5.9: Differential phase shifts of the dominant mode of the asymmetrical SWFD, DLFD and DLDF loaded finlines as a function of frequency (ε_{rf} = ε_{rd}=12.5, h_f = h_d=2.5e–4 m, h_0 = h_1=3.306e–3 m, a_0=2.1336e–3 m, a=3.556e–3 m, a_1=1.2e–3 m, H_0=500 Oe and M_0=5000 Ga)

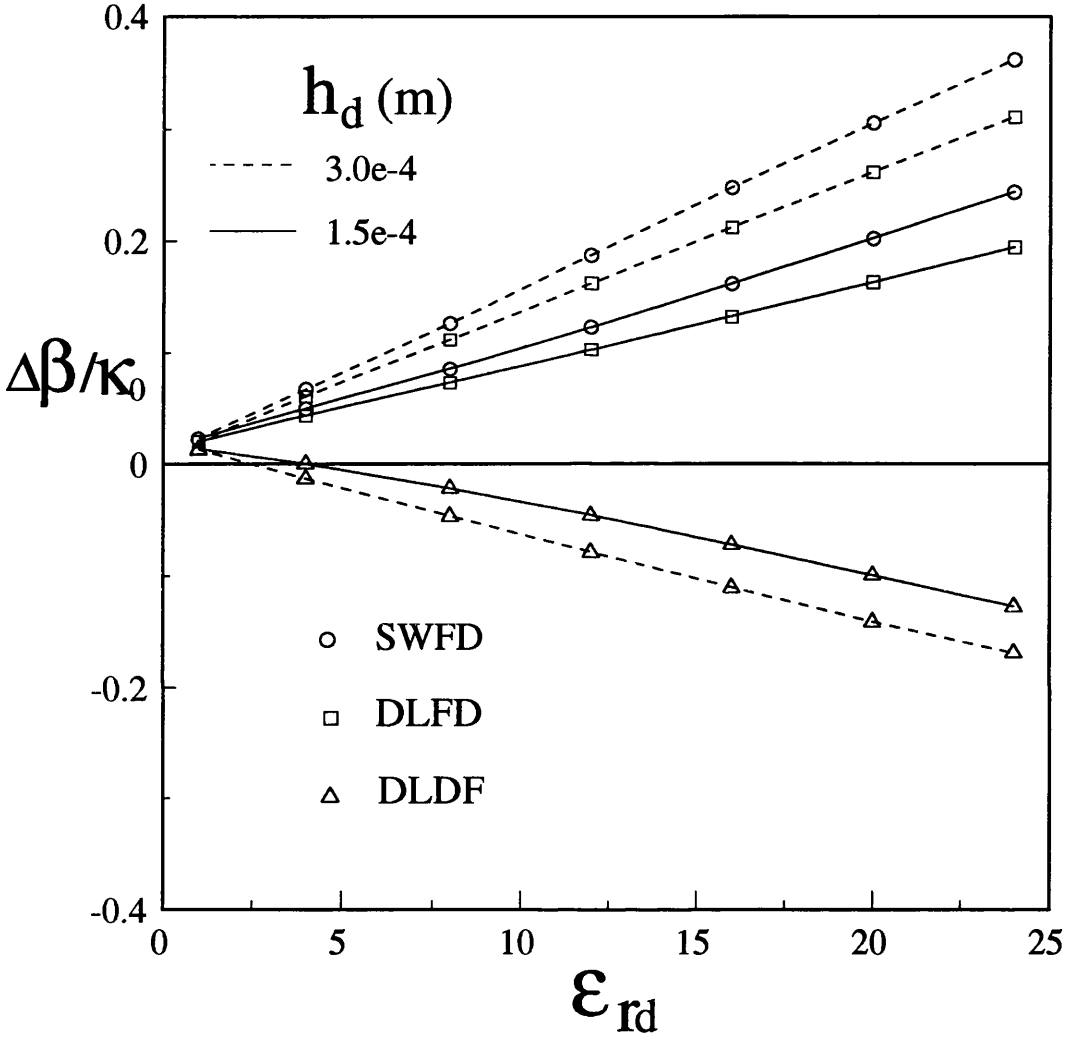

Figure 5.10: Normalized differential phase shifts of the dominant mode of the asymmetrical SWFD, DLFD and DLDF loaded finlines as a function of ε_{rd} for different values of h_d (ε_{rf}=12.5, h_f=2.5e–4 m, $h_f + h_0 = h_d + h_1$=3.556e–3 m, a_0=2.1336e–3 m, a=3.556e–3 m, a_1=1.2e–3 m, H_0=500 Oe, M_0=5000 Ga and f=30.0 GHz)

5.6.4 Dual Ferrite Case

As demonstrated in the previous subsection, the double–layer single–ferrite loaded structure can be used to achieve very high nonreciprocity by using a large value of relative permittivity of the dielectric layer. However, the bandwidth is significantly reduced as overmoding occurs at a lower frequency. The dual ferrite (DF) structure is studied in this subsection as a structure that may increase nonreciprocity without sacrificing the bandwidth. The structure is shown in Figure 5.11 and consists of metal fins sandwiched between two ferrites. These ferrites are magnetically saturated in opposite directions. Since the ellipticity of magnetic field is opposite in the two ferrites, nonreciprocity is expected to be much higher than that of the corresponding single–ferrite structure as two ferrites contribute the nonreciprocity.

Figure 5.12 shows the normalized differential phase shifts of the dominant mode of the DF structure and the SWFD one with $\varepsilon_{rd} = 19.0$ as a function of frequency. Figure 5.13 shows the normalized propagation constants of the backward wave of the first two modes of these two structures. It is clearly seen that both structures have about the same nonreciprocity for the frequency range shown in the figure, but the cut-off frequency of the first higher-order mode for the SWFD is lower by about 5 GHz than that for the DF, resulting in a narrower bandwidth for the SWFD. The bandwidth of the SWFD can be made wider by using smaller value of ε_{rd}. This however significantly reduces the nonreciprocity of this structure. This can be clearly seen from the results for the SWFD with $\varepsilon_{rd} = 12.5$, which are also included in Figures 5.12 and 5.13.

As discussed by Sharawy and Koza [18], in practice a dielectric layer has to be inserted between the two ferrites in the dual–ferrite slotline structure in order

to prevent magnetic leakage from one ferrite to the other. At the same time, the addition of this thin high–permittivity dielectric layer can greatly increase the nonreciprocity. For this reason, the modified dual–ferrite finline structure is analyzed, whose cross section is shown in Figure 5.14.

Figure 5.15 shows the normalized propagation constants of forward and backward waves of the dominant mode mode of this modified DF structure as a function of ε_{rd} for two different values of h_d. In this structure, the electromagnetic field is more concentrated near the slot (in the dielectric layer) for the forward wave than for the backward wave. As a result, the propagation constant of the forward wave increases more rapidly than that of the backward wave as ε_{rd} increases, yielding higher nonreciprocity. This is apparent in Figure 5.16, which shows differential phase shifts as a function of ε_{rd}.

Figure 5.17 shows normalized differential phase shifts of the dominant mode of the modified DF structure as a function of h_d for two different values of ε_{rd}. It is seen that the differential phase shift increases very rapidly with h_d when h_d is small. There is an optimum value of h_d for the maximum nonreciprocity. This value is quite small so that the bandwidth is not decreased much compared to the situation when $h_d = 0$.

Figure 5.18 shows the normalized differential phase shifts of the dominant mode of the modified DF structure as a function of a_1 the width of the aperture. From this figure, we find that when a_1 increases, nonreciprocity increases. Therefore, a relatively wide aperture can be chosen to realize a phase shifter with higher nonreciprocity.

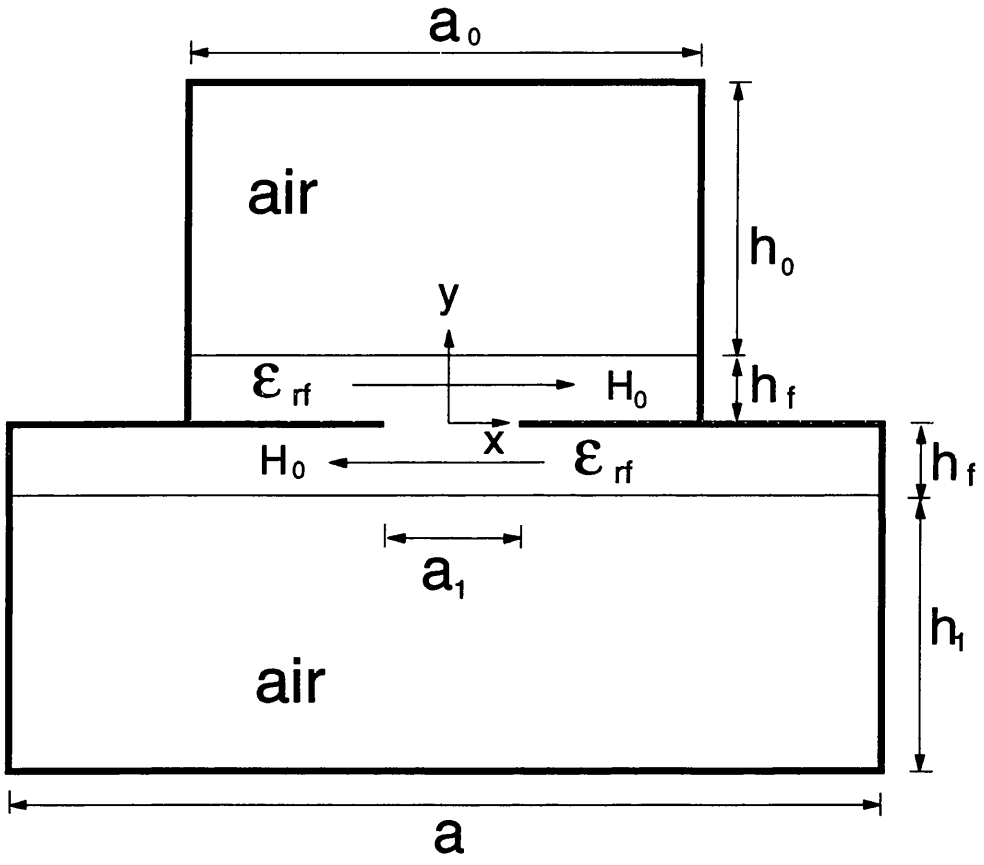

Figure 5.11: Cross section of an asymmetrical dual–ferrite (DF) loaded finline

air

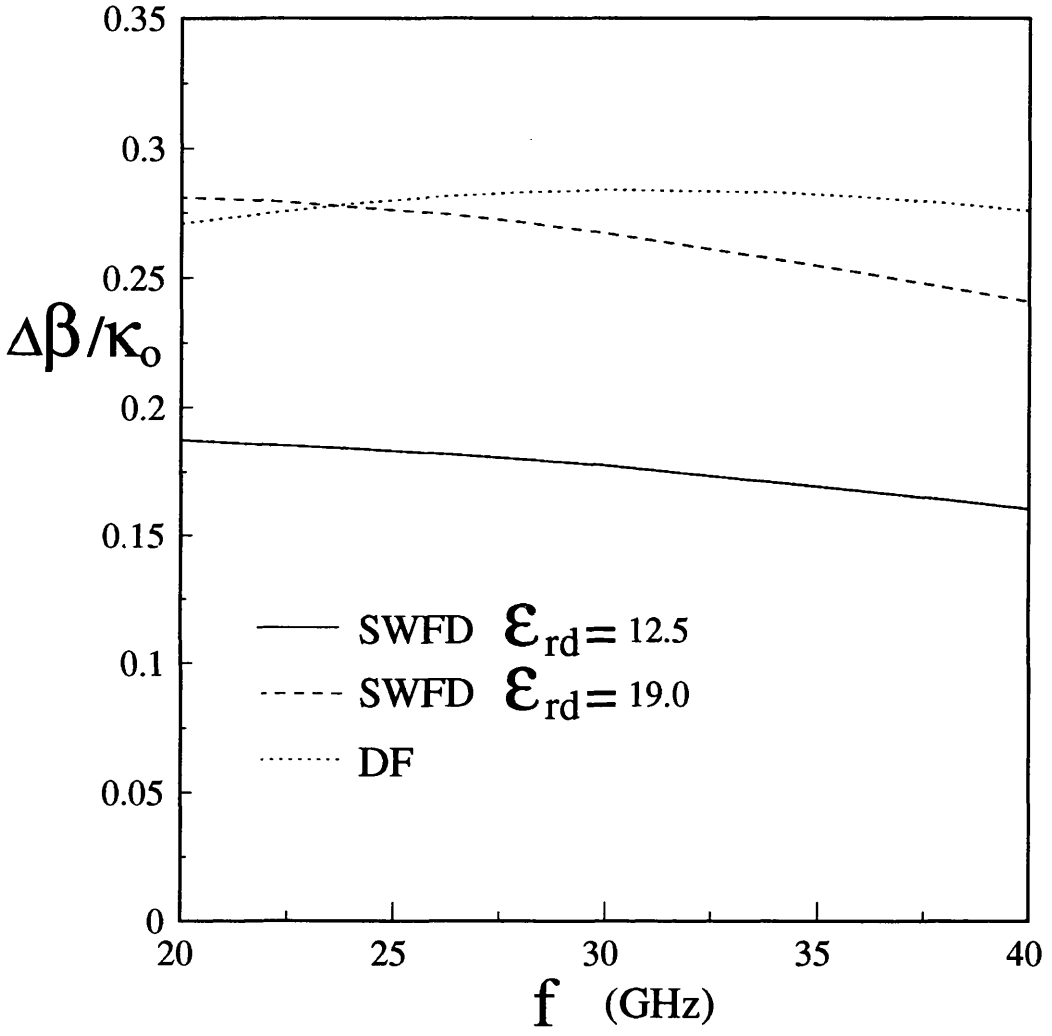

Figure 5.12: Normalized differential phase shifts of the dominant mode of the asymmetrical DF and SWFD loaded finlines as a function of frequency (ε_{rf}=12.5, $h_f = h_d$=2.5e–4 m, $h_0 = h_1$=3.306e–3 m, a_0=2.1336e–3 m, a=3.556e–3 m, a_1=1.2e–3 m, H_0=500 Oe and M_0=5000 Ga)

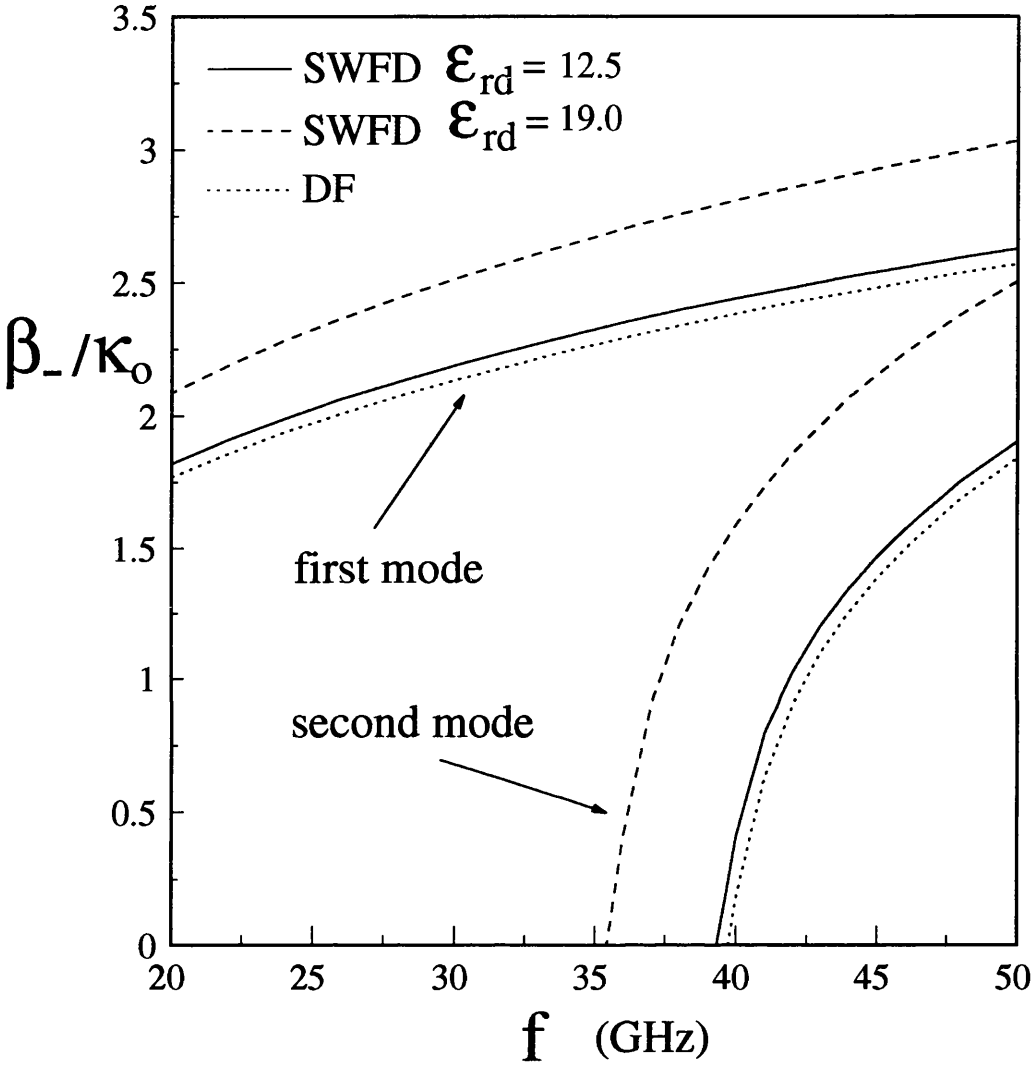

Figure 5.13: Normalized propagation constants of backward waves of the dominant and first higher-order modes of the asymmetrical DF and SWFD loaded finlines as a function of frequency (ε_{rf}=12.5, h_f = h_d=2.5e–4 m, h_0 = h_1=3.306e–3 m, a_0=2.1336e–3 m, a=3.556e–3 m, a_1=1.2e–3 m, H_0=500 Oe and M_0=5000 Ga)

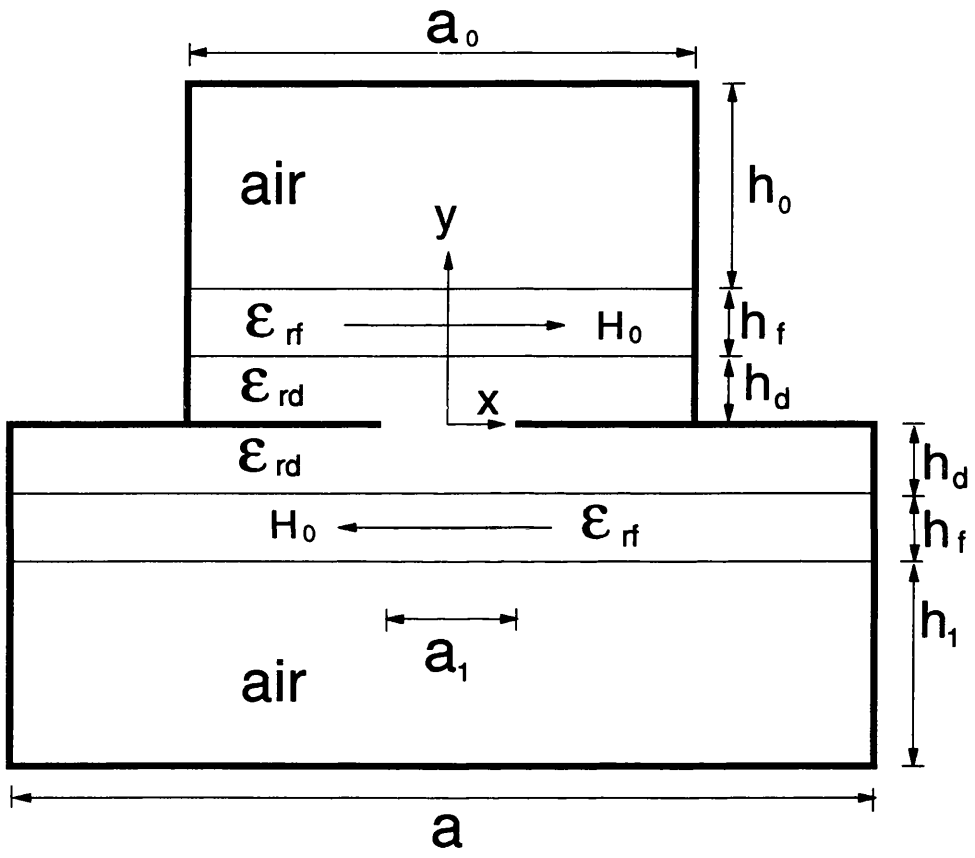

Figure 5.14: Cross section of a modified asymmetrical dual-ferrite (DF) loaded finline

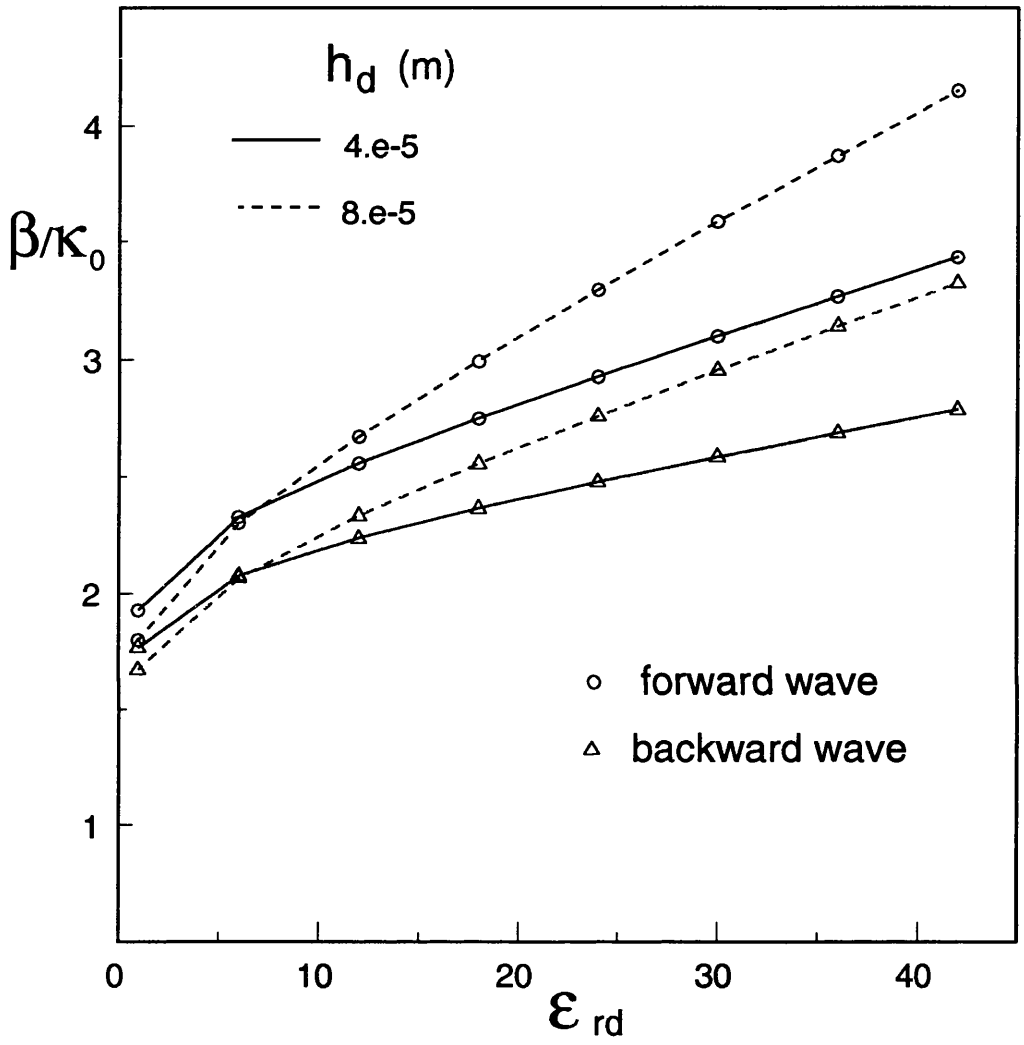

Figure 5.15: Normalized propagation constants of forward and backward waves of the dominant mode of the modified asymmetrical DF loaded finline as a function of ε_{rd} for different values of h_d (ε_{rf}=12.5, h_f=2.5e–4 m, $h_d+h_0 = h_d+h_1$=3.306e–3 m, a_0=2.1336e–3 m, a=3.556e–3 m, a_1=1.2e–3 m, H_0=500 Oe, M_0=5000 Ga and f=30.0 GHz)

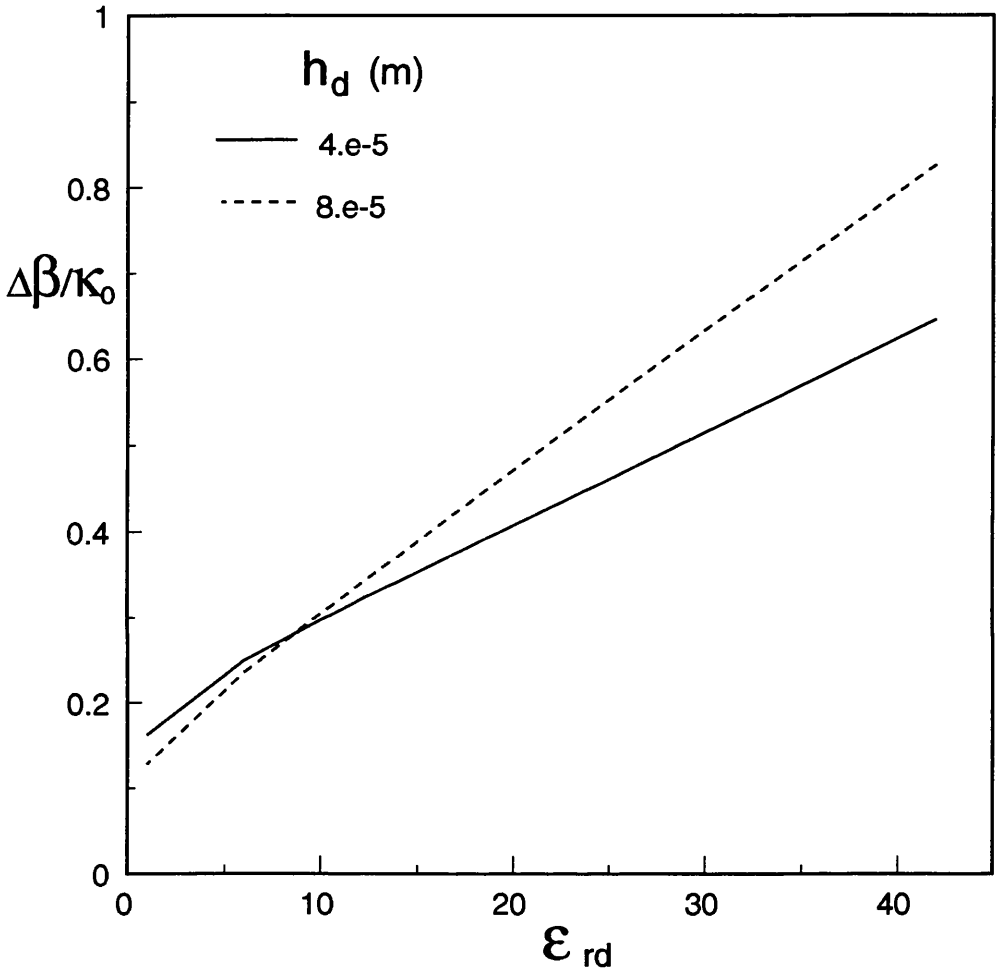

Figure 5.16: Normalized differential phase shifts of the dominant mode of the modified asymmetrical DF loaded finline as a function of ε_{rd} for different values of h_d (ε_{rf}=12.5, h_f=2.5e–4 m, $h_d + h_0 = h_d + h_1$=3.306e–3 m, a_0=2.1336e–3 m, a=3.556e–3 m, a_1=1.2e–3 m, H_0=500 Oe, M_0=5000 Ga and f=30.0 GHz)

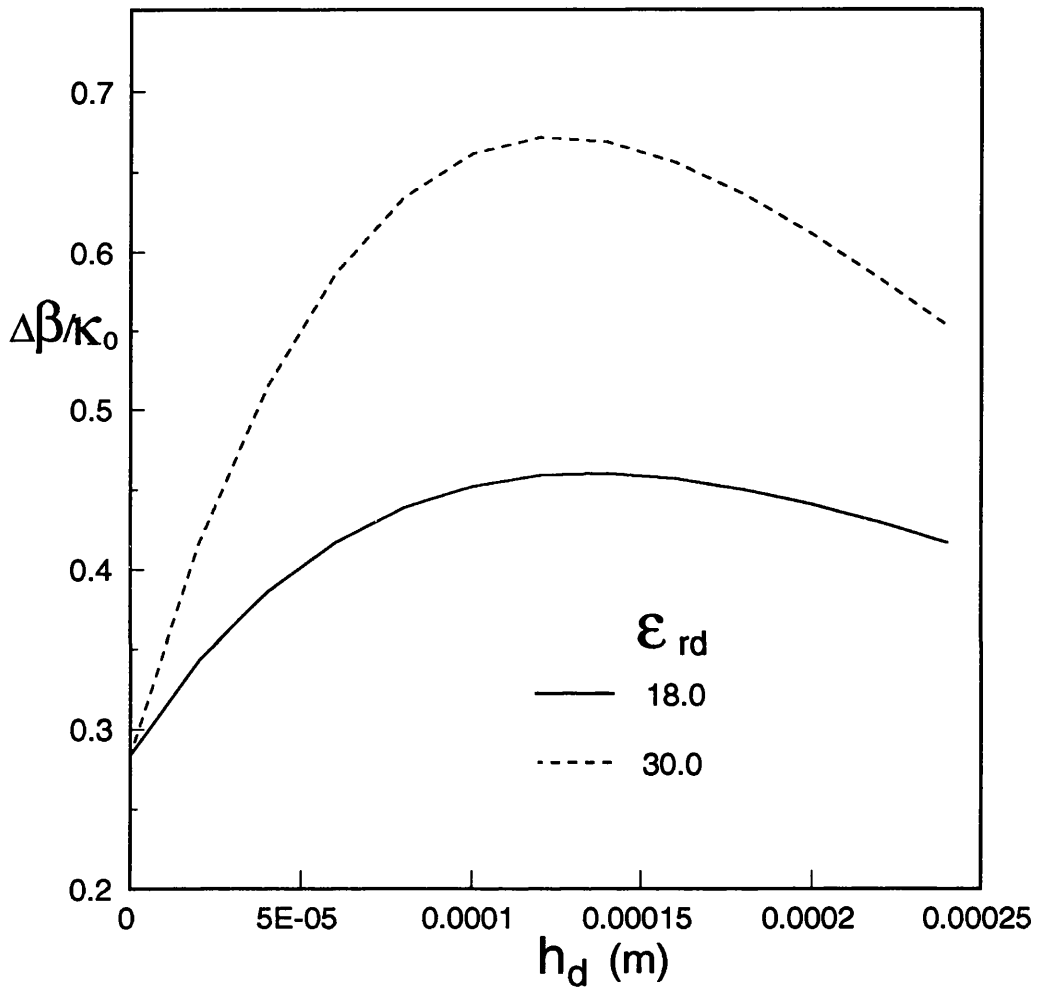

Figure 5.17: Normalized differential phase shifts of the dominant mode of the modified asymmetrical DF loaded finline as a function of h_d for different values of ε_{rd} (ε_{rf}=12.5, h_f=2.5e–4 m, $h_d + h_0 = h_d + h_1$=3.306e–3 m, a_0=2.1336e–3 m, a=3.556e–3 m, a_1=1.2e–3 m, H_0=500 Oe, M_0=5000 Ga and f=30.0 GHz)

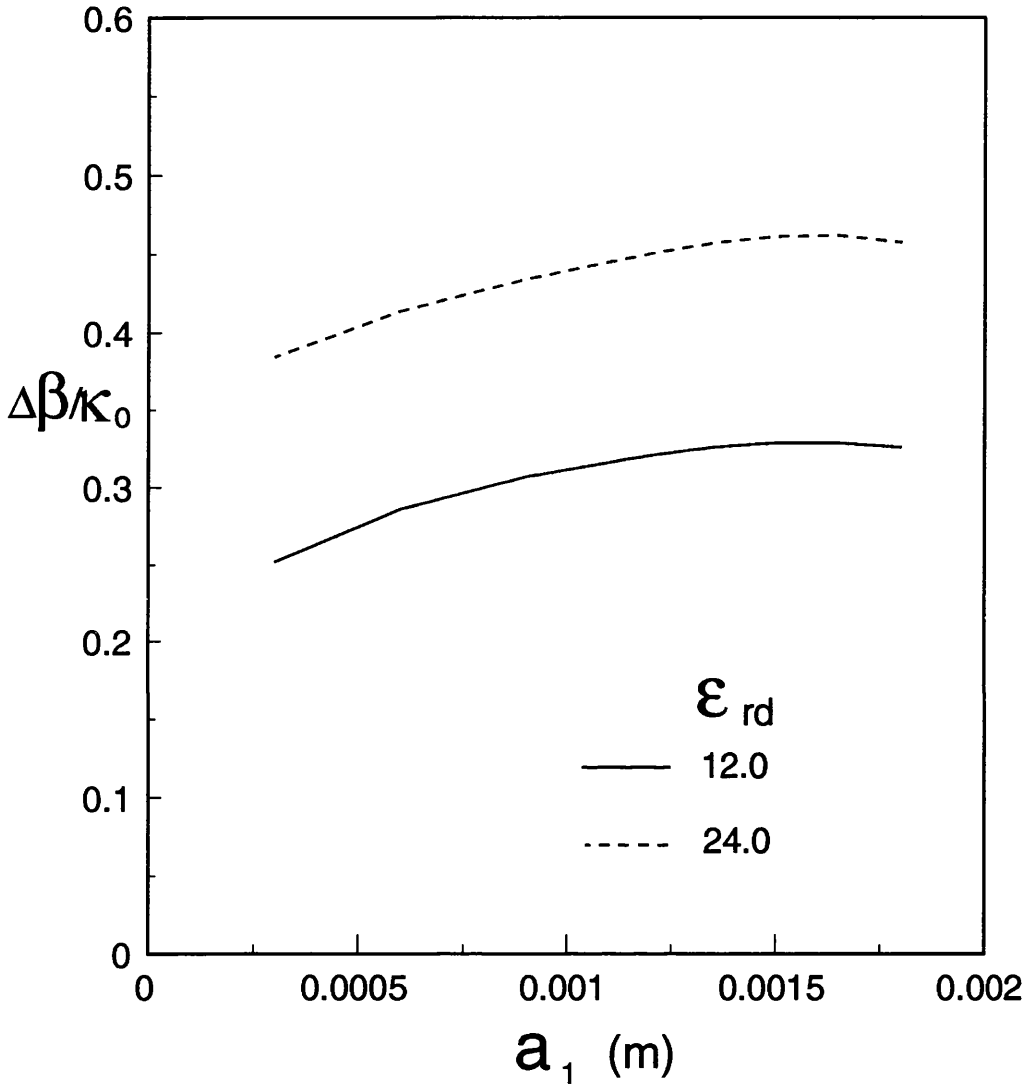

Figure 5.18: Normalized differential phase shifts of the dominant mode of the modified asymmetrical DF loaded finline as a function of a_1 for different values of ε_{rd} (ε_{rf}=12.5, h_f=2.5e–4 m, h_d=4.0e–5 m, $h_0 = h_1$=3.266e–3 m, a_0=2.1336e–3 m, a=3.556e–3 m, H_0=500 Oe, M_0=5000 Ga and f=30.0 GHz)

5.7 Ferrite Loaded Inset Dielectric Guide

The method described in the previous sections can be easily applied to analyze other planar structures containing magnetized ferrites if the boundary conditions for the field components on the interfaces are modified and suitable basis functions are chosen. In this section multilayer ferrite–loaded inset dielectric guide is analyzed and numerical results for nonreciprocal propagation characteristics are presented.

5.7.1 Analysis

The cross section of multilayer ferrite–loaded inset dielectric guide is shown in Figure 5.19. The Fourier–transformed Green's function for the groove region of this structure is identical to that in (5.31) for the lower region of the multilayer finline. On the other hand, the Fourier–transformed Green's function for the air region of this structure is the same as that in (2.38) for the air region of CPW loaded IDG. By employing the continuity conditions for the electric and magnetic fields at the $y = 0$ interface, we can obtain the same homogeneous matrix equation for the electric field expansion coefficients as (5.38). However, the elements of the coefficient matrix are different, and are given by

$$\begin{aligned} K_{im}(p,r) &= \frac{1}{2\pi}\int_{-\infty}^{\infty} \tilde{E}^b_{pi}(-\alpha)Y^a_{pr}(\alpha)\tilde{E}^b_{rm}(\alpha)d\alpha \\ &\quad + \frac{1}{a}\sum_{n=-\infty}^{\infty} \tilde{E}^b_{pi}(-\alpha_n)Y_{pr}(\alpha_n)\tilde{E}^b_{rm}(\alpha_n) \end{aligned} \tag{5.43}$$

with

$$\tilde{E}^b_{xm}(\alpha_n) = \int_{-\frac{a}{2}}^{\frac{a}{2}} E^b_{xm}(x)e^{j\alpha_n x}dx \tag{5.44}$$

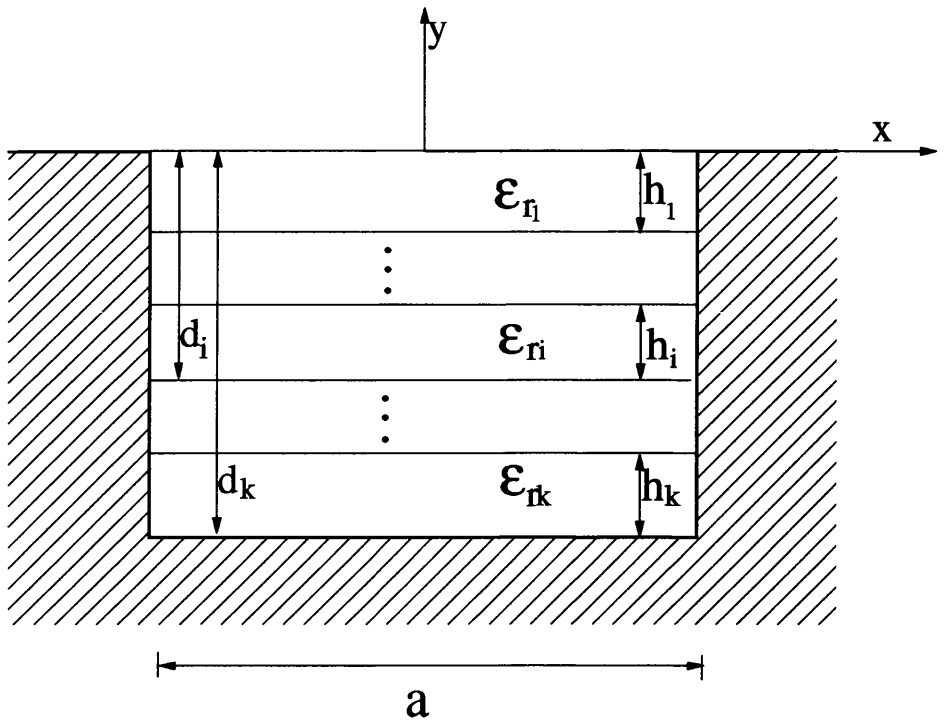

Figure 5.19: Cross section of a multilayer inset dielectric guide where any layer can be dielectric or ferrite; and coordinate system used in the analysis

$$\tilde{E}^b_{zm}(\alpha_n) = \frac{j}{\alpha_n}\int_{-\frac{a}{2}}^{-\frac{a}{2}} \frac{\partial E^b_{zm}(x)}{\partial x} e^{j\alpha_n x} dx \tag{5.45}$$

where the basis functions for the E_z even modes are chosen as

$$E^b_{xm}(x) = \frac{\partial E^b_{zm}(x)}{\partial x} = \left[1 - (\frac{2x}{a})^2\right]^{-\frac{1}{3}} C^{1/6}_{2m+1}(\frac{2x}{a}) \quad m = 0, 1, \cdots, N \tag{5.46}$$

In the above choice of basis functions, the singular conditions satisfied by the electric field components at the metal corners have been taken into account. $C^{1/6}$ are Gegenbauer polynomials. For the E_z odd modes, 2m+1 in the above equation is replaced by 2m. The first basis function is given with $m = 1$ instead of $m = 0$ for $\frac{\partial E^b_{zm}}{\partial x}(x)$ for the E_z odd modes.

5.7.2 Results

Numerical results are presented here for two–layer ferrite–loaded inset dielectric guide, whose cross section is shown in Figure 5.20.

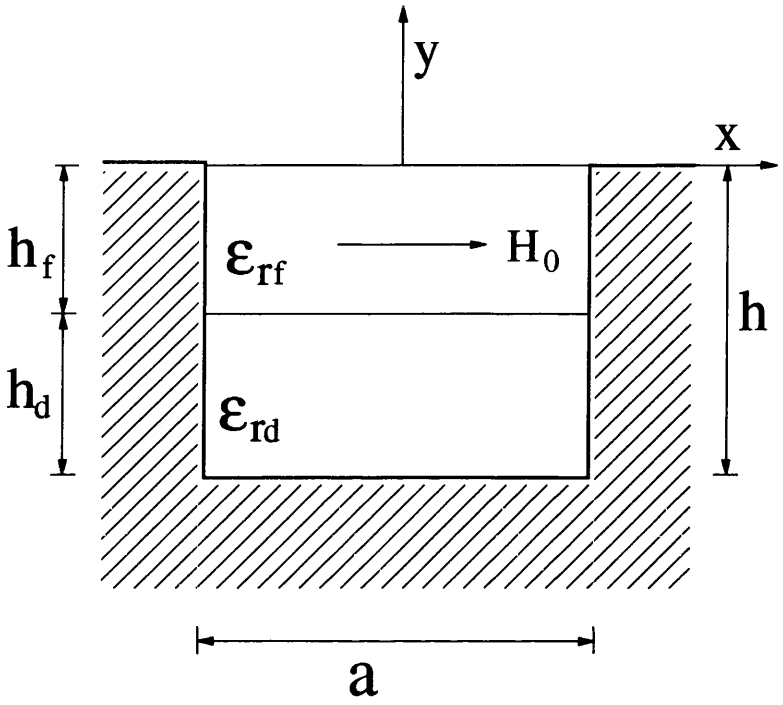

Figure 5.20: Cross section of a two–layer ferrite–loaded inset dielectric guide

Table 5.3 shows the convergence of solutions for β_+/κ_0, β_-/κ_0 and $(\beta_+ - \beta_-)/\kappa_0$ of the dominant mode with the number of the basis functions for the x and z electric field components at the $y = 0$ interface at 18 GHz. The solutions are found to converge with small values of N. In fact, convergence for β_+/κ_0 and β_-/κ_0 to four significant digits can be obtained by using $N = 2$ and convergence of $(\beta_+ - \beta_-)/\kappa_0$ to four significant digits can be achieved by using $N = 3$.

In order to assess the accuracy of our solutions, numerical results for the special case ($\kappa = 0, \mu_r = 1$) have been obtained and compared with the measured results reported by Hedges in [19]. Tables 5.4 and 5.5 show this comparison for two

N	β_+/k_0	β_-/k_0	$(\beta_+ - \beta_-)/k_0$
1	2.76557	2.59872	.16685
2	2.76532	2.59676	.16856
3	2.76529	2.59649	.16880
4	2.76528	2.59644	.16884
5	2.76528	2.59642	.16886

Table 5.3: Convergence of solutions for β_+/κ_0, β_-/κ_0 and $(\beta_+ - \beta_-)/\kappa_0$ of the dominant mode at the frequency of 18 GHz on the number of the basis functions ($\varepsilon_{rf} = 12.5$, H_0 =300 Oe, M_0 =3500 Ga, $\varepsilon_{rd} = 6.5$, h_f =1.778e–3 m, h_d =3.556e–3 m and a =3.556e–3 m)

different values of groove height. It is clearly seen that the agreement between theory and experiment is excellent. It should be noted that in this special case propagation constants are reciprocal, that is, $\beta = \beta_+ = \beta_-$.

Frequency (GHz)	β/κ_0	
	computed results	measured data [19]
6.51	1.127	1.132
7.01	1.153	1.157
7.51	1.176	1.180
7.99	1.195	1.201
8.48	1.212	1.218
8.98	1.228	1.233
9.47	1.241	1.246
9.96	1.253	1.259
10.46	1.265	1.270
10.96	1.275	1.279
11.45	1.284	1.289
11.94	1.292	1.297
12.44	1.300	1.305
12.93	1.307	1.312

Table 5.4: Comparison of the normalized propagation constants of the dominant mode of inset dielectric guide for the special case ($\kappa = 0, \mu_r = 1$) with measured data reported by Hedges in [20] ($\varepsilon_{rf} = \varepsilon_{rd} = 2.04$, a =1.016e–2 m and h =1.524e–2 m)

Frequency (GHz)	β/κ_0	
	computed results	measured data [19]
7.32	1.006	1.009
7.83	1.032	1.037
8.33	1.057	1.062
8.83	1.079	1.086
9.34	1.101	1.106
9.83	1.119	1.125
10.33	1.137	1.143
10.83	1.153	1.159
11.32	1.167	1.173
11.81	1.180	1.187
12.31	1.193	1.199
12.80	1.204	1.210

Table 5.5: Comparison of the normalized propagation constants of the dominant mode of inset dielectric guide for the special case ($\kappa = 0, \mu_r = 1$) with measured data reported by Hedges in [20] ($\varepsilon_{rf} = \varepsilon_{rd} = 2.04$, a =1.016e–2 m and h =1.016e–2 m)

Figure 5.21 shows the normalized propagation constants of the first and second E_z odd modes propagating in the positive z direction for various values of h_f/h_d. It can be seen from this figure that as h_f/h_d increases, the cut-off frequency of the first E_z odd mode increases, but the cut-off frequency of the second E_z odd mode decreases, resulting in the decrease in the single-mode bandwidth. Therefore, for the wide bandwidth, the value of h_f/h_d should be chosen to be small.

Figure 5.22 shows the normalized propagation constants of the dominant mode propagating in the positive and negative z directions for different values of ε_{rd}. It can be seen from this figure that

(a) β_+/κ_0 increases more quickly than β_-/κ_0 as ε_{rd} increases because of the difference of the field distribution between the forward and backward waves.

(b) β_+/κ_0 is smaller than β_-/κ_0 when ε_{rd} is small, but β_+/κ_0 is larger than β_-/κ_0 when ε_{rd} is large.

Figure 5.23 shows the normalized differential phase shifts of the dominant mode as a function of frequency for various values of ε_{rd}. It can be observed from the figure that

(a) when ε_{rd} is small, $|\beta_+ - \beta_-|/\kappa_0$ increases with the decrease in ε_{rd}.

(b) when ε_{rd} is large, $|\beta_+ - \beta_-|/\kappa_0$ increases with the increase in ε_{rd}.

(c) For some values of ε_{rd}, $(\beta_+ - \beta_-)/\kappa_0$ can be equal to zero at a specific frequency.

It is worth noting from Figure 5.23 that $(\beta_+ - \beta_-)/\kappa_0$ can be controlled over a wide range by changing ε_{rd}. Also, it can be clearly seen that very high nonreciprocity can be realized by using large values of ε_{rd}.

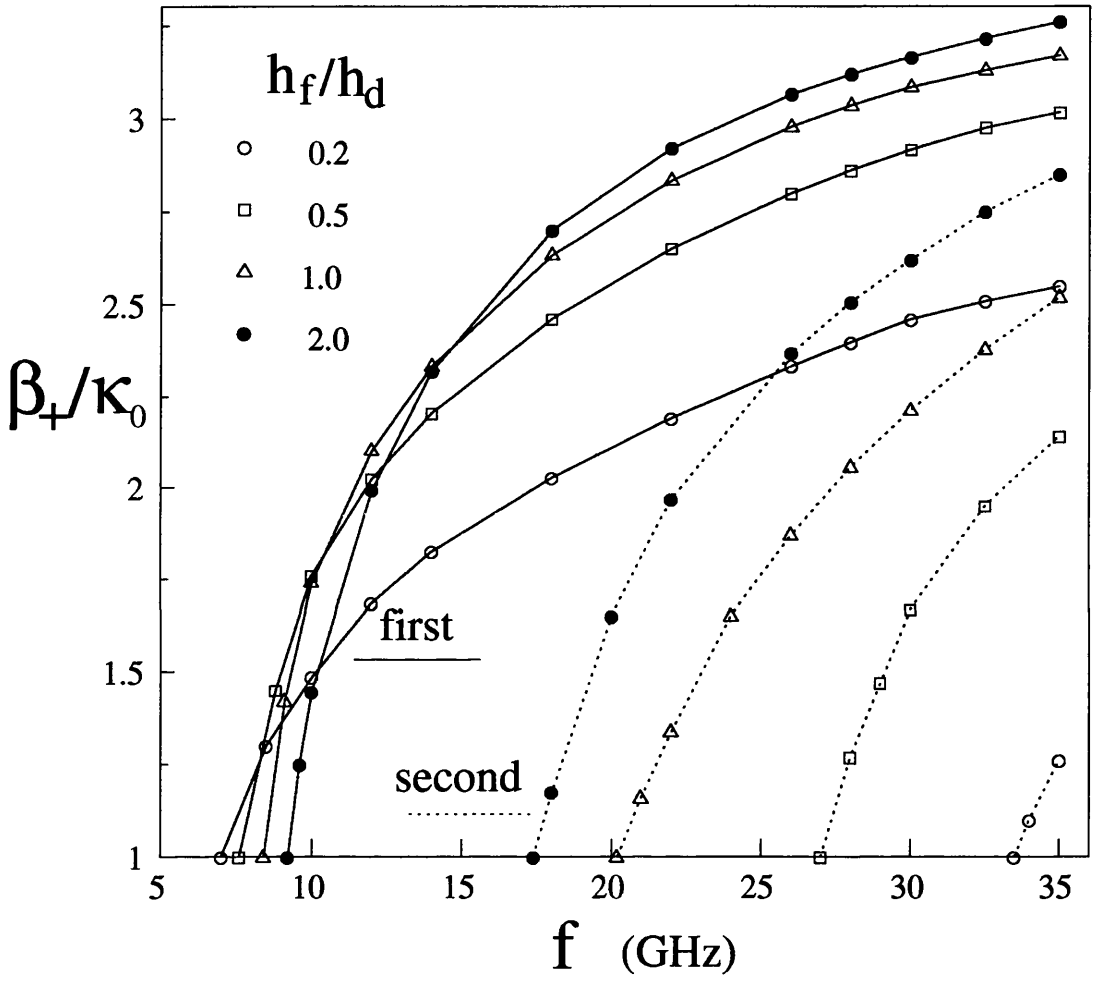

Figure 5.21: Normalized propagation constants of the first and second E_z odd modes propagating in positive z direction for various values of h_f/h_d ($\varepsilon_{rf} = 12.5$, H_0 =300 Oe, M_0 =3500 Ga, $\varepsilon_{rd} = 2.04$, h =5.334e–3 m and a =3.556e–3 m)

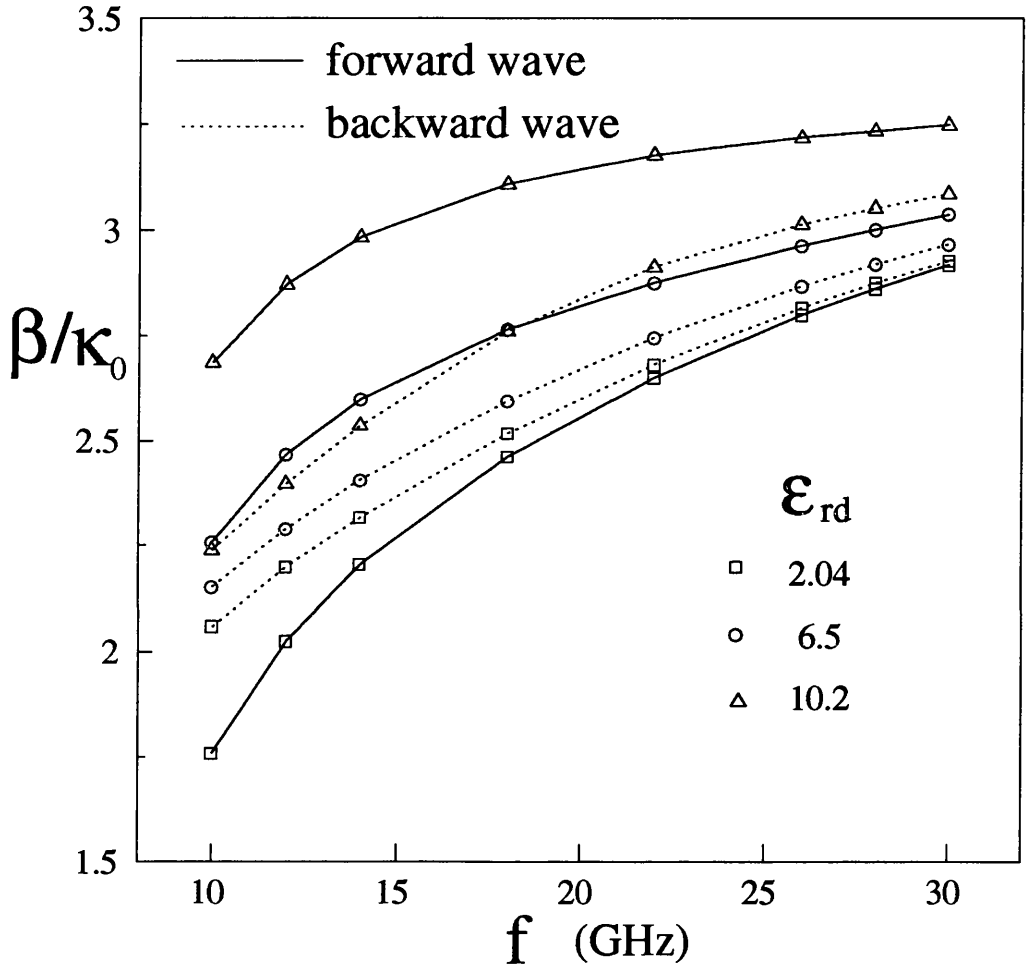

Figure 5.22: Normalized propagation constants of dominant mode propagating in positive and negative z directions for various values of ε_{rd} ($\varepsilon_{rf} = 12.5$, H_0 =300 Oe, M_0 =3500 Ga, h_f =1.778e–3 m, h_d =3.556e–3 m and a =3.556e–3 m)

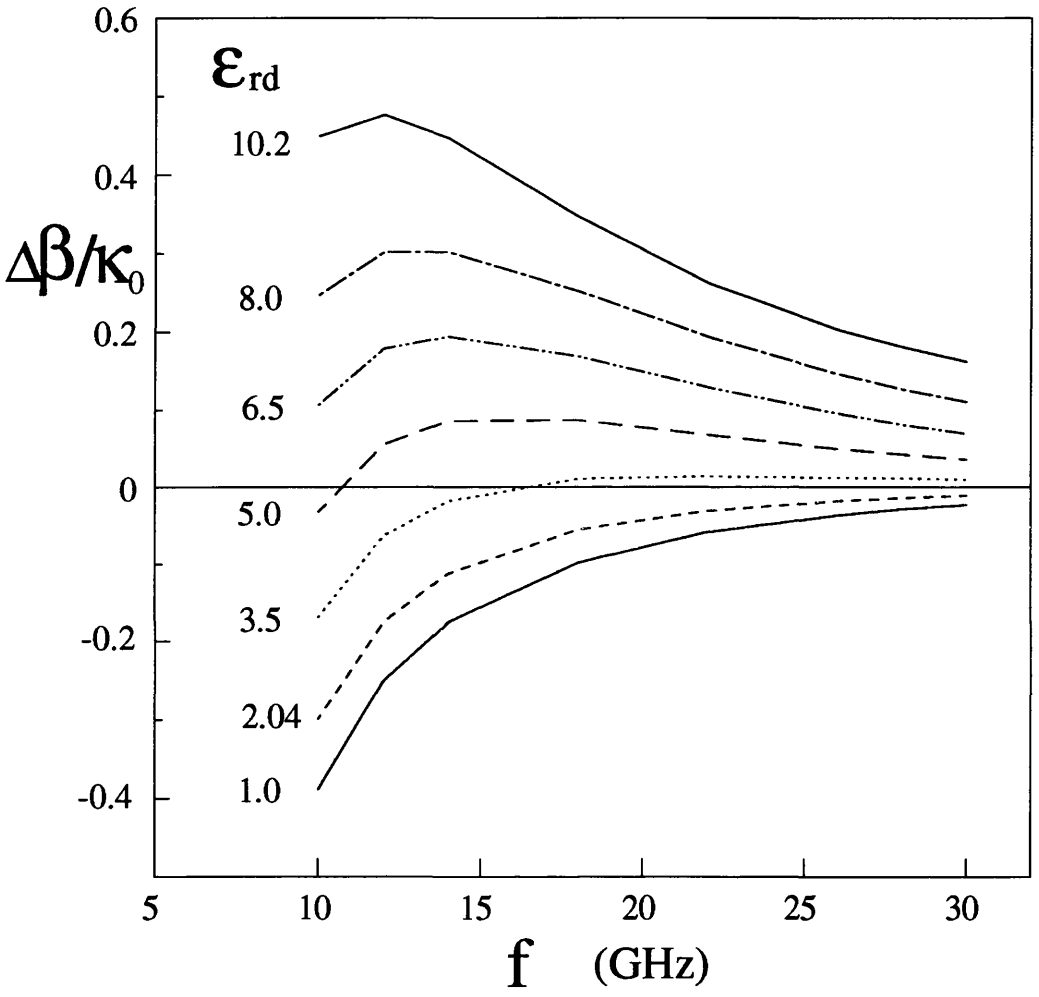

Figure 5.23: Normalized differential phase shifts of the dominant mode as a function of frequency for various values of ε_{rd} ($\varepsilon_{rf} = 12.5$, H_0 =300 Oe, M_0 =3500 Ga, h_f =1.778e–3 m, h_d =3.556e–3 m and a =3.556e–3 m)

5.8 Conclusion

An accurate analysis has been presented for the nonreciprocal propagation characteristics of asymmetrical multilayer finlines containing magnetized ferrites. The field in magnetized ferrites has been derived. A recursive algorithm has been introduced to derive the dyadic Green's function for multilayer anisotropic media.

It has been shown that compared with the conventional finlines, asymmetrical structures give higher nonreciprocity (except the double layer dielectric–ferrite one), wider bandwidth and an additional degree of freedom to obtain the propagation characteristics.

Computed results for the particular cases have been compared with calculated and measured data available in the literature, and good agreement has been found. Also, convergence of the solutions for nonreciprocal propagation constants has been shown to be very good.

Numerical results for various asymmetrical multilayer structures have been shown for various structural and material parameters. Among the two–layer configurations containing a single magnetized ferrite, the sandwich ferrite–dielectric one offers the highest nonreciprocity and the widest bandwidth. By increasing the relative permittivity of the dielectric layer, quite high nonreciprocity can be obtained with single–ferrite structures, however the bandwidth becomes narrower.

The dual ferrite structure was found to exhibit much higher nonreciprocity without sacrificing the bandwidth compared to the single ferrite structures. Further improvement in nonreciprocity can be achieved by adding thin dielectric layers between two dual ferrites. It has been found that there is an optimum value of

the thickness of the dielectric layers for maximum nonreciprocity and that the optimum value is quite small, resulting in a slight decrease in the bandwidth. Therefore, the four–layer dual–ferrite finline is very suitable for the applications to efficient nonreciprocal phase shifters.

The method has also been extended for the analysis of multilayer inset dielectric guide containing magnetized ferrites. Comparison with measured data for particular cases has shown good agreement. Numerical results for two–layer ferrite loaded IDG are presented for various values of the thickness of a ferrite and the permittivity of a dielectric.

It has been shown that for wide bandwidth the ratio of the thickness of the ferrite to that of the dielectric should be chosen to be small. It has also been found that the nonreciprocity in propagation constants can be controlled over a wide range by changing the relative permittivity of the dielectric layer. By using high values of the relative permittivity of the dielectric layer, very high nonreciprocity can be obtained.

References

[1] B. Lax and K. J. Button, "Microwave ferrites and ferrimagnetics", McGraw Hill Book Company Inc., pp.145-151, 1962

[2] Y. Chen and B. Beker, "Analysis of single and coupled microstrip lines on anisotropic substrates using differential matrix operators and the spectral domain method," *IEEE Trans. Microwave Theory Tech.*, vol.MTT–41, pp.123–128, January 1993.

[3] T. Itoh, "Spectral domain immitance approach for dispersion characteristics of generalized printed transmission lines," *IEEE Trans. Microwave Theory Tech.*, vol.MTT–28, pp.733–736, July 1980.

[4] C. H. Chan et al., "A mixed spectral–domain approach for dispersion analysis of suspended planar transmission lines with pedestals," *IEEE Trans. Microwave Theory Tech.*, vol.MTT-37, pp.1716–1723, Nov. 1989.

[5] C.M. Krowne, "Determination of the Green's function in the spectral domain using a matrix method: application to radiators or resonators immersed in a complex anisotropic layered medium," *IEEE Trans. Antennas Propagat.*, vol.AP–34, pp.247–253, Feb. 1986.

[6] F.L.Mesa, R.Marques and M. Horno, "A general algorithm for computing bidimensional spectral Green's dyad in multilayered complex bianisotropic media: the equivalent boundary method," *IEEE Trans. Microwave Theory Tech.*, vol.MTT-39, pp.1640–1649, Sept. 1991.

[7] R. E. Collin, "Field theory of guided waves", McGraw-Hill Book Company Inc., 1960.

[8] I. S. Gradshteyn and I. M. Ryshik, "Tables of integrals, series and products", Academic Press, 1965.

[9] T. Kitazawa, "Analysis of shielded striplines and finlines with finite metallization thickness containing magnetized ferrites" *IEEE Trans. Microwave Theory Tech.*, vol.MTT-39, pp.70–74, Jan. 1991.

[10] M. Geshiro and T. Itoh, "Analysis of double–layered finlines containing a magnetized ferrite," *IEEE Trans. Microwave Theory Tech.*, vol.MTT-35, pp.1377–1381, Dec. 1987.

[11] P. Espes et al., "Asymmetrical finline for space applications using millimeter waves," *IEEE Trans. Microwave Theory Tech.*, vol.MTT-37, pp.289–297, Feb. 1989.

[12] C.A. Olley, "The characterisation of unilateral finline by transverse resonance diffraction," *Ph.D thesis*, University of Bath, U.K., 1987

[13] Y. Hayashi and R. Mittra, "An analytical investigation of finlines with magnetized ferrite substrate," *IEEE Trans. Microwave Theory Tech.*, vol.MTT-31, pp.495–498, June 1983.

[14] G. Bock, "New multilayered slot line structures with high nonreciprocity," *Elec. Lett.*, vol.19, pp.966-968, Nov. 1983.

[15] G.P. Rodrigue, "A generation of microwave ferrite devices," *Proceedings of the IEEE*, vol.76, pp.121–137, February 1988.

[16] G.R. Harrison, G.H. Robinson, B.R. Savage and D.R. Taft, "Ferrimagnetic parts for microwave integrated circuits," *IEEE Trans. Microwave Theory Tech.*, vol.MTT–19, pp.577–588, July 1971.

[17] E.E. Sharawy and R.W. Jackson, "Analysis and design of microstrip–slot line for phase shifting applications," *IEEE Trans. Microwave Theory Tech.*, vol.MTT–38, pp.276–283, March 1990.

[18] E. El–Sharawy and C.J. Koza, "Dual–ferrite slot line for broadband, high–nonreciprocity phase shifters," *IEEE Trans. Microwave Theory Tech.*, vol.MTT–39, pp.2204–2210, Dec. 1991.

[19] S.J. Hedges, "The analysis of inset dielectric guide by transverse resonance diffraction," *Ph.D Thesis*, Bath University, Bath, 1987.

Chapter 6

CONCLUSION

This thesis has been concerned with the analysis of CPW loaded IDG, broadside coupled strip IDG, parallel coupled IDG, asymmetrical multilayer ferrite loaded finline and multilayer ferrite loaded IDG, and the demonstration of their applications to microwave and millimeter wave circuits. The purpose of this chapter is to draw conclusions from the work presented in this thesis and to suggest areas for further work.

6.1 Discussion of the Work Presented in this Thesis

In this section the advantages of the extended spectral domain method are first reviewed and then the main conclusions attained in chapters 2 – 5 are briefly reported.

The main features of the spectral domain method are the formulation of integral equations by using Fourier transforms and the derivation of the solution by means of Galerkin's method. This method is extended in this thesis for the analysis of

various planar waveguide structures. First, since different Fourier transforms are used in different regions, this method can be applicable to planar structures with non-uniform cross section geometries. Secondly, the recursive algorithm is obtained in terms of the 4 x 4 matrix relating tangential magnetic field components to tangential electric field components on two surfaces of a layer in order to derive the dyadic Green's function. As a result, computer program construction based on the recursive algorithm allows one to easily deal with structures having a few layers to hundreds of layers. Also, the recursive algorithm can be used to any anisotropic media provided that the 4 x 4 matrix for this case is obtained. Thirdly, in the formulation of problems, only one set of basis functions is needed for the calculation of the Fourier transforms of two tangential electric field or current components on one interface. This improves the convergence of the solutions and decreases the computational time. Finally the edge conditions have been taken into account in choosing the basis functions for all the cases. Consequently fast convergence is obtained, resulting in the good numerical efficiency. By comparison to experimental data, this extended method is shown to give very accurate results for propagation constants and characteristic impedances.

CPW loaded IDG was proposed in Chapter 2 as a planar transmission line with advantageous characteristics for millimeter-wave circuit applications. Advantages in terms of no use of air bridges for ground equalization, improvement of heat sinking, good confinement of fields, suppression of propagation of surface modes and reduction of electromagnetic interference have been pointed out. As many structural parameters can be chosen, a wide single-mode bandwidth and a wide range of impedance can be achieved, leading to great flexibility in circuit design. The dispersion in propagation constant and impedance has been found to be very small in the single-mode frequency range.

In chapter 3, broadside-coupled strip IDG was investigated. In particular the S parameters were calculated for a section of this guide using propagation constants and characteristic impedances of two fundamental modes. By suitable choice of thickness between the strips, high and low coupling value directional couplers can be designed. Return loss and directivity can be optimised by choice of the widths of strips. A simple procedure for the design of these couplers was given. The feasibility of directional couplers in the broadside coupled strip IDG configuration was demonstrated experimentally. This kind of coupler with transitions to coaxial cables was found to be easy to manufacture. The measured S parameters were easily obtained by a Network Analyzer and were in good agreement with the theoretical predictions.

Chapter 4 was devoted to the rigorous analysis of propagation constants of parallel coupled IDGs. The accurate determination of propagation constants is important for the design of this kind of coupled-line guide. By comparison with measured and approximate theoretical data available in the literature and examining limiting cases, the results obtained by the extended spectral domain method were found to be accurate. It was interesting to note that the propagation constants of the dominant even and odd modes split, but do not shift symmetrically from the corresponding value of the single IDG. Further, their difference is increased with increasing guide separation, leading to a higher coupling coefficients. It has also been found that there exists an optimum value of the slot height in order to obtain a flat coupling characteristic. With the choice of this value, the IDG coupler showed quite broadband flat coupling characteristic. Therefore, these parallel coupled IDGs are suitable for the application to broadband couplers.

The nonreciprocal propagation characteristics of asymmetrical multilayer finlines containing magnetized ferrites were analyzed in Chapter 5. Compared with the

symmetrical ones, the asymmetrical structures are found to offer an additional degree of freedom in design, wider bandwidth and higher nonreciprocity. The effects of various multilayer configurations on differential phase shift and bandwidth were investigated, and it has been shown that among the structures studied, the four-layer dual ferrite structure is the best choice for the realization of the efficient nonreciprocal phase shifters due to its highest nonreciprocity and widest bandwidth. There exists an optimum value of the thickness of the dielectric layers for maximum nonreciprocity of the structure. It has been found that the optimum value is quite small, therefore the bandwidth is not sacrificed.

With the aim of studying the possibility of realizing the efficient nonreciprocal ferrite devices in IDG , the nonreciprocal propagation characteristics of two–layer ferrite–dielectric IDG were also calculated. It has been shown that for wide bandwidth a thin ferrite should be chosen. It has also been found that with the suitable choice of the permittivity of the dielectric layer, a wide range of differential phase shifts can be achieved. Very high nonreciprocity can be also obtained by using the high value of the permittivity of the dielectric layer.

6.2 Further Work

The work presented in this thesis can be usefully continued in following ways.

1. The development of CPW loaded IDG circuit components

   The CPW loaded IDG has been found to offer attractive advantages for the use in the MMICs. For practical applications, various circuit components such as couplers and filters need to be developed and designed. The development of such new components can improve the performance of microwave

and millimeter–wave systems.

2. Extension of the developed approach to discontinuities

   For the successful design of circuits using CPW loaded IDG, the accurate characterization of discontinuities such as gap, step and T junctions is required.

3. Application of broadside coupled strip IDG to antennas

   Broadside coupled strip IDG can be used to build up a new useful leaky wave antennas. The antennas can be easily fed by microwave coaxial cables and microstrips. The appropriate technique for calculating the radiation losses from the upper strips and deriving equivalent circuit parameters will be useful for the design of the antennas with a desirable radiation pattern and low return loss.

4. Analysis of multiple coupled IDGs without and with conducting strips

   In the design of integrated circuits, coupling between various components need to be taken into account. It is necessary and important to extend the developed approach to analyze symmetrical and nonsymmetrical multiple coupled IDGs without and with conducting strips.

5. Extension of the analysis to include the ferrite loss

   The loss of a ferrite is omitted in this thesis. Ferrite loss can be taken into account by replacing γH_0 in (5.2) and (5.3) by $\gamma H_0 + j\frac{\gamma \Delta H}{2}$ where ΔH is ferrite line width. In this case the scheme for seeking the complex roots is needed. A knowledge of nonreciprocal loss characteristics is important for the analysis and design of such nonreciprocal circuit components as resonant isolators.

Appendix A

Derivation of Wave Equations in Magnetized Ferrites

Two matrix equations (5.4) and (5.5) are rewritten as

$$j\beta\tilde{E}_y + \frac{\partial\tilde{E}_z}{\partial y} = -j\omega\mu_0\tilde{H}_x \tag{A.1}$$

$$-j\beta\tilde{E}_x + j\alpha_n\tilde{E}_z = -j\omega\mu_0(\mu_r\tilde{H}_y - j\kappa\tilde{H}_z) \tag{A.2}$$

$$-\frac{\partial\tilde{E}_x}{\partial y} - j\alpha_n\tilde{E}_y = -j\omega\mu_0(j\kappa\tilde{H}_y + \mu_r\tilde{H}_z) \tag{A.3}$$

$$j\beta\tilde{H}_y + \frac{\partial\tilde{H}_z}{\partial y} = j\omega\varepsilon_0\varepsilon_{ri}\tilde{E}_x \tag{A.4}$$

$$-j\beta\tilde{H}_x + j\alpha_n\tilde{H}_z = j\omega\varepsilon_0\varepsilon_{ri}\tilde{E}_y \tag{A.5}$$

$$-\frac{\partial\tilde{H}_x}{\partial y} - j\alpha_n\tilde{H}_y = j\omega\varepsilon_0\varepsilon_{ri}\tilde{E}_z \tag{A.6}$$

From (A.2), we obtain

$$\tilde{H}_y = \frac{-j\beta\tilde{E}_x + j\alpha_n\tilde{E}_z}{-j\omega\mu_0\mu_r} + \frac{j\kappa\tilde{H}_z}{\mu_r} \tag{A.7}$$

From (A.5), we obtain

$$\tilde{E}_y = \frac{-j\beta\tilde{H}_x + j\alpha_n\tilde{H}_z}{j\omega\varepsilon_0\varepsilon_{ri}} \tag{A.8}$$

Substituting (A.7) and (A.8) into (A.3) and (A.6), we have

$$(\alpha_n^2 + \kappa_i^2\frac{\kappa^2}{\mu_r} - \kappa_i^2\mu_r]\tilde{H}_z + \frac{j\omega\varepsilon_0\varepsilon_{ri}\kappa\alpha_n}{\mu_r}\tilde{E}_z =$$
$$\alpha_n\beta\tilde{H}_x + j\omega\varepsilon_0\varepsilon_{ri}\frac{\partial\tilde{E}_x}{\partial y} + \frac{j\omega\varepsilon_0\varepsilon_{ri}\kappa\beta}{\mu_r}\tilde{E}_x \tag{A.9}$$

$$\frac{j\omega\mu_0\kappa\alpha_n}{\mu_r}\tilde{H}_z - (\frac{\alpha_n^2}{\mu_r} - \kappa_i^2)\tilde{E}_z = j\omega\mu_0\frac{\partial\tilde{H}_x}{\partial y} - \frac{\alpha_n\beta}{\mu_r}\tilde{E}_x \tag{A.10}$$

Multiplying (A.9) by $(\frac{\alpha_n^2}{\mu_r} - \kappa_i^2)$ and multiplying (A.10) by $j\omega\varepsilon_0\varepsilon_{ri}\kappa\alpha_n/\mu_r$ and adding yields

$$[(\alpha_n^2 - \kappa_i^2\mu_r)^2 - (\kappa_i^2\kappa)^2]\tilde{H}_z =$$
$$\alpha_n\beta(\alpha_n^2 - \kappa_i^2\mu_r)\tilde{H}_x - \kappa_i^2\kappa\alpha_n\frac{\partial\tilde{H}_x}{\partial y}$$
$$-j\omega\varepsilon_0\varepsilon_{ri}\kappa\beta\kappa_i^2\tilde{E}_x + j\omega\varepsilon_0\varepsilon_{ri}(\alpha_n^2 - \kappa_i^2\mu_r)\frac{\partial\tilde{E}_x}{\partial y} \tag{A.11}$$

Similarly eliminating $\tilde{H}_z$ from (A.9) and (A.10), we obtain

$$[(\alpha_n^2 - \kappa_i^2\mu_r)^2 - (\kappa_i^2\kappa)^2]\tilde{E}_z =$$
$$j\omega\mu_0\kappa\alpha_n^2\beta\tilde{H}_x - j\omega\mu_0[\mu_r(\alpha_n^2 - \kappa_i^2\mu_r) + \kappa_i^2\kappa^2]\frac{\partial\tilde{H}_x}{\partial y}$$
$$+\alpha_n\beta(\alpha_n^2 - \kappa_i^2\mu_r)\tilde{E}_x - \kappa_i^2\kappa\alpha_n\frac{\partial\tilde{E}_x}{\partial y} \tag{A.12}$$

Substituting (A.7) and (A.8) into (A.4) and (A.1), respectively, we have

$$(\beta^2 - \kappa_i^2\mu_r)\tilde{E}_x - \alpha_n\beta\tilde{E}_z + j\omega\mu_0\beta\kappa\tilde{H}_z - j\omega\mu_0\mu_r\frac{\partial\tilde{H}_z}{\partial y} = 0 \tag{A.13}$$

$$(\beta^2 - \kappa_i^2)\tilde{H}_x - \alpha_n\beta\tilde{H}_z + j\omega\varepsilon_0\varepsilon_{ri}\frac{\partial\tilde{E}_z}{\partial y} = 0 \tag{A.14}$$

Substituting (A.11) and (A.12) into (A.13) and (A.14) and carrying out some algebraic manipulation, we obtain two coupled equations for $\tilde{H}_x$ and $\tilde{E}_x$

$$\frac{\partial^2 \tilde{H}_x}{\partial y^2} - \gamma_h^2 \tilde{H}_x = \eta_h \tilde{E}_x \tag{A.15}$$

$$\frac{\partial^2 \tilde{E}_x}{\partial y^2} - \gamma_e^2 \tilde{E}_x = \eta_e \tilde{H}_x \tag{A.16}$$

where

$$\gamma_h^2 = \frac{\alpha_n^2}{\mu_r} + \beta^2 - \kappa_i^2, \quad \gamma_e^2 = \alpha_n^2 + \beta^2 - \kappa_i^2 \mu_e \tag{A.17}$$

$$\eta_h = j\omega\varepsilon_0\varepsilon_{ri}\kappa\alpha_n/\mu_r, \quad \eta_e = -j\omega\mu_0\kappa\alpha_n/\mu_r \tag{A.18}$$

$$\mu_e = \mu_r - \kappa^2/\mu_r, \quad \kappa_i^2 = \omega^2\mu_0\varepsilon_0\varepsilon_{ri} \tag{A.19}$$

Appendix B

Determination of Submatrices $[P_i]$, $[R_i]$, $[S_i]$ and $[T_i]$

1. $[P_i]$ and $[R_i]$

For the ferrite layer:

$$[P_i] = [N_P][W]_2^{-1} \tag{B.1}$$

$$[R_i] = [N_R][W]_2^{-1} \tag{B.2}$$

where $[W]_2^{-1}$ is a 4 x 2 matrix consisting of the last two columns of the inverse of the following matrix $[W]$.

$$[W] = \begin{bmatrix} 0 & 1 & 0 & ZB \\ a_{21} & a_{22} & a_{23}B & a_{24}B \\ T_+ & 1 & ZT_- & Z \\ a_{41} & a_{42} & a_{43} & a_{44} \end{bmatrix} \tag{B.3}$$

$$[N_P] = \begin{bmatrix} a_{31} & a_{32} & a_{33} & a_{34} \\ -YT_+ & -Y & -T_- & -1 \end{bmatrix} \tag{B.4}$$

$$[N_R] = \frac{1}{P_+} \begin{bmatrix} a_{11} & a_{12} & a_{13}B & a_{14}B \\ 0 & -Y & 0 & -B \end{bmatrix} \tag{B.5}$$

with

$$a_{11} = C_2\gamma_+ Y + C_4\gamma_+; \quad a_{12} = C_1 Y + C_3$$

$$a_{13} = C_2\gamma_- + C_4\gamma_- Z; \quad a_{14} = C_1 + C_3 Z$$

$$a_{21} = C_6\gamma_+ Y + C_2\gamma_+; \quad a_{22} = C_5 Y + C_1$$

$$a_{23} = C_6\gamma_- + C_2\gamma_- Z; \quad a_{24} = C_5 + C_1 Z$$

$$a_{31} = C_1 Y T_+ + C_2\gamma_+ Y + C_3 T_+ + C_4\gamma_+$$

$$a_{32} = C_1 Y + C_2\gamma_+ Y T_+ + C_3 + C_4\gamma_+ T_+$$

$$a_{33} = C_1 T_- + C_2\gamma_- + C_3 Z T_- + C_4\gamma_- Z$$

$$a_{34} = C_1 + C_2\gamma_- T_- + C_3 Z + C_4\gamma_- Z T_-$$

$$a_{41} = C_5 Y T_+ + C_6\gamma_+ Y + C_1 T_+ + C_2\gamma_+$$

$$a_{42} = C_5 Y + C_6\gamma_+ Y T_+ + C_1 + C_2\gamma_+ T_+$$

$$a_{43} = C_5 T_- + C_6\gamma_- + C_1 Z T_- + C_2\gamma_- Z$$

$$a_{44} = C_5 + C_6\gamma_- T_- + C_1 Z + C_2\gamma_- Z T_-$$

$$C_0 = (\alpha_n^2 - \kappa_i^2\mu_r)^2 - (\kappa_i^2\kappa)^2$$

$$C_1 = \alpha_n\beta(\alpha_n^2 - \kappa_i^2\mu_r)/C_0$$

$$C_2 = -\kappa_i^2\kappa\alpha_n/C_0$$

$$C_3 = -j\omega\varepsilon_0\varepsilon_{ri}\kappa\beta\kappa_i^2/C_0$$

$$C_4 = j\omega\varepsilon_0\varepsilon_{ri}(\alpha_n^2 - \kappa_i^2\mu_r)/C_0$$

$$C_5 = j\omega\mu_0\kappa\beta\alpha_n^2/C_0$$

$C_6 = -j\omega\mu_0[\mu_r(\alpha_n^2 - \kappa_i^2\mu_r) + \kappa_i^2\kappa^2]/C_0$

$B = P_+/\cosh\gamma_- h_i, \;\; P_+ = \cosh\gamma_+ h_i$

$T_+ = \tanh\gamma_+ h_i, \;\; T_- = \tanh\gamma_- h_i$

$Z = \eta_e/(\gamma_-^2 - \gamma_e^2)$

$Y = \eta_h/(\gamma_+^2 - \gamma_h^2)$

$\gamma_\pm^2 = 0.5(\gamma_h^2 + \gamma_e^2 \pm \sqrt{(\gamma_h^2 - \gamma_e^2)^2 + 4\eta_h\eta_e})$

For the dielectric layer:

$$[P_i] = \frac{1}{\alpha_n^2 + \beta^2}\begin{bmatrix} \beta^2 G_1 - \alpha_n^2 G_2 & -\alpha_n\beta(G_1 + G_2) \\ -\alpha_n\beta(G_1 + G_2) & \alpha_n^2 G_1 - \beta^2 G_2 \end{bmatrix} \tag{B.6}$$

$$[R_i] = \frac{1}{\alpha_n^2 + \beta^2}\begin{bmatrix} \beta^2 G_3 - \alpha_n^2 G_4 & -\alpha_n\beta(G_3 + G_4) \\ -\alpha_n\beta(G_3 + G_4) & \alpha_n^2 G_3 - \beta^2 G_4 \end{bmatrix} \tag{B.7}$$

where

$G_1 = -jr_i/(\omega\mu_0 \tanh r_i h_i), \;\; G_3 = G_1/\cosh r_i h_i$

$G_2 = -j\omega\varepsilon_0\varepsilon_{ri}/(r_i \tanh r_i h_i). \;\; G_4 = G_2/\cosh r_i h_r$

$r_i^2 = \alpha_n^2 + \beta^2 - \kappa_0^2\varepsilon_{ri}, \;\; \kappa_0^2 = \omega^2\mu_0\varepsilon_0$

2. $[S_i]$ and $[T_i]$

$[S_i]$ and $[T_i]$ can be easily obtained from the expressions of $[R_i]$ and $[P_i]$ by replacing h_i by -h_i, respectively.

Appendix C

Calculations of Fourier Transforms of Basis Functions

1. Fourier transforms of basis functions in (5.42)

For the E_z even modes

$$F_1^e = \int_{-\frac{a_1}{2}}^{\frac{a_1}{2}} \left[1 - (\frac{2x}{a_1})^2\right]^{-\frac{1}{2}} \; T_{2m+1}(\frac{2x}{a_1}) \; e^{j\alpha_n x} \; dx \tag{C.1}$$

Substituting $x = \frac{a_1}{2}t$ into (C.1) gives:

$$F_1^e = j \; a_1 \int_0^1 \left(1 - t^2\right)^{-\frac{1}{2}} \; T_{2m+1}(t) \; \sin(\frac{\alpha_n a_1}{2} t) \; dt \tag{C.2}$$

From the mathematical tables [1]:

$$\int_0^1 \left(1 - t^2\right)^{-\frac{1}{2}} \; T_{2m+1}(t) \; \sin(bt) \; dt = (-1)^m \; \frac{\pi}{2} \; J_{2m+1}(b) \tag{C.3}$$

where J_{2m+1} is the Bessel function of order $2m + 1$.

By comparing (C.2) with (C.3), b is found to equal $\frac{\alpha_n a_1}{2}$ and so:

$$F_1^e = (-1)^m \; \frac{j\pi a_1}{2} \; J_{2m+1}(\frac{\alpha_n a_1}{2}) \tag{C.4}$$

Similarly, for the E_z odd modes

$$F_1^o = \int_{-\frac{a_1}{2}}^{\frac{a_1}{2}} \left[1-(\frac{2x}{a_1})^2\right]^{-\frac{1}{2}} T_{2m}(\frac{2x}{a_1})\ e^{j\alpha_n x}\ dx$$
$$= (-1)^m \frac{\pi a_1}{2}\ J_{2m}(\frac{\alpha_n a_1}{2}) \qquad \text{(C.5)}$$

2. Fourier transforms of basis functions in (5.46)

For the E_z even modes

$$F_2^e = \int_{-\frac{a}{2}}^{\frac{a}{2}} \left[1-(\frac{2x}{a})^2\right]^{-\frac{1}{3}} C_{2m+1}^{1/6}(\frac{2x}{a})\ e^{j\alpha_n x}\ dx \qquad \text{(C.6)}$$

Putting $x = \frac{a}{2}t$ into (C.6) gives:

$$F_2^e = j\ a \int_0^1 \left(1-t^2\right)^{-\frac{1}{3}} C_{2m+1}^{1/6}(t)\ \sin(\frac{\alpha_n a}{2}t)\ dt \qquad \text{(C.7)}$$

From the mathematical tables [1]:

$$\int_0^1 \left(1-t^2\right)^{v-\frac{1}{2}} C_{2m+1}^{v}(t)\ \sin(bt)\ dt$$
$$= (-1)^m\ \pi\ \frac{\Gamma(2m+1+2v)\ J_{2m+1+v}(b)}{(2m+1)!\ \Gamma(v)\ (2b)^v} \qquad \text{(C.8)}$$

where Γ is the Gamma function.

By comparing (C.7) with (C.8), b and v are found to equal $\frac{\alpha_n a}{2}$ and $\frac{1}{6}$ respectively, and so:

$$F_2^e = (-1)^m\ j\pi a\ \frac{\Gamma(2m+1+1/3)\ J_{2m+1+1/6}(\frac{\alpha_n a}{2})}{(2m+1)!\ \Gamma(1/6)\ (\alpha_n a)^{1/6}} \qquad \text{(C.9)}$$

Similarly, for the E_z odd modes

$$\begin{aligned} F_2^o &= \int_{-\frac{a}{2}}^{\frac{a}{2}} \left[1-(\frac{2x}{a})^2\right]^{-\frac{1}{3}} \; C_{2m}^{1/6}(\frac{2x}{a}) \; e^{j\alpha_n x} \; dx \\ &= (-1)^m \; \pi a \frac{\Gamma(2m+1/3) \; J_{2m+1/6}(\frac{\alpha_n a}{2})}{(2m)! \; \Gamma(1/6) \; (\alpha_n a)^{1/6}} \end{aligned} \tag{C.10}$$

3. Fourier transforms of basis functions in (2.63)

For the E_z odd modes

$$F_3^o = (\int_{-\frac{w_1}{2}-s_1}^{-\frac{w_1}{2}} + \int_{\frac{w_1}{2}}^{\frac{w_1}{2}+s_1}) \; \left(1-x'^2\right)^{-\frac{1}{2}} \; T_m(x') \; e^{j\alpha_n x} \; dx \tag{C.11}$$

where

$$x' = \frac{2\,(|x|-x_0)}{s_1}, \qquad x_0 = \frac{w_1+s_1}{2} \tag{C.12}$$

Considering the even parity of the basis functions and substituting $t = \frac{2\,(x-x_0)}{s_1}$ into (C.11), we have

$$F_3^o = s_1 \int_{-1}^{1} \left(1-t^2\right)^{-\frac{1}{2}} \; T_m(t) \; \cos\alpha_n(\frac{s_1}{2}t + x_0) \; dt \tag{C.13}$$

By using trigonometric formula, the above equation becomes

$$\begin{aligned} F_3^o &= s_1 \; [\; \cos(\alpha_n x_0) \int_{-1}^{1} \left(1-t^2\right)^{-\frac{1}{2}} \; T_m(t) \; \cos\frac{\alpha_n s_1}{2}t \; dt \\ &\quad - \sin(\alpha_n x_0) \int_{-1}^{1} \left(1-t^2\right)^{-\frac{1}{2}} \; T_m(t) \; \sin\frac{\alpha_n s_1}{2}t \; dt] \end{aligned} \tag{C.14}$$

where the sine and cosine transforms are evaluated as follows

$$\int_{-1}^{1} \left(1-t^2\right)^{-\frac{1}{2}} \; T_m(t) \; \cos\frac{\alpha_n s_1}{2}t \; dt$$

$$= \begin{cases} 2\int_0^1 (1-t^2)^{-\frac{1}{2}} \; T_m(t) \; \cos\frac{\alpha_n s_1}{2} t \; dt & \text{for } m = 2k \\ 0 & \text{for } m = 2k+1 \end{cases}$$

$$= \begin{cases} (-1)^k \; \pi \; J_{2k}(\frac{\alpha_n s_1}{2}) & \text{for } m = 2k \\ 0 & \text{for } m = 2k+1 \end{cases} \qquad \text{(C.15)}$$

$$\int_{-1}^{1} \left(1-t^2\right)^{-\frac{1}{2}} \; T_m(t) \; \sin\frac{\alpha_n s_1}{2} t \; dt$$

$$= \begin{cases} 2\int_0^1 (1-t^2)^{-\frac{1}{2}} \; T_m(t) \; \sin\frac{\alpha_n s_1}{2} t \; dt & \text{for } m = 2k+1 \\ 0 & \text{for } m = 2k \end{cases}$$

$$= \begin{cases} (-1)^k \; \pi \; J_{2k+1}(\frac{\alpha_n s_1}{2}) & \text{for } m = 2k+1 \\ 0 & \text{for } m = 2k \end{cases} \qquad \text{(C.16)}$$

In the above derivation, the even and odd parity of Chebychev polynomials is taken into account, and (C.3) and the following formula from the tables [1] are used

$$\int_0^1 \left(1-t^2\right)^{-\frac{1}{2}} \; T_{2k}(t) \; \cos(bt) \; dt = (-1)^k \frac{\pi}{2} \; J_{2k}(b) \qquad \text{(C.17)}$$

In the same way, for the E_z even modes

$$\begin{aligned} F_3^e \; &= \; -\int_{-\frac{w_1}{2}-s_1}^{-\frac{w_1}{2}} \left(1-x'^2\right)^{-\frac{1}{2}} \; T_m(x') \; e^{j\alpha_n x} \; dx \\ &\quad + \int_{\frac{w_1}{2}}^{\frac{w_1}{2}+s_1} \left(1-x'^2\right)^{-\frac{1}{2}} \; T_m(x') \; e^{j\alpha_n x} \; dx \\ &= \; j \; s_1 \; [\; \sin(\alpha_n x_0) \; \int_{-1}^{1} \left(1-t^2\right)^{-\frac{1}{2}} \; T_m(t) \; \cos\frac{\alpha_n s_1}{2} t \; dt \\ &\quad + \; \cos(\alpha_n x_0) \; \int_{-1}^{1} \left(1-t^2\right)^{-\frac{1}{2}} \; T_m(t) \; \sin\frac{\alpha_n s_1}{2} t \; dt] \end{aligned} \qquad \text{(C.18)}$$

4. Fourier transforms of basis functions in (3.19)

For the E_z odd modes

$$F_4^o = \left(\int_{-\frac{a}{2}}^{-\frac{w_1}{2}} + \int_{\frac{w_1}{2}}^{\frac{a}{2}}\right) \; (1-x')^{-\frac{1}{3}} (1+x')^{-\frac{1}{2}} \; P_m^{(-\frac{1}{3},-\frac{1}{2})}(x') \; e^{j\alpha_n x} \; dx \qquad \text{(C.19)}$$

$$x' = \frac{2(|x| - x_0)}{w_s} \tag{C.20}$$

$$x_0 = \frac{a + w_1}{4} \quad w_s = \frac{a - w_1}{2} \tag{C.21}$$

Considering the even parity of the basis functions and substituting $t = 2(x - x_0)/s_1$ into (C.19), we have

$$F_4^o = w_s \int_{-1}^{1} (1-t)^{-\frac{1}{3}}(1+t)^{-\frac{1}{2}} \; P_m^{(-\frac{1}{3},-\frac{1}{2})}(t) \; \cos\alpha_n(\frac{w_s}{2}t + x_0) \; dt \tag{C.22}$$

By using trigonometric formula, the above equation becomes

$$\begin{aligned} F_4^o \;=\; & w_s \; [\; \cos(\alpha_n x_0) \int_{-1}^{1} (1-t)^{-\frac{1}{3}}(1+t)^{-\frac{1}{2}} \; P_m^{(-\frac{1}{3},-\frac{1}{2})}(t) \; \cos\frac{\alpha_n w_s}{2}t \; dt \\ & - \sin(\alpha_n x_0) \int_{-1}^{1} (1-t)^{-\frac{1}{3}}(1+t)^{-\frac{1}{2}} \; P_m^{(-\frac{1}{3},-\frac{1}{2})}(t) \; \sin\frac{\alpha_n w_s}{2}t \; dt] \end{aligned} \tag{C.23}$$

where the sine and cosine transforms are evaluated as follows. From the mathematical tables [2]:

$$\begin{aligned} Q(u,v,m,b) \;=\; & \int_{-1}^{1}(1-t)^u(1+t)^v \; P_m^{(u,v)}(t) \; e^{-jbt} \; dt \\ =\; & (-1)^m \; j^m \; 2^{m+u+v+1} \; b^m \; (m!)^{-1} \; B(m+u+1, m+v+1) \\ & e^{jb} \; {}_1F_1(m+u+1, 2m+u+v+2, -2jb) \end{aligned} \tag{C.24}$$

where $B(x,y)$ is the Beta function defined by [1]

$$B(x,y) = \frac{\Gamma(x)\Gamma(y)}{\Gamma(x+y)} \tag{C.25}$$

and ${}_1F_1(a,b,z)$ is Kummer's confluent hypergeometric function. The explicit expression for it can found in [3] as series of alternating terms

$${}_1F_1(a,b,z) = \sum_{n=0}^{\infty} \frac{(a)_n}{(b)_n} \frac{z^n}{n!} \tag{C.26}$$

with

$$(a)_n = a(a+1)(a+2)\ldots(a+n-1), \qquad (a)_0 = 1 \tag{C.27}$$

The series in (C.26) converges rapidly for small values of z. For greater values of z the previous series becomes numerically unmanageable so that it is necessary to take asymptotic expansion of the Kummer's function [3] for $|z| > 10$

$$\begin{aligned} \frac{{}_1F_1(a,b,z)}{\Gamma(b)} &= \frac{e^{\pm j\pi a}\ z^{-a}}{\Gamma(b-a)} \sum_{n=0}^{R-1} \frac{(a)_n\ (1+a-b)_n}{n!}\ (-z)^{-n} \\ &\quad + \frac{e^z\ z^{a-b}}{\Gamma(a)} \sum_{n=0}^{S-1} \frac{(b-a)_n\ (1-a)_n}{n!}\ z^{-n} \end{aligned} \tag{C.28}$$

where the upper sign is taken if $-\frac{\pi}{2} < \arg(z) < \frac{3\pi}{2}$ and the lower sign is taken if $-\frac{3\pi}{2} < \arg(z) < -\frac{\pi}{2}$.

Substituting $u = -\frac{1}{3}$, $v = -\frac{1}{2}$ and $b = -\frac{\alpha_n w_s}{2}$ into (C.24), we can obtain the sine and cosine transforms in (C.23)

$$\begin{aligned} &\int_{-1}^{1} (1-t)^{-\frac{1}{3}}(1+t)^{-\frac{1}{2}}\ P_m^{(-\frac{1}{3},-\frac{1}{2})}(t)\ \cos\frac{\alpha_n w_s}{2}t \\ &\qquad = \text{Re}\ [Q(-\frac{1}{3},-\frac{1}{2},m,-\frac{\alpha_n w_s}{2})] \end{aligned} \tag{C.29}$$

$$\begin{aligned} &\int_{-1}^{1} (1-t)^{-\frac{1}{3}}(1+t)^{-\frac{1}{2}}\ P_m^{(-\frac{1}{3},-\frac{1}{2})}(t)\ \sin\frac{\alpha_n w_s}{2}t \\ &\qquad = \text{Im}\ [Q(-\frac{1}{3},-\frac{1}{2},m,-\frac{\alpha_n w_s}{2})] \end{aligned} \tag{C.30}$$

Therefore, (C.23) can be rewritten as

$$\begin{aligned} F_4^o &= w_s \left[\cos(\alpha_n x_0) \text{ Re } [Q(-\frac{1}{3}, -\frac{1}{2}, m, -\frac{\alpha_n w_s}{2})] \right. \\ &\quad \left. - \sin(\alpha_n x_0) \text{ Im } [Q(-\frac{1}{3}, -\frac{1}{2}, m, -\frac{\alpha_n w_s}{2})] \right. \end{aligned} \tag{C.31}$$

In the same way, for the E_z even modes

$$\begin{aligned} F_4^e &= -\int_{-\frac{a}{2}}^{-\frac{w_1}{2}} (1-x')^{-\frac{1}{3}}(1+x')^{-\frac{1}{2}} \; P_m^{(-\frac{1}{3},-\frac{1}{2})}(x') \; e^{j\alpha_n x} \; dx \\ &\quad + \int_{\frac{w_1}{2}}^{\frac{a}{2}} (1-x')^{-\frac{1}{3}}(1+x')^{-\frac{1}{2}} \; P_m^{(-\frac{1}{3},-\frac{1}{2})}(x') \; e^{j\alpha_n x} \; dx \\ &= j \; w_s \left[\sin(\alpha_n x_0) \text{ Re } [Q(-\frac{1}{3}, -\frac{1}{2}, m, -\frac{\alpha_n w_s}{2})] \right. \\ &\quad \left. + \cos(\alpha_n x_0) \text{ Im } [Q(-\frac{1}{3}, -\frac{1}{2}, m, -\frac{\alpha_n w_s}{2})] \right. \end{aligned} \tag{C.32}$$

References

[1] I. S. Gradshteyn and I. M. Ryshik, "Tables of integrals, series and products", Academic Press, 1965.

[2] H. Bateman, "Tables of integral transforms", McGraw Hill Book Company Inc., 1954.

[3] M. Abramowitz and I.A. Stegun, "Handbook of mathematical functions with formulas, graphs and mathematical tables," National Bureau of Standards, Applied Mathematics, Series 55, 1964.